TUDelft

Delft University of Technology

Spatiotemporally Resolved Corrosion Inhibition Studies of Lithium Salts for Aerospace Aluminium Alloys

Li, Z.

DOI
10.4233/uuid:6beced66-bea9-4dcd-984f-8c9244846acd

Publication date
2024

Document Version
Final published version

Citation (APA)
Li, Z. (2024). *Spatiotemporally Resolved Corrosion Inhibition Studies of Lithium Salts for Aerospace Aluminium Alloys*. [Dissertation (TU Delft), Delft University of Technology]. https://doi.org/10.4233/uuid:6beced66-bea9-4dcd-984f-8c9244846acd

Important note
To cite this publication, please use the final published version (if applicable).
Please check the document version above.

Spatiotemporally Resolved Corrosion Inhibition Studies of Lithium Salts for Aerospace Aluminium Alloys

Spatiotemporally Resolved Corrosion Inhibition Studies of Lithium Salts for Aerospace Aluminium Alloys

Dissertation

for the purpose of obtaining the degree of doctor
at Delft University of Technology,
by the authority of the Rector Magnificus Prof. dr. ir. T.H.J.J. van der Hagen,
chair of the Board for Doctorates,
to be defended publicly on
Friday June 21 2024 at 10:00 o'clock

by

Ziyu LI

Master of Engineering in Materials Science and Engineering,
University of Science and Technology Beijing, China.
Born in Shandong, China.

This dissertation has been approved by the promotors.

Composition of the doctoral committee:

Rector Magnificus   Chairman
Prof. dr. ir. J.M.C. Mol   Delft University of Technology, promotor
Dr. ir. A.M. Homborg   Delft University of Technology, copromotor
Dr. Y. Gonzalez-Garcia   Delft University of Technology, copromotor

Independent members:

Prof. dr. J. Dik   Delft University of Technology
Prof. dr. M. L. Zheludkevich University of Kiel / Helmholtz-Zentrum Hereon
Prof. dr. M.G. Olivier   University of Mons
Prof. dr. C. Blanc   Université de Toulouse / ENSIACET-INPT
Prof. C.A. Dransfeld   Delft University of Technology, reserve member

Keywords: Hexavalent-chromium-free inhibitor; Lithium-based conversion layer; Electrochemical noise; SECM; Localized corrosion; Corrosion inhibition; Intermetallic particles; Aluminium alloy

Content

Summary

Over many decades, intensive studies have been performed towards safe and sustainable substitutes for chromate corrosion inhibitors in active corrosion protection coatings for aerospace aluminium alloys. The proposed candidates must provide similar corrosion protection as compared to that of chromate-based compounds and be cost-effective for viable introduction in industrial applications. Lithium salts have been recognised for their passivation ability on aluminium alloys through generating a lithium-based conversion layer since the 1980s. In 2010, it was discovered that organic coatings loaded with lithium salts acting as leachable inhibitor provided promising corrosion inhibition under accelerated corrosion test conditions. The formation of a protective layer with a variety of layered configurations is the key feature providing an effective physical barrier to corrosive conditions. Although extensive research has been performed to understand the inhibition mechanism as well as the layer formation process, electrochemical monitoring and local electrochemical imaging during the formation process and subsequent degradation of the lithium-based conversion layer were still lacking.

The scientific objective of this Ph.D. thesis is to gain a more thorough understanding of the formation stages and corrosion mechanism of the lithium-based conversion layer using spatiotemporally resolved electrochemistry and to link the observations to previous findings. The knowledge and understanding of local electrochemical reactions are essential for a profound understanding of the formation and inhibition mechanism and to motivate further optimization of these novel active coating techniques in the future. To this aim, Chapter 2 firstly introduces the current development of lithium-based inhibitor and coating technologies to for the corrosion protection of aluminium alloys.

The electrochemical methods used in this work are electrochemical noise (EN) and scanning electrochemical microscopy (SECM), combined with a number of different surface analytical techniques. The experimental part in this thesis can be divided into two parts: (i) characterisation of the lithium-based conversion layer and its corrosion resistance using EN (Chapters 3 and 4) and (ii) SECM investigations of the formation stages of the conversion layer and its corrosion protection mechanism (Chapters 5 and 6).

Chapter 3 is devoted to the application of EN to monitor the lithium-based conversion layer formation process in real-time and to examine its corrosion protection properties. Three different components were observed in the EN signals, associated with high-, medium- and low-frequency contributions. These could be attributed to the detachment of hydrogen bubbles from the surface, localized corrosion surrounding intermetallic particles (IMPs) and general corrosion, respectively. In addition, the conversion layer was still generally protective even though local damages occurred. In Chapter 4, the influence of ambient ageing on the corrosion resistance of lithium-based conversion layers is investigated using EN. The conversion layers with short ageing times exhibited an initially high noise resistance but a lower protectiveness when localized corrosion occurs. For the case of longer ageing treatments, the conversion layers showed a more stable and higher corrosion resistance. This phenomenon was caused by the instability of the freshly-formed lithium-based conversion layer. At wet regions, the conversion layer continued to develop locally due to the release of lithium carbonate, which contributed to the improvement of the corrosion protection with ageing time.

Chapter 5 is devoted to the application of SECM to characterise the progressive conversion layer formation stages by measuring the local surface reactivity at different formation stages. Three types of IMPs, including the S-, θ- and constituent phase, acted as cathodic areas at the beginning of immersion in a borate buffer solution. The surface reactivity initially exhibited an increasing trend and then gradually decreased until passivation. The passivation over θ- and constituent particles preceded passivation of the S-phase particles. In Chapter 6, the corrosion protection mechanism of the lithium-based conversion layer is studied. For the freshly-formed conversion layer, based on the studies in Chapter 4, further investigation revealed that the entire bilayer structure undergoes a gradual dissolution upon re-immersion in a lithium-free corrosive environment. Localized corrosion mainly occurred at and around the S- and large constituent phase particles. The trenching around the S-phase was caused by the relatively high electrochemical activity, whereas the localized corrosion around large constituent phases was caused by the lower conversion layer corrosion protection. In addition, the corrosion process developed faster around the S-phase, leading to particle undercutting at an earlier stage than for constituent particles.

In this thesis it is shown that EN and SECM are powerful tools which are able to provide corrosion information with high spatial and temporal resolution. Local characterisation at a microscale level is of pivotal importance for further elucidation of the corrosion- and inhibition mechanisms. Once this local activity is linked to the information on real-time corrosion kinetics from EN measurements successfully, this greatly increases the potential of EN for industrial corrosion monitoring.

X

Samenvatting

Decennialang zijn er intensieve onderzoeken uitgevoerd naar duurzame alternatieven voor chromaat-houdende corrosie-inhibitoren in actieve corrosiewerende coatings voor aluminiumlegeringen die worden toegepast in de luchtvaartindustrie. Mogelijk geschikte kandidaten moeten een vergelijkbare corrosiebescherming bieden als die van op chromaat gebaseerde verbindingen en daarbij ook nog kosteneffectief zijn voor daadwerkelijke industriële implementatie. Lithiumzouten staan reeds sinds de jaren tachtig bekend om hun passiveringsvermogen op aluminiumlegeringen door het genereren van een op lithium gebaseerde conversielaag. In 2010 werd ontdekt dat organische coatings met lithiumzouten als uitloogbare inhibitor, veelbelovende corrosiebescherming bieden onder versnelde corrosietestcondities. De aanwezigheid van een beschermende laag met een variërende gelaagde samenstelling vormt een effectieve fysieke corrosiebarrière. Ondanks uitgebreid onderzoek om het inhibitiemechanisme en het laagvormingsproces beter te doorgronden, ontbraken tot nog toe elektrochemische monitoring en lokale elektrochemische analyse, zowel tijdens het vormingsproces als bij het daaropvolgende degradatiemechanisme van de op lithium gebaseerde conversielagen.

Het wetenschappelijke doel van dit proefschrift is het verkrijgen van een dieper inzicht in de vormingsfasen en het corrosiemechanisme van de op lithium gebaseerde conversielaag met behulp van in-situ elektrochemie. Deze waarnemingen worden gekoppeld aan eerdere bevindingen. De kennis en het begrip van lokale elektrochemische reacties zijn essentieel voor een diepgaand begrip van het vormings- en remmingsmechanisme en tevens voor verdere toekomstige optimalisatie van deze nieuwe actieve coatingtechnieken. Teneinde dit doel te bereiken behandelt Hoofdstuk 2 eerst de ontwikkeling van op lithium gebaseerde inhibitoren en bespreekt het inhibitor- en coatingtechnologie voor de corrosiebescherming van aluminiumlegeringen.

De in-situ elektrochemische methoden die in dit werk worden gebruikt zijn elektrochemische ruis (EN) en scanning elektrochemische microscopie (SECM), gecombineerd met een aantal verschillende oppervlakte-analysetechnieken. Het experimentele deel van dit proefschrift bestaat uit twee delen: (i) karakterisering van op lithium gebaseerde conversielagen, inclusief corrosieweerstand, met

behulp van EN (hoofdstukken 3 en 4) en (ii) SECM-onderzoek van de verschillende vormingsfasen en het corrosiebeschermingsmechanisme van de conversielagen (hoofdstukken 5 en 6).

Hoofdstuk 3 is gewijd aan het realtime monitoren van het op lithium gebaseerde vormingsproces van de conversielaag en het onderzoeken van de corrosiebeschermingseigenschappen middels EN. Er werden drie verschillende componenten waargenomen in de EN-signalen, elk geassocieerd met een hoog-, midden- of laagfrequente bijdrage. Deze kunnen worden toegeschreven aan respectievelijk loslating van waterstofbellen van het oppervlak, plaatselijke corrosie rond intermetallische deeltjes (IMP's) en algemene corrosie. Bovendien was de conversielaag in zekere mate nog steeds beschermend, ook al ontstond er lokale aantasting. In Hoofdstuk 4 wordt de invloed van atmosferische veroudering op de corrosieweerstand van op lithium gebaseerde conversielagen onderzocht met behulp van EN. De conversielagen met relatief korte verouderingstijden vertonen aanvankelijk weliswaar een hoge ruisweerstand, maar een lagere beschermingsgraad tegen lokale corrosie. Bij langdurigere verouderingsbehandelingen vertonen de conversielagen een stabielere en hogere corrosieweerstand. Dit fenomeen wordt veroorzaakt door de relatieve instabiliteit van een vers gevormde conversielaag. Bij verdergaande veroudering blijft de conversielaag zich op vochtige locaties plaatselijk verder ontwikkelen door het vrijkomen van lithiumcarbonaat, wat in dat geval bijdraagt aan de verbetering van de corrosiebescherming.

Hoofdstuk 5 is gewijd aan de toepassing van SECM om de progressieve stadia van de vorming van conversielagen te karakteriseren door de lokale oppervlaktereactiviteit in verschillende vormingsstadia te meten. Drie soorten IMP's, waaronder de S-, θ- en samengestelde fase, fungeren als kathodische locaties aan het begin van de blootstelling aan een boraatbufferoplossing. Aanvankelijk vertoont de oppervlaktereactiviteit een stijgende trend, waarna deze geleidelijk afneemt tot aan het stadium van passivatie. De passivatie van de θ- en samengestelde fasen gaat vooraf aan de passivatie van de S-fase. In Hoofdstuk 6 wordt het corrosiebeschermingsmechanisme van de op lithium gebaseerde conversielaag bestudeerd. Voor de vers gevormde conversielaag, gebaseerd op de resultaten uit Hoofdstuk 4, blijkt dat de gehele dubbellaags structuur

geleidelijk in oplossing gaat bij blootstelling aan een lithiumvrije, corrosieve omgeving. Lokale corrosie vindt voornamelijk plaats op en rond de S- en samengestelde fasen. De vorming van diepe putvormige aantasting, of ondermijning, rond de S-fase wordt veroorzaakt door de lokaal relatief hoge elektrochemische activiteit, terwijl lokale corrosie rond de grotere samengestelde fase-deeltjes wordt veroorzaakt door een gebrek aan corrosiebescherming in de onderste conversielaag. Bovendien ontwikkelt het corrosieproces zich rond de S-fase sneller, waardoor deze deeltjes in een eerder stadium worden ondermijnd dan de samengestelde fase-deeltjes.

In dit proefschrift wordt aangetoond dat EN en SECM krachtige technieken zijn die in staat zijn om corrosie-informatie te verschaffen met een hoge resolutie in respectievelijk tijd en ruimte. Lokale karakterisering op microniveau is echter cruciaal voor de verdere bestudering van de verschillende corrosie- en inhibitiemechanismen. Zodra deze lokale activiteit met succes aan EN-signalen wordt gekoppeld, vergroot dit naar verwachting aanzienlijk het potentieel van EN voor industriële corrosiemonitoring.

CHAPTER 1

Introduction

1.1. Background and Motivation

Aluminium represents the legacy base element within contemporary industries, for lightweight applications in both aerospace and automotive sectors, but also beyond. The aluminium matrix can be alloyed with other elements such as magnesium, zinc, copper and silicon, featuring commendable solubility as a primary constituent in alloy formation. Additionally, the addition of other elements (of <1% solubility) such as manganese, chromium, zirconium, titanium etc, serves to adeptly tailor diverse alloy properties during and after processing [1,2]. Aluminium alloys usually require mechanical or thermal treatments to reach desired properties after solidification [3]. Diverse alloying elements contribute to multiple categories of intermetallic phases, generating highly complex and heterogeneous microstructures [4]. These intricate microstructures lead to local degradation upon exposure to corrosive conditions and therefore form a durability challenge for practical applications of aluminium alloys. Adequate surface treatments are necessary strategies to enhance the corrosion resistance of aluminium alloy surfaces by the application of single- or multi-layered protective films [5,6]. As shown in **Fig. 1.1**, a multi-layered structure of an organic coating forms a physicochemical barrier for aircraft structures. In case of physical coating damage, inhibitors loaded in the primer will be released to form a protective layer within the scratch area. Traditionally, the aerospace industry has been adopting intrinsically toxic and carcinogenic hexavalent chromium-based inhibitors as highly effective corrosion inhibition compounds [7].
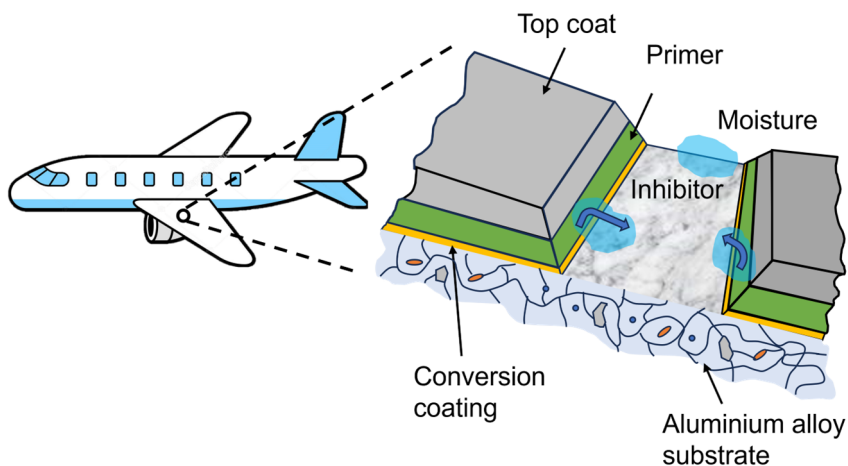
Fig. 1.1 Illustration of the corrosion protective organic coating scheme for aerospace aluminium alloys, adapted from reference [8].

For decades, academic and industrial researchers have studied and assessed many potentially effective, safe and environmentally friendly inhibitor and coating concepts on aerospace aluminium alloys for the replacement of toxic chromate-leaching coatings. Recently, it was shown that organic coatings loaded with lithium salts as corrosion inhibitive compound presented effective corrosion inhibition on aluminium alloys [9–11]. While a series of researches have been conducted to understand the inhibiting mechanism and the protection layer provided by lithium-based conversion coatings, there was a lack of spatiotemporally resolved studies which is essential to understand the progress of the corrosion process and the inhibiting mechanism on a local scale. For this reason, the local electrochemical and chemical reactions occurring as a function of time, remained partially unknown.

The metal corrosion process is typically an electrochemical process at the metal-environment interface during which specific anodic and cathodic sites develop on the metal surface, leading to locally varying micro-chemical environments, such as spatially different pH and metal ion concentration [12]. The addition of an inhibitor will also change the type, sequence and intensity of electrochemical and chemical reaction processes occurring at the anodic and cathodic zones. In general, the size of the anodic and cathodic regions is in the micrometre or even nanometre scale [13]. Therefore, it is difficult to measure and record the local interfacial chemical environment through conventional (electro)chemical characterization methods.

Electrochemical noise (EN) has been proven a powerful tool to monitor corrosion processes in real time, and has been used to identify and quantify localized corrosion, coating failure and screening of corrosion inhibitors [14–16]. EN is a passive detection method, which implies that it will not cause any interference with the corrosion process. However, EN cannot directly identify the location of interfacial electrochemical reactions, which makes it difficult to determine the type of electrochemical and chemical reaction. Scanning electrochemical microscopy (SECM) is a local electrochemical technique, which can provide information on local morphology, electrochemical imaging of electroactive sites and species distribution at the interface with high spatial resolution [17]. As a scanning probe technique, SECM can only be operated in a limited area, which makes it difficult to capture all the details of a corrosion process. Additionally, the scanning nature of SECM mapping does not allow continuous monitoring of time-dependent processes at a specific site. Therefore, the combination of EN and SECM is of vital importance to spatiotemporally resolve corrosion and corrosion inhibition processes.

1.2. Lithium and the corrosion protection of aluminium alloys

The discovery of lithium salts possessing passivation capacity dates back to the late 1980s when Gui and Devine reported the unexpected passivation of aluminium panels polarized in an alkaline lithium-containing solution [18]. Later, Rangel et al. showed the irreversibility of the conversion layer formation reactions using cyclic voltammetry (CV) [19,20].
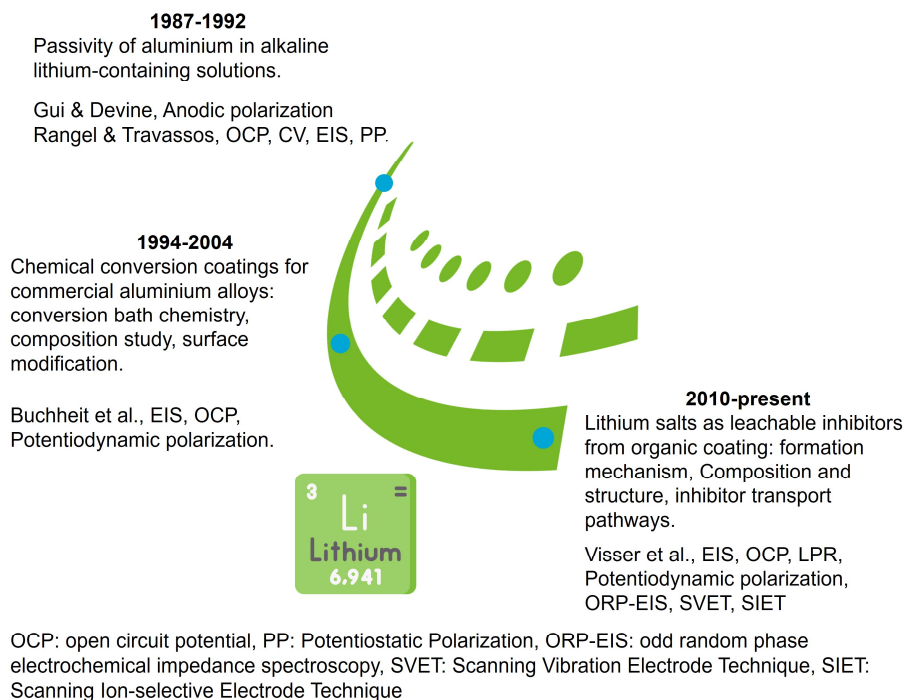
These observations were further investigated by Buchheit et al. in the 1990s. A detailed compositional analysis, conversion process optimization and surface modifications were reported on a variety of commercial aluminium alloys. Their work elucidated that the protective abilities of a lithium-based conversion layer was caused by the formation of a Li-aluminium-hydroxide-carbonate-hydrate layer which belongs to the category of layer double hydroxide (LDH) coatings [21]. Furthermore, it was reported that post-treatment like heating or incorporating inhibiting compounds could effectively enhance the corrosion protection of the conversion coatings [22,23]. Moreover, tuning the chemistry of the conversion bath, such as by adding specific oxidants, were also shown to contribute substantially to the corrosion protection provided by the lithium-based conversion layer. [24]. After this, attempts were made to integrate the lithium-based conversion process into an organic coating system, yet the results were not very satisfactory [25]. Although a number of studies have been performed to optimize the conversion procedures, lithium-based conversion processing still trails traditional chromate-based protection which typically only need several minutes of immersion under ambient conditions to be effective.

In 2010, Visser and Hayes proposed a novel organic coating system where leachable lithium salts were loaded inside the primer to provide active corrosion protection [10]. The promising results after a 168h neutral salt spray test (ASTM B-117) revealed that the corrosion protection was comparable to that of traditional hexavalent chromium inhibitors. Thanks to advanced high-resolution analytical techniques, the distribution of lithium ions inside the organic primer, the morphology and composition of the protective layer on the protected aluminium alloy surfaces were characterized, which benefited the understanding of the protective layer formation mechanism [26,27].

In recent studies, lithium-based conversion layers were formed in a lithium carbonate solution whose concentration was used to mimic the local concentration of lithium carbonate at the artificial coating defect of a lithium-leaching organic coating [28,29].

The results demonstrate that the lithium-based conversion layer consists of a top columnar Li/Al LDH layer and an inner dense lithium-containing pseudoboehmite phase which is shown to be the dominant barrier for corrosion protection. During the conversion immersion period, the Li/Al LDH structure firstly forms on the alloy surface, followed by the formation of the inner layer which is generated under relatively mild pH conditions [30]. For an organic coating system, the leaching rate and varying local pH cause the morphology to be different from that on bare aluminium alloys. The lithium-containing pseudoboehmite appears on the alloy surface first, due to the initial concentration of lithium carbonate and the relatively low pH. With the increase of the local concentration of lithium carbonate and pH, partial lithium-containing pseudoboehmite converts to Li/Al LDH, which is firstly observed at the edge regions of the artificial defect. The Li/Al LDH propagates laterally until the entire exposed surface is covered. Moreover, a middle porous layer which contains both Li/Al LDH and lithium-containing pseudoboehmite might appear locally. Neutral salt spray test with a duration of 2 h (ASTM B117) were shown to be sufficient to provide conditions to obtain a noteworthy improvement of the impedance modulus, indicating that the lithium-leaching coating is able to provide fast and effective corrosion protection [31].

Among the selected electrochemical characterization methods, traditional macroscopic measurements including potentiodynamic polarization, linear polarization resistance (LPR) and electrochemical impedance spectroscopy (EIS) were still dominant, and the characterization resolution at the microscale was limited. **Fig. 1.2** illustrates the main stages of the evolution of the lithium-based coating technology from the very first observations onwards, and the employed common electrochemical characterization methods.

1987-1992
Passivity of aluminium in alkaline lithium-containing solutions.

Gui & Devine, Anodic polarization
Rangel & Travassos, OCP, CV, EIS, PP.

1994-2004
Chemical conversion coatings for commercial aluminium alloys: conversion bath chemistry, composition study, surface modification.

Buchheit et al., EIS, OCP, Potentiodynamic polarization.

2010-present
Lithium salts as leachable inhibitors from organic coating: formation mechanism, Composition and structure, inhibitor transport pathways.

Visser et al., EIS, OCP, LPR, Potentiodynamic polarization, ORP-EIS, SVET, SIET

3 Li = Lithium 6.941

OCP: open circuit potential, PP: Potentiostatic Polarization, ORP-EIS: odd random phase electrochemical impedance spectroscopy, SVET: Scanning Vibration Electrode Technique, SIET: Scanning Ion-selective Electrode Technique

Fig. 1.2 Evolution of the lithium-based coating technology and relevant electrochemical characterization methods.

1.3. Research aims and experimental approach

The scientific objective of this study is to spatiotemporally resolve the evolution of the interfacial electrochemical reactions during the lithium-based conversion layer formation and its corrosion protective behaviour in a lithium-free corrosive electrolyte by the implementation of EN and SECM. Electrochemical measurements are linked to the morphological and compositional evolution using microscopic surface characterization techniques. Therefore, the investigations presented in this thesis can be divided into three main parts, i.e. studies on:

a)   The application of EN to temporally resolve the lithium-based conversion layer growth on AA2024-T3;

b)   The influence of ambient ageing of freshly formed lithium-based conversion layers on AA2024-T3 on its corrosion protective properties using EN;

c) The understanding of the different stages of the formation and the corrosion protective performance of the lithium-based conversion layer on AA2024-T3 in lithium-free solutions using SECM.

1.4. Outline of the thesis

The structure of the thesis is illustrated graphically in **Fig. 1.3**. The current chapter introduces the research motivation, discusses the commonly applied electrochemical methods in previous studies and briefly describes the research approach. Subsequently, Chapter 2 (literature review) is devoted to a detailed description and summary of the state-of-the-art of lithium-based inhibitor and coating technology. Also, several challenging future scientific topics are proposed. Chapters 3 and 4 are devoted to studying the possibility of using EN to characterize the lithium-based conversion layer. Chapter 3 focuses on the temporally resolved characterization during the lithium-based conversion layer formation and the corrosion behaviour of the freshly formed conversion layer. Chapter 4 describes the influence of ambient ageing post-treatment on the corrosion protective performance of a freshly formed lithium-based conversion layer using EN. Chapter 5 investigates the application of SECM in the study of the different local morphological and electrochemical evolution stages of the conversion layer at and around different intermetallic particles. Chapter 6 focuses on the study of the corrosion protection mechanism of the freshly formed and ambiently aged lithium-based conversion layer in a lithium-free NaCl solution using SECM and EN. Finally, overall conclusions and recommendations are drawn in Chapter 7.
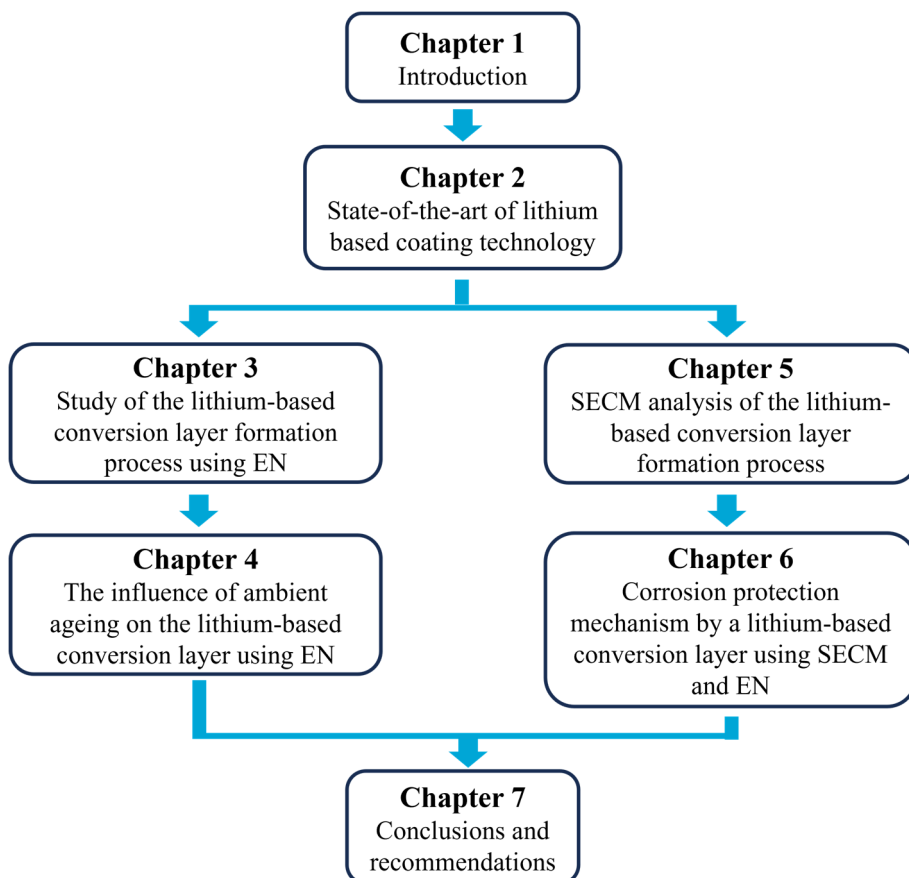
Fig. 1.3 Thesis outline.

References

[1] A. E., N. Birbilis, J. M.C., S. J., X. Zhou, G. E., High Strength Al-Alloys: Microstructure, Corrosion and Principles of Protection, in: Z. Ahmad (Ed.), Recent Trends Process. Degrad. Alum. Alloys, InTech, 2011.

[2] N. Birbilis, T.H. Muster, and R.G. Buchheit, Corrosion of Aluminum Alloys, in: Corros. Mech. Theory Pract., 3rd ed., CRC Press, 2011.

[3] J.G. Kaufman, Introduction to Aluminum Alloys and Tempers, ASM International, 2000.

[4] A. Boag, A.E. Hughes, A.M. Glenn, T.H. Muster, D. McCulloch, Corrosion of AA2024-T3 Part I: Localised corrosion of isolated IM particles, Corros. Sci. 53 (2011) 17–26.

[5] R.L. Twite, G.P. Bierwagen, Review of alternatives to chromate for corrosion protection of aluminum aerospace alloys, Prog. Org. Coat. 33 (1998) 91–100.

[6] P. Visser, H. Terryn, J.M.C. Mol, Aerospace Coatings, in: A.E. Hughes, J.M.C. Mol, M.L. Zheludkevich, R.G. Buchheit (Eds.), Act. Prot. Coat. New-Gener. Coat. Met., Springer Netherlands, Dordrecht, 2016: pp. 315–372.

[7] O. Gharbi, S. Thomas, C. Smith, N. Birbilis, Chromate replacement: what does the future hold?, Npj Mater. Degrad. 2 (2018) 12.

[8] F.H. Scholes, S.A. Furman, A.E. Hughes, T.A. Markley, Corrosion in artificial defects. I: Development of corrosion, Corros. Sci. 48 (2006) 1812–1826.

[9] P. Visser, Y. Liu, H. Terryn, J.M.C. Mol, Lithium salts as leachable corrosion inhibitors and potential replacement for hexavalent chromium in organic coatings for the protection of aluminum alloys, J. Coat. Technol. Res. 13 (2016) 557–566.

[10] P. Visser, Y. Liu, X. Zhou, T. Hashimoto, G.E. Thompson, S.B. Lyon, L.G.J. van der Ven, A.J.M.C. Mol, H.A. Terryn, The corrosion protection of AA2024-T3 aluminium alloy by leaching of lithium-containing salts from organic coatings, Faraday Discuss. 180 (2015) 511–526.

[11] P. Visser, S. Ranade, J.S. Laird, A.M. Glenn, A.E. Hughes, H. Terryn, J.M.C. Mol, Li leaching from Li carbonate-primer: Transport pathway development from the scribe edge of a primer/topcoat system, Prog. Org. Coat. 158 (2021) 106284.

[12] N. Jadhav, V.J. Gelling, Review—The Use of Localized Electrochemical Techniques for Corrosion Studies, J. Electrochem. Soc. 166 (2019) C3461–C3476.

[13] A. Kosari, H. Zandbergen, F. Tichelaar, P. Visser, P. Taheri, H. Terryn, J.M.C. Mol, In-situ nanoscopic observations of dealloying-driven local corrosion from surface initiation to in-depth propagation, Corros. Sci. 177 (2020) 108912.

[14] A.M. Homborg, T. Tinga, E.P.M. van Westing, X. Zhang, G.M. Ferrari, J.H.W. de Wit, J.M.C. Mol, A Critical Appraisal of the Interpretation of Electrochemical Noise for Corrosion Studies, CORROSION 70 (2014) 971–987.

[15] R.A. Cottis, Interpretation of Electrochemical Noise Data, CORROSION 57 (2001) 265–285..

[16] S.S. Jamali, A critical review of electrochemical noise measurement as a tool for evaluation of organic coatings, Prog. Org. Coat. (2016) 12.

[17] D. Polcari, P. Dauphin-Ducharme, J. Mauzeroll, Scanning Electrochemical Microscopy: A Comprehensive Review of Experimental Parameters from 1989 to 2015, Chem. Rev. 116 (2016) 13234–13278.

[18] J. Gui, T.M. Devine, Influence of lithium on the corrosion of aluminum, Scr. Metall. 21 (1987) 853–857.

[19] C.M. Rangel, M.A. Travassos, The passivation of aluminium in lithium carbonate/bicarbonate solutions, Corros. Sci. 33 (1992) 327–343.

[20] C.M. Rangel, M.A. Travassos, R.C. Newman, Lithium based chemical conversion coatings for aluminum alloys, (1996).

[21] C.A. Drewien, M.O. Eatough, D.R. Tallant, C.R. Hills, R.G. Buchheit, Lithium-aluminum-carbonate-hydroxide hydrate coatings on aluminum alloys: Composition, structure, and processing bath chemistry, J. Mater. Res. 11 (1996) 1507–1513.

[22] R.G. Buchheit, G.E. Stoner, Chromate-free corrosion resistant talc coatings for aluminum alloys, Sandia National Labs., Albuquerque, NM (United States), 1992.

[23] H. Guan, R.G. Buchheit, Corrosion Protection of Aluminum Alloy 2024-T3 by Vanadate Conversion Coatings, CORROSION 60 (2004) 284–296.

[24] W. Zhang, R.G. Buchheit, Hydrotalcite Coating Formation on Al-Cu-Mg Alloys from Oxidizing Bath Chemistries, CORROSION 58 (2002) 591–600.

[25] R.B. Leggat, W. Zhang, R.G. Buchheit, S.R. Taylor, Performance of Hydrotalcite Conversion Treatments on AA2024-T3 When Used in a Coating System, CORROSION 58 (2002) 322–328.

[26] A. Kosari, P. Visser, F. Tichelaar, S. Eswara, J.-N. Audinot, T. Wirtz, H. Zandbergen, H. Terryn, J.M.C. Mol, Cross-sectional characterization of the conversion layer formed on AA2024-T3 by a lithium-leaching coating, Appl. Surf. Sci. 512 (2020) 145665.

[27] K. Marcoen, P. Visser, G.F. Trindade, M.-L. Abel, J.F. Watts, J.M.C. Mol, H. Terryn, T. Hauffman, Compositional study of a corrosion protective layer formed by leachable lithium salts in a coating defect on AA2024-T3 aluminium alloys, Prog. Org. Coat. 119 (2018) 65–75.

[28] P. Visser, Y. Gonzalez-Garcia, J.M.C. Mol, H. Terryn, Mechanism of Passive Layer Formation on AA2024-T3 from Alkaline Lithium Carbonate Solutions in the Presence of Sodium Chloride, J. Electrochem. Soc. 165 (2018) C60–C70.

[29] A. Kosari, F. Tichelaar, P. Visser, H. Zandbergen, H. Terryn, J.M.C. Mol, Laterally-resolved formation mechanism of a lithium-based conversion layer at the

matrix and intermetallic particles in aerospace aluminium alloys, Corros. Sci. 190 (2021) 109651.

[30] A. Kosari, F. Tichelaar, P. Visser, P. Taheri, H. Zandbergen, H. Terryn, J.M.C. Mol, Nanoscopic and in-situ cross-sectional observations of Li-based conversion coating formation using liquid-phase TEM, Npj Mater. Degrad. 5 (2021) 1–9.

[31] P. Visser, M. Meeusen, Y. Gonzalez-Garcia, H. Terryn, J.M.C. Mol, Electrochemical Evaluation of Corrosion Inhibiting Layers Formed in a Defect from Lithium-Leaching Organic Coatings, J. Electrochem. Soc. 164 (2017) C396–C406.

CHAPTER 2

Review of the State of Art of Li-based Inhibitors and Coating Technology[1]

Abstract

The quest for novel alternatives to hexavalent-chromium-based corrosion inhibitors is of utmost significance and urgency. Strict international health and safety regulations, due to growing concerns regarding the impact of hexavalent chromium on human health and the environment, have pushed the commercial introduction of many alternative inhibitor types, but the implementation of alternative active protective primers for structural parts in the aerospace industry is still pending. This endeavour has proven to be remarkably challenging, as the potential replacement coating types must meet numerous functional requirements encompassing cost-effectiveness and exceptional corrosion protection for intrinsically corrosion susceptible aerospace aluminium alloys. In recent years, considerable attention has been drawn to lithium salts as environmentally friendly corrosion inhibitors forming the basis for a novel active protective coating technology. The involvement of lithium ions has been shown to play a pivotal role in the conversion process of aluminium alloy surfaces by stabilizing the reaction products, thereby facilitating the gradual development of a protective layer with a multi-layered configuration, which exhibits considerable variability in morphology, depending on local chemical and electrochemical conditions. The versatility of the lithium-based corrosion protection extends to their application as corrosion inhibiting pigments in organic coatings or as a pre-treatment, directly forming conversion layers, thereby enhancing their practical implementation. However, previous chromate replacement reviews only introduced the promising outcomes provided by the lithium technology, omitting key details of its development and formation mechanism. This paper critically reviews and summarizes the studies conducted to date on lithium-based inhibitor technologies for the corrosion protection of aluminium alloys as well as topics to be investigated in the future.

2.1. Introduction

Aerospace aluminium alloys have found extensive use in the aerospace industry and other transport sectors due to their notably high strength-to-weight ratio, favourable elastic moduli, malleability, formability, and cost-effectiveness [1–4]. Alloying elements which form various hardening precipitates significantly enhance the mechanical properties of aluminium alloys [5]. However, the addition of multiple elements also contributes to a complex and highly heterogeneous microstructure which makes aluminium alloys susceptible to localized corrosion [4,6–8]. Therefore, the corrosion protective demands in practical applications for reliable and effective pre-treatments and coatings applied to aluminium alloys are enormous [9]. For decades, the application of hexavalent-chromium-based inhibitors by spraying or immersing metallic parts into chromate-based aqueous solutions and by leaching from chromate-containing organic coatings for the protection of aluminium alloys have been a reliable corrosion protection strategy with an extensive track record [10–14]. Hexavalent chromium compounds have long been used as effective inhibitors due to their ability to form a dense, active and self-healing corrosion protective layer on the surface of various aluminium alloys, providing excellent corrosion protection [15]. However, the toxicity and environmental concerns associated with hexavalent chromium inhibitors have led to a growing and urgent demand for alternative, environmentally friendly inhibitors [13,16].

In response to this demand, significant efforts have been implemented for the exploration of chromate-free protective schemes for industrial applications. These processes can be mainly divided into two groups: chromate-free pre-treatments and chromate-free organic coatings [17–24]. Ideally, these alternative processes should exhibit similar performances to chromates, i.e., providing effective corrosion protection to the substrate under various harsh service environments and manifesting self-healing properties when defects are generated on the protected surfaces. For surface treatments, various technologies including molybdate [25], vanadate [26], permanganate [27], phosphates [28], silanes [29], sol-gels [30], and rare earth-based compounds [31,32] etc for chemical conversion coatings, have been proposed. As for organic coating systems, most of the recommended inhibitors are inorganic based, such as vanadate [33] and praseodymium [34] as leaching inhibitors, and Mg-rich or Al-rich primers [35,36] as galvanic inhibition strategies. Lithium (Li) salts possess the advantages of being promising candidates, both as chemicals for conversion treatments [20,37,38] and as compounds that are leachable from organic coatings [39–43].

The introduction of Li in the scope of pretreatments dates back to the 1980s when Gui et al. [38] generated a Li-based conversion layer on AA6061-T6 by applying anodic polarization in a deaerated Li_2CO_3 solution. The resulting passivation effect was not observed when the panels were tested in Li-free carbonate solutions. Similarly, local passivation of the crack wall observed from Al-Li alloy 2090 was enabled under an alkaline and CO_2-bearing environment [44], but this dilute Li containing environment could not generate a uniform passivation layer over the entire alloy surface. Rangel et al. [45,46] then provided evidence for the irreversible formation of a Li-based conversion layer, applied in a conversion bath of 0.5 M Li_2CO_3, using cyclic voltammetry on pure aluminium coupons. In addition, it was also noticed that the presence of oxygen is a key factor for the growth of the Li-based conversion layer under open circuit potential (OCP) conditions. Besides the commonly employed Li_2CO_3, LiOH or Li_2SO_4 were noted to enable passivation of aluminium alloys as well [45,46]. A detailed compositional analysis, conversion process optimization and surface modifications were reported by the pioneering work from Buchheit et al. [20,21,37,47–55] for a variety of commercial aluminium alloys. In the beginning, using a higher concentration (0.1 M) of Li_2CO_3 combined with LiOH for pH adjustment, an immersion duration of 15 mins under OCP was applied to produce an effective protective film, which made it more suitable for industrial applications. However, this process duration is still longer than traditional chromate-based conversion treatments, which is usually no more than 180 s at ambient conditions [56]. X-ray diffraction analysis revealed that the composition of the film was mainly polycrystalline $Li_2[Al_2(OH)_6]_2CO_3 \cdot nH_2O$, which is a common Li/Al layered double hydroxide (LDH) layer [37,57]. Later, further studies indicated that elevating the conversion bath temperature, the addition of oxidizing agents to the conversion bath and post heat treatment of the freshly-formed conversion layer in air or distilled water, produced a film with a higher corrosion resistance by effectively reducing the porosity of the conversion layer [54]. Furthermore, the addition of transition- or rare earth compounds into the freshly-formed conversion layer provides the LDH layer with enhanced corrosion protection and self-healing abilities [58–60]. For instance, it was shown that a Li/Al LDH-based conversion layer sealed by immersion in Ce-containing solutions, exhibits self-healing behaviour due to the presence of Ce ions [61]. Earlier studies were usually performed at a relatively high concentration and high pH of Li_2CO_3 (e.g., 0.05 M or 0.1 M) [38].

The protective layer formation process by leaching from coatings shows notable differences compared to that for the "static" conversion process within the electrochemical cell. Immersion of aluminium alloys in a lower concentration of Li_2CO_3 (0.01 M) was investigated only recently, since this specified concentration was believed to be comparable to the local concentration of Li_2CO_3 within an exposed artificial scratch in an organic coating, loaded with Li_2CO_3 [62–65]. In other words, a simplified environment was created to mimic the local environment involving a complex organic coating system. An artificial scratch deep into the alloy surface was created to evaluate the active corrosion protection process [39,40]. Visser et al. [39,66] have incorporated Li salts, such as Li_2CO_3 and Li-oxalate in polyurethane and epoxy coatings and studied the leaching of the Li ions and the active corrosion protective properties in a scribe after exposure to continuous salt spray testing (ASTM B117) and demonstrated the formation of a protective Li-containing layer. Marcoen et al. [67] monitored the leaching of Li salts into a coating defect as a function of salt spray exposure time by time-of-flight secondary ion mass spectrometry (ToF-SIMS). The scribes were completely covered with a Li-containing protective layer within 15 min. Initially, a Li-pseudoboehmite barrier layer formed on the substrate surface and after longer exposure times, Li/Al LDH started to form and eventually covered the surface. Trentin et al. [68] investigated the role of Li salts in PMMA-silica coatings. They found that increasing the Li_2CO_3 loading could enhance the corrosion protection, and the incorporation of Li ions resulted in significant modification of the hybrid structure through the formation of a dense and highly cross-linked hybrid network. Subsequent work studied the ion transport pathways within the organic coating and revealed its complex diffusion mechanism [69,70]. These studies enable researchers to understand how Li-based inhibitors are delivered from the primer matrix when exposed to an electrolyte and hence allow the further development of a complex coating constitution for optimal leaching kinetics. Apart from the corrosion protection of aerospace aluminium alloys, applications of Li salts to Portland cement paste containing an aluminium substrate were reported recently [71]. AA1100 encapsulated in Portland cement pastes is effectively protected with the addition of $LiNO_3$ or Li_2CO_3 through the formation of a protective film.

More recently studies of the Li-based conversion process already have moved into the microscale or nanoscale level to help elucidate the mechanism of the growth stages and influential factors which are important for the realization of a relatively fast formation rate and enhanced corrosion protection [72]. **Fig.2.1** summarises (i)

the performance and formation mechanism of the Li-based conversion coatings, (ii) the performance and action of inhibitors at Li leaching organic coating defects, and (iii) its in-coating mobility and leaching properties based on previous work, which will be subsequently presented in further detail in the next sections. Finally, this review provides a concise outlook on the overall applications of Li salts for the corrosion protection of aluminium alloys.
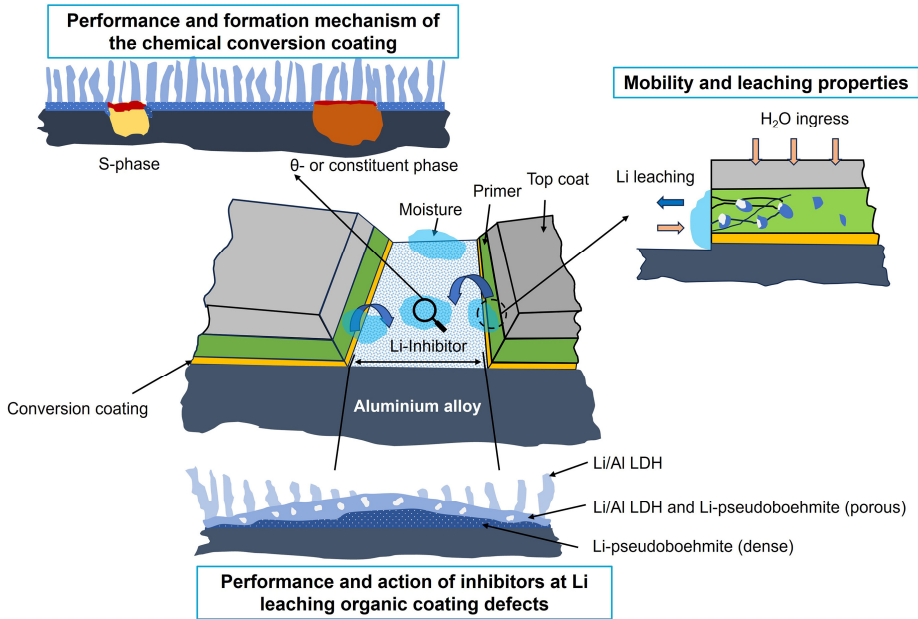
Fig. 2.1 Li-based inhibitors and coating technology including (i) the performance and formation mechanism of the chemical conversion coating, (ii) the performance and action of inhibitors at Li leaching organic coating defects, and (iii) the mobility and leaching properties of Li salts.

## 2.2. Li-based chemical conversion coating performance and mechanism

LDH materials represent a class of compounds categorized as anionic clays, exhibiting intricately adjustable brucite-like structures [73]. These compounds exhibit a distinct arrangement wherein mixed metal M^I/M^{II} and M^{III}/M^{IV} hydroxide layers exhibit a positive charge, which is counterbalanced by anions (denoted as A^{y-}) and water molecules within the interlayered region. The major group of LDHs can be formulated as $[M^{II}_{1-x}M^{III}_x(OH)_2]^{x+}(A^{y-})_{x/y} \cdot nH_2O$, where M^{II} and M^{III} are

divalent and trivalent metal cations, respectively, and A^{y-} represents the interlayer anions, x is in the range of 0.22–0.33 [74]. The isomorphous replacement of trivalent cations for divalent cations in the hydroxide layer of LDHs leads to excess positive charges in the layer. LDH chemical conversion coatings have attracted attention recently as corrosion protective films for various metal substrates [75–79]. LDHs have gained significant attention in the realm of corrosion protection owing to their characteristics including cost-effectiveness, high surface area, favourable adhesion to substrates, eco-friendly nature, ion-exchange capabilities, self-healing, and the accessibility of a diverse array of anionic and cationic components [80–82]. For instance, a Zn/Al LDH layer was synthesized on AA2024-T3 including the intercalation of the inhibitor diethyldithiocarbamate through an ion-exchange procedure, which provided active corrosion protection to the substrate [82]. Vieira et al. [83] reported that the corrosion protection provided by the Mg/Al LDH conversion coating could be extended by the release of incorporated Ce ions. Except for serving as a physical barrier layer, LDH particles could be doped into sol-gel coating systems to enhance the corrosion protection through absorbing aggressive anion ions or releasing stored inhibitors [84–86].

In addition to M^{II}/M^{III} compositional LDHs, another distinct category of LDHs is represented by Li/Al LDHs, bearing the formula $[LiAl_2(OH)_6]^+ A_{1/y}^{y-} \cdot nH_2O$. Within the framework of the Li/Al LDH structure, the Li cations are positioned in the unoccupied octahedral sites within the aluminium hydroxide layer, where the aluminium ions occupy two-thirds of these octahedral sites, thereby contributing to the positive charges characterizing the hydroxide layer [74]. The process of intercalating Li salts into the structures necessitates the perturbation of the hydrogen bonding networks, along with the reconfiguration of the hydroxide layers. Notably, a previously reported activation energy of 27 kJ mol^{-1} has been associated with the intercalation reaction of gibbsite involving Li species [87]. In addition, the intercalation process is reversible. For instance, the de-intercalation process occurs when the freshly-formed Li/Al LDH is exposed to a Li-free liquid environment leading to crystalline aluminium hydroxide products [88]. A detailed structure of Li/Al LDHs and its de-intercalation through calcination is provided in **Fig. 2.2** [89]. The reversible intercalation capability has been widely used in the extraction and collection of Li ions from salt lake brines [90–92]. It has been reported that the Li/Al LDH layer retains the highest charge density of all LDHs, thus indicating a higher anion exchange capacity as compared to other types of LDHs [93].

LDH conversion coatings grown on metallic substrates can be prepared generally using one step in-situ growth or co-precipitation methods [94]. The process of co-precipitation is based on crystallization of LDH in an alkaline solution containing M^{I} and/or M^{II} and M^{III} cations precursors. The metal substrate is also a source of metal cations. However, for the case of one step in-situ growth method, all cations must originate from the metal substrate, which makes it limited to certain alloys. Heating usually is necessary for the effective crystallization of LDH coatings for which temperature elevation, hydrothermal growth, and steam treatment are common heating procedures [94].
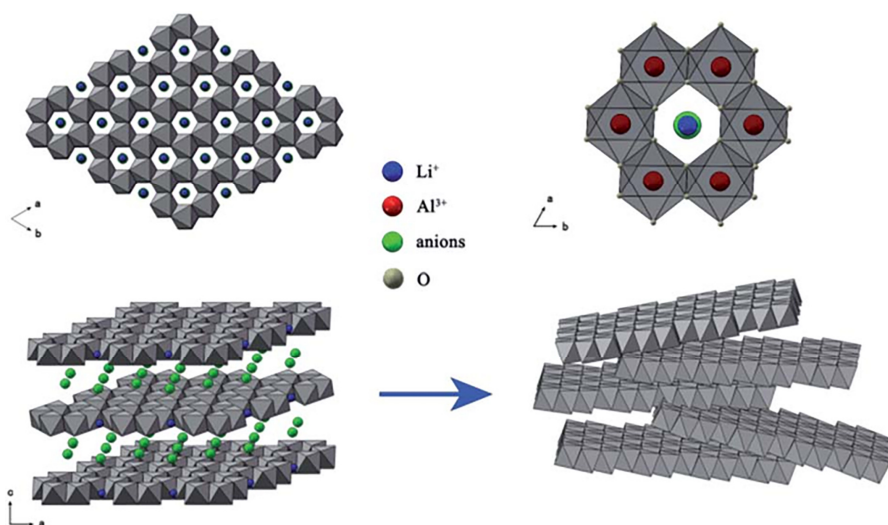

Fig. 2.2 Crystal structure of Li/Al LDH and its de-intercalation process. Reprinted from [89] with permission from the Royal Society of Chemistry.

One performance criterion for Li-based conversion layers is their stand-alone corrosion protection. Multiple tests performed by Buchheit et al. [47,50,51] like salt spray testing, potentiodynamic polarization, and electrochemical impedance spectroscopy (EIS) were used to evaluate the performance of the Li-based conversion layer in order to determine its eligibility for substituting traditional hexavalent chromium. The structure, properties and performance of the Li-based conversion layers strongly depend on the bath chemistry. For instance, the addition of LiOH for pH adjustment, of aluminate salts for promoting the precipitation, and of oxidants for improving the oxidizing power are necessary to develop high quality conversion layers; the conversion bath solely containing Li_2CO_3 cannot reach the benchmark set

by traditional hexavalent-chromium-based inhibitors [54]. It was observed that the conversion layer improved the corrosion resistance by inhibiting both anodic and cathodic reactions due to the uniformly grown film covering both the aluminium matrix and intermetallic particles (IMPs) [48]. The corrosion protection provided by the conversion layer was sufficient to inhibit pitting corrosion on AA1100 and AA6061-T6 during ASTM B-117 salt spray exposure but failed to provide effective protection on AA2024-T3 based on identical conversion bath procedures, due to the higher Cu content of the latter [48]. In general, the corrosion protection provided by the conversion layers grown over AA2024-T3 is more difficult to pass the salt spray test requirements compared to that of AA6061-T6 under the same procedures since AA2024-T3 is intrinsically less corrosion resistant [50]. Thickening the conversion layer by extending the immersion duration, removing the enriched surface Cu during the conversion growth process, or sealing by incorporating other inhibitors are effective corrosion protection methods to withstand salt spray exposure especially for aluminium alloys with high Cu content [52]. Another factor that should be paid attention to is the self-healing property of the conversion layer. Buchheit et al. [54] observed that AA2024-T3 panels treated in the lithium salt bath containing oxidizing agents presented an increased low-frequency impedance modulus value with exposure time. This "healing" effect may be attributed to the low-temperature hydrothermal sealing of the coating. Another possible reason is that LDH layers can serve as chloride ion sorbent due to their anion exchange abilities. By this way, the chloride scavenging effect hinders chloride ions to reach the surface of the substrate [95,96]. Yan et al. [97] observed the self-healing capacity of a Zn/Al LDH grown on pure aluminium substrates. This self-healing was due to the local dissolution of the original Zn/Al LDH close to the scratch upon exposure to the corrosive electrolyte, which provided suitable conditions for the recrystallization of the Zn/Al LDH at the defect. This mechanism was also postulated to explain the self-healing ability of certain Li/Al LDHs [98,99]. In summary, Li-based conversion layers may be able to provide stand-alone corrosion protection comparable to that provided by traditional hexavalent-chromium-based chemistries, but at the cost of longer immersion time, relatively high energy consumption for application at elevated temperatures and complex and strict application procedures, which may have hampered its introduction in industrial applications. The demonstrated self-repair capability of LDH conversion coatings [97–99] suggests that effective corrosion protection can be achieved even without external inhibitor intercalation; however, a more in-depth exploration of its corrosion protection efficiency is still needed.

The formation process of the Li-based conversion layer includes a rapid dissolution caused by the highly aggressive (pH 13) conversion bath followed by a protective conversion layer growth covering the entire alloy surface. Rangel et al. [45,46] predicted a dual structure of the conversion layers through the interpretation of EIS spectra which was confirmed by Buchheit et al., however, the thickness of the dense layer is very thin under high alkaline conditions [37,52]. Experimental studies have revealed that the aluminium surface undergoes mainly two dissolution and one precipitation stage when exposed to water or alkaline environments: (i) the dissolution of a naturally formed oxide layer and the appearance of an amorphous hydroxide layer, (ii) the dissolution of the amorphous layer to aluminate species, and (iii) the precipitation of these species as hydroxide products [50,100]. As a result, a dual layer with a poorly crystalline boehmite or pseudoboehmite inner barrier layer and a crystal boehmite or bayerite (longer ageing times) outer non-barrier layer. Pseudoboehmite here is more prevalent since it forms rapidly but not readily crystallizes [50]. A highly alkaline solution does not change this procedure but accelerates the dissolution and postpones the precipitation due to a higher solubility of aluminate ions. The presence of Li ions in alkaline solutions also does not change this reaction sequence but will alter the precipitation products, resulting in a more corrosion protective film. Previous studies showed that the outer Li/Al LDH layer here was merely a minor corrosion barrier, the inner layer was the dominant contributor for corrosion protection [62,101]. One example of the Li-based conversion layer structure grown on the aluminium matrix is shown in **Fig. 2.3**, which includes a distinct inner dense layer (red arrow) and a columnar outer layer (blue arrow). Li ions distribute within the entire inner and outer layer (shown in **Fig. 2.4**), and the inner layer mainly consists of Li-pseudoboehmite. It has been reported that amorphous aluminium hydroxide can serve as Li-sorbents to collect Li from brine lakes, and a low Li content limits an effective transformation of amorphous aluminium hydroxide into crystalline Li/Al LDH [102–104].
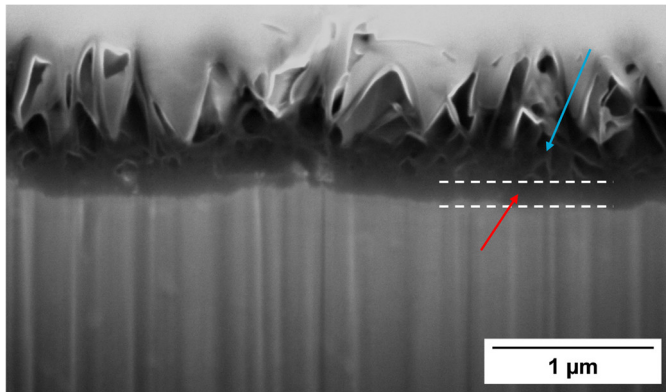
Fig. 2.3 Cross-sectional image of the Li-based conversion layer on AA2024-T3. The panel (Exposed surface: 10 mm in diameter) was immersed in a 0.01 M Li$_2$CO$_3$ and 0.01 M NaCl solution (volume: 0.321 mL) for a duration of 7 h. The red arrow refers to the inner dense layer while the blue arrow indicates the outer columnar layer.

Recent studies conducted by Visser et al. [62] and Kosari et al. [101] discussed the conversion bath containing Li$_2$CO$_3$ and NaCl to establish a detailed Li-based conversion layer formation model. While the Li-based conversion layer immersed in a lower concentration Li$_2$CO$_3$ (0.01 M) failed to provide similar corrosion protection compared to that formed at higher concentrations, the reported conversion layer formation mechanism remained the same. The formation model that was established is provided in **Fig. 2.5**.

TEM image	Al EF-TEM map	Li EF-TEM map
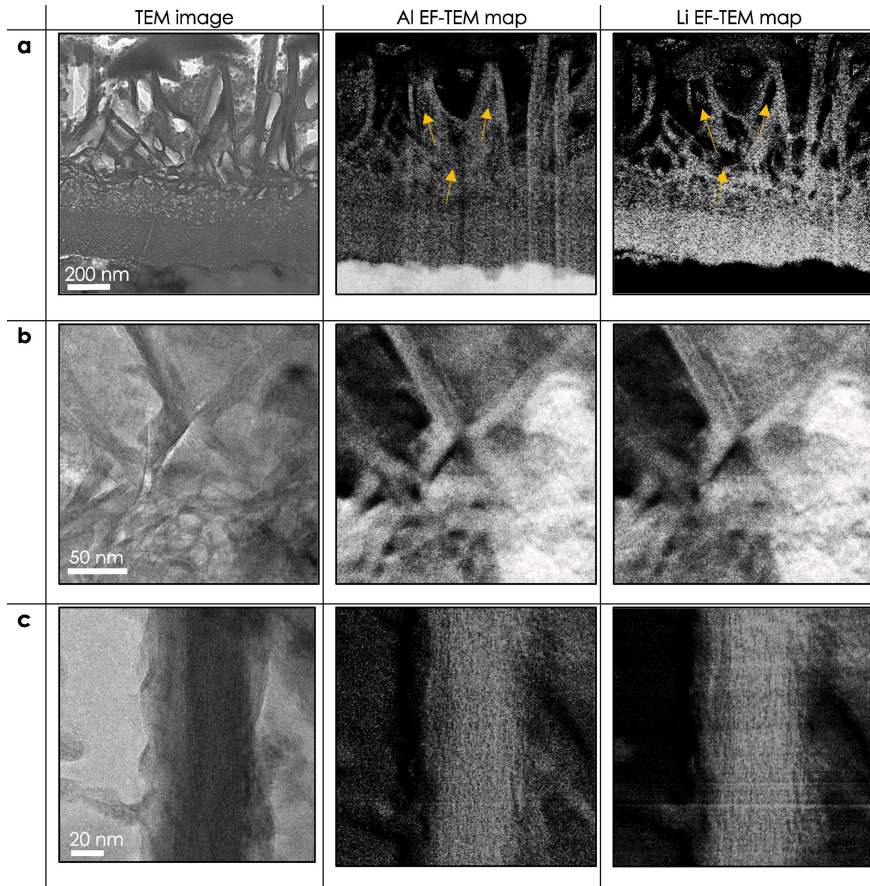
Fig. 2.4 Bright field transmission electron microscopy (TEM) images and the corresponding energy filtered (EF)-TEM maps of Al and Li distribution of the Li-based conversion coating from an Li leaching organic coating sample with defect after 168 h neutral salt spray: (a) the entire layer formed in the peripheral region; the yellow arrows indicate Li-free region, (b) at columnar layer/porous layer interface and (c) a single columnar LDH top layer [105].

The existence of three types of IMPs (S-, θ- and constituent phases) is considered here. The entire formation process discussed in these works can be divided into five stages: After exposure to the aggressive conversion bath (pH ≥ 10), the air-formed oxide layer experiences a fast dissolution followed by the dissolution of the aluminium matrix and the dealloying of IMPs, most notably the electrochemically active S-phase (Stage I) [62,101]. This morphological change is reflected by a sharp drop in the OCP. The initial dissolution rate might differ between intermetallic particles and the Al matrix and even vary within the aluminium matrix [72]. This

phenomenon is caused by the heterogeneous compositional distribution across the aluminium alloy surface. During stage II, the Al matrix still undergoes massive dissolution and the S-phase first exhibits a fast dealloying which results in surface enrichment of Cu, leading to the transition of the S-phase from an anodic to cathodic nature and accompanied by the appearance of trenches around its perimeter [101]. The Cu enrichment drives the OCP in the positive direction. Meanwhile, the crystalline Li/Al LDH is not formed until the concentration of aluminate ions at the alloy/solution interface reaches a supersaturation threshold concentration. Considering the high pH at the alloy/solution interface during the initial stages (I and II), aluminate is more chemically stable in the medium. The decease of pH and gradual saturation of aluminate over time slow down the dissolution kinetics of the aluminium alloy surface, especially when the dissolution front penetrates deeper, thus generating a larger diffusion distance [72]. At stage III, the columnar Li/Al LDH appears when the local concentration of aluminate reaches supersaturation [72,101]. Nevertheless, different regions attain aluminate supersaturation asynchronously. Areas with a higher aluminium dissolution rate reach aluminate supersaturation earlier. For example, the appearance of the top columnar layer over the S-phase on AA2024-T3 precedes that over adjacent aluminium matrix (this even already occurs at the end of stage II), whereas the relatively electrochemically stable θ-phase and constituent phase do not show evidence of the formation of a columnar layer earlier than the aluminium matrix [101]. The aluminium source for the S-phase originates from the dealloying of its aluminium content. The θ-phase and constituent phase both experience a slight dealloying, but this limited dealloying cannot provide sufficient aluminium to support the precipitation of crystal Li/Al LDH. In addition, the newly formed Li/Al LDH may dissolve again at the location closer to the solution side [72]. At stage IV, the size and number of Li/Al LDH plates both increase over the aluminium matrix as well as over the S-phase. Meanwhile, the Li/Al LDH starts to appear over the θ-phase and constituent phase. This local supersaturation is mainly caused by the lateral propagation of the aluminate ions from the adjacent aluminium matrix. Finally, at stage V, the densification of the Li/Al LDH slows down the diffusion process between the metal/LDH interface and the liquid environment, which results in a lower pH at the metal/LDH interface. A lower pH and also a lower supply of Li ions enables the densification and thickening of the inner protective layer. Simultaneously, the top LDH layer exhibits sustained growth via the precipitation of lithium-containing species, leading to the coarsening of its columnar structure. It should be noted that the inner dense layer is absent above S-, θ-, and constituent phases due to an insufficient supply of dissolved aluminium, which may

create weak spots in the protective layer. Upon reaching Stage V, the system attains a state of pseudo-stability, reflected by a plateau in the OCP curve, which is attributed to the passivation effect induced by the mature Li-based conversion layer. Currently, detailed conversion layer formation mechanism analysis is only performed on AA2024-T3. While a similar conversion layer growth mechanism is expected on other commercial aluminium alloys, its investigations are still pending. This is due to the presence of compositionally varying IMPs in various aluminium alloys, potentially giving rise to disparate effects on the local development of the Li-based conversion layer especially at IMPs.
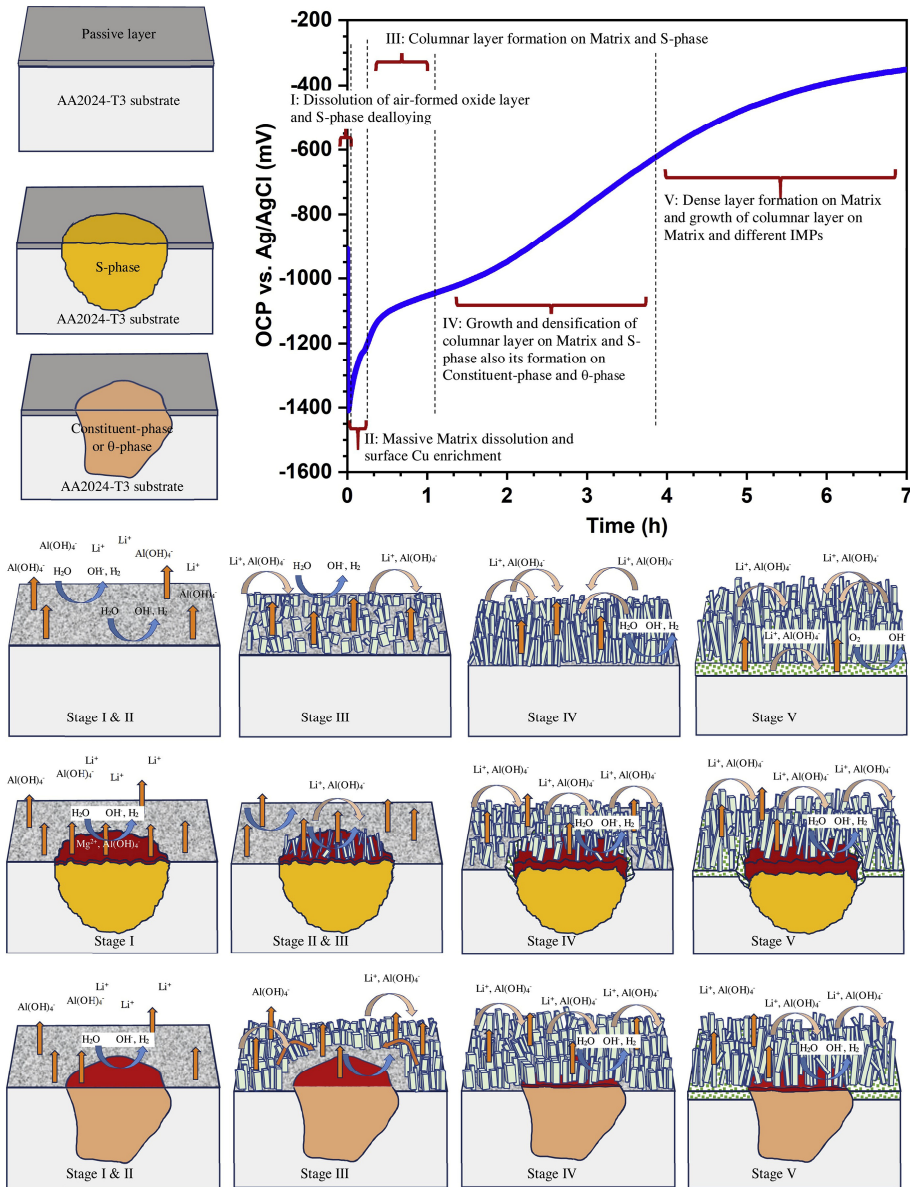
Fig. 2.5 *Schematic overview of the formation mechanism of the Li-conversion layer on AA2024-T3. The conversion layer formation stages are linked to the OCP. This schematic depicts the local morphological variation of the layer formation at the alloy matrix and IMPs [101].*

Usually, for bulk specimens the conversion layer consists of a bilayer structure, whereas ultra-thin samples prepared for liquid-phase TEM (LP-TEM)

characterization contain an extra middle porous structure [72,101]. It has been reported that the porous structure observed for layers formed from the organic coating system consists of a mixture of Li-pseudoboehmite and Li/Al LDH [105]. This difference might be attributed to variations in local liquid environments, which is caused by the different ratio of the exposed surface to the volume of the electrolyte. For the bulk material, a higher surface-to-volume ratio shows a faster pH decrease during the conversion layer growth period since the hydroxyl ions are consumed continuously. A moderate pH is beneficial for the stability of the top columnar layer as well as the formation of the inner dense layer [72]. This explains why the transitional middle porous layer between the outer crystalline LDH layer and the inner dense layer is not observed to grow over the bulk sample, since the local pH close to the conversion layer is less aggressive for the case of bulk samples. In addition, the top LDH layer is very porous and the protective behaviour is dependent on the thickness of the inner barrier layer at the interface between the metal and the protective coating [106].

Based on the formation mechanism mentioned above, several influential conversion bath factors on the Li-based conversion layer growth are discussed here. Local supersaturation of the aluminate ions necessitates the growth of the Li-based conversion layer. Therefore, adding aluminate ions (by dissolution of pure aluminium in the conversion bath or the addition of aluminate salts) into the conversion bath containing lithium salts enables a better performance in salt spray tests [49]. Another finding that supports the importance of the supersaturation of aluminate ions is that the conversion layer formation is very sensitive to the volume of the conversion electrolyte (containing 0.01 M Li_2CO_3) [72]. A small volume of electrolyte generates a conversion layer providing a higher corrosion resistance. The experimental results from Kosari et al. [101] show that it takes several hundreds of seconds to reach local supersaturation, which implies that a certain amount of aluminate ions may diffuse away from the alloy surface and does not contribute to the formation of the Li/Al LDH. A smaller liquid volume is beneficial to restrict the diffusion of aluminate ions. Therefore, it appears that shortening the duration for realizing the supersaturation of aluminate ions favours a high-quality conversion layer formation. Alloying elements also play an important role in the quality of the Li-based conversion layer. Up to now, only the effect of Cu was reported by Buchheit et al., which shows that its presence is detrimental for the quality of the Li-based conversion layer. Aluminium alloy surfaces enriched with Cu generate a thinner conversion layer as compared to Cu-free alloy surfaces [52]. Moreover, a freshly-formed Li-based conversion layer,

generated in a conversion bath at pH 11.5, on AA2024-T3 showed a much higher corrosion resistance after immediate re-immersion in a high pH (approximately 13.5) conversion bath containing Li_2CO_3, LiOH, and $NaAlO_2$. This is due to the removal of the surface enriched Cu when exposed to a high pH solution containing carbonate ions. A possible reason to explain the unfavourable effect of Cu is that it acts as a noble element. Cu enrichment over the alloy surface during the conversion layer formation drastically increases the OCP which impedes the hydrogen evolution for a short period. Meanwhile, a fast dissolution of aluminium is necessary to provide sufficient aluminate ions in order to reach the supersaturation state before the formation of the conversion layer. Therefore, fast cathodic reactions are very important for the counterbalance of the rapid anodic dissolution. Oxygen reduction is insufficient to support a large cathodic current, due to its limited supply by the diffusion through air, which hinders the continuous supply of aluminate ions. This explanation also corresponds to the finding that the conversion bath added with oxidizing agents is favourable to enhance the corrosion resistance of the conversion layer, since these oxidants consume electrons which promotes the aluminium dissolution. The distribution of Cu throughout the entire Li-based conversion layer has been reported before [72], but its influence on the structural stability of the Li-based conversion layer still requires further investigation. Cu aside, the effects of other noble alloying elements still remain uncertain, which necessitates additional study.

Except for a qualified stand-alone corrosion protection capacity provided by the chemical conversion coating, another criterion to evaluate Li-based conversion layers is their interfacial bonding to organic coatings, as well as the overall corrosion protection within a coating system. Some early work performed by Buchheit et al. [53] revealed that Li-based conversion layers prepared by nine different conversion baths showed favourable stand-alone performance compared to bare AA2024-T3, but worse behaviour for an organic coating system, i.e. a Li-based conversion layer covered by commercial primers compared to the non-conversion coated but primed sample. One possible reason lies in the reversibility of the intercalation of the conversion layer formation process. The liberation of ions during the de-intercalation beneath the primer establishes an osmotic gradient, thereby promoting the ingress of water from the external environment.

2.3. Li-based inhibitor coating technology and performance

Apart from the studies on the Li-based chemical conversion layers, the exploration of Li-containing species as leachable corrosion inhibitors that can be incorporated into organic coatings makes notable progress. The incorporation of Li salts in a coating was based on the previous studies of the Li-based chemical conversion coating [47–51,55]. The hypothesis whether it was possible to generate a protective film in a defect directly from a coating was postulated based on this prior work. In 2010, the utilization of Li salts loaded in a coating as a replacement for $SrCrO_4$ primers was first reported by Visser et al. [107], revealing fast, effective and irreversible corrosion protection after a neutral salt spray test exposure for 168 h [39,108]. The primer was a fully formulated polyurethane primer system consisting of the pigment TiO_2 and extenders MgO and $BaSO_4$ and the inhibitor, Li_2CO_3. AA2024-T3 panels were anodized in tartaric-sulfuric acid according to aerospace requirements (AIPI 02-01-003) before spraying the Li-containing primer. The Li-containing primer has been proven to provide comparable corrosion protection as traditional hexavalent-chromium-containing organic coatings [42]. Although Li salts may not be the candidate that offers the highest intrinsic corrosion inhibition properties as compared to certain organic inhibitors like benzotriazole (BTA) [109] and 2-mercaptobenzothiazole (2-MBT) [110] when exposed to an inhibitor-containing electrolyte, they do show the highest remaining inhibition, i.e. irreversibility, when subsequently exposed to a non-inhibitor containing corrosive solution [108]. This irreversibility of corrosion inhibition is an important factor when selecting favourable candidates, especially for long-term corrosion protection after the depletion of loaded inhibitors inside the coating matrix [108]. The results reveal that the Li-based protective layer formed inside a scratch still provides constant corrosion protection even after a re-immersion of 5 days in a Li-free solution, whereas BTA and 2-MBT both present a reversible nature, resulting in severe corrosion of the aluminium alloy in case of a diminishing supply of inhibitors.

Assessment of the protective efficiency of organic coatings loaded with Li salts is commonly achieved through the introduction of an artificial scratch (usually 1mm in width) in these coatings, and comparing its corrosion performance to reference clear coating systems, i.e. in the absence of inhibitors [39–43]. Optical images of different samples are shown in **Fig. 2.6**. After a 168 h salt spray exposure, the scribed reference samples showed the presence of a large number of corrosion products (**Fig. 2.6b**). Localised corrosion such as pitting and intergranular corrosion is observed as well [39]. By contrast, the specimen with Li inhibitors presented negligible corrosion

damage (**Fig. 2.6c,** 2.**6d**)and the substrate of the scribe was shown to be covered with a multi-layered structure [40,111]. **Fig. 2.7** shows a representative structure of the Li-based conversion layer from the artificial defect of a coating sample, which includes a top columnar layer, a porous middle layer, and an inner dense layer. A detailed discussion of this protective coating formation at the coating defect will be presented later.
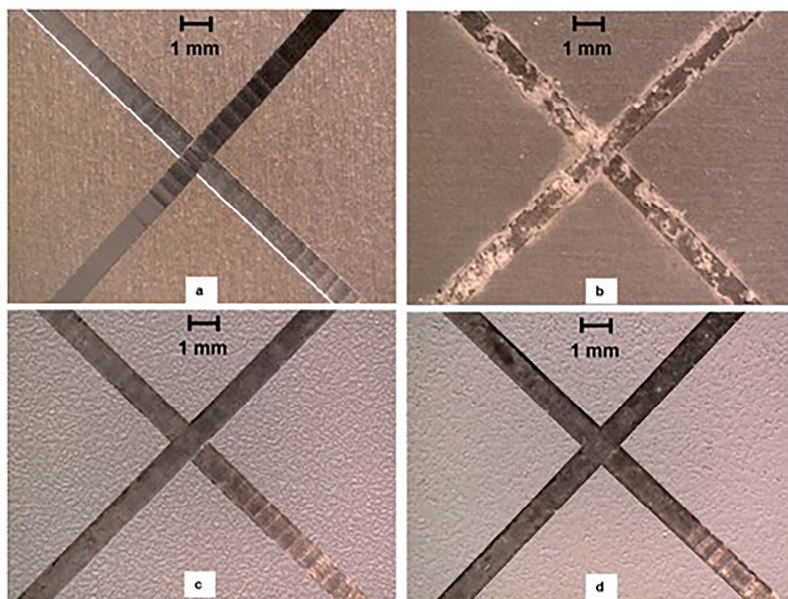
Fig. 2.6 Optical images of coated AA2024-T3 samples with artificial scribes before and after 168 h neutral salt spray exposure (a) unexposed (b) without inhibitor, (c) lithium carbonate loaded and (d) lithium oxalate loaded coating. Reprinted from [39] with permission from the Royal Society of Chemistry.

A quantitative analysis of the corrosion resistance regarding the film generated within the scribed region after the salt spray test has been performed through various electrochemical characterization techniques [40,42,63,64,108,112]. EIS measurements are often performed to characterize the corrosion protective properties of the formed conversion layers [40,108]. It has been reported that the low-frequency impedance modulus values of a Li_2CO_3 containing coating system are about one order of magnitude higher as compared to that of a reference Li-salt free system, and that the low-frequency impedance modulus of a Li-oxalate-loaded sample is about two times higher than that of a Li_2CO_3-containing sample [40,42,106]. Moreover, higher impedance modulus values in the medium frequency range (1-100 Hz) indicate the

formation of a protective film as well. The increased and broadened phase angle values of the lithium-loaded specimens after 168 h salt spray exposure observed in the corresponding Bode plots suggest the formation of a thicker and more stable (oxide) layer in the defect area. Using microcapillary cell techniques [113,114], potentiodynamic polarization measurements can be performed at a small exposed surface in the scribed area after a 168 h salt spray exposure. Compared to the unexposed samples, the corrosion current for samples loaded with Li salts reduces almost one order of magnitude and the corresponding pitting potential drastically rises up to more than 1500 mV vs. AgCl, 3M KCl [42]. It should be noted however that the results present a scattered distribution due to the heterogeneous nature of the coating layer and substrate, as a result of different local chemical conditions during its formation. A duration of 2 hours of exposure to a salt spray test has been documented to be a noteworthy improvement of the impedance modulus value in the low- and mid-frequency range since the protective film, especially the inner dense layer, starts to cover the exposed surface effectively [106]. Furthermore, an investigation into the efficacy of a Li_2CO_3-loaded coating has revealed an inhibition efficiency of approximately 80% within 2 h of exposure, which subsequently increases to an impressive 95% after 48 h. Remarkably, this heightened level of inhibition remains relatively stable, even after prolonged exposure times.
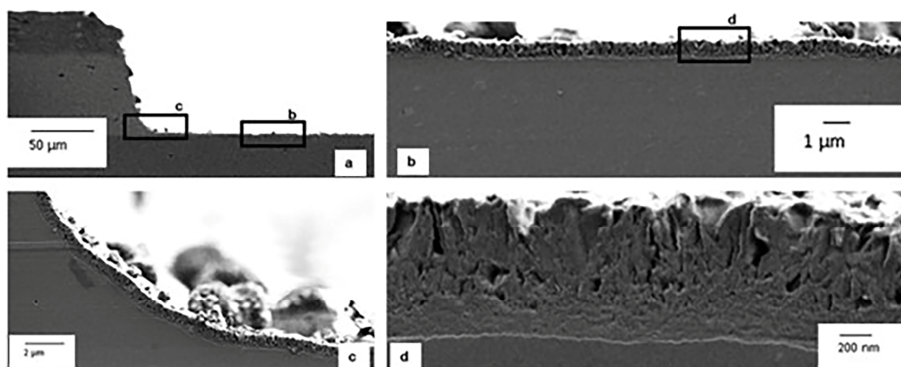
Fig. 2.7 SEM cross-sectional views of protective layers generated from a lithium carbonate loaded coating after 168 h neutral salt spray exposure (a) scribed area, (b) middle region of the scribe, (c) curved location of the bottom of the scribe, (d) detailed multi-layered morphology of the conversion layer. Reprinted from [39] with permission from the Royal Society of Chemistry.

Up to now, most measurements and analysis on coating samples were focused on AA2024-T3. For other aluminium alloys, the evaluation of the corrosion protection

of Li salts leaching organic coating was performed on AA7075, AA5083, and AA6014 so far [111]. **Fig. 2.8** shows the fitting results from EIS measurements for samples with artificial scratches before and after the 168 h neutral salt spray test. R_{oxide} and C_{oxide} indicate the resistance and capacitance values of the oxide layer, respectively, which refers to the native oxide layer for the case without inhibitors, and the inner dense layer for the samples loaded with inhibitors. R_{pol} and C_{dl} represent the polarisation resistance and the double layer capacitance at the metal/oxide interface, respectively. It is obvious that the trend of increased resistances and decreased capacitances is identical for AA2024, AA7075, and AA5083, which is consistent with the presence of the Li-containing protective layer in the defect area. AA2024 still presents the lowest corrosion resistance but the highest inhibiting effect is realized in the presence of Li_2CO_3. The distinct behaviour of AA6014 is attributed to its intrinsic self-passivating property. These tests indicate that the active protective behaviour of Li leaching organic coatings is to a certain extent relatively independent on the metallurgy nature and complexity of the aluminium alloys.
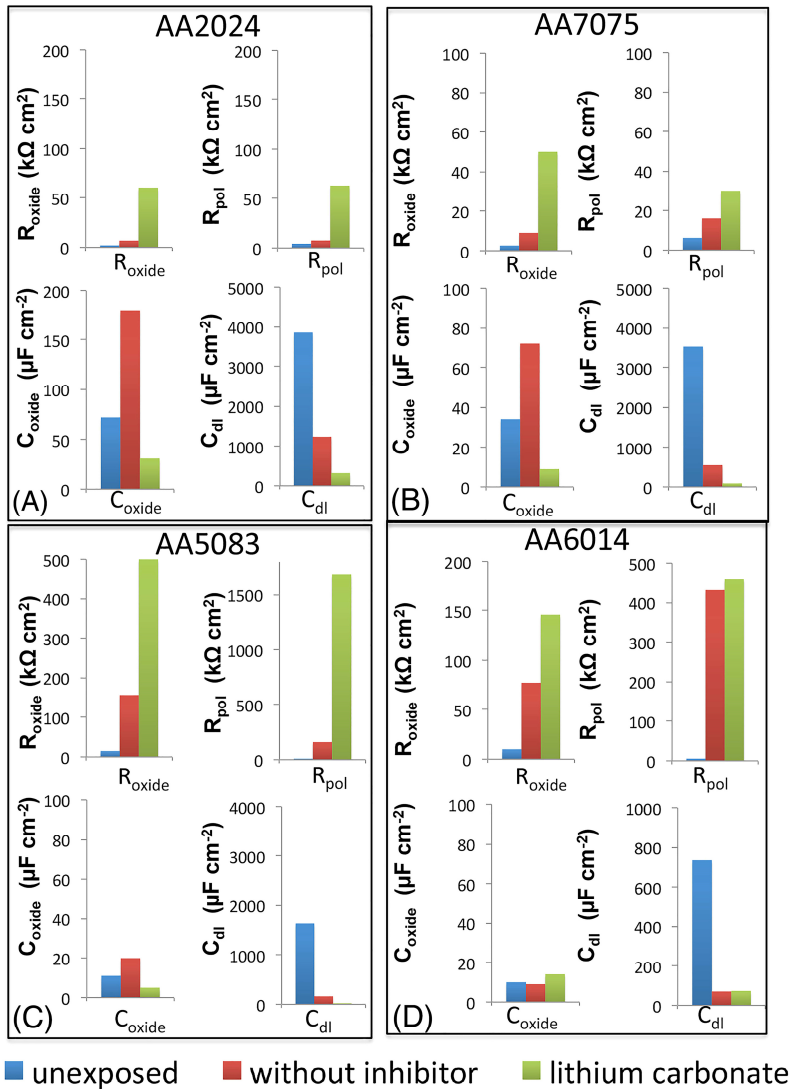
Fig. 2.8 Results of the electrochemical parameters including oxide resistance (R$_{oxide}$), polarisation resistance (R$_{pol}$), oxide capacitance (C$_{oxide}$), and double layer capacitance (C$_{dl}$) inside the artificial defects of different aluminium alloys covered by coatings loaded with and without Li$_2$CO$_3$ before and after neutral salt spray test: A, AA2024; B, AA7075; C, AA5083; and D, AA6014 [111].

2.4. Li-based inhibitor action in coating defects

It is important to investigate the diffusion process from the coating matrix to and within a coating defect area. A crucial parameter is the effective coverage distance of

the released inhibitor against corrosion inside a defect area, commonly referred to as chemical throwing power [115,116]. This process entails a transport with stochastic nature, accelerated by the concentration gradient of inhibitors, facilitating the mobility of inhibitors from regions enriched with inhibitors to sites that require protection [117]. Owing to the fast initial dissolution of lithium salts, a critical local concentration is achieved at the edge region of the scribe, which guarantees a considerable throwing distance, and hence a considerable scribe coverage. It has been reported that even a relatively low lithium salt load (e.g., 2.5% pigment volume concentration (PVC)) can already effectively protect the exposed scribed area for up to a width of 6 mm [66]. The released Li ions can relatively uniformly cover the entire defective area with a width of 1 mm within 15 min. However, due to variations in local conditions such as pH and local concentrations of lithium ions, distinctly different morphologies and chemical compositions are generated at different locations within the coating defect [40].

Compared to the conversion layer formation process in the conversion bath, the growth stages of the Li-based protective layer are much more complex due to the varying leaching kinetics of the Li salts from the coating matrix [118]. In general, the local pH and the concentration of Li ions gradually increase over time in the beginning. This trend initially occurs adjacent to the cut edge and subsequently gradually propagates towards the centre of the scribe. A detailed schematic overview showing the formation of the Li-based protective layer inside the artificial scratch over time can be seen in **Fig. 2.9**. This formation process inside a defect can be divided into five stages [67]. Initially (stage I), rapid leaching of Li salts enables a sharp increase in pH due to the hydrolysis of carbonate anions. Although the local pH was reported to be lower than that of the conversion bath [43], this is sufficient to cause thinning of the air-formed aluminium oxide layer [119]. Simultaneously, the unprotected surface area is exposed to the aggressive chloride-containing environment. At stage II, anodic dissolution of the alloy surface is triggered and simultaneously an aluminium hydroxide gel forms, which is thicker than that formed in the conversion bath due to a milder alkaline condition [120]. This gel layer will gradually expand from the edge to the central area and transform into pseudoboehmite. Pseudoboehmite exposed to a Li-containing solution in turn transforms to Li-pseudoboehmite due to the intercalation of Li ions [43]. At stage III, Li-pseudoboehmite gradually develops towards the central area and in the meantime the concentration of Li salts reaches a certain threshold near the edge area, leading to the transformation of Li-pseudoboehmite into a columnar Li/Al LDH structure, since

LDH is more stable in a more alkaline (pH≥10) environment [20,121,122]. With prolonged exposure time in a salty electrolyte, a continuous rise in the concentration of Li species within the central region of the scribe is reached. This elevated concentration of Li ions facilitates the growth of LDH within the central area of the scribe (stage IV). Finally, at stage V, a columnar LDH layer progressively expands laterally at the surface until a complete coverage of the scribe by LDH is achieved. Furthermore, differently to the bilayer structure as generated in the conversion bath, the Li-based protective layer inside a scratch comprises of three distinct layers: an inner dense layer, a middle porous layer and an outer columnar layer [26]. As mentioned in section 2, the middle porous layer is in fact a transition zone that gradually evolves from Li-pseudoboehmite to Li/Al LDH. The ratio between these three layers also varies locally: areas close to the cut edge contain a higher ratio of columnar Li/LDH, whereas regions around the central area are mostly composed of Li-pseudoboehmite [39]. At last, pseudoboehmite is expected to be the dominant composition in the central region when the diffusion distance is large enough, e.g., for a scribe width of 6mm.
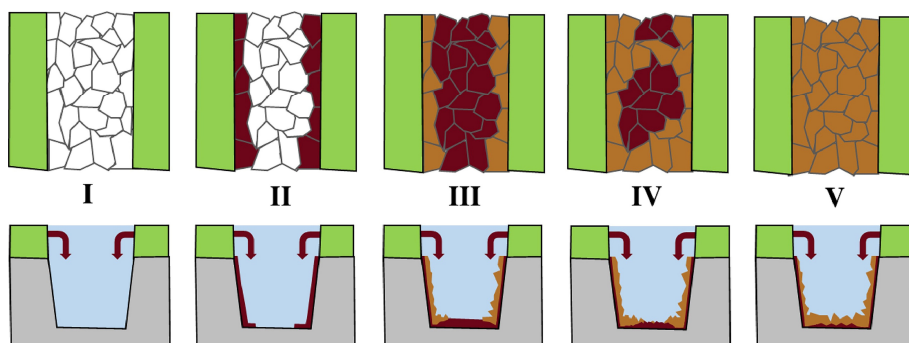
Fig. 2.9 Schematic representation of the growth stages of the protective layer inside a scratch (1 mm in width) of an organic coating under exposure of a neutral salt spray. The dark red and brown colours (Stages II to V) indicate Li-pseudoboehmite and Li/Al LDH, respectively. Reprinted from [67] with permission from Elsevier.

2.5. Li-based inhibitor mobility in and leaching from coatings

Understanding how inorganic inhibitor particles are distributed within a coating microstructure is helpful for understanding their leaching behaviour and for optimizing the design of future coating systems [123]. Previous studies on the leaching behaviour of hexavalent-chromium-based inhibitors revealed that inhibitor particles aggregate in clusters within the polymeric matrix and that the leaching of

corrosion occurs through the dissolution of interconnected soluble particles and ion mobility within such media does not follow pure Fickian diffusion. The voids resulting from dissolved chromate particles can form transport paths within the coating in combination with the low density areas, facilitating the release of inhibitors and the ingress of electrolyte [123,124]. These pathways possess significance due to the large size of the chromium ion, thereby precluding diffusion through the epoxy but permitting transport exclusively through channels formed by the dissolution of chromium-based particles [125].

The assessment of Li distributions in organic coatings poses challenges in electron beam spectroscopy owing to the low energy Li K-alpha line position and lack of detector sensitivity [67]. As a result, other techniques have been explored to determine the Li distribution within primers. Alpha-Particle Induced Gamma-ray Emission (PIGE) mapping, for example, was used to map the Li distribution within the polyurethane primer coating. This study showed that the observed Li-containing particles were often connected by small channels in the polyurethane matrix and around the individual particles [126].

The depletion of Li-containing particles from the coating matrix is a complex process in which inorganic phases and mechanical stress are reported to be involved [69,118]. First, the leaching of lithium salts from an organic coating system without a topcoat under neutral salt spray test exposure will be discussed. The release properties of Li ions from organic coatings depend on the solubility of different Li salts, the loading of Li salts in the primer matrix, and the microstructure of the matrix [66,127]. Water uptake and leaching kinetics of inhibitors for inhibited primers are one of the important subjects of previous studies [128–130]. Upon exposure to a liquid environment, water uptake occurs quickly within the first few hours through the free volume of the polymer [128,129,131–133]. It has been reported that the characteristic size of the free volume of polyurethane is approximately 3.7 Å, which is larger than the diameter of a water molecule at 3.0 Å [134]. In addition, the process of ion uptake generally exhibits a deceleration, which particularly counts for chloride, typically occurring at a rate approximately two orders of magnitude lower as compared to the rate of water diffusion [132]. Therefore, water uptake is the main factor which is influential for the behaviour of the primer at an early-stage. Subsequently, some absorbed water will reach the interface between the polymer matrix and the particles underneath the top area of the primer, where hydrolysis reactions will occur. The presence of water results in the dissolution of Li_2CO_3 particles and slight dissolution

of MgO particles. Later, the local electrolyte develops surrounding the Li_2CO_3 particles, generating a high concentration and thus absorbing water from the nearby primer matrix due to osmotic effects [132]. The origin of the induced internal stress is attributed to the difference between hydrostatic and osmotic pressures, which may lead to local rupture and delamination around the Li_2CO_3 particles. The creation of those channels results in a fractal network that functions as a porous medium, leading to a deeper penetration toward the metal/primer interface after longer exposure times [69]. Once these channels are connected to the external surface, the electrolyte with dissolved Li_2CO_3 will be released or at least redistributed within the network.

Parallel to the process of water uptake, the formation of a uniform depletion zone of Li_2CO_3 occurs rapidly in the upper part of the primer, which can be seen in **Fig. 2.10** [69]. Energy dispersive X-ray spectroscopy (EDS) was used to characterize the distribution of different types of particles under various exposure times [69]. The elemental colour indications are shown in the legend positioned at the bottom of each map (Li_2CO_3 particles in red colour). Only Li_2CO_3 particles directly connected to the external electrolyte dissolve after short exposure times (less than 8 h). The dissolution of Li_2CO_3 particles positioned deeper (occurring after exposure time longer than 96 h) are related to the delamination/dissolution of Li_2CO_3 particles which will be discussed later. This fast initial dissolution of Li_2CO_3 is also reflected in the high early-stage Li-ion release rate detected by inductively coupled plasma atomic emission spectroscopy (ICP-AES) [69]. Following the initial fast release of Li, Mg and, to a lesser extent, Ba are released as well. The initially high release of Li rapidly drops to a low ongoing release, which may result from the exhaustion of the leachable Li_2CO_3 particles that are connected to the external surface [69]. Subsequently, localized depletion of Li_2CO_3 extends deeper into the coating underneath this zone, indicating the involvement of the clusters of Li_2CO_3 particles in the release process [118]. This gradual dissolution does not necessarily propagate as a distinct "front" through the cluster, where particles closer to the surface must fully dissolve before particles further away from the surface can dissolve. Instead, it occurs through the concurrent dissolution of particles at varying depths within the clusters, which is governed by the transport of inhibitor within the cluster/void channels through the electrolyte.
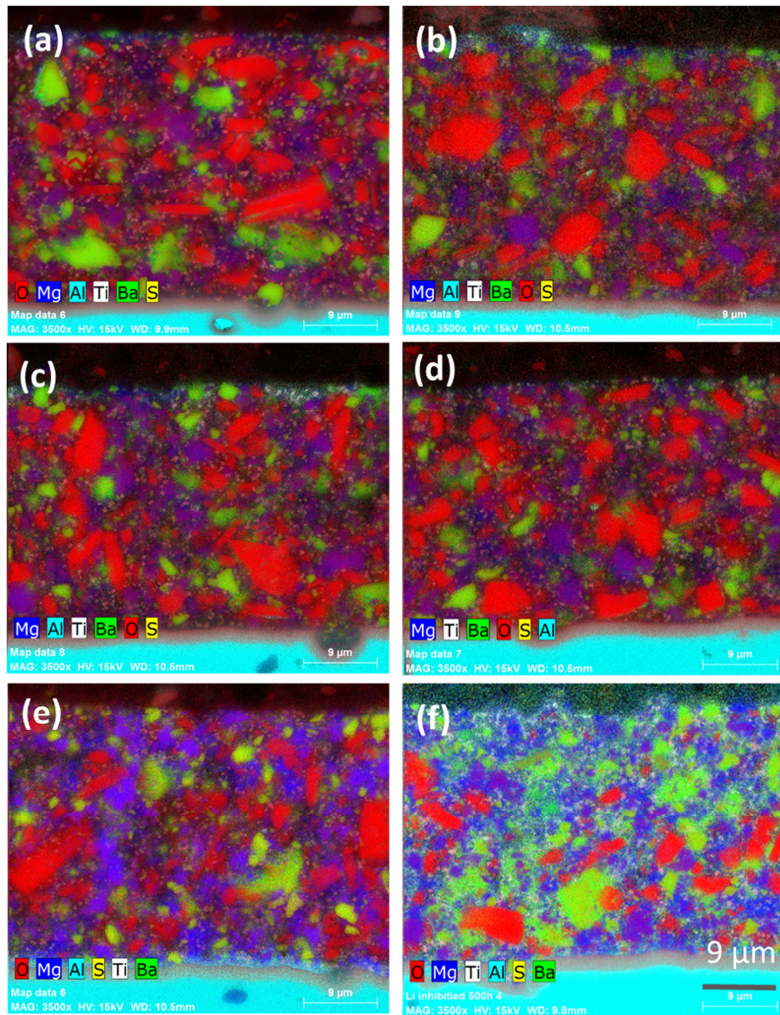
Fig. 2.10 EDS maps of leaching from a Li$_2$CO$_3$ containing primer at different exposure times under neutral salt spray. (a) 0 h, (b), 8 h, (c) 48 h, (d), 96 h, (e) 168 h and (f) 500 h. Reprinted from [69] with permission from Elsevier.

Exterior surfaces and some internal structural areas of aircraft are coated with chemical resistant topcoats [17]. This will influence the water uptake of the coating and the inhibitor leaching kinetics. External mechanical forces may cause crevices, cracks or scratches in the coating, causing the exposure of the Li-containing primer and the metallic substrate to the external environment. Therefore, it is meaningful to discuss the leaching behaviour into a defect from the cut edge of the Li-containing primer underneath a topcoat. Unlike the leaching from the as-primed surface, here

only a small cross section of the primer is exposed to the liquid environment, i.e., the scribe edge. However, hydration process, dissolution reactions of inorganic particles, and the generation of networks are still involved in this case. A summarizing mechanistic overview of samples after a salt spray test can be seen in **Fig. 2.11** [70]. Before exposure, the scribe damage influences the coating microstructure 20 to 25 μm away from the scribe edge, leading to the deformation of the primer and detachment around Li_2CO_3 (red colour) and $BaSO_4$ (yellow colour) particles. This detachment creates a loose structure close to the cut edge and provides networks for relatively fast early-stage ingress of electrolyte. After a sufficiently long exposure time (500 h), the depletion of inorganic particles (mainly Li_2CO_3, MgO and $BaSO_4$) at the area affected by deformation occurs, whereas the particles further away from the cut edge show a partial dissolution which is associated with the propagation of the channels within the primer. After an exposure of 48 h, dissolution sites appear, surrounding Li_2CO_3 particles (red arrows in the middle figures) at a distance of over 2000 μm away from the scribe, as well as a small number of detachment at the primer/Li_2CO_3 interface (pink arrows in the middle figures). A limited dissolution of $BaSO_4$ is also observed and marked by yellow arrows. No cracks in the primer matrix are observed. After an exposure duration of 168 h, more dissolution and detachment sites around and in Li_2CO_3 particles, as well as the dissolution sites of $BaSO_4$ particles, are observed. However, the number of detachment sites increases, indicating that the diffusion networks extend wider and deeper into the primer matrix. In addition, cracks are present inside the primer, extending from the dissolution or detachment sites. The partial dissolution and the appearance of cracks are related to the uptake of water. Considering the diffusion distance, water ingress through the topcoat is more dominant for the area relatively far away from the scribe. The osmotic and swelling pressures caused by the water uptake generates inner stresses, which makes certain sites more susceptible to mechanical degradation. These results indicate that besides the inhibitor component, also other particles with non-inhibiting functionalities are involved in the process of inhibitor release. For this reason, tailoring the composition of the organic coating system is of vital importance to optimize the leaching behaviour of loaded inhibitors [135]. In the context of organic coatings relying on the release of inhibitors by the leaching process, the optimization of the transport of inhibitor ions constitutes a pivotal objective. For example, the shape, size and distribution of the inhibitor clusters play an important role in the leaching kinetics [136], and these parameters are strongly influenced by the PVC and other non-inhibitive compounds. Relevant studies focussing on the optimization of the coating microstructure design are still relatively limited for Li leaching coatings.
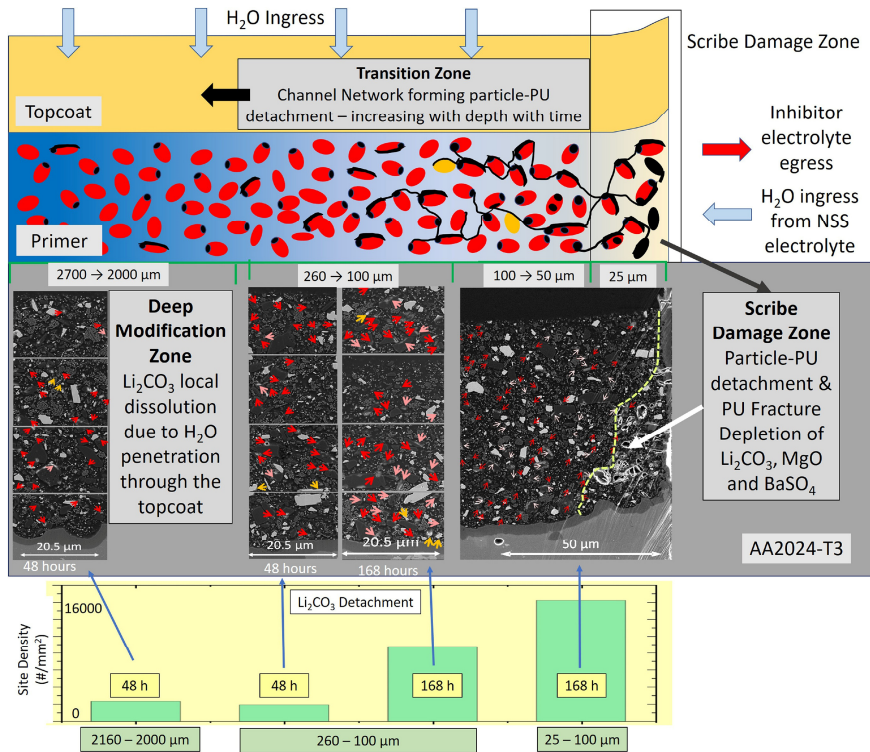
Fig. 2.11 Schematic representation of the leaching characteristics of a AA204-T3 substrate including primer and topcoat. Reprinted from [70] with permission from Elsevier.

2.6. Conclusions and outlook

Li-based inhibition technology has demonstrated its performance potential for the replacement of conventional chromate inhibitors for both conversion surface treatment as well as leachable inhibitors from active protective coatings for aluminium alloys. In addition to their significant corrosion protection performance, Li salts also have the advantages of being environmentally friendly and cost-effective, as well as offering irreversible long-term corrosion protection.

Nonetheless, current studies indicate that Li-based conversion treatments still require a longer process time to reach comparable corrosion protection as compared to chromate-based conversion treatments. This potentially hinders its industrial use. Feasible strategies should be developed in order to modify the composition of the conversion bath in order to shorten the conversion treatment while maintaining or even improving its corrosion protection performance. Detailed studies on the

influence of alloying elements from different commercial aluminium alloys, the extra additives, especially those components which can improve the quality of the conversion layer such as oxidants and aluminate salts, still remain to be performed.

For an organic coating system, the morphological layer evolution at a coating defect is different to that on aluminium alloy panels exposed to bulk electrolytes which are characterized by relatively stable pH values and Li concentrations. In the bulk electrolyte case, firstly a Li/Al LDH is formed which is more stable in a highly alkaline solution, followed by the generation of a dense inner layer. The conversion coating approach is more based on the precipitation of LDH in a super saturated solution. By contrast, in the case of the organic coating system, the lower initial pH and Li concentration initially triggers the anodic dissolution of the exposed alloy surface, leading to the formation of a dense Li-pseudoboehmite. With an increase in the concentration of Li salts and pH, Li-pseudoboehmite is partially converted into Li/Al layered double hydroxide (LDH). Current studies on the elucidation of the protective layer formation mechanism for organic coating conditions are mainly performed using Li_2CO_3 and NaCl, and mostly limited to the case of AA2024-T3. Therefore, the protective layer formation mechanism under a more complex environment (e.g., the influence of other common dynamic atmospheric corrosion conditions) and other aluminium alloys still need more investigation in the future. In addition, understanding the stability of the protective layer and how this can be optimized is also a relevant subject of further study.

The microstructure of the coating matrix plays a vital role in the leaching behaviour of inhibitors. Particles inside the primer matrix without inhibition abilities influence the formation of distinct inhibitor delivery pathways. Therefore, a more profound understanding of the inner transportation networks is necessary for an optimization of the coating design to improve the active corrosion protection efficiency. Moreover, the porous Li/Al LDH structure contributes little to the corrosion protection. This effect can be utilized by chemical conversion treatments since the chemistry of the conversion bath and post-treatment can be controlled. On the contrary, for the case of the Li salts leaching organic coating, it remains challenging to control the top LDH layer. This might be an interesting topic for future research where a more profound understanding and control of leaching kinetics are addressed.

References

[1] N. L. Sukiman, X. Zhou, N. Birbilis, A.E. Hughes, J.M. C. Mol, S. J., X. Zhou, G. E., Durability and Corrosion of Aluminium and Its Alloys: Overview, Property Space, Techniques and Developments, in: Z. Ahmad (Ed.), Alum. Alloys - New Trends Fabr. Appl., InTech, 2012.

[2] A.E. Hughes, C. MacRae, N. Wilson, A. Torpy, T.H. Muster, A.M. Glenn, Sheet AA2024-T3: a new investigation of microstructure and composition, Surf. Interface Anal. 42 (2010) 334–338.

[3] A. Boag, A.E. Hughes, N.C. Wilson, A. Torpy, C.M. MacRae, A.M. Glenn, T.H. Muster, How complex is the microstructure of AA2024-T3?, Corros. Sci. 51 (2009) 1565–1568.

[4] A. E., N. Birbilis, J. M.C., S. J., X. Zhou, G. E., High Strength Al-Alloys: Microstructure, Corrosion and Principles of Protection, in: Z. Ahmad (Ed.), Recent Trends Process. Degrad. Alum. Alloys, InTech, 2011.

[5] J.L. García-Hernández, C.G. Garay-Reyes, I.K. Gómez-Barraza, M.A. Ruiz-Esparza-Rodríguez, E.J. Gutiérrez-Castañeda, I. Estrada-Guel, M.C. Maldonado-Orozco, R. Martínez-Sánchez, Influence of plastic deformation and Cu/Mg ratio on the strengthening mechanisms and precipitation behavior of AA2024 aluminum alloys, J. Mater. Res. Technol. 8 (2019) 5471–5475.

[6] S.J. Andersen, C.D. Marioara, J. Friis, S. Wenner, R. Holmestad, Precipitates in aluminium alloys, Adv. Phys. X 3 (2018) 1479984.

[7] C. Blanc, B. Lavelle, G. Mankowski, The role of precipitates enriched with copper on the susceptibility to pitting corrosion of the 2024 aluminium alloy, Corros. Sci. 39 (1997) 495–510.

[8] N. Birbilis, Y.M. Zhu, S.K. Kairy, M.A. Glenn, J.-F. Nie, A.J. Morton, Y. Gonzalez-Garcia, H. Terryn, J.M.C. Mol, A.E. Hughes, A closer look at constituent induced localised corrosion in Al-Cu-Mg alloys, Corros. Sci. 113 (2016) 160–171.

[9] A.E. Hughes, J.M.C. Mol, M.L. Zheludkevich, R.G. Buchheit, eds., Active Protective Coatings: New-Generation Coatings for Metals, Springer Netherlands, Dordrecht, 2016.

[10] G.O. Ilevbare, J.R. Scully, J. Yuan, R.G. Kelly, Inhibition of Pitting Corrosion on Aluminum Alloy 2024-T3: Effect of Soluble Chromate Additions vs Chromate Conversion Coating, Corrosion 56 (2000).

[11] A.E. Hughes, R.J. Taylor, B.R.W. Hinton, Chromate Conversion Coatings on 2024 Al Alloy, Surf. Interface Anal. 25 (1997) 223–234.

[12] P. Campestrini, H. Terryn, J. Vereecken, J.H.W. de Wit, Chromate Conversion Coating on Aluminum Alloys : III. Corrosion Protection, J. Electrochem. Soc. 151 (2004) B370.

[13] O. Gharbi, S. Thomas, C. Smith, N. Birbilis, Chromate replacement: what does the future hold?, Npj Mater. Degrad. 2 (2018) 12.

[14] T. Prosek, D. Thierry, A model for the release of chromate from organic coatings, Prog. Org. Coat. 49 (2004) 209–217.

[15] M. Kendig, S. Jeanjaquet, R. Addison, J. Waldrop, Role of hexavalent chromium in the inhibition of corrosion of aluminum alloys, Surf. Coat. Technol. 140 (2001) 58–66.

[16] R. Saha, R. Nandi, B. Saha, Sources and toxicity of hexavalent chromium, J. Coord. Chem. 64 (2011) 1782–1806.

[17] P. Visser, H. Terryn, J.M.C. Mol, Aerospace Coatings, in: A.E. Hughes, J.M.C. Mol, M.L. Zheludkevich, R.G. Buchheit (Eds.), Act. Prot. Coat. New-Gener. Coat. Met., Springer Netherlands, Dordrecht, 2016: pp. 315–372.

[18] M. Becker, Chromate-free chemical conversion coatings for aluminum alloys, Corros. Rev. 37 (2019) 321–342.

[19] I. Milošev, G.S. Frankel, Review—Conversion Coatings Based on Zirconium and/or Titanium, J. Electrochem. Soc. 165 (2018) C127.

[20] R.G. Buchheit, M.D. Bode, G.E. Stoner, Corrosion-Resistant, Chromate-Free Talc Coatings for Aluminum, CORROSION 50 (1994) 205–214.

[21] M.W. Kendig, R.G. Buchheit, Corrosion Inhibition of Aluminum and Aluminum Alloys by Soluble Chromates, Chromate Coatings, and Chromate-Free Coatings, CORROSION 59 (2003) 379–400.

[22] R. Berger, U. Bexell, T. Mikael Grehk, S.-E. Hörnström, A comparative study of the corrosion protective properties of chromium and chromium free passivation methods, Surf. Coat. Technol. 202 (2007) 391–397.

[23] L. Selegård, T. Poot, P. Eriksson, J. Palisaitis, P.O.Å. Persson, Z. Hu, K. Uvdal, In-situ growth of cerium nanoparticles for chrome-free, corrosion resistant anodic coatings, Surf. Coat. Technol. 410 (2021) 126958.

[24] Y. Castro, E. Özmen, A. Durán, Integrated self-healing coating system for outstanding corrosion protection of AA2024, Surf. Coat. Technol. 387 (2020) 125521.

[25] O. Lopez-Garrity, G.S. Frankel, Corrosion Inhibition of Aluminum Alloy 2024-T3 by Sodium Molybdate, J. Electrochem. Soc. 161 (2013) C95.

[26] D.S. Kharitonov, J. Sommertune, C. Örnek, J. Ryl, I.I. Kurilo, P.M. Claesson, J. Pan, Corrosion inhibition of aluminium alloy AA6063-T5 by vanadates: Local surface chemical events elucidated by confocal Raman micro-spectroscopy, Corros. Sci. 148 (2019) 237–250.

[27] V. Moutarlier, M.P. Gigandet, B. Normand, J. Pagetti, EIS characterisation of anodic films formed on 2024 aluminium alloy, in sulphuric acid containing molybdate or permanganate species, Corros. Sci. 47 (2005) 937–951.

[28] J.-A. Hill, T. Markley, M. Forsyth, P.C. Howlett, B.R.W. Hinton, Corrosion inhibition of 7000 series aluminium alloys with cerium diphenyl phosphate, J. Alloys Compd. 509 (2011) 1683–1690.

[29] D.O. Flamini, M. Trueba, S.P. Trasatti, Aniline-based silane as a primer for corrosion inhibition of aluminium, Prog. Org. Coat. 74 (2012) 302–310.

[30] V. Dalmoro, J.H.Z. dos Santos, E. Armelin, C. Alemán, D.S. Azambuja, Sol–gel hybrid films based on organosilane and montmorillonite for corrosion inhibition of AA2024, J. Colloid Interface Sci. 426 (2014) 308–313.

[31] A.K. Mishra, R. Balasubramaniam, Corrosion inhibition of aluminum alloy AA 2014 by rare earth chlorides, Corros. Sci. 49 (2007) 1027–1044.

[32] K.A. Yasakau, M.L. Zheludkevich, S.V. Lamaka, M.G.S. Ferreira, Mechanism of Corrosion Inhibition of AA2024 by Rare-Earth Compounds, J. Phys. Chem. B 110 (2006) 5515–5528.

[33] M.B. Jensen, M.J. Peterson, N. Jadhav, V.J. Gelling, SECM investigation of corrosion inhibition by tungstate- and vanadate-doped polypyrrole/aluminum flake composite coatings on AA2024-T3, Prog. Org. Coat. 77 (2014) 2116–2122.

[34] R. Samiee, B. Ramezanzadeh, M. Mahdavian, E. Alibakhshi, Corrosion Inhibition Performance and Healing Ability of a Hybrid Silane Coating in the Presence of Praseodymium (III) Cations, J. Electrochem. Soc. 165 (2018) C777.

[35] J. Lin, D. Battocchi, G.P. Bierwagen, Inhibitors for prolonging corrosion protection of Mg-rich primer on Al alloy 2024-T3, J. Coat. Technol. Res. 14 (2017) 497–504.

[36] X. Wang, G.S. Frankel, Protection Mechanism of Al-Rich Epoxy Primer on Aluminum Alloy 2024-T3, Corrosion 73 (2017) 1192–1195.

[37] C.A. Drewien, M.O. Eatough, D.R. Tallant, C.R. Hills, R.G. Buchheit, Lithium-aluminum-carbonate-hydroxide hydrate coatings on aluminum alloys: Composition, structure, and processing bath chemistry, J. Mater. Res. 11 (1996) 1507–1513.

[38] J. Gui, T.M. Devine, Influence of lithium on the corrosion of aluminum, Scr Met. U. S. 21:6 (1987).

[39] P. Visser, Y. Liu, X. Zhou, T. Hashimoto, G.E. Thompson, S.B. Lyon, L.G.J. van der Ven, A.J.M.C. Mol, H.A. Terryn, The corrosion protection of AA2024-T3 aluminium alloy by leaching of lithium-containing salts from organic coatings, Faraday Discuss. 180 (2015) 511–526.

[40] Y. Liu, P. Visser, X. Zhou, S.B. Lyon, T. Hashimoto, M. Curioni, A. Gholinia, G.E. Thompson, G. Smyth, S.R. Gibbon, D. Graham, J.M.C. Mol, H. Terryn, Protective Film Formation on AA2024-T3 Aluminum Alloy by Leaching of Lithium Carbonate from an Organic Coating, J. Electrochem. Soc. 163 (2015) C45.

[41] Y. Liu, P. Visser, X. Zhou, S.B. Lyon, T. Hashimoto, A. Gholinia, G.E. Thompson, G. Smyth, S.R. Gibbon, D. Graham, J.M.C. Mol, H. Terryn, An investigation of the corrosion inhibitive layers generated from lithium oxalate-containing organic

coating on AA2024-T3 aluminium alloy, Surf. Interface Anal. 48 (2016) 798–803.

[42] P. Visser, Y. Liu, H. Terryn, J.M.C. Mol, Lithium salts as leachable corrosion inhibitors and potential replacement for hexavalent chromium in organic coatings for the protection of aluminum alloys, J. Coat. Technol. Res. 13 (2016) 557–566.

[43] P. Visser, A. Lutz, J.M.C. Mol, H. Terryn, Study of the formation of a protective layer in a defect from lithium-leaching organic coatings, Prog. Org. Coat. 99 (2016) 80–90.

[44] R.G. Buchheit, F.D. Wall, G.E. Stoner, J.P. Moran, Anodic Dissolution-Based Mechanism for the Rapid Cracking, Preexposure Phenomenon Demonstrated by Aluminum-Lithium-Copper Alloys, Corrosion 51 (1995).

[45] C.M. Rangel, M.A. Travassos, The passivation of aluminium in lithium carbonate/bicarbonate solutions, Corros. Sci. 33 (1992) 327–343.

[46] C.M. Rangel, M.A. Travassos, Li-based conversion coatings on aluminium: An electrochemical study of coating formation and growth, Surf. Coat. Technol. 200 (2006) 5823–5828.

[47] R.G. Buchheit, G.E. Stoner, Chromate-free corrosion resistant talc coatings for aluminum alloys, Sandia National Labs., Albuquerque, NM (United States), 1992.

[48] R.G. Buchheit, C.A. Drewien, M.A. Martinez, G.E. Stoner, Chromate-free corrosion resistant conversion coatings for aluminum alloys, Sandia National Lab. (SNL-NM), Albuquerque, NM (United States), 1995.

[49] C.A. Drewien, R.G. Buchheit, Issues for conversion coating of aluminum alloys with hydrotalcite, Sandia National Labs., Albuquerque, NM (United States), 1993.

[50] R.G. Buchheit, Alkaline oxide conversion coatings for aluminum alloys, Sandia National Lab. (SNL-NM), Albuquerque, NM (United States), 1996.

[51] R.G. Buchheit, M.A. Martinez, C.B. Cooper, Corrosion Resistant Coatings for Aluminum by Hydrothermal Film Formation in Alkaline Li-Salt Solutions, MRS Online Proc. Libr. OPL 432 (1996) 273.

[52] R.G. Buchheit, Copper removal during formation of corrosion resistant alkaline oxide coatings on Al–Cu–Mg alloys, J. Appl. Electrochem. 28 (1998) 503–510.

[53] R.B. Leggat, W. Zhang, R.G. Buchheit, S.R. Taylor, Performance of Hydrotalcite Conversion Treatments on AA2024-T3 When Used in a Coating System, CORROSION 58 (2002) 322–328.

[54] W. Zhang, R.G. Buchheit, Hydrotalcite Coating Formation on Al-Cu-Mg Alloys from Oxidizing Bath Chemistries, CORROSION 58 (2002) 591–600.

[55] F. Wong, R.G. Buchheit, Utilizing the structural memory effect of layered double hydroxides for sensing water uptake in organic coatings, Prog. Org. Coat. 51 (2004) 91–102.

[56] O. Lunder, J.C. Walmsley, P. Mack, K. Nisancioglu, Formation and characterisation of a chromate conversion coating on AA6060 aluminium, Corros. Sci. 47 (2005)

1604–1624.

[57] G.R. Williams, D. O'Hare, A Kinetic Study of the Intercalation of Lithium Salts into Al(OH)3, J. Phys. Chem. B 110 (2006) 10619–10629.

[58] C.J. Wang, D. O'Hare, Topotactic synthesis of layered double hydroxide nanorods, J. Mater. Chem. 22 (2012) 23064–23070.

[59] B. Pillado, B. Mingo, R. del Olmo, E. Matykina, A.M. Kooijman, Y. Gonzalez−Garcia, R. Arrabal, M. Mohedano, LDH conversion films for active protection of AZ31 Mg alloy, J. Magnes. Alloys 11 (2023) 201–216.

[60] D. Mata, M. Serdechnova, M. Mohedano, C. L. Mendis, S. V. Lamaka, J. Tedim, T. Hack, S. Nixon, M. L. Zheludkevich, Hierarchically organized Li–Al-LDH nano-flakes: a low-temperature approach to seal porous anodic oxide on aluminum alloys, RSC Adv. 7 (2017) 35357–35367.

[61] R.G. Buchheit, S.B. Mamidipally, P. Schmutz, H. Guan, Active Corrosion Protection in Ce-Modified Hydrotalcite Conversion Coatings, CORROSION 58 (2002) 3–14.

[62] P. Visser, Y. Gonzalez-Garcia, J.M.C. Mol, H. Terryn, Mechanism of Passive Layer Formation on AA2024-T3 from Alkaline Lithium Carbonate Solutions in the Presence of Sodium Chloride, J. Electrochem. Soc. 165 (2018) C60–C70.

[63] Z. Li, A. Homborg, Y. Gonzalez-Garcia, A. Kosari, P. Visser, A. Mol, Evaluation of the formation and protectiveness of a lithium-based conversion layer using electrochemical noise, Electrochimica Acta 426 (2022) 140733.

[64] Z. Li, A. Homborg, Y. Gonzalez-Garcia, P. Visser, M. Soleimani, A. Mol, The Effect of Ambient Ageing on the Corrosion Protective Properties of a Lithium-Based Conversion Layer, J. Electrochem. Soc. 170 (2023) 031504.

[65] Z. Li, G. Li, P. Visser, A. Homborg, Y. Gonzalez-Garcia, A. Mol, Local scanning electrochemical microscopy analysis of a lithium-based conversion layer on AA2024-T3 at progressive stages of formation, Electrochimica Acta 469 (2023) 143270.

[66] P. Visser, K. Marcoen, G.F. Trindade, M.-L. Abel, J.F. Watts, T. Hauffman, J.M.C. Mol, H. Terryn, The chemical throwing power of lithium-based inhibitors from organic coatings on AA2024-T3, Corros. Sci. 150 (2019) 194–206.

[67] K. Marcoen, P. Visser, G.F. Trindade, M.-L. Abel, J.F. Watts, J.M.C. Mol, H. Terryn, T. Hauffman, Compositional study of a corrosion protective layer formed by leachable lithium salts in a coating defect on AA2024-T3 aluminium alloys, Prog. Org. Coat. 119 (2018) 65–75.

[68] A. Trentin, S.V. Harb, M.C. Uvida, S.H. Pulcinelli, C.V. Santilli, K. Marcoen, S. Pletincx, H. Terryn, T. Hauffman, P. Hammer, Dual Role of Lithium on the Structure and Self-Healing Ability of PMMA-Silica Coatings on AA7075 Alloy, ACS Appl. Mater. Interfaces 11 (2019) 40629–40641.

[69] J.S. Laird, P. Visser, S. Ranade, A.E. Hughes, H. Terryn, J.M.C. Mol, Li leaching

from Lithium Carbonate-primer: An emerging perspective of transport pathway development, Prog. Org. Coat. 134 (2019) 103–118.

[70] P. Visser, S. Ranade, J.S. Laird, A.M. Glenn, A.E. Hughes, H. Terryn, J.M.C. Mol, Li leaching from Li carbonate-primer: Transport pathway development from the scribe edge of a primer/topcoat system, Prog. Org. Coat. 158 (2021) 106284.

[71] X. Li, S. Caes, T. Pardoen, G. De Schutter, T. Hauffman, B. Kursten, Inhibition effect of lithium salts on the corrosion of AA1100 aluminium alloy in ordinary Portland cement pastes, Corros. Sci. 221 (2023) 111325.

[72] A. Kosari, F. Tichelaar, P. Visser, P. Taheri, H. Zandbergen, H. Terryn, J.M.C. Mol, Nanoscopic and in-situ cross-sectional observations of Li-based conversion coating formation using liquid-phase TEM, Npj Mater. Degrad. 5 (2021) 40.

[73] C. Jing, B. Dong, A. Raza, T. Zhang, Y. Zhang, Corrosion inhibition of layered double hydroxides for metal-based systems, Nano Mater. Sci. 3 (2021) 47–67.

[74] D. Tonelli, I. Gualandi, E. Musella, E. Scavetta, Synthesis and Characterization of Layered Double Hydroxides as Materials for Electrocatalytic Applications, Nanomaterials 11 (2021) 725.

[75] M.A. Iqbal, L. Sun, A.T. Barrett, M. Fedel, Layered Double Hydroxide Protective Films Developed on Aluminum and Aluminum Alloys: Synthetic Methods and Anti-Corrosion Mechanisms, Coatings 10 (2020) 428.

[76] Y. Cao, D. Zheng, F. Zhang, J. Pan, C. Lin, Layered double hydroxide (LDH) for multi-functionalized corrosion protection of metals: A review, J. Mater. Sci. Technol. 102 (2022) 232–263.

[77] A.C. Bouali, M. Serdechnova, C. Blawert, J. Tedim, M.G.S. Ferreira, M.L. Zheludkevich, Layered double hydroxides (LDHs) as functional materials for the corrosion protection of aluminum alloys: A review, Appl. Mater. Today 21 (2020) 100857.

[78] A.C. Bouali, M.H. Iuzviuk, M. Serdechnova, K.A. Yasakau, D. Drozdenko, A. Lutz, K. Fekete, G. Dovzhenko, D.C.F. Wieland, H. Terryn, M.G.S. Ferreira, I.A. Zobkalo, M.L. Zheludkevich, Mechanism of LDH Direct Growth on Aluminum Alloy Surface: A Kinetic and Morphological Approach, J. Phys. Chem. C 125 (2021) 11687–11701.

[79] I. Mohammadi, T. Shahrabi, M. Mahdavian, M. Izadi, Zn-Al layered double hydroxide as an inhibitive conversion coating developed on AA2024-T3 by one-step hydrothermal crystallization: Crystal structure evolution and corrosion protection performance, Surf. Coat. Technol. 409 (2021) 126882.

[80] K. Lin, X. Luo, X. Pan, C. Zhang, Y. Liu, Enhanced corrosion resistance of LiAl-layered double hydroxide (LDH) coating modified with a Schiff base salt on aluminum alloy by one step in-situ synthesis at low temperature, Appl. Surf. Sci. 463 (2019) 1085–1096.

[81] A.C. Bouali, M.H. Iuzviuk, M. Serdechnova, K.A. Yasakau, D.C.F. Wieland, G.

Dovzhenko, H. Maltanava, I.A. Zobkalo, M.G.S. Ferreira, M.L. Zheludkevich, Zn-Al LDH growth on AA2024 and zinc and their intercalation with chloride: Comparison of crystal structure and kinetics, Appl. Surf. Sci. 501 (2020) 144027.

[82] I. Mohammadi, T. Shahrabi, M. Mahdavian, M. Izadi, Chemical modification of LDH conversion coating with diethyldithiocarbamate as a novel anti-corrosive film for AA2024-T3, J. Ind. Eng. Chem. 95 (2021) 134–147.

[83] D.E.L. Vieira, A.N. Salak, M.G.S. Ferreira, J.M. Vieira, C.M.A. Brett, Ce-substituted Mg-Al layered double hydroxides to prolong the corrosion protection lifetime of aluminium alloys, Appl. Surf. Sci. 573 (2022) 151527.

[84] D. Álvarez, A. Collazo, M. Hernández, X.R. Nóvoa, C. Pérez, Characterization of hybrid sol–gel coatings doped with hydrotalcite-like compounds to improve corrosion resistance of AA2024-T3 alloys, Prog. Org. Coat. 68 (2010) 91–99.

[85] A. Collazo, M. Hernández, X.R. Nóvoa, C. Pérez, Effect of the addition of thermally activated hydrotalcite on the protective features of sol–gel coatings applied on AA2024 aluminium alloys, Electrochimica Acta 56 (2011) 7805–7814.

[86] E. Alibakhshi, E. Ghasemi, M. Mahdavian, B. Ramezanzadeh, A comparative study on corrosion inhibitive effect of nitrate and phosphate intercalated Zn-Al- layered double hydroxides (LDHs) nanocontainers incorporated into a hybrid silane layer and their effect on cathodic delamination of epoxy topcoat, Corros. Sci. 115 (2017) 159–174.

[87] A.M. Fogg, D. O'Hare, Study of the Intercalation of Lithium Salt in Gibbsite Using Time-Resolved in Situ X-ray Diffraction, Chem. Mater. 11 (1999) 1771–1775.

[88] K.A. Tarasov, V.P. Isupov, L.E. Chupakhina, D. O'Hare, A time resolved, in-situ X-ray diffraction study of the de-intercalation of anions and lithium cations from [LiAl2(OH)6]nX·qH2O (X = Cl−, Br−, NO3−, SO42−), J. Mater. Chem. 14 (2004) 1443–1447.

[89] L. Huang, J. Wang, Y. Gao, Y. Qiao, Q. Zheng, Z. Guo, Y. Zhao, D. O'Hare, Q. Wang, Synthesis of LiAl2-layered double hydroxides for CO2 capture over a wide temperature range, J. Mater. Chem. A 2 (2014) 18454–18462.

[90] J. Chen, H. Yuan, J. Yu, M. Yan, Y. Yang, S. Lin, Regulating lithium extraction based on intercalated SO42− in Li/Al-LDHs, J. Colloid Interface Sci. 649 (2023) 694–702.

[91] Y. Lee, D.-Y. Jung, Lithium intercalation and deintercalation of thermally decomposed LiAl2-layered double hydroxides, Appl. Clay Sci. 228 (2022) 106631.

[92] Y. Lee, J.-H. Cha, D.-Y. Jung, Lithium separation by growth of lithium aluminum layered double hydroxides on aluminum metal substrates, Solid State Sci. 110 (2020) 106488.

[93] S.-L. Wang, C.-H. Lin, Y.-Y. Yan, M.K. Wang, Synthesis of Li/Al LDH using aluminum and LiOH, Appl. Clay Sci. 72 (2013) 191–195.

[94] V. Kasneryk, M. Serdechnova, C. Blawert, M.L. Zheludkevich, LDH has been

grown: What is next? Overview on methods of post-treatment of LDH conversion coatings, Appl. Clay Sci. 232 (2023) 106774.

[95] H.N. McMurray, G. Williams, Inhibition of Filiform Corrosion on Organic-Coated Aluminum Alloy by Hydrotalcite-Like Anion-Exchange Pigments, Corrosion 60 (2004) 219–228.

[96] Y. Su, S. Qiu, D. Yang, S. Liu, H. Zhao, L. Wang, Q. Xue, Active anti-corrosion of epoxy coating by nitrite ions intercalated MgAl LDH, J. Hazard. Mater. 391 (2020) 122215.

[97] T. Yan, S. Xu, Q. Peng, L. Zhao, X. Zhao, X. Lei, F. Zhang, Self-Healing of Layered Double Hydroxide Film by Dissolution/Recrystallization for Corrosion Protection of Aluminum, J. Electrochem. Soc. 160 (2013) C480.

[98] B. Yang, Y. Ma, Z. Liang, Y. Liao, Z. Wang, P. Zhu, A superhydrophobic and corrosion resistant layered double hydroxides coating on AA2099-T83 Al-Cu-Li alloy, Surf. Coat. Technol. 405 (2021) 126629.

[99] J. Li, K. Lin, X. Luo, H. Zhang, Y.F. Cheng, X. Li, Y. Liu, Enhanced corrosion protection property of Li-Al layered double hydroxides (LDHs) film modified by 2-guanidinosuccinic acid with excellent self-repairing and self-antibacterial properties, Appl. Surf. Sci. 480 (2019) 384–394.

[100] T. Hurlen, A.T. Haug, Corrosion and passive behaviour of aluminium in weakly alkaline solution, Electrochimica Acta 29 (1984) 1133–1138.

[101] A. Kosari, F. Tichelaar, P. Visser, H. Zandbergen, H. Terryn, J.M.C. Mol, Laterally-resolved formation mechanism of a lithium-based conversion layer at the matrix and intermetallic particles in aerospace aluminium alloys, Corros. Sci. 190 (2021) 109651.

[102] V.P. Isupov, Intercalation compounds of aluminum hydroxide, J. Struct. Chem. 40 (1999) 672–685.

[103] T.P. Belova, Experimental studies in the sorptive extraction of boron and lithium from thermal waters, J. Volcanol. Seismol. 11 (2017) 136–142.

[104] M. Yu, H. Li, N. Du, W. Hou, Understanding Li-Al-CO3 layered double hydroxides. (I) Urea-supported hydrothermal synthesis, J. Colloid Interface Sci. 547 (2019) 183–189.

[105] A. Kosari, P. Visser, F. Tichelaar, S. Eswara, J.-N. Audinot, T. Wirtz, H. Zandbergen, H. Terryn, J.M.C. Mol, Cross-sectional characterization of the conversion layer formed on AA2024-T3 by a lithium-leaching coating, Appl. Surf. Sci. 512 (2020) 145665.

[106] P. Visser, M. Meeusen, Y. Gonzalez-Garcia, H. Terryn, J.M.C. Mol, Electrochemical Evaluation of Corrosion Inhibiting Layers Formed in a Defect from Lithium-Leaching Organic Coatings, J. Electrochem. Soc. 164 (2017) C396–C406.

[107] P. Visser, S.A. Hayes, Low-temperature-curable coating composition useful as

anticorrosive primer coating for non-ferrous metal substrates, particularly aluminum or aluminum alloy, comprises film-forming resin, curing agent, and lithium salt, patent nr. WO2010112605-A1, (2010), WO2010112605A1, 2010.

[108] P. Visser, H. Terryn, J.M.C. Mol, On the importance of irreversibility of corrosion inhibitors for active coating protection of AA2024-T3, Corros. Sci. 140 (2018) 272–285.

[109] I. Recloux, F. Andreatta, M.-E. Druart, L.B. Coelho, C. Cepek, D. Cossement, L. Fedrizzi, M.-G. Olivier, Stability of benzotriazole-based films against AA2024 aluminium alloy corrosion process in neutral chloride electrolyte, J. Alloys Compd. 735 (2018) 2512–2522.

[110] A.C. Balaskas, M. Curioni, G.E. Thompson, Effectiveness of 2-mercaptobenzothiazole, 8-hydroxyquinoline and benzotriazole as corrosion inhibitors on AA 2024-T3 assessed by electrochemical methods, Surf. Interface Anal. 47 (2015) 1029–1039.

[111] P. Visser, H. Terryn, J.M.C. Mol, Active corrosion protection of various aluminium alloys by lithium-leaching coatings, Surf. Interface Anal. 51 (2019) 1276–1287.

[112] M. Meeusen, P. Visser, L. Fernández Macía, A. Hubin, H. Terryn, J.M.C. Mol, The use of odd random phase electrochemical impedance spectroscopy to study lithium-based corrosion inhibition by active protective coatings, Electrochimica Acta 278 (2018) 363–373.

[113] J. Li, B. Hurley, R. Buchheit, Microelectrochemical Characterization of the Effect of Rare Earth Inhibitors on the Localized Corrosion of AA2024-T3, J. Electrochem. Soc. 162 (2015) C563.

[114] T. Suter, H. Böhni, A new microelectrochemical method to study pit initiation on stainless steels, Electrochimica Acta 42 (1997) 3275–3280.

[115] J.R. Scully, F. Presuel-Moreno, M. Goldman, R.G. Kelly, N. Tailleart, User-Selectable Barrier, Sacrificial Anode, and Active Corrosion Inhibiting Properties of Al-Co-Ce Alloys for Coating Applications, Corrosion 64 (2008) 210–229.

[116] B. Kannan, C.F. Glover, H.N. McMurray, G. Williams, J.R. Scully, Performance of a Magnesium-Rich Primer on Pretreated AA2024-T351 in Full Immersion: a Galvanic Throwing Power Investigation Using a Scanning Vibrating Electrode Technique, J. Electrochem. Soc. 165 (2018) C27.

[117] J.R. Scully, N. Tailleart, F. Presuel-Moreno, 9 - Tunable multifunctional corrosion-resistant metallic coatings containing rare earth elements, in: M. Forsyth, B. Hinton (Eds.), Rare Earth-Based Corros. Inhib., Woodhead Publishing, 2014: pp. 267–290.

[118] A. Hughes, J. Laird, C. Ryan, P. Visser, H. Terryn, A. Mol, Particle Characterisation and Depletion of Li2CO3 Inhibitor in a Polyurethane Coating, Coatings 7 (2017) 106.

[119] R.T. Foley, Localized Corrosion of Aluminum Alloys—A Review, Corrosion 42

(1986) 277–288.

[120] R.T. Foley, T.H. Nguyen, The Chemical Nature of Aluminum Corrosion: V . Energy Transfer in Aluminum Dissolution, J. Electrochem. Soc. 129 (1982) 464.

[121] L. Anicăi, A.C. Manea, T. Visan, Lithium-AluminIum Hydroxide Hydrate thin Layers on Al Based Substrates - New Ecological Process for Corrosion Resistance Increase, Mol. Cryst. Liq. Cryst. 418 (2004) 41–53.

[122] M.R. Tabrizi, S.B. Lyon, G.E. Thompson, J.M. Ferguson, The long-term corrosion of aluminium in alkaline media, Corros. Sci. 32 (1991) 733–742.

[123] A.E. Hughes, A. Trinchi, F.F. Chen, Y.S. Yang, I.S. Cole, S. Sellaiyan, J. Carr, P.D. Lee, G.E. Thompson, T.Q. Xiao, Revelation of Intertwining Organic and Inorganic Fractal Structures in Polymer Coatings, Adv. Mater. 26 (2014) 4504–4508.

[124] A.E. Hughes, A. Trinchi, F.F. Chen, YS. Yang, S. Sellaiyan, J. Carr, P.D. Lee, G.E. Thompson, T.Q. Xiao, Structure and Transport in Coatings from Multiscale Computed Tomography of Coatings—New Perspectives for Eelectrochemical Impedance Spectroscopy Modeling?, Electrochimica Acta 202 (2016) 243–252.

[125] S. Sellaiyan, A.E. Hughes, S.V. Smith, A. Uedono, J. Sullivan, S. Buckman, Leaching properties of chromate-containing epoxy films using radiotracers, PALS and SEM, Prog. Org. Coat. 77 (2014) 257–267.

[126] J.S. Laird, A.E. Hughes, C.G. Ryan, P. Visser, H. Terryn, J.M.C. Mol, Particle induced gamma and X-ray emission spectroscopies of lithium based alloy coatings, Nucl. Instrum. Methods Phys. Res. Sect. B Beam Interact. Mater. At. 404 (2017) 167–172.

[127] S.Gh.R. Emad, X. Zhou, S.B. Lyon, G.E. Thompson, Y. Liu, G. Smyth, D. Graham, D. Francis, S.R. Gibbon, Influence of volume concentration of active inhibitor on microstructure and leaching behaviour of a model primer, Prog. Org. Coat. 102 (2017) 71–81.

[128] E. Javierre, S.J. García, J.M.C. Mol, F.J. Vermolen, C. Vuik, S. van der Zwaag, Tailoring the release of encapsulated corrosion inhibitors from damaged coatings: Controlled release kinetics by overlapping diffusion fronts, Prog. Org. Coat. 75 (2012) 20–27.

[129] P. Klomjit, R.G. Buchheit, Characterization of inhibitor storage and release from commercial primers, Prog. Org. Coat. 114 (2018) 68–77.

[130] N. Madelat, B. Wouters, E. Jalilian, G. Van Assche, A. Hubin, H. Terryn, T. Hauffman, Differentiating between the diffusion of water and ions from aqueous electrolytes in organic coatings using an integrated spectro-electrochemical technique, Corros. Sci. 212 (2023) 110919.

[131] J. Mardel, S.J. Garcia, P.A. Corrigan, T. Markley, A.E. Hughes, T.H. Muster, D. Lau, T.G. Harvey, A.M. Glenn, P.A. White, S.G. Hardin, C. Luo, X. Zhou, G.E. Thompson, J.M.C. Mol, The characterisation and performance of Ce(dbp)3-inhibited epoxy coatings, Prog. Org. Coat. 70 (2011) 91–101.

[132] G.M. Geise, D.R. Paul, B.D. Freeman, Fundamental water and salt transport properties of polymeric materials, Prog. Polym. Sci. 39 (2014) 1–42.

[133] S. Mondal, J.L. Hu, Z. Yong, Free volume and water vapor permeability of dense segmented polyurethane membrane, J. Membr. Sci. 280 (2006) 427–432.

[134] M.F. Ferreira Marques, C. Lopes Gil, P.M. Gordo, Zs. Kajcsos, A.P. de Lima, D.P. Queiroz, M.N. de Pinho, Free-volume studies in polyurethane membranes by positron annihilation spectroscopy, Radiat. Phys. Chem. 68 (2003) 573–576.

[135] S.Gh.R. Emad, S. Gad, Q. Ai, Y. Wan, S. Morsch, T.L. Burnett, Y. Liu, S.B. Lyon, J. Li, X. Zhou, Manipulating transport paths of inhibitor pigments in organic coating by addition of other pigments, Prog. Org. Coat. 172 (2022) 107072.

[136] S.Gh.R. Emad, X. Zhou, S. Morsch, S.B. Lyon, Y. Liu, D. Graham, S.R. Gibbon, How pigment volume concentration (PVC) and particle connectivity affect leaching of corrosion inhibitive species from coatings, Prog. Org. Coat. 134 (2019) 360–372.

CHAPTER 3

Evaluation of the Formation and Protectiveness of a Lithium-based Conversion Layer Using Electrochemical Noise[1]

[1] **Z. Li**, A. Homborg, Y. Gonzalez-Garcia, A. Kosari, P. Visser, A. Mol, Evaluation of the formation and protectiveness of a lithium-based conversion layer using electrochemical noise, Electrochimica Acta. 426 (2022) 140733.

Abstract

The formation process of a lithium-based conversion layer on AA2024-T3 and its corrosion protective behaviour are studied using electrochemical noise (EN). Wavelet transform, as well as noise resistance analysis, have been employed to interpret the EN data. The EN data confirmed five different stages during the conversion layer growth, accompanied by anodic dissolution, increasing corrosion protection of the conversion layer, and adsorption, growth and desorption of hydrogen bubbles simultaneously. The detachment of hydrogen bubbles, localized and uniform corrosion generate different features in the EN signals with energy maxima in high, intermediate and low frequency bands, respectively. In addition, EN results show that the lithium-based conversion layer still provides efficient protection after re-immersion in a corrosive environment, even though localized damage occurs. Moreover, the EN data corresponds well with the morphological layer formation and breakdown observed with microscopy techniques. The results demonstrate that EN is a powerful tool to provide continuous time- and frequency-resolved information about the inhibition efficiency.

Keywords: Aluminium alloy, electrochemical noise, hexavalent chromium replacement, corrosion inhibition, lithium-based conversion layer

3.1. Introduction

Aluminium alloys widely applied in the aerospace industry, such as AA2024-T3, are highly susceptible to localized corrosion in aggressive aqueous solutions. The main reason is the inhomogeneous distribution of copper-rich intermetallic particles, which significantly improve the alloys' mechanical properties [1–3]. Generally, to extend the service life of aluminium alloys, the use of inhibitors is one of the most common methods for corrosion protection [4–6].

Over the last decades, the most commonly used technologies to enhance the corrosion protection of aluminium alloys are based on hexavalent chromium chemistries, including chromate-based inhibitors and conversion coatings [7]. However, due to the high toxicity and carcinogenicity of these compounds, the REACH Regulation of the European Union has decided to restrict the usage of hexavalent chromium [6]. Currently, many alternative strategies for developing chromate-free inhibitors are proposed. These inhibitors can be divided into several categories, including oxo-anionic, cationic, metal, metal oxide, and organic inhibitors [8]. While several approaches have been reported to achieve promising results, relatively few single or mixed inhibitors exhibit similar protection efficiency compared with chromate-containing systems [9,10]. Lithium salts have drawn extensive attention for replacing hexavalent-chromium-based corrosion inhibitors due to their robust passivating capability on various aluminium alloys over the recent years [8,11–15]. The earliest report on the passivation function of lithium salts dates back to 1987 when Gui and Devine [16] showed that AA6061-T6 in an alkaline lithium carbonate solution presented passivity under anodic polarization stimulation. Later, Drewien et al. [17] observed that Li-Al layered double hydroxide (LDH) coatings formed by alkaline lithium salt immersion followed by a low-temperature heat treatment in air or water was capable of providing favourable barrier properties as compared to traditional chromate conversion coatings. The supersaturation of aluminate ions in the solution seems to be an essential step for the formation of the conversion layer. In 2010, Visser et al. [18,19] developed a novel coating system where lithium salts are incorporated into organic coatings, serving as a leachable inhibitor to provide active and irreversible corrosion protection.

Morphological and compositional variation of the lithium conversion layer during immersion has been well studied [20,21]. It was revealed that lithium ions are distributed evenly throughout the conversion layer, resulting in a multi-layered structure, the composition of the multi-layered structure varied in the artificial defect

in the organic coating due to the differences in the local environment. Usually, the conversion layer consisted of a top columnar layer composed of Li-Al LDH and a dense inner layer composed of an amorphous lithium-containing pseudoboehmite phase [20]. In addition, a porous intermediate layer which contains both amorphous and crystalline compounds may also appear in some local regions inside the defect [20]. To evaluate the lithium-based conversion layer formation on AA2024-T3 in a lithium carbonate solution containing chloride ions, Visser et al. set up an electrochemical cell to mimic the local aqueous environments of a scribed area [14]. Three consecutive stages, including oxide thinning, hydroxide film formation and layer growth were proposed with the additional supporting evidence from compositional and morphological observations.

Moreover, Kosari et al. [22] investigated the local layer formation process with sub-micron resolution at and around intermetallic particles on AA2024-T3. The entire layer formation process (including a columnar outer layer and an inner dense layer, resulting from a 7-h exposure) was analysed using top-view and cross-sectional observations, supplemented with the recorded open circuit potential (OCP). This revealed that the conversion layer formation process consisted of five distinct stages. The entire conversion layer formation process evolves morphologically, compositionally and electrochemically. AA2024-T3 surface doesn't acquire obvious passivation at stages I and II, during which the passivation is lost and active matrix dissolution, and dealloying of intermetallic particles occurs. The conversion layer formation and growth are mainly associated with the later stages (stage III to stage V). Kosari et al. [22] also found that the passivation process is not synchronized between the aluminium matrix and different intermetallic particles. It was found that the columnar layer formation process on the S-phase preceded that on the aluminium matrix and on other types of intermetallic particles due to the higher electrochemical activity and faster dissolution rate the of S-phase, leading to an earlier local supersaturation of aluminate ions and the formation of a columnar layer over the S-phase.

An extensive number of traditional electrochemical techniques like linear polarization resistance (LPR) and electrochemical impedance spectroscopy (EIS) have been applied to evaluate the corrosion protective properties of the lithium-based conversion layer [14,19,23]. However, these measurements only presented electrochemical information at several discrete time points. Therefore, rapid electrochemical reactions might not be identified. In other words, a detailed

continuous and time-resolved evolution of electrochemical reactions during the formation process of the lithium-based conversion layer has not been studied and discussed to a large extent yet. Electrochemical noise (EN) is a technique which records a potential and current signal simultaneously and continuously without external perturbation of the system. The capability to monitor rapidly changing electrochemical processes has been reported in prior studies [24–28]. EN has been successfully applied to study conversion layer formation on different metals. For example, Tan et al. [29] investigated the chromate conversion coating (CCC) formation process on aluminium using EN analysis and proved that CCC protection only was established after aging treatments. Liu et al. [30] studied the in-situ formation process in the time and frequency domain of a stannate CCC on AZ91D magnesium alloys. It revealed that there were two separate stages, including an incubation stage accompanied by the nucleation and nuclei dissolution process, and a periodical growth stage consisting of growth and dissolution of hemispherical particles during the CC formation process.

In this paper, EN is applied to investigate the lithium-based conversion layer formation process in-situ and continuously, using wavelet transform and noise resistance analysis. In addition, EN was employed to study the irreversibility behaviour of the lithium-based conversion layer in a neutral sodium chloride solution.

3.2. Experimental Methods

3.2.1. Materials and experimental set-up.

A single commercial bare AA2024-T3 sheet provided by Goodfellow in 0.8 mm thickness served as working electrode material. A commercial pure Al sheet (99.999 % purity) of 1 mm thickness was used for control experiments. Two identical specimens with a size of 8 mm × 20 mm were cut out from larger panels. The two samples were embedded in epoxy resin at an interdistance of 2 mm after spraying a primer at four edges to avoid crevice corrosion. Later, the embedded sample was sanded up to grit 4000 with SiC paper and then left in ambient environment for 24 h before the experiments. The pure Al samples were polished on a soft cloth using alumina slurries of 0.5 μm and 0.05 μm after sanding. The adhesive copper tape was connected to both samples separately for electrical connection. In this electrochemical cell, two identical exposed working electrodes were created by covering the working electrode surfaces using a water-proof tape with a round hole of 10 mm diameter. Then an O-ring with a diameter of 10 mm was fitted to the round defect of tape and pressed by a PMMA cell to hold the electrolyte.

Laboratory-grade chemicals used in this work were ordered from Sigma-Aldrich (St. Louis, MO, USA).

The measurements were performed in a traditional three-electrode system which contains two identical working electrodes and a saturated Ag/AgCl reference electrode. All measurements were conducted under open circuit potential conditions. In order to mimic the liquid environment on exposed coupons from previous work [22], 321 μL electrolyte containing 0.01 M NaCl and 0.01 M Li_2CO_3 (pH 10.9) was added into the reaction cell to provide a relatively thin film (approx. 4 mm), as illustrated in **Fig. 3.1**. Electrolyte containing 0.01 M NaCl and 0.01 M Na_2CO_3 (pH 11.0) was used to compare the behaviour of AA2024-T3 in the electrolyte with or without lithium ions.

All experiments were performed in the open air. The exposure duration time for coupons to the electrolyte was 14500 s and the room temperature was controlled at 20 °C. A Compactstat from Ivium Technologies was used to record current and potential signals simultaneously, serving as zero resistance ammeter (ZRA in **Fig. 3.1**) and potentiometer (E in **Fig. 3.1**). The Compactstat was put into a Faradaic cage to avoid the influence of electromagnetic disturbance caused by external sources. The Compactstat was controlled by a Windows-based PC software. The sampling frequency chosen for this work was 20Hz and a low-pass filter of 10Hz was used to avoid aliasing. The EN data were processed using Matlab from MathWorks. Morphological information was obtained using a JEOL JSM-6500F field emission scanning electron microscope (SEM) with the secondary electron detector using an acceleration voltage of 15 kV at a working distance of 10 mm. All experiments were performed at least in triplicate, while the results shown in the supporting document were performed at least two times.
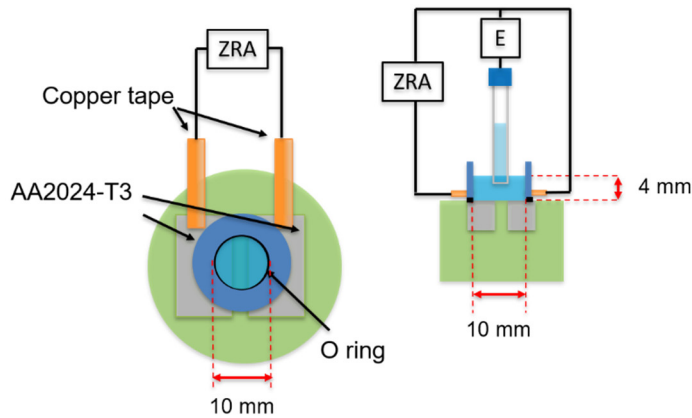
Fig. 3.1 Layout of the electrochemical cell

3.2.2. EN analysis. Many natural signals are nonstationary and nonlinear, producing a direct current (DC) drift in the raw signals [31]. DC drift is visible as a variation of statistical parameters over time, e.g., a slow alteration of a system under investigation over time. A possible cause of DC drift in the electrochemical current noise could be an increasing asymmetry between working electrodes over the course of a measurement [32,33]. The low frequency contribution generated by DC drift may cause inaccurate and false results on the outcome of data analysis and should be removed prior to further data analysis [31]. There are various methods suitable for this purpose, like moving average, polynomial and linear trend removal, wavelet analysis and empirical mode decomposition [25]. Linear detrending is firstly excluded since this technique is likely to leave behind part of the DC drift. Moving average trend removal (MAR) is also not highly recommended according to previous studies [34]. Estimating nonuniform drift over long times is very difficult using MAR, which may drastically reduce the analysed frequency range. MAR may therefore lead to inaccurate standard deviation data. For polynomial detrending, the main disadvantage is the user-defined parameter of the polynomial order: a higher order may attenuate the lowest frequencies that can still be attributed to corrosion. In addition, it is difficult to select an optimal polynomial degree automatically. Therefore, considering the drawbacks of these traditionally used trend removal methods, wavelet analysis, a commonly used time-frequency method for trend removal [31], is chosen in this study. An eight-level discrete wavelet decomposition with a Daubechies 4 wavelet is reported to effectively remove the DC trend on the

one hand, while maintaining the useful corrosion information on the other hand [31,35,36]. In this work, all trend removal was performed using this method.

Noise resistance, defined as the ratio between the standard deviations of the potential and current fluctuations after trend removal, is expected to be close to the DC limit of the polarization resistance [37,38]. In general, the time window for the calculation of standard deviations has a fixed size. If a moving time window which is shorter than the total recording time is employed, the noise resistance varies as a function of time.

As a mathematical tool, wavelets have been widely used to extract information from many different types of data, including e.g., audio signals and images [25]. In this paper, an analytic Morlet wavelet was used to generate the continuous wavelet transform (CWT) spectrum. A CWT spectrum simultaneously presents the energy distribution in the EN signal over time and frequency. For the CWT process, the signal was matched to a series of compressed or stretched versions of a wavelet by shifting the wavelet along the time axis. Compressing or stretching a wavelet is referred to as scaling, corresponding to the scaling parameter. Generally, CWT coefficient C (a, b) is acquired by continuously varying the values of the scale parameter "a", and the position parameter "b". Scale parameter "a" corresponds to frequency and position parameter "b" denotes time. The amplitude, representing the local energy of the signal, is calculated and then plotted against scale parameter "a" and position parameter "b" to generate a time-frequency plot. Discrete wavelet transform (DWT) involves a similar process. The difference between CWT and DWT lies in the scaling factor and the time points. For the CWT, an arbitrary scaling factor is used and each scaled wavelet is shifted quasi-continuously along the time axis. However, the scaling factor for DWT is always two. In this way, DWT is more computation efficient. As a result, the CWT spectrum appears smoother as compared to an energy distribution plot from DWT [39].

3.2.3. Irreversibility and corrosion protection. The irreversibility properties and protectiveness of the lithium-based conversion layer were also assessed using EN. To generate a relatively uniform and compact conversion layer, hydrogen bubbles from the alkaline bath were removed by gently stirring the electrolyte every 10 mins until no visible bubbles were left on the sample surfaces. After each initial exposure to the electrolyte, the solution was removed immediately. The exposed sample surface was rinsed gently using 0.01 M NaCl for 1 min to remove the residual lithium carbonate

entirely. Then a volume of 0.321 μL 0.01 M NaCl solution was refilled to the electrochemical cell. The re-immersion period also lasted for 14500 s.

3.3. Results and Discussion

3.3.1. EN data analysis and morphological characterization. The current and potential noise signals were recorded simultaneously as described in section 3.2.1. **Fig. 3.2a** and **Fig. 3.2b** show the EN raw data obtained for the experiments on 0.01 M NaCl-0.01 M Li_2CO_3 (NaCl-Li_2CO_3) and 0.01 M NaCl-0.01 M Na_2CO_3 (NaCl-Na_2CO_3), respectively. The potential signals both exhibit a quick drop and then a gradual increase. In contrast, the current signals both present a large value with significant oscillations at the start which gradually reduce over time.
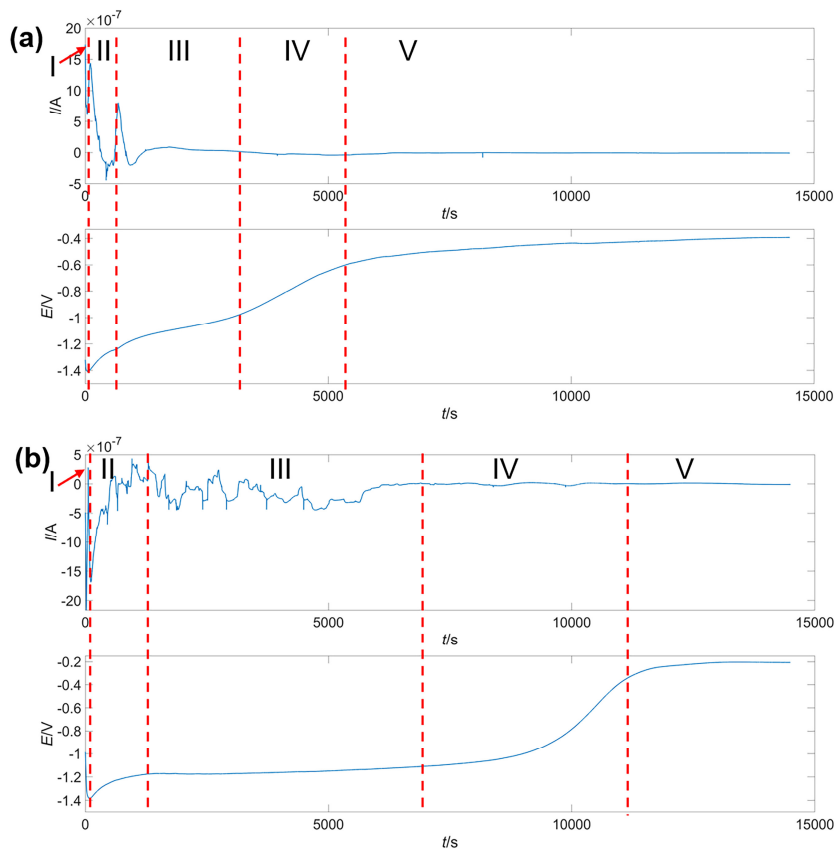
Fig. 3.2 EN current and potential signal for AA2024-T3 exposed in (a) 0.01 M NaCl and 0.01 M Li_2CO_3 solution, and (b) 0.01 M NaCl and 0.01 M Na_2CO_3 for a duration of 14500 s.

According to previous studies [14,22], steady passivation occurred during the alkaline bath immersion both in the NaCl-Li$_2$CO$_3$ and in the NaCl-Na$_2$CO$_3$ system. The passivation process can be divided into five different stages according to the potential variation. For the EN behaviour of the AA2024-T3 sample exposed in NaCl-Li$_2$CO$_3$ solution, the potential has a sharp decrease to a minimum of -1408 mV during the first 60 s, accompanied by a relatively large current value of several microamperes (Stage I). Later, several potential increases follow. The first potential rise reaches a small plateau of -1225 mV at t=700 s, where the current signal also presents a sharp alteration with small spikes (Stage II). The second potential rise reaches approximately -1000 mV at t=3000 s, representing stage III. In this stage, the amplitudes of the current fluctuations gradually decay to a level of several tens of nanoamperes. The third rise in the potential is associated with stage IV, where potential values gradually reach up to -600 mV at t=5400 s and the current values slightly decrease but are still in the same order of magnitude as the current fluctuations in stage III. Finally, the system reaches a relatively stable state where the potential slowly reaches up to -400 mV after an immersion period of 14500 s. The current reaches a value of less than 10 nA (stage V).

Similarly, the signal variation of the AA2024-T3 sample exposed in NaCl-Na$_2$CO$_3$ electrolyte (Figure 2.b) presents a sharp initial potential decrease and four sequential potential rises as well. The potential initially drops to -1385 mV at t=80 s (stage I) and then reaches a plateau value of -1170 mV at t=1400 s (stage II). Stage III shows a stable potential at around -1170 mV, while the current signal fluctuates significantly. Stage IV starts at t=7200 s with an "S" shape potential rise and ends when the potential reaches -240 mV at t=12000 s. The current value gradually decreases to a stable value of several tens of nanoamperes during this stage. During stage V, the system reaches a stabile state where the potential slightly changes to -200 mV, while the current value does not present an obvious change as compared to the late fourth stage. According to the studies of Kosari et al. [22], local supersaturation of aluminate ions firstly occurs on the S-phase during the second stage, leading to the growth of a columnar-like conversion layer at the location of the S-phase in the existence of lithium ions. This local passivation explains why the potential value of the small plateau shown in **Fig. 3.2a** is slightly higher than that of **Fig. 3.2b**.

3.3.2. Morphological characterization. The surface of the samples was analysed by SEM at the different stages identified during the EN analysis. **Fig. 3.3a-3.3f** show

top-view SEM images of the AA2024-T3 surface after different periods of exposure to 0.01 M NaCl + 0.01 M Li$_2$CO$_3$ solution. The time intervals include t=60 s (late first stage), t=200 s (early second stage), t=700 s (late second stage), t=2000 s (third stage), t=4000 s (fourth stage), and t=14500 s (fifth stage). After the initial immersion period (**Fig. 3.3a** and 3.**3b**), a roughened morphology appears on the sample surface, indicating corrosion of the alloy matrix. The alloy surface experiences dissolution of the oxide film in the first stage, followed by dissolution of the aluminium matrix and dealloying of intermetallic particles at the second stage [22]. After 700 s (**Fig. 3.3c**), more severe corrosion is observed, but a columnar-like morphology starts to appear at the late second stage. The growing columnar outer layer explains the gradual decrease of the current signal at the third stage, since the protective layer gradually inhibits the diffusion of corrosive ions and the dissolution of the matrix. A clearer columnar structure is observed on the alloy surface after an exposure of 2000 s (**Fig. 3.3d**). With increasing exposure time (**Fig. 3.3e and 3.3f**), the columnar outer layer keeps growing in harmony with a dense inner layer providing an enhanced corrosion protection [14]. This corresponds to the EN signals of **Fig. 3.2a**, which shows a diminishing EN current and a higher OCP.

Fig. 3.4a-3.4e show SEM images for the exposure to 0.01 M NaCl + 0.01 M Na$_2$CO$_3$ solution at t=80 s (late first stage), t=1400 s (second stage), t=4000 s (third stage), t=10000 s (fourth stage), and t=14500 s (fifth stage). In this case, a typical corrosion-attack morphology of the aluminium matrix in alkaline environments is present [40]. Irregular corrosion products cover an increasing number of locations at the surface with immersion time. Although this corrosion product layer still inhibits the dissolution of the matrix to some extent, its protective effect is far less effective as compared to the lithium-containing conversion layer (as was shown in **Fig. 3.2**).
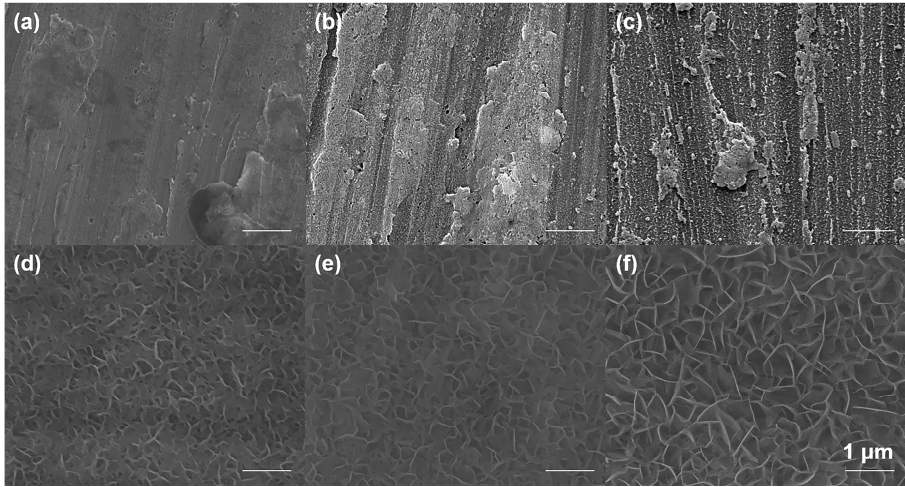
Fig. 3.3 Top-view SEM images of the AA2024-T3 surface exposed in 0.01 M NaCl and 0.01 M Li$_2$CO$_3$ at different exposure times: (a) 60 s; (b) 200 s; (c) 700 s; (d) 2000s; (e) 4000 s; (f) 14500 s.
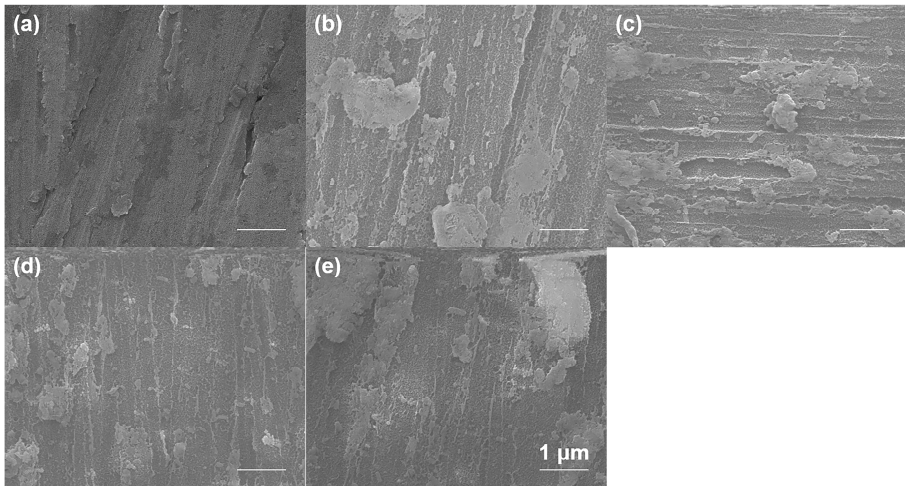
Fig. 3.4 Top-view SEM images of the AA2024-T3 surface exposed in 0.01 M NaCl and 0.01 M Na$_2$CO$_3$ at different exposure times: (a) 80 s; (b) 1400 s; (c) 4000 s; (d) 10000 s; (e) 14500 s.

To avoid the interference of low-frequency energy and to focus on the transient signals appearing in the current signal, **Fig. 3.5a and 3.5b** show the raw data from 0 to 3000 s after trend removal for the samples exposed in NaCl-Li$_2$CO$_3$ and NaCl-

Na$_2$CO$_3$ electrolyte, respectively (Detailed view of timeframe between 600 s and 700 s of Fig. 5a and 5b are shown in Fig. 5a' and Fig. 5b', respectively).
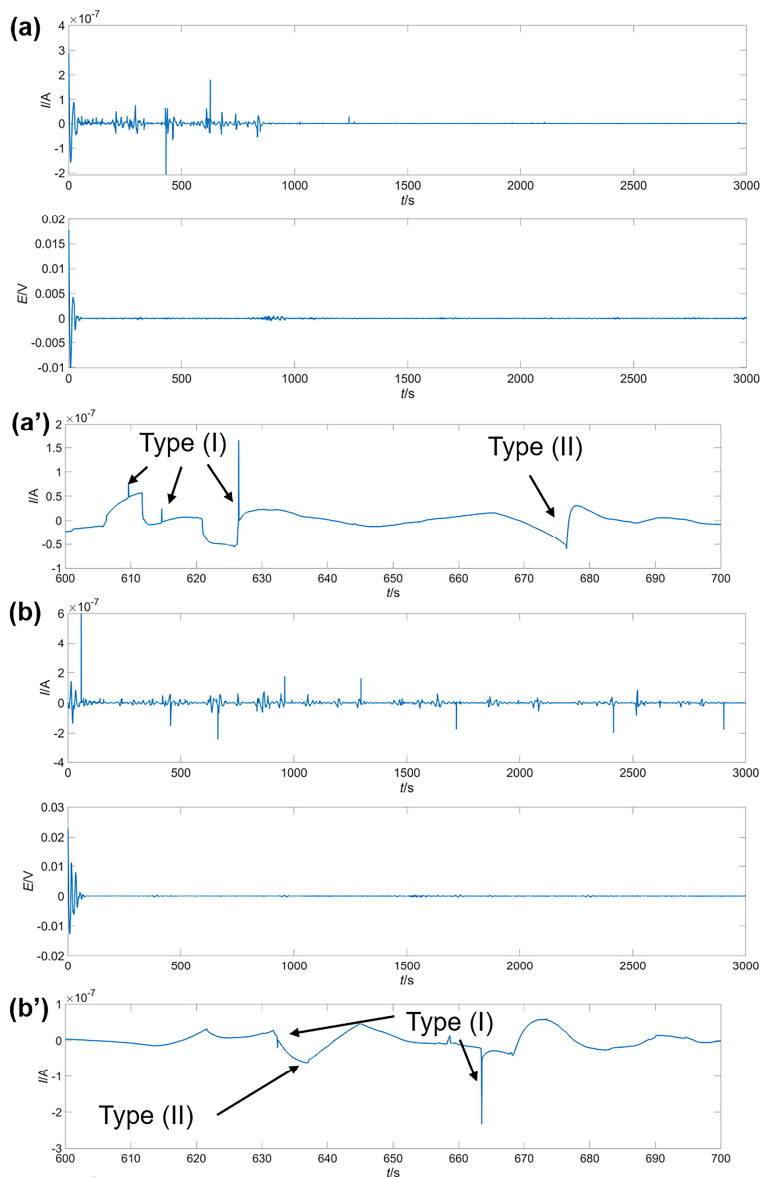
Fig. 3.5 Current and potential signal after trend removal of samples exposed in (a) 0.01 M NaCl and 0.01 M Li$_2$CO$_3$ solution for a duration of 3000 s, (a') Detailed view of timeframe between 600 s and 700 s, and (b) 0.01 M NaCl and 0.01 M Na$_2$CO$_3$ solution for a duration of 3000 s, (b') Detailed view of timeframe between 600 s and 700 s.

In the presence of lithium ions, the current signal oscillations mainly appear in the first 1000 s, followed by a relatively stable passive state. This indicates that localized electrochemical reactions mainly occur in the initial alkaline bath immersion period and that lithium ions are beneficial for the passivation and stabilization of the corroding surface of AA2024-T3. However, for the measurements without lithium ions, transient oscillations last considerably longer, which means that the corrosion process proceeds without effective suppression. The potential signals for both immersion conditions appear to exhibit nearly the same shape without noticeable oscillations, except for the first 100 s. Another interesting finding is that two types of transients appear, each with a distinct time span. The high frequency transients (type I) usually last no more than 0.5 s, while the duration of the intermediate frequency transients (type II) is usually in the order of several seconds. Both transient types correspond to different phenomena. This will be discussed in detail later.
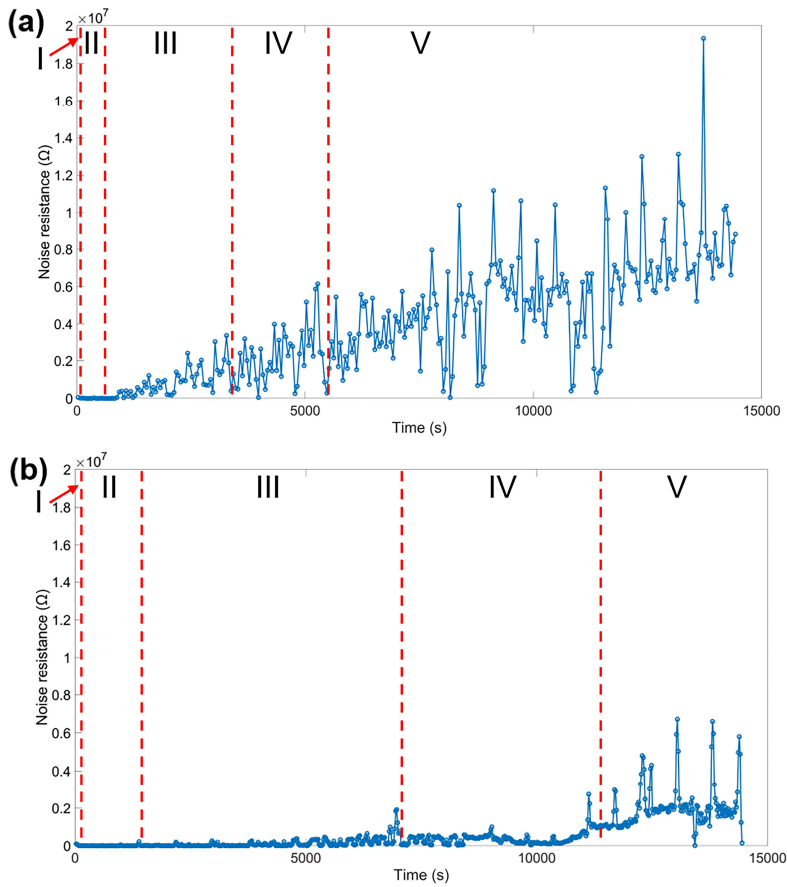
Fig. 3.6 Noise resistance calculated for AA2024-T3 electrodes immersed in (a) 0.01 M NaCl and 0.01 M Li$_2$CO$_3$ solution, and (b) 0.01 M NaCl and 0.01 M Na$_2$CO$_3$ solution for a duration of 14500 s.

As a statistical parameter, the value of the noise resistance is inversely proportional to the corrosion rate [29,38,41]. **Fig. 3.6a** and **3.6b** show the variation of noise resistance as a function of time in the NaCl-Li$_2$CO$_3$ and NaCl-Na$_2$CO$_3$ solution, respectively. The calculated noise resistance values for the two different systems are both relatively smooth and low at the beginning, owing to the highly corrosive alkaline electrolytes. This is followed by an increasing trend, along with increasing fluctuation amplitudes. It is evident that the action of lithium ions increases the noise resistance of AA2024-T3. In addition, the increase of the noise resistance occurs earlier as compared to the case without lithium ions, indicating that surface passivation in the electrolyte containing lithium ions precedes the process of the

benchmark group without lithium ions. This corresponds well with the morphological observations. The noise resistance in **Fig. 3.6a** is still relatively small at the early third stage, indicating that the sample surface is not yet fully covered by the conversion layer. In this case, the columnar structure cannot fully inhibit the diffusion of corrosive electrolyte. With the growth of the columnar structure and the increasing coverage of the conversion layer, the noise resistance increases. The noise resistance in the fourth and fifth stages mainly indicates a passive state and full coverage of the conversion layer. The noise resistance steadily increases, but with more significant oscillations due to the competitive growth and dissolution of the substrate [8,14,22].

In order to study the temporal evolution and the dominant corrosion process simultaneously, **Fig. 3.7a and 3.7b** show the CWT spectrum of the EN current for AA2024-T3 samples exposed in $NaCl$-Li_2CO_3 and $NaCl$-Na_2CO_3 from 0 to 1500 s in the time-frequency domain and the corresponding optical images after an immersion period of 14500 s, respectively.
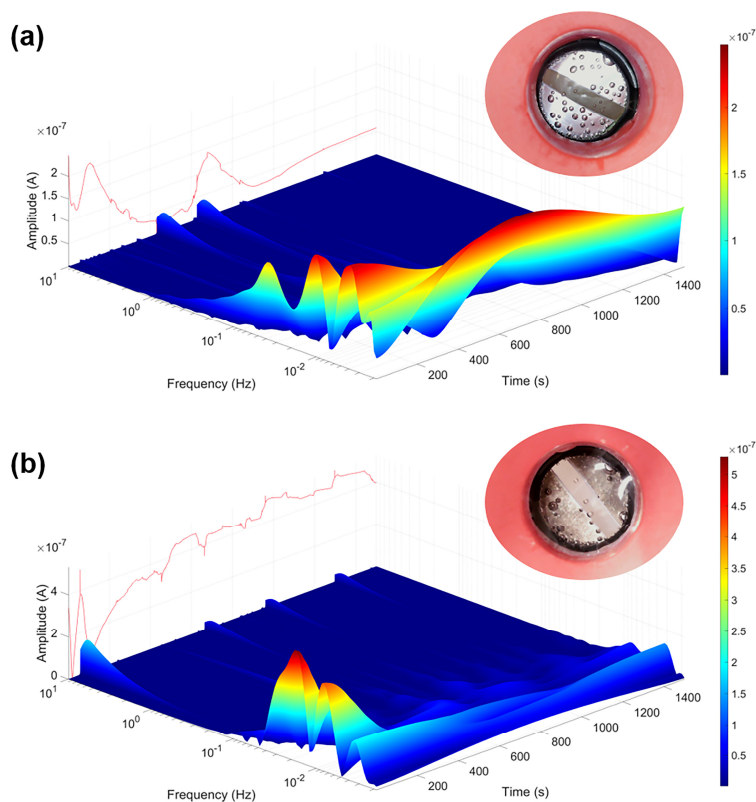
Fig. 3.7 CWT spectrum of the EN current for AA2024-T3 exposed in (a) 0.01 M NaCl and 0.01 M Li₂CO₃ solution, and (b) 0.01 M NaCl and 0.01 M Na₂CO₃ solution, from 0 to 1500 s.

As shown in the spectra and indicated in red, most of the energy is concentrated in the low-frequency band, below 10^{-2} Hz. This is due to the fast uniform dissolution, which is typical for aluminium alloys that are exposed to highly corrosive alkaline electrolytes. Different local maxima are present in the high-frequency band, above 1 Hz, and are expected to be caused by the detachment of hydrogen bubbles from the AA2024-T3 surface. A fresh surface that was initially protected by the bubble is suddenly exposed to the corrosive solution, causing an increase of the exposed area. This leads to a sudden increase in the current. Video evidence for the bubble detachment and the corresponding high-frequency transient occurrence is shown in **Movie S3.1** and **Fig. S3.1**. The number of high-frequency transients of samples exposed to NaCl-Na₂CO₃ electrolyte is higher than that of samples exposed to NaCl-Li₂CO₃, visible in **Fig. 3.5**. This indicates that more hydrogen bubbles detach in the

absence of lithium ions. In addition, as shown in the corresponding optical figures, the quantitative difference in high-frequency transients is inversely proportional to the number of bubbles still present at the sample surface. This further proves that this type of high-frequency transients is related to the detachment of hydrogen bubbles. To avoid the interference of low-frequency energy and to make the transient signals appear more clearly, the EN current CWT spectra from **Fig. 3.7** are plotted again in **Fig. 3.8,** after the removal of the low-frequency band using an eight-level Daubechies 4 wavelet. The first 100 s are omitted to avoid the interference of fast current variations due to the instability of the samples immediately after exposure to highly corrosive electrolytes.
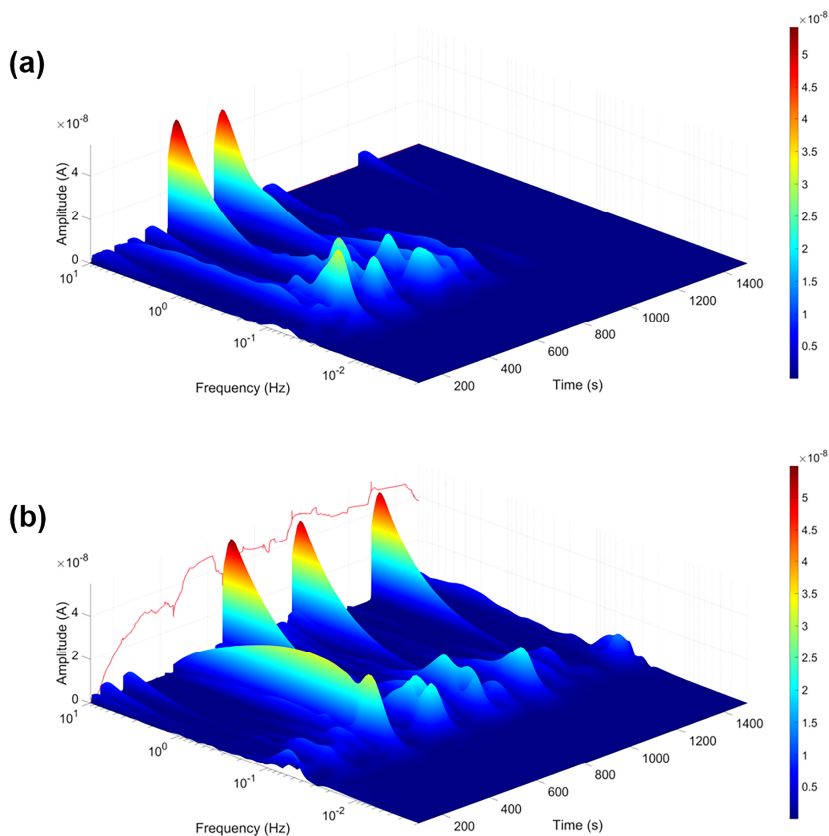
Fig. 3.8 CWT spectrum of the EN current after removal of the DC drift for AA2024-T3 exposed in (a) 0.01 M NaCl and 0.01 M Li₂CO₃, and (b) 0.01 M NaCl and 0.01 M Na₂CO₃, from 100 to 1500 s.

Two parallel electrochemical reactions with distinct frequencies are present, which corresponds well with the results in **Fig. 3.5**. For the samples exposed in NaCl-Li$_2$CO$_3$ solution, the amplitudes of these two reactions gradually decrease to zero in the early phase of the third stage (approximately 800 s). In contrast, the sample immersed in NaCl-Na$_2$CO$_3$ continuously exhibits two parallel electrochemical reactions. According to previous morphological and compositional studies on intermetallic particles of AA2024-T3, it is known that aluminium matrix dissolution, dealloying and copper enrichment of intermetallic particles are the dominant electrochemical reactions during the second stage and early third stage [22]. Therefore, the intermediate frequency range of the EN current signal can be attributed to the dealloying of intermetallic particles and micro-galvanic reactions between the aluminium matrix and (partially) dealloyed intermetallic particles [42]. For the purpose of verification, the CWT spectrum of pure Al from 100 to 1500 s is shown in **Fig. S3.2**. It is clear that high-frequency energy caused by hydrogen bubbles is still visible in the spectrum, whereas the amplitudes at intermediate frequencies are significantly lower.

3.3.3. Corrosion protection evaluation of the lithium-based conversion layer.

Excellent irreversible corrosion-protective properties are an important indicator for the long-term protection of inhibitors [19]. In order to verify this, the corrosion characteristics of AA2024-T3 that were previously exposed in a NaCl-Li$_2$CO$_3$ solution or a NaCl-Na$_2$CO$_3$ solution (further denoted as 'treated') are compared to bare AA2024-T3 (further denoted as 'untreated'). **Fig. 3.9a-3.9c** present the EN data for treated AA2024-T3 in NaCl-Li$_2$CO$_3$ solution and NaCl-Na$_2$CO$_3$ solution, and for untreated AA2024-T3, all three exposed in 0.01 M NaCl solution, respectively. Their corresponding top-view observations are shown in **Fig. 3.10**.
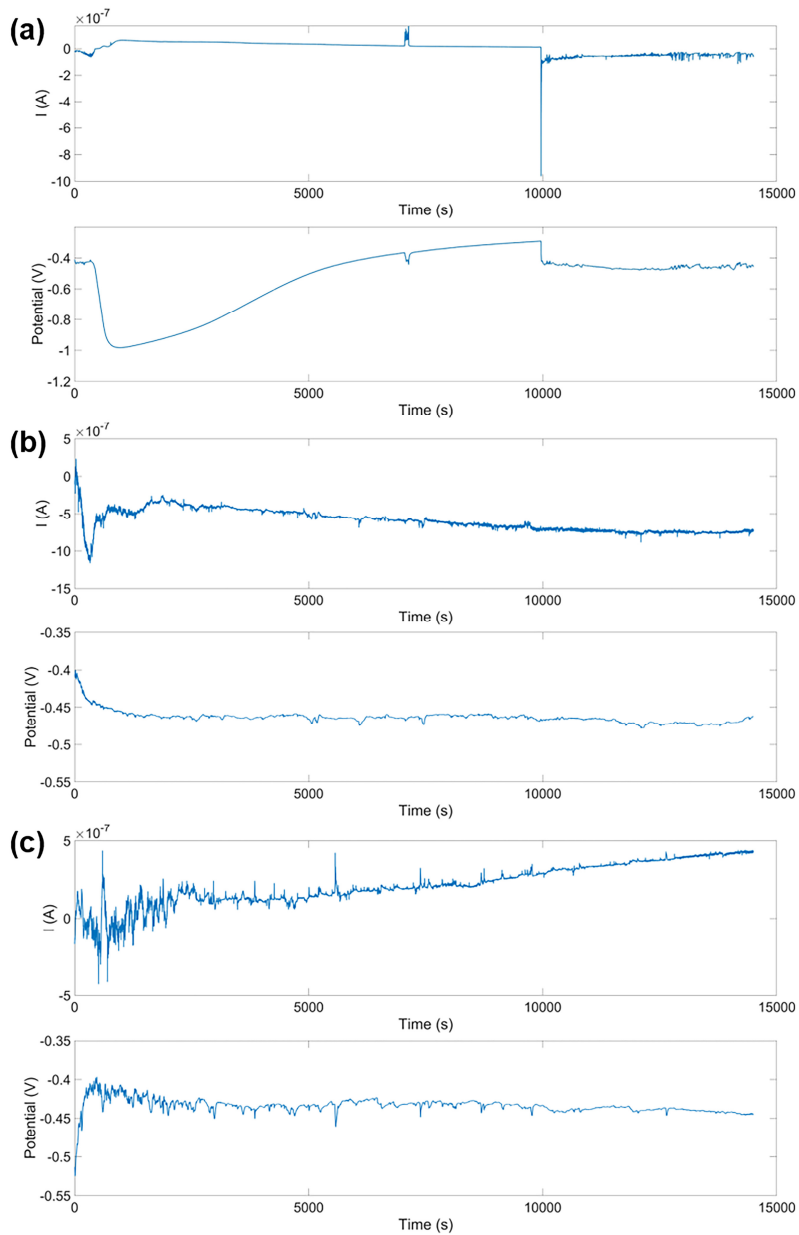
Fig. 3.9 EN current and potential signal for (a) AA2024-T3 treated in 0.01 M NaCl and 0.01 M Li$_2$CO$_3$ bath for 14500 s, and (b) AA2024-T3 treated in 0.01 M NaCl and 0.01 M Na$_2$CO$_3$ bath for 14500 s, and (c) untreated AA2024-T3 exposed in 0.01 M NaCl electrolyte for 14500 s.
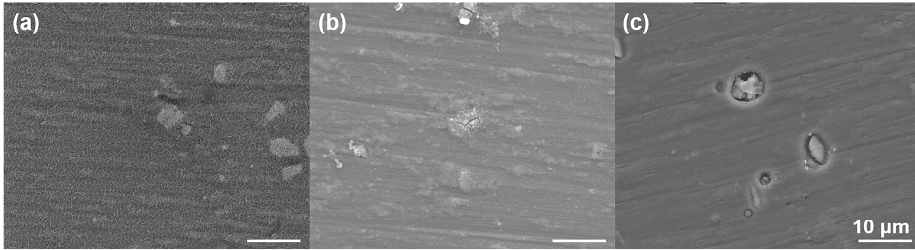
Fig. 3.10 Top-view SEM images of the AA2024-T3 surface (a) treated in a 0.01 M NaCl and 0.01 M Li₂CO₃ solution for 14500 s, (b) treated in a 0.01 M NaCl and 0.01 M Na₂CO₃ solution for 14500 s, and (c) untreated AA2024-T3 exposed in a 0.01 M NaCl solution for 14500 s.

For the treated sample in NaCl-Li$_2$CO$_3$, the potential initially decreases to almost -1000 mV and then gradually increases to nearly -300 mV. The initial potential drop may be attributed to the release of the residue of carbonate ions that are incorporated into the columnar sublayer of the conversion layer or limited dissolution of the Li-intercalated LDH/pseudoboehmite, which causes a local alkaline environment. At a later stage, the potential gradually increases due to the consumption or dilution of carbonate ions. The pH variation during the re-immersion period also indicates that the solution turned into a weak alkaline condition with time (**Fig. S3.3**). Finally, an instantaneous potential drop occurs, after which the potential remains at a relatively stable value at around -450 mV. Similarly, the current signal exhibits an obvious passive state before the sudden potential drop, with negligible fluctuations and a low DC value. After this drop, the current abruptly increases and reaches a relatively stable value of approximately 50 nA. From **Fig. 3.10a**, obvious pitting cannot be observed. Corrosion activity after the breakdown of the conversion layer may mainly occur being masked by the outer columnar layer. For AA2024-T3 specimens treated in NaCl-Na$_2$CO$_3$ solution, the porous corrosion product layer cannot prevent the alloy surface from corrosion attack at all.

On the contrary, the porous layer even promotes further corrosion since the current signal shown in **Fig. 3.9b** shows an even higher net value than untreated AA2024-T3 shown in **Fig. 3.9c**. Cracks at certain locations are present under the formed corrosion products, indicating localised corrosion processes (**Fig. 3.10b**) For untreated AA2024-T3, the potential initially increases due to the dealloying of intermetallic particles. This is followed by a copper enrichment and redistribution process [26,42]. At a later stage, the potential signal gradually stabilizes at around -440 mV, which is close to the potential value of the treated samples in NaCl-Li$_2$CO$_3$ after the sudden

potential drop, and to the potential value of the treated samples in NaCl-Na$_2$CO$_3$ solution. From **Fig. 3.10c**, it is obvious that corrosion mainly occurs around intermetallic particles. Therefore, it can be concluded that the drastic potential drop results from the breakdown of the lithium-based conversion layer by chloride ions exposing the underlying AA2024-T3 substrate.

To investigate the difference in the time-frequency domain of samples with and without the protection of the lithium-based conversion layer, **Fig. 3.11a-3.11d** present the CWT spectra of the EN potential noise for samples treated in NaCl-Li$_2$CO$_3$ solution within a timeframe of 2000 s before and after the breakdown, for samples treated in NaCl-Na$_2$CO$_3$ solution and for untreated AA2024-T3, respectively.
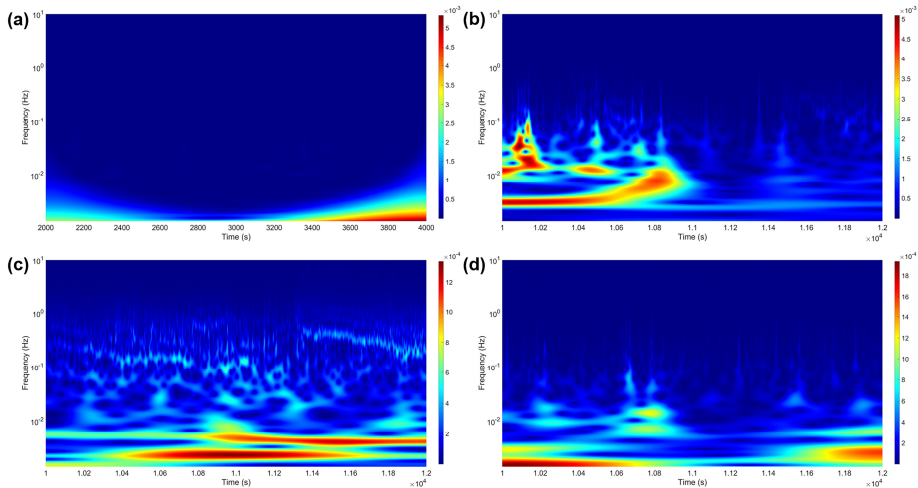
Fig. 3.11 CWT spectrum of the EN potential noise for AA2024-T3 treated in NaCl-Li$_2$CO$_3$ solution exposed in 0.01 M NaCl solution from (a) 2000 to 4000 s and (b) 10000 to 12000 s. CWT spectrum of the EN potential noise for AA2024-T3 treated in NaCl-Na$_2$CO$_3$ solution (c) and untreated AA2024-T3 (d) exposed in 0.01 M NaCl solution from 10000 to 12000 s.

Treated AA2024-T3 samples in NaCl-Li$_2$CO$_3$ solution exhibit an obvious passive state from 2000 to 4000 s owing to the protection provided by the lithium-based conversion layer (**Fig. 3.11a**), while metastable and stable pitting events are observed after the drastic potential drop between 10000 to 12000 s (**Fig. 3.11b**). This is caused by the local breakdown of the conversion layer by chlorides. However, for samples treated in NaCl-Na$_2$CO$_3$ (**Fig. 3.11c**) and untreated specimens (**Fig. 3.11d**), the

dominant energy contribution in the CWT spectra is associated to stable pitting. In other words, the pitting corrosion process is less likely to stop once it is triggered by corrosive ions without the protection of the lithium-based conversion layer. This explanation also corresponds well to **Fig. 3.10**, since no obvious pitting is observed when the alloy surface is covered by the lithium-based conversion layer. Therefore, in the presence of the lithium-based conversion layer, even though localized corrosion occurs at the surface, there is a more significant change that a certain percentage of the pitting process is still supressed by the conversion layer. This leads to a combination of metastable- and stable pitting corrosion.

Moreover, to quantitively investigate the corrosion protection capability of the lithium-based conversion layer, **Fig. 3.12** shows the noise resistance variation as a function of time of untreated AA2024-T3, treated AA2024-T3 in NaCl-Na$_2$CO$_3$ solution and NaCl-Li$_2$CO$_3$ solution.
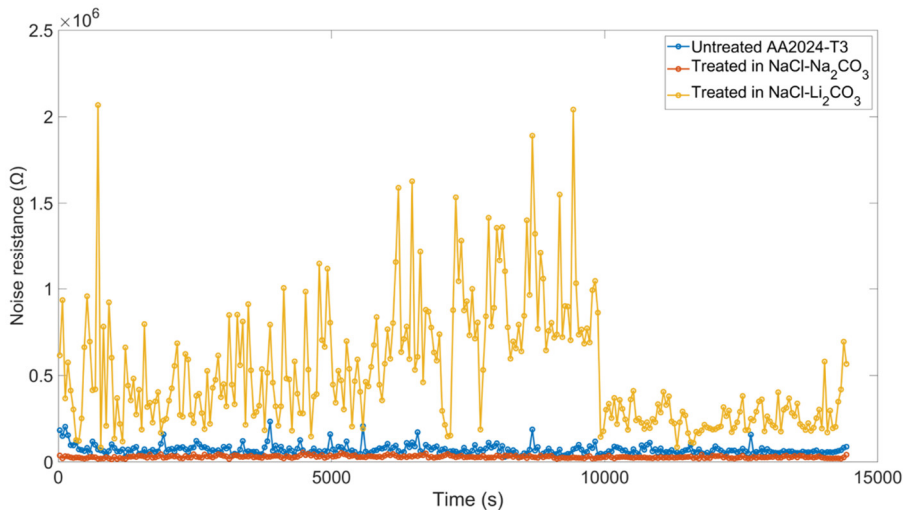
Fig. 3.12 Noise resistance calculated for treated AA2024-T3 in NaCl-Li$_2$CO$_3$ solution, in NaCl-Na$_2$CO$_3$ solution and for untreated AA2024-T3 electrodes, immersed in 0.01 M NaCl solution from 0 to 14500 s.

As seen in **Fig. 3.12**, the noise resistance of the samples protected by the lithium-based conversion layer increases slightly over time before the breakdown, followed by a sudden drop, which remains at a relatively stable value. However, the resistance of the sample with the lithium-based conversion layer after the breakdown of the conversion layer is still nearly an order of magnitude larger than that of samples

treated in NaCl-Na$_2$CO$_3$ and of untreated AA2024-T3 samples. This confirms that the lithium-based conversion layer is still able to provide corrosion protection toAA2024-T3, even while local conversion layer breakdown occurs.

3.4. Conclusions

Electrochemical noise has been proven to be a powerful technique to obtain in-situ, frequency- and time-resolved information about the lithium-based conversion layer formation mechanism and its robust protectiveness. The following conclusions were drawn:

1) The detachment of hydrogen bubbles, localized and uniform corrosion generate different features in the EN signals with energy maxima in high, intermediate and low frequency bands, respectively.

2) Hydrogen evolution, trenching of the matrix and dealloying of intermetallic particles are dominant localized electrochemical reactions occurring simultaneously in the first two stages and the early third stage. After that, the growth of a passive conversion layer is the dominant process.

3) Lithium ions favour the stabilization of corrosion products and significantly delay the corrosion degradation of AA2024-T3.

4) The lithium-based conversion layer is still protective after re-immersion in an NaCl containing electrolyte where lithium ions are absent, despite the local breakdown of the protective film.

References

[1] A. Boag, R.J. Taylor, T.H. Muster, N. Goodman, D. McCulloch, C. Ryan, B. Rout, D. Jamieson, A.E. Hughes, Stable pit formation on AA2024-T3 in a NaCl environment, Corros. Sci. 52 (2010) 90–103.

[2] N. Birbilis, Y.M. Zhu, S.K. Kairy, M.A. Glenn, J.-F. Nie, A.J. Morton, Y. Gonzalez-Garcia, H. Terryn, J.M.C. Mol, A.E. Hughes, A closer look at constituent induced localised corrosion in Al-Cu-Mg alloys, Corros. Sci. 113 (2016) 160–171.

[3] A. Kosari, F. Tichelaar, P. Visser, H. Zandbergen, H. Terryn, J.M.C. Mol, Dealloying-driven local corrosion by intermetallic constituent particles and dispersoids in aerospace aluminium alloys, Corros. Sci. 177 (2020) 108947.

[4] R. Rosliza, W.B. Wan Nik, H.B. Senin, The effect of inhibitor on the corrosion of aluminum alloys in acidic solutions, Mater. Chem. Phys. 107 (2008) 281–288.

[5] A.K. Mishra, R. Balasubramaniam, Corrosion inhibition of aluminum alloy AA 2014 by rare earth chlorides, Corros. Sci. 49 (2007) 1027–1044.

[6] O. Gharbi, S. Thomas, C. Smith, N. Birbilis, Chromate replacement: what does the future hold?, Npj Mater. Degrad. 2 (2018) 12.

[7] P. Santa Coloma, U. Izagirre, Y. Belaustegi, J.B. Jorcin, F.J. Cano, N. Lapeña, Chromium-free conversion coatings based on inorganic salts (Zr/Ti/Mn/Mo) for aluminum alloys used in aircraft applications, Appl. Surf. Sci. 345 (2015) 24–35.

[8] P. Visser, Y. Liu, X. Zhou, T. Hashimoto, G.E. Thompson, S.B. Lyon, L.G.J. van der Ven, A.J.M.C. Mol, H.A. Terryn, The corrosion protection of AA2024-T3 aluminium alloy by leaching of lithium-containing salts from organic coatings, Faraday Discuss. 180 (2015) 511–526.

[9] G. Bierwagen, R. Brown, D. Battocchi, S. Hayes, Active metal-based corrosion protective coating systems for aircraft requiring no-chromate pretreatment, Prog. Org. Coat. 67 (2010) 195–208.

[10] M. Becker, Chromate-free chemical conversion coatings for aluminum alloys, Corros. Rev. 37 (2019) 321–342.

[11] Y. Liu, P. Visser, X. Zhou, S.B. Lyon, T. Hashimoto, M. Curioni, A. Gholinia, G.E. Thompson, G. Smyth, S.R. Gibbon, D. Graham, J.M.C. Mol, H. Terryn, Protective Film Formation on AA2024-T3 Aluminum Alloy by Leaching of Lithium Carbonate from an Organic Coating, J. Electrochem. Soc. 163 (2015) C45.

[12] P. Visser, Y. Liu, H. Terryn, J.M.C. Mol, Lithium salts as leachable corrosion inhibitors and potential replacement for hexavalent chromium in organic coatings for the protection of aluminum alloys, J. Coat. Technol. Res. 13 (2016) 557–566.

[13] P. Visser, A. Lutz, J.M.C. Mol, H. Terryn, Study of the formation of a protective layer in a defect from lithium-leaching organic coatings, Prog. Org. Coat. 99 (2016) 80–90.

[14] P. Visser, Y. Gonzalez-Garcia, J.M.C. Mol, H. Terryn, Mechanism of Passive Layer Formation on AA2024-T3 from Alkaline Lithium Carbonate Solutions in the Presence of Sodium Chloride, J. Electrochem. Soc. 165 (2018) C60–C70.

[15] P. Visser, H. Terryn, J.M.C. Mol, Active corrosion protection of various aluminium alloys by lithium-leaching coatings, Surf. Interface Anal. 51 (2019) 1276–1287.

[16] J. Gui, T.M. Devine, Influence of lithium on the corrosion of aluminum, Scr. Metall. 21 (1987) 853–857.

[17] R.G. Buchheit, M.D. Bode, G.E. Stoner, Corrosion-Resistant, Chromate-Free Talc Coatings for Aluminum, CORROSION 50 (1994) 205–214.

[18] P. Visser, S. A. Hayes, Anti-corrosive coating composition, WIP Organization (Ed.), WO 112605 (2010): A1.

[19] P. Visser, H. Terryn, J.M.C. Mol, On the importance of irreversibility of corrosion inhibitors for active coating protection of AA2024-T3, Corros. Sci. 140 (2018) 272–285.

[20] A. Kosari, P. Visser, F. Tichelaar, S. Eswara, J.-N. Audinot, T. Wirtz, H. Zandbergen, H. Terryn, J.M.C. Mol, Cross-sectional characterization of the conversion layer formed on AA2024-T3 by a lithium-leaching coating, Appl. Surf. Sci. 512 (2020) 145665.

[21] K. Marcoen, P. Visser, G.F. Trindade, M.-L. Abel, J.F. Watts, J.M.C. Mol, H. Terryn, T. Hauffman, Compositional study of a corrosion protective layer formed by leachable lithium salts in a coating defect on AA2024-T3 aluminium alloys, Prog. Org. Coat. 119 (2018) 65–75.

[22] A. Kosari, F. Tichelaar, P. Visser, H. Zandbergen, H. Terryn, J.M.C. Mol, Laterally-resolved formation mechanism of a lithium-based conversion layer at the matrix and intermetallic particles in aerospace aluminium alloys, Corros. Sci. 190 (2021) 109651.

[23] P. Visser, M. Meeusen, Y. Gonzalez-Garcia, H. Terryn, J.M.C. Mol, Electrochemical Evaluation of Corrosion Inhibiting Layers Formed in a Defect from Lithium-Leaching Organic Coatings, J. Electrochem. Soc. 164 (2017) C396.

[24] A.M. Homborg, T. Tinga, E.P.M. Van Westing, X. Zhang, G.M. Ferrari, J.H.W. De Wit, J.M.C. Mol, A Critical Appraisal of the Interpretation of Electrochemical Noise for Corrosion Studies, CORROSION 70 (2014) 971–987.

[25] D.-H. Xia, Y. Behnamian, Electrochemical noise: a review of experimental setup, instrumentation and DC removal, Russ. J. Electrochem. 51 (2015) 593–601.

[26] A.M. Homborg, E.P.M. van Westing, T. Tinga, G.M. Ferrari, X. Zhang, J.H.W. de Wit, J.M.C. Mol, Application of transient analysis using Hilbert spectra of electrochemical noise to the identification of corrosion inhibition, Electrochimica Acta 116 (2014) 355–365.

[27] P.J. Denissen, A.M. Homborg, S.J. Garcia, Interpreting Electrochemical Noise and Monitoring Local Corrosion by Means of Highly Resolved Spatiotemporal Real-

Time Optics, J. Electrochem. Soc. 166 (2019) C3275–C3283.

[28] D.-H. Xia, S. Song, Y. Behnamian, W. Hu, Y.F. Cheng, J.-L. Luo, F. Huet, Review—Electrochemical Noise Applied in Corrosion Science: Theoretical and Mathematical Models towards Quantitative Analysis, J. Electrochem. Soc. 167 (2020) 081507.

[29] Y.-J. Tan, S. Bailey, B. Kinsella, Studying the formation process of chromate conversion coatings on aluminium using continuous electrochemical noise resistance measurements, Corros. Sci. 44 (2002) 1277–1286.

[30] X. Liu, T. Zhang, Y. Shao, G. Meng, F. Wang, In-situ study of the formation process of stannate conversion coatings on AZ91D magnesium alloy using electrochemical noise, Corros. Sci. 52 (2010) 892–900.

[31] A.M. Homborg, T. Tinga, X. Zhang, E.P.M. van Westing, P.J. Oonincx, J.H.W. de Wit, J.M.C. Mol, Time–frequency methods for trend removal in electrochemical noise data, Electrochimica Acta 70 (2012) 199–209.

[32] F. Mansfeld, Z. Sun, Technical Note: Localization Index Obtained from Electrochemical Noise Analysis, Corrosion 55 (1999) 915–918.

[33] F. Mansfeld, Z. Sun, C.H. Hsu, Electrochemical noise analysis (ENA) for active and passive systems in chloride media, Electrochimica Acta 46 (2001) 3651–3664.

[34] U. Bertocci, F. Huet, R.P. Nogueira, P. Rousseau, Drift Removal Procedures in the Analysis of Electrochemical Noise, CORROSION 58 (2002) 337–347.

[35] I. Mohammadi, T. Shahrabi, M. Mahdavian, M. Izadi, Sodium diethyldithiocarbamate as a novel corrosion inhibitor to mitigate corrosion of 2024-T3 aluminum alloy in 3.5 wt% NaCl solution, J. Mol. Liq. 307 (2020) 112965.

[36] M.J. Bahrami, M. Shahidi, S.M.A. Hosseini, Comparison of electrochemical current noise signals arising from symmetrical and asymmetrical electrodes made of Al alloys at different pH values using statistical and wavelet analysis. Part I: Neutral and acidic solutions, Electrochimica Acta 148 (2014) 127–144.

[37] H. Ashassi-Sorkhabi, D. Seifzadeh, M.G. Hosseini, EN, EIS and polarization studies to evaluate the inhibition effect of 3H-phenothiazin-3-one, 7-dimethylamin on mild steel corrosion in 1M HCl solution, Corros. Sci. 50 (2008) 3363–3370.

[38] R.A. Cottis, Interpretation of Electrochemical Noise Data, CORROSION 57 (2001) 265–285.

[39] R.A. Cottis, A.M. Homborg, J.M.C. Mol, The relationship between spectral and wavelet techniques for noise analysis, Electrochimica Acta 202 (2016) 277–287.

[40] K.C. Emregül, A.A. Aksüt, The behavior of aluminum in alkaline media, Corros. Sci. 42 (2000) 2051–2067.

[41] Y.J. Tan, S. Bailey, B. Kinsella, The monitoring of the formation and destruction of corrosion inhibitor films using electrochemical noise analysis (ENA), Corros. Sci. 38 (1996) 1681–1695.

[42] A. Kosari, H. Zandbergen, F. Tichelaar, P. Visser, P. Taheri, H. Terryn, J.M.C. Mol, In-situ nanoscopic observations of dealloying-driven local corrosion from surface initiation to in-depth propagation, Corros. Sci. 177 (2020) 108912.
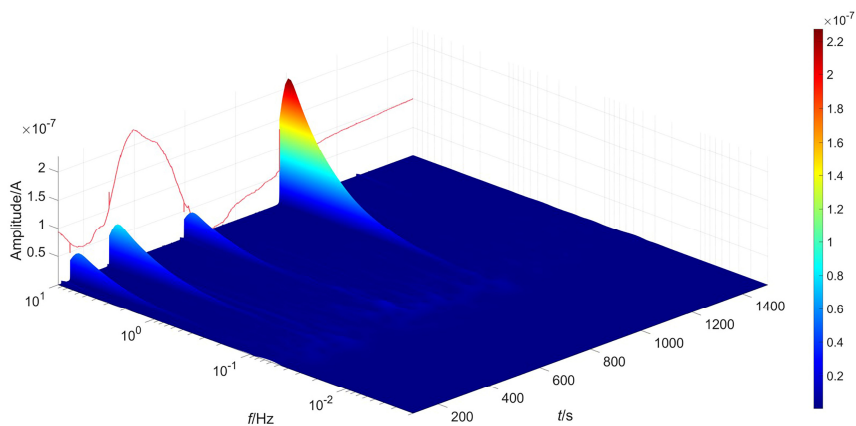
Supplementary Information for Chapter 3

*Movie S3.1 Hydrogen detachment corresponding to the transient shown in Fig. S4.1.*
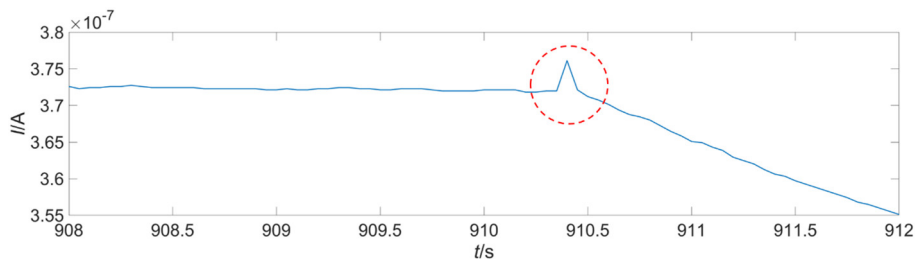
Fig. S3.1 Timeframe containing a high-frequency transient of AA2024-T3 exposed to a solution containing 0.01 M NaCl and 0.01 M Na$_2$CO$_3$, from 908 s to 912 s, corresponding to movie S1.

Fig. S3.2 CWT spectrum of the EN current noise after removal of DC drift for Al exposed in 0.01 M NaCl and 0.01 M Li₂CO₃ solution, from 100 to 1500 s.
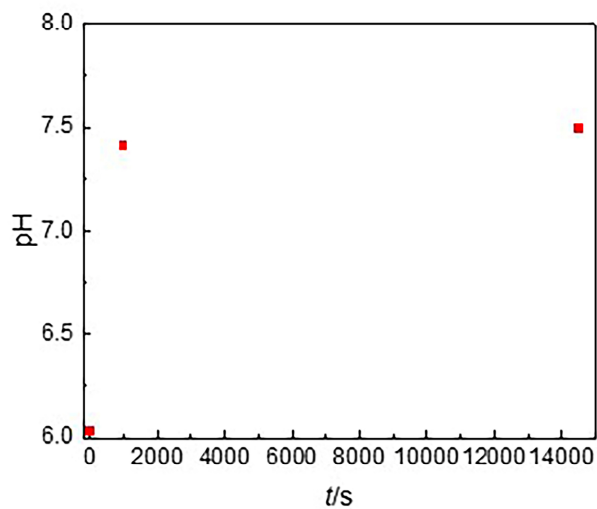
Fig. S3.3 pH variation during the reimmersion period.

CHAPTER 4

The Effect of Ambient Ageing on the Corrosion Protective Properties of a Lithium-based Conversion Layer[1]

[1] **Z. Li,** A. Homborg, Y. Gonzalez-Garcia, P. Visser, M. Soleimani, A. Mol, The Effect of Ambient Ageing on the Corrosion Protective Properties of a Lithium-Based Conversion Layer, J. Electrochem. Soc. 170 (2023) 031504.

Abstract

The influence of ageing under ambient conditions on the corrosion protective behaviour of a lithium-based conversion layer on AA2024-T3 is studied in this work. Conversion layers aged at ambient conditions for relatively short times (0 h and 4 h), show an initial high degree of corrosion inhibition but a much lower protectiveness after the inhibition stage terminates. Conversion layers with relatively long ageing times (24 h and 72 h) show a rather stable corrosion resistance which is higher than that of short-time aged samples. It is hypothesized that the freshly-formed conversion layer has trapped a certain amount of lithium ions and water molecules, leading to ongoing and heterogeneous growth of the conversion layer with time under ambient indoor conditions. Moreover, conversion layers with short ageing times show early-stage active corrosion protection by lithium-ion release.

Keywords: Aluminium alloy, lithium-based conversion layer, ageing, corrosion inhibition, electrochemical noise

4.1. Introduction

Aluminium alloys are widely applied in the aerospace industry for their favourable workability and high strength-to-weight ratio due to the presence of strengthening alloying elements like copper or zinc [1–4]. However, these alloying elements usually contribute to the generation of a complex and heterogeneous microstructure, leading to the increased susceptibility of localised corrosion [5–7]. Therefore, most aluminium alloys cannot be practically applied without adequate surface treatments [8].

Numerous surface treatment techniques have been developed to provide effective surface protection for aluminium alloys, such as organic coatings [9,10], anodizing [11–13], sol-gel synthesis [14–16] and chemical conversion films [17–19]. Chemical conversion coatings are often favoured because of their easy preparation process and cost-effectiveness. Conversion treatments can change the metallic interface from an active to a passive state and conversion films can also be used as base layers to strengthen the adhesion force of the organic coatings [8,19]. Chromate conversion coatings (CCCs), most notably hexavalent chromium (Cr(VI)), have been employed in the protection of many aerospace aluminium alloys to suppress corrosion and to improve surface adhesion [8,20,21]. However, the European Regulation Registration, Evaluation, Authorization and restriction of Chemicals (REACH) announced a ban on Cr(VI) in 2013 due to its high toxicity and carcinogenicity [22].

As a consequence, the replacement of chromate conversion coatings by novel eco-friendly conversion treatments has been strongly motivated. Among various alternatives, lithium salts have been introduced as a candidate to replace Cr(VI)-based chemistries due to their competitive price and potential protection efficiency [23–26]. Initially, it was reported that aluminium underwent inhibition when exposed to an alkaline electrolyte containing lithium ions [23,24]. Further studies revealed that lithium ions were readily intercalated into the aluminium hydroxide, stabilizing the corrosion products when the alloy surface was exposed to an aggressive alkaline environment [25,26]. Further studies from Buchheit et al. [27–29] revealed that the enhanced corrosion protection is caused by the formation of an Al-Li layered double hydroxide layer. This surface modification passed a 168-hour salt spray test. Another breakthrough in the application of lithium salts came from Visser et al. in 2010, when a polyurethane organic coating loaded with lithium salts was proven to provide effective corrosion inhibition by the formation of a protective conversion layer in coating defects during the neutral salt spray test (ASTM B-117) [30]. The active and

barrier protection properties of the lithium-based inhibitor coating technology have been well documented over the last years by a wide variety of electrochemical, microscopic and spectroscopic studies [31–39], indicating that the application of lithium salts represents a promising strategy for the further replacement of Cr(VI)-containing protective coatings.

Compactness and integrity are important characteristics of the protective abilities of a conversion layer. However, freshly formed chromate-free conversion coatings usually are rich in defects or cracks due to dehydration. [40–46] The defect areas provide pathways for corrosive electrolyte ingress leading to a significant decrease of the corrosion protection performance of conversion layers [41]. Dehydration usually is inevitable since conversion coatings are formed in an aqueous environment, resulting in water entrapment within the coatings. Drying or ageing treatment will cause water evaporation and generate newly-formed defects due to the dehydration-driven shrinkage of the conversion layers [41,43]. However, the influence of an ageing treatment after conversion layer formation is reported to not always lead to decreasing corrosion protective properties. It was reported by Li et al. that trivalent chromium process (TCP) coatings underwent dehydration and condensed after ageing at elevated temperatures (≤100 °C), accompanied by the generation of a low defect-density conversion layer [40]. Moreover, longer ageing at room temperature was reported to also enhance the corrosion resistance of the TCP coating by a factor 4, which was attributed to the formation of an aluminium oxide layer and increasing hydrophobicity of the conversion coating. On the other hand, other studies have reported a negative impact of ageing on corrosion protectiveness of TCP coatings [42,43]. This might be due to the different conversion treatment parameters and post-formation ageing conditions, which result in different physico-chemical and electrochemical properties. While prior studies show that lithium-based conversion layers show promise among chromate-free conversion coatings, the influence of post-formation ageing on its corrosion protectiveness has remained yet unknown.

In the present work, the influence of ageing duration under indoor ambient conditions on the protectiveness of lithium-based conversion layers was studied using Electrochemical noise (EN) and top-view and cross-sectional micrographs. Earlier work has shown that EN analysis can be a powerful technique to study the corrosion protective behaviour of the lithium-based conversion layer [47]. Top-view and cross-sectional micrographs were obtained by focused ion beam-scanning electron microscopy (FIB-SEM) to distinguish layer morphology changes to the conversion

layers upon ageing and upon re-immersion to a corrosive solution to underpin the differences in corrosion protective behaviour caused by ageing under ambient indoor conditions.

4.2. Experimental Methods

4.2.1. Material and experimental set-up. All working electrode material originated from a single commercial AA2024-T3 sheet provided by Goodfellow in 0.8 mm thickness. From this sheet, smaller rectangular specimens with a size of 8 mm × 18 mm and 20 mm × 20 mm were produced. The former was used for EN measurements and the latter were employed for immersion tests. Two specimens with a size of 8 mm × 18 mm were embedded in a commercial epoxy resin at a spacing of 2 mm after spraying a primer at four edges to avoid crevice corrosion. The EN control group consisted of embedded samples with a 5 mm spacing. All samples were ground up to grit 4000 SiC abrasive paper, gently cleaned with distilled water, dried by compressed air, and left in an ambient lab environment for 24 h before the start of the experiments. For samples with two identical panels, the electrical connection to external equipment was realized by two conductive copper tapes. For all samples, water-proof tape was used to cover the surfaces with a circular opening of either 10 mm or 15 mm in diameter to fix and limit the exposed area. The latter was only used for the pH measurement. The detailed setup of the electrochemical cell was described in Chapter 3 [47]. Laboratory-grade chemicals used in this work were ordered from Sigma-Aldrich (St. Louis, MO, USA).

4.2.2. Sample preparation. EN samples were covered by tape with a circular recess of 10 mm in diameter. 0.01 M NaCl and 0.01 M Li_2CO_3 (pH 10.9) solution was prepared to enable the formation of a lithium-based conversion layer and to mimic the local aqueous environment of a scribed area, which is consistent with previous work by the authors [37,47]. A 4 mm high electrolyte layer (0.321 mL) was established for experimental sample sets aiming to mimic the local liquid environment inside an artificial defect on an inhibitor-loaded organic coating [48]. For the control groups, 0.321 mL solution was added to the cell containing the samples at a 5 mm spacing and 1 mL solution was added into the cell, including the samples at a 2 mm spacing, to generate different lithium-based conversion layers. All experiments were performed under aerated conditions. Hydrogen bubbles generated during layer formation were gently removed every 10 min to form a relatively uniform lithium-based conversion layer. The exposure duration for coupons in 0.01 M NaCl and 0.01 M Li_2CO_3 solution was 14500 s (approximately 4 h). Later, the

original electrolyte was removed, and the freshly formed conversion layers were gently rinsed using 0.01 M NaCl to remove superficially adsorbed lithium carbonate. Subsequently, samples were left in a lab environment at approximately 20 °C, 40% relative humidity for 0 h, 4 h, 24 h, and 72 h, respectively. Finally, samples were re-immersed in a 0.321 mL 0.01 M NaCl solution for 14500 s (approximately 4 h). EN current and potential responses were recorded simultaneously. The EN experimental procedure is shown in **Fig. 4.1**.
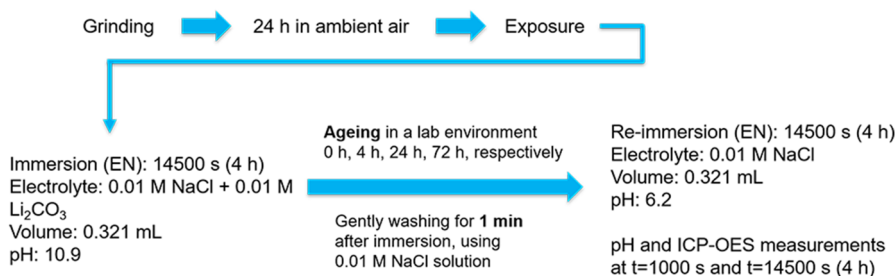
Fig. 4.1 Sequence diagram of the experimental procedure for the EN, pH and ICP-OES measurements.

Single panels covered by the water-proof tape with a 10 mm diameter recess were used for SEM observation to avoid static charging of epoxy resin in the SEM. Here, the entire procedure (conversion layer growth, ageing and re-immersion) is identical to the one mentioned above for the EN measurements. Similarly, single panels covered by the tape with a 15 mm diameter recess were adopted for pH measurements since 0.321 mL is not suitable to obtain the minimum volume for a pH measurement during re-immersion. To establish a 4 mm electrolyte layer thickness for the immersion and re-immersion stages, 0.703 mL 0.01 M NaCl and 0.01 M Li_2CO_3, and 0.703 mL 0.01 M NaCl were added, respectively.

4.2.3. pH and ICP-OES measurement. The pH values of the solution during re-immersion were measured by using a pH meter (Metrohm, 913 pH Meter). The dissolved lithium and aluminium ions from the lithium-based conversion layers were measured by Inductively Coupled Plasma-Optical Emission Spectroscopy (ICP-OES, Spectro, Arcos-EOP). Wavelengths relevant for Al detection are at 396.2 nm, 394.4 nm, and 167.0 nm, respectively while wavelength used for Li detection is at 670.8 nm. Detection limits for Al and Li are 0.01 mg/kg. The measurements were conducted at least in triplicate.

4.2.4. Focused Ion Beam-Scanning Electron Microscopy (FIB-SEM) characterization. To understand how ageing time altered the conversion layer, a series of cross-sectioning experiments were performed using a FIB-SEM (Helios G4 PFIB UXe, Thermo Fisher Scientific, USA) equipped with a xenon plasma focused ion beam (PFIB), operating at optimum conditions of an accelerating voltage of 30 kV and a beam current of 1 nA. The cross-sectional and top-view SEM morphological characterizations were performed at 10 keV collecting emitted secondary electrons (SE) in ultra-high-resolution mode. The chemical composition of different regions was estimated using Energy Dispersive Spectroscopy (EDS). It is worth noting that, to avoid any possible damage to the lithium-based conversion layer depositing, a protective Pt or C overlay coating was intentionally omitted.

4.2.5. Electrochemical Noise (EN) Measurements. A traditional three-electrode EN setup containing two identical working electrodes and an Ag/AgCl/Saturated KCl reference electrode was used in this study. Potential values presented in this work are with respect to this reference electrode unless mentioned differently. All EN measurements were performed under open circuit conditions. A Compactstat from Ivium Technologies was used to record current and potential signals simultaneously, serving as a zero-resistance ammeter (ZRA) and potentiometer. The Compactstat was placed inside a Faradaic cage to avoid interference from external electromagnetic sources. The sampling frequency was set at 20 Hz and a low-pass filter of 10 Hz was used to avoid aliasing. The EN data were processed using Matlab from MathWorks. All EN tests were performed at least in triplicate.

4.2.6. EN signal processing. In an EN measurement between two nominally identical corroding electrodes, these two electrodes are likely to behave non-stationary [49]. This causes an increasing asymmetry between these two electrodes. [50,51] In the EN current noise, the DC component does not contain information related to the electrochemical reactions occurring on the electrode surfaces other than the above-mentioned asymmetry. If this DC drift is not effectively removed, usually the relatively large amounts of energy present at the associated lower timescales may dominate over more useful, higher-frequency information during the data processing. Various methods can be used for DC drift removal, like moving average, polynomial and linear trend removal, wavelet analysis and empirical mode decomposition [52,53]. In this work, an eight-level discrete wavelet transform (DWT) with a Daubechies 4 wavelet was adopted due to its effective DC drift removal capacity while retaining sufficient useful corrosion information in the data [50,51]. This

method has already proven to be effective in our previous work [47]. One application of EN in the time domain is to determine the variation in barrier properties of the lithium-based conversion layer over the course of the measurement by the noise resistance. It has been reported that the noise resistance is comparable to the near-DC polarization resistance [54,55]. Noise resistance is calculated as the ratio between the standard deviations of potential and current, after DC drift removal, within a user-defined time window. In the time-frequency domain, an energy distribution plot (EDP) was adopted to analyse the dominant timescales in an EN signal, and to study the relative contribution of reactions within specific frequency ranges [56]. The time scales shown in an EDP range from relatively short, medium to long and correspond to activation-, mixed-, and diffusion-controlled processes, respectively [52]. The number of time scales is user-defined. It is generally accepted that an eight-level decomposition is sufficient to characterize corrosion characteristics [57]. Besides DWT, the continuous wavelet transform (CWT) spectrum was applied to extract time-frequency information using an analytic Morlet wavelet. For the CWT procedure, the signal is matched to a series of compressed or stretched variants of a wavelet. The duration of the wavelet corresponds to a specific frequency range. The CWT spectrum reveals the energy distribution of the EN signal over time and frequency simultaneously.

4.3. Results and Discussion

4.3.1. Corrosion resistance of the conversion layers. **Fig. 4.2** shows EN current and potential signals recorded for the conversion layers during the re-immersion exposure for different ageing times. It is clear that for samples with 0 h (**Fig. 4.2a**) and 4 h (**Fig. 4.2b**) ageing, the potential signals show an initial drop and then a gradual increase, accompanied by relatively smooth current signals. At a later stage, an exposure stage including a relatively large number of transients in the signals follows. After 0 h ageing, this transition is accompanied by an instantaneous drop of the potential values and a very sharp increase of the absolute current values. The potential signal of the 0 h aged sample has a larger potential drop (minimum value close to -1000 mV) as compared to that of the 4 h aged coupon (minimum value close to -700 mV). In addition, the transition to the exposure stage also occurs at a later stage on the 0 h aged sample. In our previous work, the 0 h ageing data during re-immersion in 0.01 M NaCl solution was also analysed [47]. The large potential drop at the beginning can be attributed to the release of trapped lithium carbonate ions inside the previously formed conversion layer, which provides an extra active inhibition effect [47]. This effect will be discussed in detail later. For samples with 24 h (**Fig. 4.2c**)

and 72 h (**Fig. 4.2d**) ageing, the initial potential drop is nearly absent, and the corrosion process starts as from the early-stage exposure to the NaCl electrolyte. The smooth potential and current signals in **Fig. 4.2a** and **4.2b** are similar to the EN signals when AA2024-T3 was exposed to the lithium carbonate containing solution [47]. The authors designate this period as the inhibition stage, and the following period containing large amounts of transients as the corrosion stage. The corrosion stage occurs earlier for samples having undergone longer ageing times. It is therefore evident that the ageing treatment has a significant impact on the electrochemical properties and related corrosion protection provided by the lithium-based conversion layer.
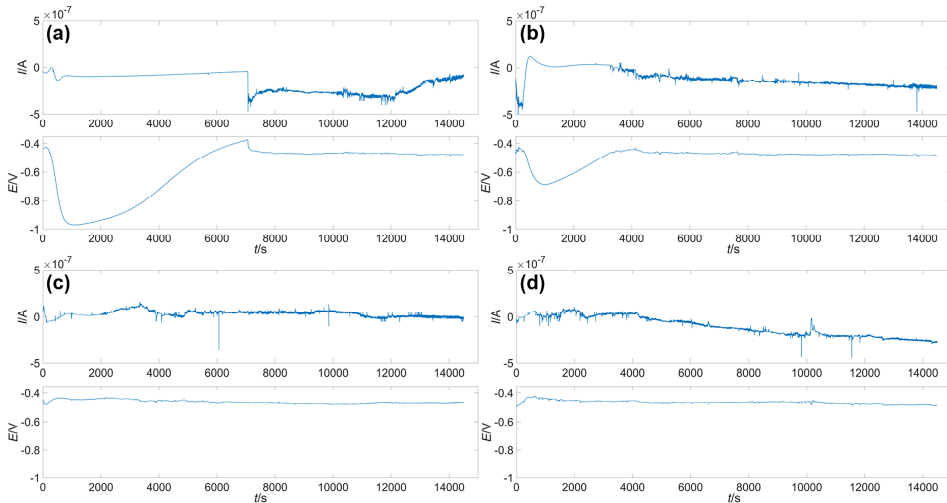
Fig. 4.2 EN current (top) and potential (bottom) signals for AA2024-T3 initially treated in 0.01 M NaCl and 0.01 M Li₂CO₃ solution for 14500 s (approximately 4 h), and then exposed in 0.01 M NaCl after ambient ageing for (a) 0 h, (b) 4 h, (c) 24 h, and (d) 72 h.

For the purpose of investigating the barrier properties of the lithium-based conversion layer with different ageing times, the noise resistance is calculated. The results are presented in **Fig. 4.3**.
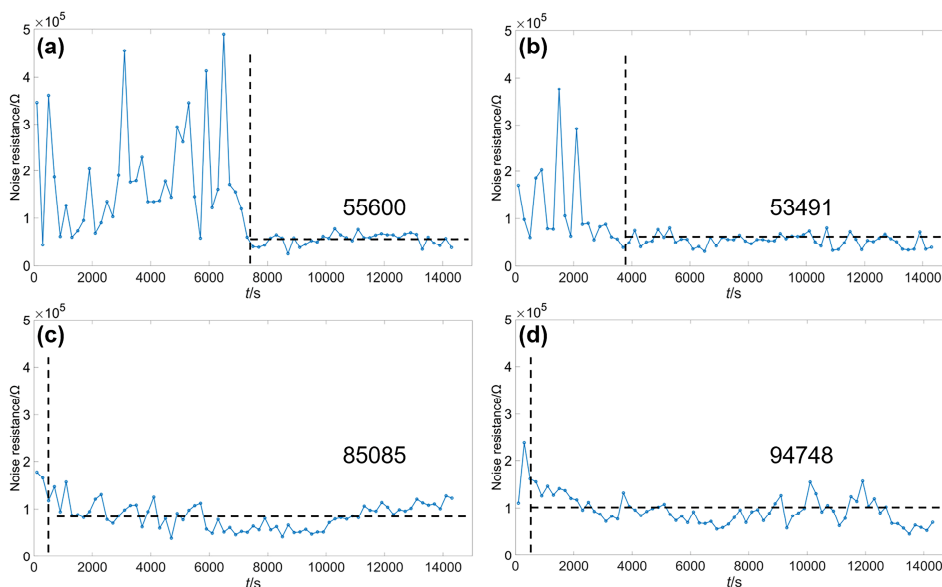
Fig. 4.3 Noise resistance calculated for AA2024-T3 initially exposed in 0.01 M NaCl and 0.01 M Li$_2$CO$_3$ solution for 14500 s (approximately 4 h) and subsequently exposed in 0.01 M NaCl after ambient ageing for (a) 0 h, (b) 4 h, (c) 24 h, and (d) 72 h. The vertical dashed lines indicate the transition from inhibition to corrosion stage. The numbers (unit: Ω) shown in the figure indicate average noise resistance values in the corrosion stage.

The horizontal black dashed lines represent the average value of the noise resistance after the potential signals reach a relatively stable value. The approximate start of this stage is indicated by a vertical dashed line. In **Fig. 4.3a** and **Fig. 4.3b**, it is observed that the noise resistance presents a higher value with large oscillations before the sudden potential decrement. The 0 h aged sample exhibits the largest noise resistance at the beginning, and the oscillations decrease significantly during the corrosion stage. In **Fig. 4.3c** and **Fig. 4.3d**, for the 24 h and 72 h aged samples, respectively, the noise resistance is relatively stable during the entire re-immersion. As for the average resistance value of samples with different ageing times, an interesting finding is that the noise resistance exhibits a very small drop for the 4 h aged sample and then a notable improvement with longer ageing treatments. Therefore, long-time ageing treatments seem beneficial for enhancing the protective behaviour of the lithium-based conversion layer. To explain the phenomenon of improved corrosion protection capabilities for samples with longer ageing times in relation to the longer inhibited state for samples with shorter ageing times, compositional and morphological characterizations are required.

4.3.2. Dissolution behaviour of the conversion layers. The noise resistance, with its relatively large oscillations during the inhibition stage, follows a similar trend as the lithium-based conversion layer's growth characteristics at later stages, with a competitive dissolution and growth in the solution containing lithium carbonate [47,58,59]. Therefore, this behaviour during the re-immersion tests may indicate the presence of residual lithium carbonate trapped in the conversion layer. This presence of lithium carbonate should be reflected in the pH, due to the alkaline nature of the carbonate ions [48], and in the existence of dissolved lithium ions using ICP-OES measurements. Two time points (t=1000 s, and t=14500 s (approximately 4 h)) were selected to monitor the variation of pH and the released lithium and aluminium elements.

The pH variation of the conversion layers with different ageing treatments during re-immersion is shown in **Fig. 4.4**.
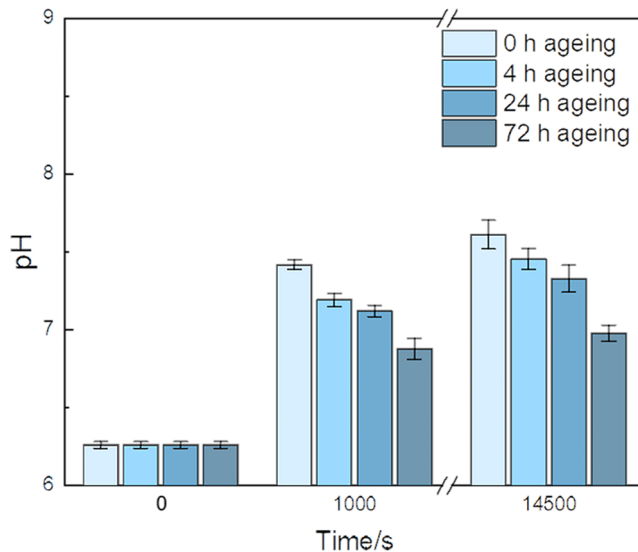
Fig. 4.4 pH variation of the 0.01 M NaCl solution at selected re-immersion times for the differently aged samples.

It is observed that all the samples experience a gradual pH increase during re-immersion and that the 0 h aged sample reaches the highest pH at two selected re-immersion times (t=1000 s, t=14500 s (approximately 4 h)). In addition, the pH increase upon re-immersion decreases with the ageing time. This observation implies

that the release of alkalinizing species, such as carbonate ions, will gradually drop with extended ageing times. The dissolved amount of lithium and aluminium ions at t=1000 s and t=14500 s (approximately 4 h) is shown in **Fig. 4.5**. The dissolved lithium ions also present a decreasing trend with extended ageing times, corresponding well with the trend of the pH evolution, i.e. the carbonate ion release. The dissolved aluminium ions in the solution show a gradually rising trend with ageing time. This behaviour is caused by the earlier start of corrosion for longer-aged samples. Moreover, the adverse trends between dissolved lithium and aluminium ions confirm that the released lithium ions mainly originate from trapped lithium inside the conversion layer instead of the dissolution of the conversion layer itself. Consequently, the amount of mobile lithium ions within the conversion layer becomes smaller with extended ageing.
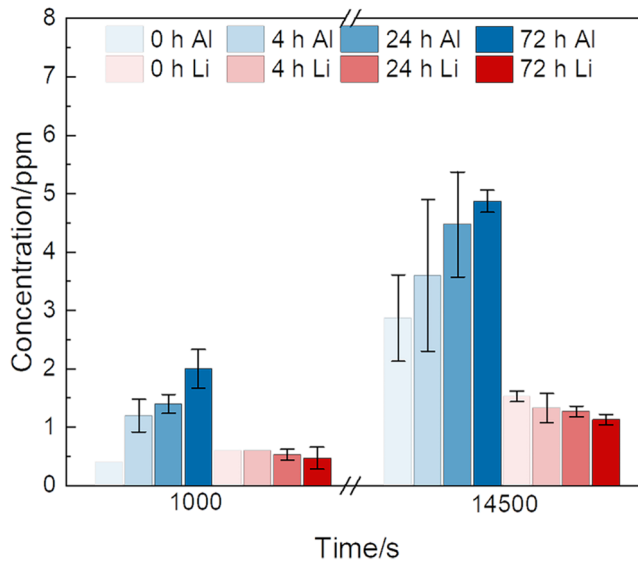
Fig. 4.5 ICP-OES analysis of Al and Li ions released from the differently aged conversion layers. The standard deviation is calculated based on three data points.

4.3.3. SEM characterisation of the conversion layers. The top views of the lithium-based conversion layers dried under ambient indoor conditions for different ageing times are shown in **Fig. 4.6a-4.6d**, respectively.
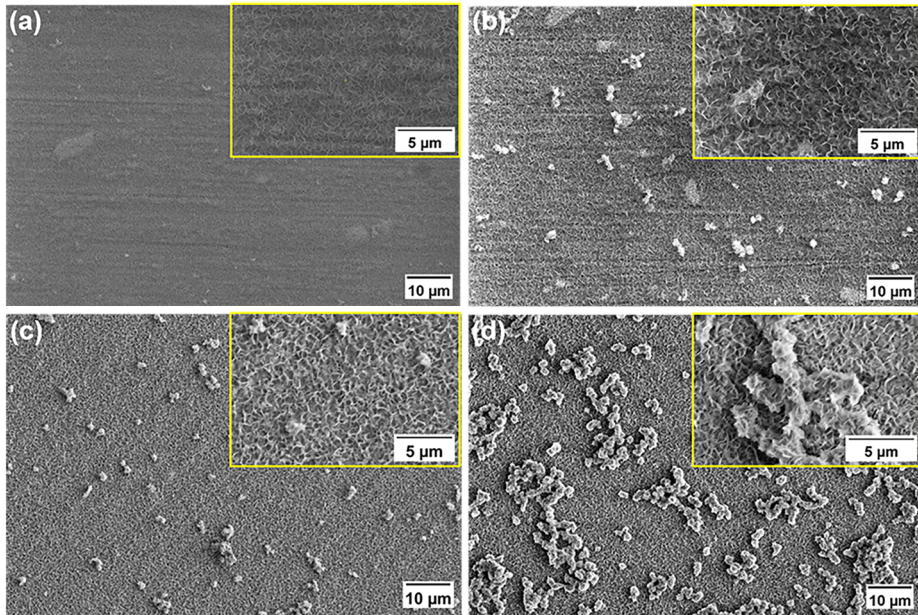
Fig. 4.6 Top-view SEM images of the AA2024-T3 surface after immersion in an 0.01 M NaCl and 0.01 M Li₂CO₃ solution for 14500 s (approximately 4 h) and ambient ageing for (a) 0 h, (b) 4 h, (c) 24 h, and (d) 72 h.

A distinct morphological change with ageing time can be observed. Macroscopic cracks or crevices caused by dehydration are not observed for any of the differently aged samples, indicating that transients observed in **Fig. 4.2** are likely to be attributed to the damage of the conversion layer during re-immersion. The morphology of the top columnar structure does not show an obvious growth or coarsening, but a large number of small particles appear on the top columnar layer for prolonged ageing. These particles show a similar porous structure as the top layer. In addition, both the size and coverage density of the particles increase with ageing time.

As reported previously, the lithium-based conversion layer formed on AA2024-T3 consists of a columnar top layer and an inner porous-to-dense layer [37]. **Fig. 4.7** shows the cross-sectional characterization of the conversion layers in the bare areas with different ageing treatments.
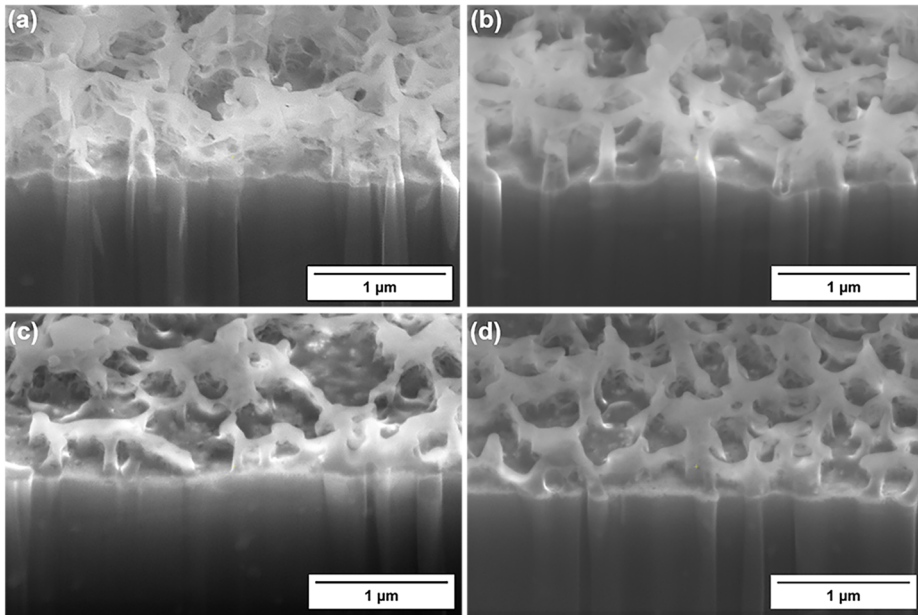
Fig. 4.7 Cross-sectional observations of the conversion layer immersed in 0.01 M NaCl and 0.01 M Li₂CO₃ solution for 14500 s (approximately 4 h) after (a) 0 h, (b) 4 h, (c) 24 h, and (d) 72 h ageing, respectively.

The conversion layer shown here consists of a well-developed outer columnar layer, but shows a less developed inner layer as compared to prior work [37], predominantly caused by the relatively short conversion layer formation time in the present work. Furthermore, the cross-sectional micrographs confirm the top-view observation of the absence of macroscopic layer cracking or shrinkage from dehydration. **Fig. 4.8** shows the top-view and cross-sectional view of the conversion layer after re-immersion in 0.01 M NaCl solution for samples with 0 h, 4 h, 24 h, and 72 h ageing, respectively.
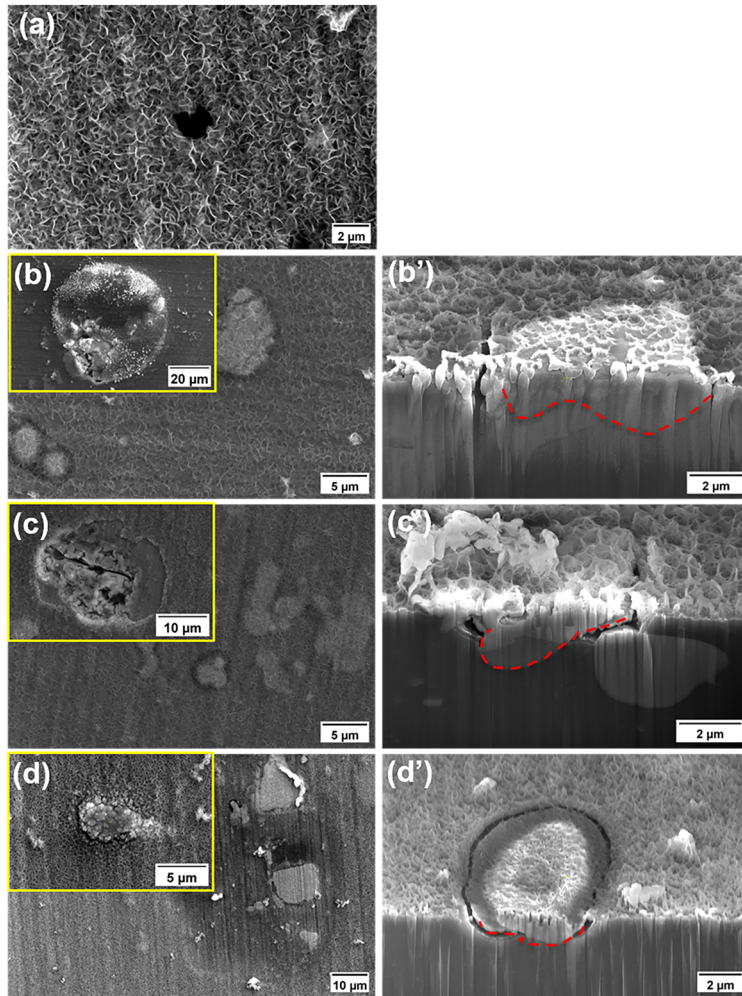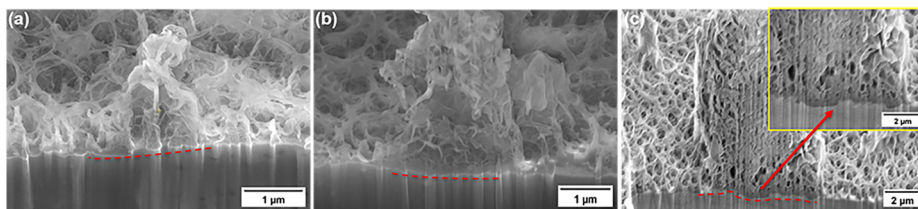
Fig. 4.8 Top-view and cross-sectional observations of the conversion layer after immersion in 0.01 M NaCl and 0.01 M Li$_2$CO$_3$ solution for 14500 s (approximately 4 h), ageing for (a) 0 h, (b), (b') 4 h, (c), (c') 24 h and (d), (d') 72 h under ambient indoor conditions and re-immersion in a 0.01 M NaCl solution for 14500 s (approximately 4 h). Intermetallic contours are marked by the red dashed lines.

The conversion layer with 0 h ageing (**Fig. 4.8a**) presents the highest layer integrity as compared to the three other groups. Only few small pits are observed in the conversion layer, in line with the observation that the 0 h aged sample shows the longest inhibition stage: corrosion is only triggered at a later stage as compared to the other samples. **Fig. 4.8b-4.8d** and **Fig. 4.8b'-4.8d'** indicate local corrosion,

breakdown of the conversion layer and the presence of trenches around intermetallic phases for samples with 4 h, 24 h, and 72 h of ageing. Intermetallic phases surrounded by trenches are marked with a red dashed line. Trenches are a quite common morphological phenomenon during the corrosion stage of aluminium alloys [7,60], even in case of the presence of cerium as inhibitor [61]. It can be inferred that the not fully-developed inner layer may provide local channels for corrosive ion ingress. Local conversion layer failure may occur due to the development of corrosion products at the substrate - conversion layer interface. The weak corrosion protection at the areas adjacent to intermetallic phases may be attributed to the lack of a protective dense inner layer covering the intermetallic phases [36,37]. More detailed information about the growth stage of the conversion layer at and around the areas of intermetallic phases can be found elsewhere [37]. Electrochemical impedance spectroscopy studies revealed that the dense inner layer normally dominates the corrosion protection provided by the entire conversion layer, whereas the top columnar layer is merely a minor contributor [58].

A higher-magnification cross-sectional view of the conversion layer-covered particles is shown in **Fig. 4.9**. From the side view, the porous structure is more evident, and these aged particles seem to penetrate slightly into the aluminium matrix to form a more pronounced inner dense layer as shown in **Fig. 4.9**, in particular in **Fig. 4.9c** representing the longest aged sample, i.e. 72 h. The interface between the substrate and inner dense layer is each time indicated with a red dashed line.

Fig. 4.9 Cross-sectional observations of the particles grown on the conversion layer after immersion in a 0.01 M NaCl and 0.01 M Li₂CO₃ solution for 14500 s (approximately 4 h) and ageing for (a) 4 h, (b) 24 h, and (c) 72 h under ambient indoor conditions. The red dashed lines indicate the interface between substrate and inner dense layer.

The elemental compositions of the conversion layer and the particles on samples with different ageing times as measured by EDS are shown in **Table 4.1**. As background information, an example of the selection of EDS points is shown in **Fig. S4.1**. The

results show that the bare conversion layer and the ageing-formed particles share the same elemental constituents, which agrees with previous studies of the compositional characterization of the lithium-based conversion layer growing either on aluminium alloys, or inside the scratch of lithium-containing organic coatings [36,62]. Lithium and hydrogen are not listed due to the limitation of the EDS technique to detect such light elements [36]. In addition, ageing treatments from 4 h to 72 h under ambient indoor conditions do not significantly change the elemental compositions of the conversion layer or the aged particles. However, the particles do contain a higher content of oxygen and carbon and a lower percentage of aluminium. The higher content of carbon confirms the existence of trapped lithium carbonate ions, since carbonate is virtually the only carbon source for the growth of the conversion layer, whereas the percentage of carbon dioxide in the air is considered too low. The compositional differences are likely to originate from the different formation conditions. The bare conversion layer is formed in the electrolyte, whereas particles only appear after atmospheric exposure.

Table 4.1 Elemental composition of matrix and particles for the conversion layer with different ageing treatment. The standard deviations are based on five data points each.

Element (atomic %)	0 h		4 h		24 h		72 h	
	Matrix	Particle	Matrix	Particle	Matrix	Particle	Matrix	Particle
C	5.4±1.2	-	4.8±2.0	10.0±1.8	4.7±2.4	13.9±1.7	4.8±2.5	11.6±2.6
O	35.1±5.1	-	35.1±4.0	46.6±3.1	33.5±3.4	45.5±1.1	34.9±1.3	46.4±1.4
Mg	1.4±0.11	-	1.4±0.2	1.0±0.1	1.5±0.1	1.1±0.1	1.5±0.2	0.9±0.1
Al	56.7±6.2	-	57.4±5.0	40.9±3.4	58.9±4.3	38.6±1.9	57.6±3.1	40.1±2.4
Cu	1.0±0.1	-	1.4±0.8	0.7±0.1	1.1±0.2	0.8±0.1	0.9±0.1	0.7±0.2
Cl	0.3±0.1	-	0.5±0.1	0.8±0.1	0.3±0.1	0.2±0.1	0.3±0.1	0.3±0.1

4.3.4. Time-frequency analysis of the EN current signals. To further study the corrosion behaviour of the conversion layer during the corrosion stage, EN analysis was adopted to characterize the electrochemical properties in the time-frequency domain. The continuous wavelet transform has already been applied in earlier work to analyse the conversion layer growth and its irreversibility properties [47]. While the noise resistance is able to reveal the variations of the barrier properties of the conversion layers with different ageing times, the dominant types of corrosion are not reflected clearly in the time domain. For the CWT analysis presented here, four timeframes with a duration of 1000 s each are selected from the current signals in

Fig. 4.2 at the early stages of the corrosion dominant phase, in order to exclude the influence of lithium carbonate as much as possible. Another criterium for the selection of suitable timeframes is that the system should be in a relatively stable state, i.e. the corresponding potential signals should be relatively stable. This is the case for the timeframe between 7500 s and 8500 s for the 0 h aged sample, between 4500 s and 5500 s for the 4 h aged sample, between 3500 s and 4500 s for the 24 h aged sample and between 2500 s and 3500 s for the 72 h aged sample.

In this work, the current signals are adopted because the EN current noise is able to reveal the corrosion intensity as well. **Fig. 4.10** shows the CWT spectrum of the four different timeframes. It is observed that the corrosion rate exhibits an increase and then a gradual decrease with increased ageing times, according to the maximum values of the scale bars, which corresponds well with the observations from the noise resistance. The 4 h aged sample shows the highest corrosion rate, which might be caused by the combination of a lower local concentration of lithium carbonate and the fact that the aged conversion layer does not fully develop within only 4 hours. The distribution of the signal energy over time and frequency reveals the dominant electrochemical kinetics with the highest energy contribution and its evolution over time [57].
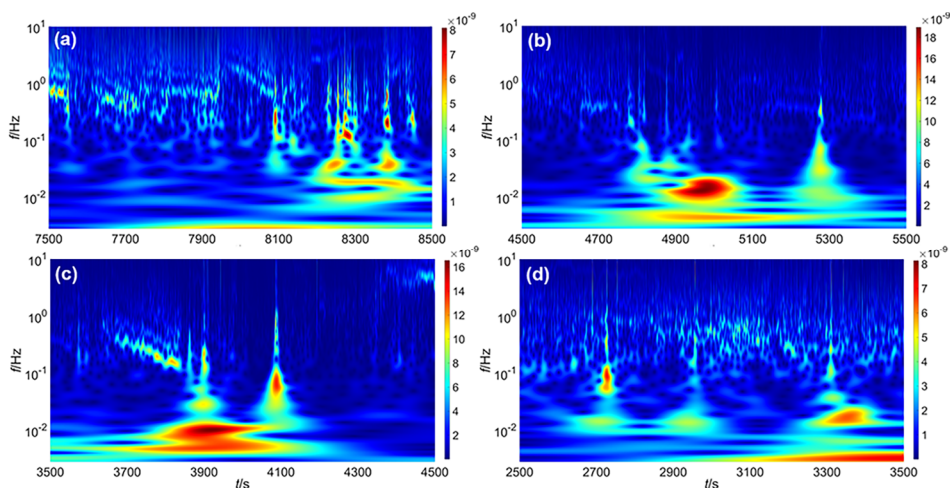
Fig. 4.10 CWT spectrum of the EN current noise for AA2024-T3 immersed in 0.01 M NaCl and 0.01 M Li₂CO₃ solution for a duration of 14500 s (approximately 4 h) and exposed in 0.01 M NaCl solution after ageing in the air for (a) 0 h, (b) 4 h, (c) 24 h, and (d) 72 h.

From **Fig. 4.10**, it can be observed that the largest energy peak marked in red shifts towards lower frequencies from 0 h to 4 h and then slightly back in the high-frequency direction. A clearer view of the energy-frequency distribution is shown in the EDPs in **Fig. 4.11**. Here, the relative energy contribution of D2 and D3, D7 and D8 are added together since these represent activation-controlled and diffusion-controlled processes, respectively. A detailed relative energy distribution value is shown in **Table S4.1**. In this study, activation-controlled processes usually are attributed to fast metastable pitting and repassivation which is related to the influence of inhibition, while diffusion-control corresponds to a stable, gradually proceeding (localized corrosion) process [57]. It is observed that the 0 h aged sample possesses the largest energy contribution in D2+D3, indicating a high local concentration of lithium carbonate even though the corrosion process suppresses the inhibition function. The energy contribution of D7+D8 shows an increasing and then a decreasing trend, which is opposite to the trend of the noise resistance or corrosion intensity from the CWT spectrum. As mentioned before, the 4 h aged conversion layer contains a lower concentration of lithium carbonate, whereas the barrier properties do not improve notably. A smaller energy contribution of diffusion-controlled processes for samples with longer ageing times indicates that the longer-aged conversion layer is more able to suppress stable localized corrosion.
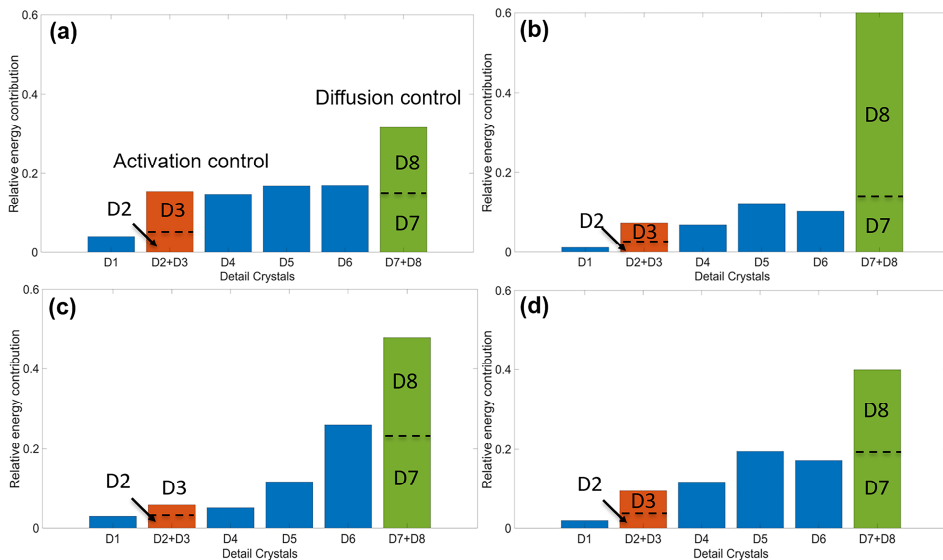

Fig. 4.11 Energy distribution plots of the EN current signals for AA2024-T3 immersed in 0.01 M NaCl and 0.01 M Li₂CO₃ solution for 14500 s (approximately 4 h) and

exposed to 0.01 M NaCl after ambient ageing for (a) 0 h, (b) 4 h, (c) 24 h and (d) 72 h.
Timeframes are between (a) 7500 and 8500 s, (b) 4500 and 5500 s, (c) 3500 and 3500 s
and (d) 2500 and 3500 s.

4.3.5. Entrapment of water and lithium carbonate ions. While the residual 0.01 M
NaCl solution still forms a very thin aqueous layer on the surface after initial rinsing,
it is very difficult to support the continuous growth of the conversion layer for 72 h
when exposed to ambient air. Water evaporation is able to remove all surface
adsorbed water within several hours. Previous studies have revealed that the
columnar layer and the dense inner layer both contain trapped water, especially the
inner layer which is composed of amorphous lithium-incorporated aluminium
hydroxides [36,63].

To study the potential entrapment of the lithium and carbonate ions inside the
conversion layer, two electrochemical cells with lower surface-to-volume ratio
during the conversion formation period, generated by either increasing the volume of
electrolyte or reducing the exposed surface, are adopted. Their corresponding re-
immersion EN signals only show a relatively minor potential drop, as shown in **Fig.
4.12**. This implies that the amount of trapped lithium carbonate is nearly negligible
in that case and this also suggests that the local alkalinity during the inhibition stage
is not caused by the dissolution of the aluminium hydroxide gel. A high surface-to-
volume ratio results in a sharper pH decrease during the layer growth stage, since the
growth of the conversion layer consumes hydroxyl ions. A lower pH will cause a
slower matrix dissolution rate and benefits the formation of the inner dense layer [59].
Thus, the inner dense layer might play an essential role in trapping mobile lithium
carbonate, but the detailed mechanism still requires further investigation.
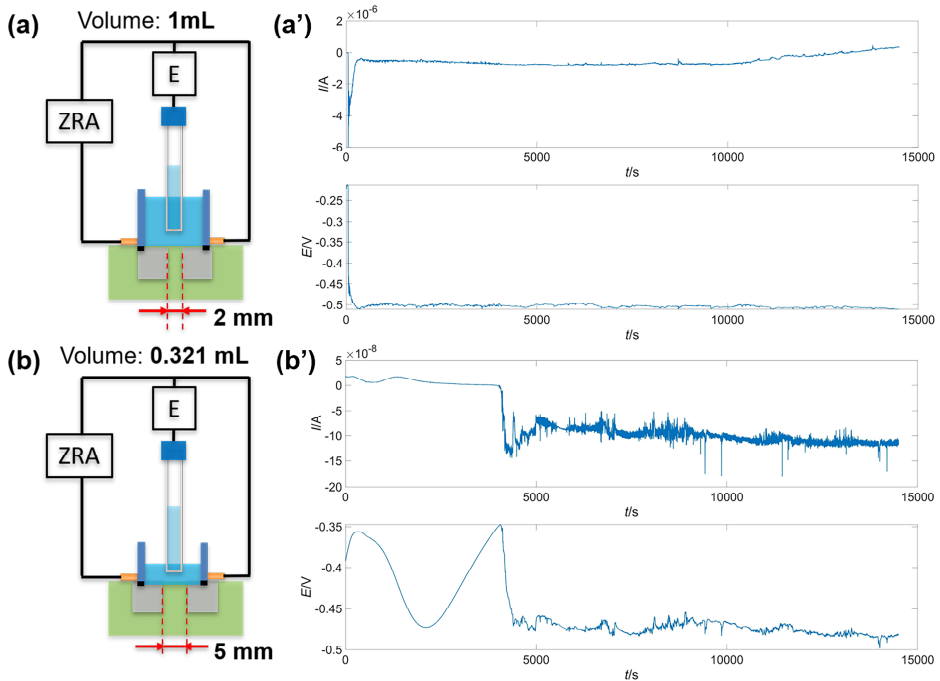
Fig. 4.12 Electrochemical cell set-up of immersion treatment with different surface area-to-volume ratios and corresponding re-immersion EN current and potential signals in 0.01 M NaCl solution for 14500 s (approximately 4 h).

4.3.5. Morphological evolution model. Based on the results and discussion above, it is inferred that the appearance of particles on the conversion layer is due to the heterogeneous growth of the conversion layer. A schematic overall morphological evolution model is depicted in **Fig. 4.13**. A thin electrolyte layer remains on the conversion layer surface after the removal of the original lithium-containing solution. Although the surface has been gently rinsed by 0.01 M NaCl solution, the conversion layer still traps some mobile ions like lithium, carbonate and aluminate, as well as water molecules. At a later stage, the continuous thin water layer gradually discretizes to local regions due to water evaporation. The continuous growth of the conversion layer only occurs where water still exists and lithium, carbonate, aluminate ions and water will be gradually consumed locally. It has been reported before that the formation of the columnar structure is promoted by local environments exhibiting a relatively higher pH and lithium ion concentration [32]. The highly limited aqueous volume generates a higher concentration of lithium ions and the carbonate generates a higher pH. The ultra-thin water layer also enables the supply of oxygen, which in

105

turn plays a critical role in the formation of the Li-Al layered double hydroxide (LDH) structure [24,28]. This explains why the particles exhibit a porous structure and why the oxygen and carbon contents are higher than those at uniform conversion layer surface areas. In addition, the high local pH also promotes corrosion of the aluminium matrix underneath the water layer, forming a thicker inner dense layer at the location of the particles. Although the continuous growth of the conversion layer is mainly heterogeneous during ageing, the bare regions of the conversion layer may still develop to a small extent, resulting in slightly improved barrier properties. In addition, the influence of intermetallic particles on the continuous growth of the conversion layer still remains unclear, which requires further study in the future.
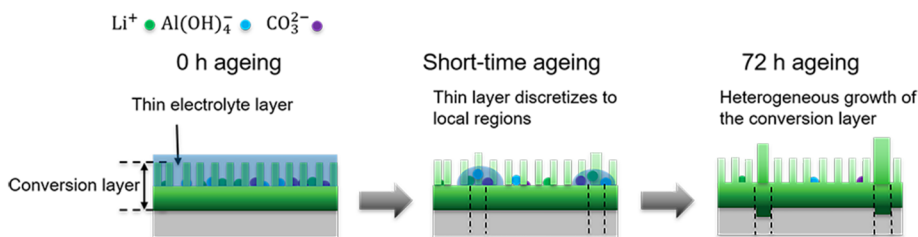
Fig. 4.13 Schematic of morphological evolution during the ageing treatment.

Time-dependent morphological and compositional variations of the conversion layer led to distinct EN signals as shown in **Fig. 4.2**. Based on the general model as proposed in **Fig. 4.13**, **Fig. 4.14** further explains the differences in time-dependent behaviour of the conversion layers with four different ageing treatments during re-immersion. For the 0 h aged conversion layer, the trapped lithium carbonate leaches from the conversion layer immediately at the beginning of re-immersion, leading to a local pH increase. Although the local environment becomes more aggressive, the presence of lithium and carbonate ion provide the growth conditions of the lithium-based conversion layer. The large oscillations observed in the noise resistance (**Fig. 4.3a** and **4.3b**) indicate the competitive dissolution and growth of the conversion layer [48]. The local concentration of lithium and carbonate ions continues to decrease during re-immersion and the inhibition stage terminates when the local concentration becomes lower than the minimum amount that is required for effective protection. The appearance of superimposed transient signals indicates that localised corrosion is dominant. For samples with longer ageing treatments, the concentration of available lithium carbonate is lower at the beginning due to the consumption of lithium carbonate by the continuous growth of the conversion layers during ageing.

Therefore, the dominant corrosion stage initiates earlier in these cases as compared to samples with shorter ageing times. For samples with 72 h ageing treatment, the initial concentration of mobile lithium carbonate is lower than the minimum demand for inhibition. Therefore, inhibition does not occur during the re-immersion period for the samples with long ageing times.
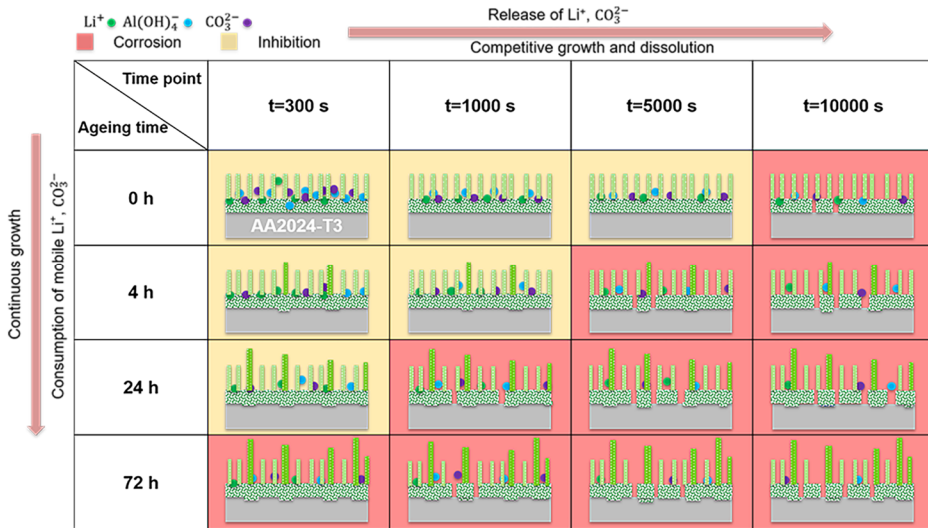
Fig. 4.14 Schematic representation of the compositional and morphological evolution of the conversion layer during re-immersion for different preceding ambient ageing times.

4.4. Conclusions

In this work, the influence of an ambient ageing treatment on the protective behaviour of lithium-based conversion layers is studied. Ageing for different durations up to 72 h under ambient indoor conditions causes a distinct difference in corrosion protective properties of these conversion layers. The freshly-formed lithium-based layer traps water and lithium carbonate. This trapped mobile lithium carbonate will be incorporated into the conversion layer gradually and locally during ageing, leading to a heterogenous growth of the conversion layer. The fresh conversion layer is able to temporarily maintain an inhibited state with high corrosion resistance and shows active inhibition through leaching of entrapped lithium carbonate during the first stage of the re-immersion tests. At a later stage, the conversion layer shows a much lower resistance after the depletion of leachable lithium carbonate as compared to the longer-aged conversion layers. Long-time ageing treatment significantly decreases

the initial active protection ability but improves the overall corrosion barrier resistance of the conversion layer, as a result of the ongoing development of the conversion layer during ageing.

References

[1]   N. L. Sukiman, X. Zhou, N. Birbilis, A.E. Hughes, J.M. C. Mol, S. J., X. Zhou, G. E., Durability and Corrosion of Aluminium and Its Alloys: Overview, Property Space, Techniques and Developments, in: Z. Ahmad (Ed.), Alum. Alloys - New Trends Fabr. Appl., InTech, 2012.

[2]   A. E., N. Birbilis, J. M.C., S. J., X. Zhou, G. E., High Strength Al-Alloys: Microstructure, Corrosion and Principles of Protection, in: Z. Ahmad (Ed.), Recent Trends Process. Degrad. Alum. Alloys, InTech, 2011.

[3]   A.E. Hughes, C. MacRae, N. Wilson, A. Torpy, T.H. Muster, A.M. Glenn, Sheet AA2024-T3: a new investigation of microstructure and composition, Surf. Interface Anal. 42 (2010) 334–338.

[4]   A. Boag, A.E. Hughes, N.C. Wilson, A. Torpy, C.M. MacRae, A.M. Glenn, T.H. Muster, How complex is the microstructure of AA2024-T3?, Corros. Sci. 51 (2009) 1565–1568.

[5]   A. Boag, A.E. Hughes, A.M. Glenn, T.H. Muster, D. McCulloch, Corrosion of AA2024-T3 Part I: Localised corrosion of isolated IM particles, Corros. Sci. 53 (2011) 17–26.

[6]   N. Birbilis, Y.M. Zhu, S.K. Kairy, M.A. Glenn, J.-F. Nie, A.J. Morton, Y. Gonzalez-Garcia, H. Terryn, J.M.C. Mol, A.E. Hughes, A closer look at constituent induced localised corrosion in Al-Cu-Mg alloys, Corros. Sci. 113 (2016) 160–171.

[7]   A. Kosari, F. Tichelaar, P. Visser, H. Zandbergen, H. Terryn, J.M.C. Mol, Dealloying-driven local corrosion by intermetallic constituent particles and dispersoids in aerospace aluminium alloys, Corros. Sci. 177 (2020) 108947.

[8]   M. Becker, Chromate-free chemical conversion coatings for aluminum alloys, Corros. Rev. 37 (2019) 321–342.

[9]   A.E. Hughes, J.M.C. Mol, M.L. Zheludkevich, R.G. Buchheit, eds., Active Protective Coatings: New-Generation Coatings for Metals, Springer Netherlands, Dordrecht, 2016.

[10]   P. Visser, H. Terryn, J.M.C. Mol, Aerospace Coatings, in: A.E. Hughes, J.M.C. Mol, M.L. Zheludkevich, R.G. Buchheit (Eds.), Act. Prot. Coat. New-Gener. Coat. Met., Springer Netherlands, Dordrecht, 2016: pp. 315–372.

[11]   H. Costenaro, A. Lanzutti, Y. Paint, L. Fedrizzi, M. Terada, H.G. de Melo, M.-G. Olivier, Corrosion resistance of 2524 Al alloy anodized in tartaric-sulphuric acid at different voltages and protected with a TEOS-GPTMS hybrid sol-gel coating, Surf. Coat. Technol. 324 (2017) 438–450.

[12]   M. Saenz de Miera, M. Curioni, P. Skeldon, G.E. Thompson, The behaviour of second phase particles during anodizing of aluminium alloys, Corros. Sci. 52 (2010) 2489–2497.

[13]   M. Paz Martinez-Viademonte, S.T. Abrahami, M.D. Havigh, K. Marcoen, T. Hack, M. Burchardt, H. Terryn, The Role of Anodising Parameters in the Performance of Bare and Coated Aerospace Anodic Oxide Films, Coatings. 12 (2022) 908.

[14]   N.N. Voevodin, J.W. Kurdziel, R. Mantz, Corrosion protection for aerospace aluminum alloys by Modified Self-assembled NAnophase Particle (MSNAP) sol–gel, Surf. Coat. Technol. 201 (2006) 1080–1084.

[15]   A. Conde, A. Durán, J.J. de Damborenea, Polymeric sol–gel coatings as protective layers of aluminium alloys, Prog. Org. Coat. 46 (2003) 288–296.

[16]   A. Trentin, S.V. Harb, M.C. Uvida, S.H. Pulcinelli, C.V. Santilli, K. Marcoen, S. Pletincx, H. Terryn, T. Hauffman, P. Hammer, Dual Role of Lithium on the Structure and Self-Healing Ability of PMMA-Silica Coatings on AA7075 Alloy, ACS Appl. Mater. Interfaces. 11 (2019) 40629–40641.

[17]   M. Becker, Chromate-free chemical conversion coatings for aluminum alloys, Corros. Rev. 37 (2019) 321–342.

[18]   P. Santa Coloma, U. Izagirre, Y. Belaustegi, J.B. Jorcin, F.J. Cano, N. Lapeña, Chromium-free conversion coatings based on inorganic salts (Zr/Ti/Mn/Mo) for aluminum alloys used in aircraft applications, Appl. Surf. Sci. 345 (2015) 24–35.

[19]   I. Milošev, G.S. Frankel, Review—Conversion Coatings Based on Zirconium and/or Titanium, J. Electrochem. Soc. 165 (2018) C127.

[20]   J.K. Hawkins, H.S. Isaacs, S.M. Heald, J. Tranquada, G.E. Thompson, G.C. Wood, An investigation of chromate inhibitors on aluminium using fluorescence detection of X-ray absorption, Corros. Sci. 27 (1987) 391–399.

[21]   A.E. Hughes, R.J. Taylor, B.R.W. Hinton, Chromate Conversion Coatings on 2024 Al Alloy, Surf. Interface Anal. 25 (1997) 223–234.

[22]   O. Gharbi, S. Thomas, C. Smith, N. Birbilis, Chromate replacement: what does the future hold?, Npj Mater. Degrad. 2 (2018) 12.

[23]   J. Gui, T.M. Devine, Influence of lithium on the corrosion of aluminum, Scr Met. U. S. 21:6 (1987).

[24]   C.M. Rangel, M.A. Travassos, The passivation of aluminium in lithium carbonate/bicarbonate solutions, Corros. Sci. 33 (1992) 327–343.

[25]   G.R. Williams, D. O'Hare, A Kinetic Study of the Intercalation of Lithium Salts into Al(OH)3, J. Phys. Chem. B. 110 (2006) 10619–10629.

[26]   C.M. Rangel, M.A. Travassos, Li-based conversion coatings on aluminium: An electrochemical study of coating formation and growth, Surf. Coat. Technol. 200 (2006) 5823–5828.

[27]   R.G. Buchheit, M.D. Bode, G.E. Stoner, Corrosion-Resistant, Chromate-Free Talc Coatings for Aluminum, CORROSION. 50 (1994) 205–214.

[28]   C.A. Drewien, M.O. Eatough, D.R. Tallant, C.R. Hills, R.G. Buchheit, Lithium-aluminum-carbonate-hydroxide hydrate coatings on aluminum alloys: Composition, structure, and processing bath chemistry, J. Mater. Res. 11 (1996) 1507–1513.

[29]   M.W. Kendig, R.G. Buchheit, Corrosion Inhibition of Aluminum and Aluminum Alloys by Soluble Chromates, Chromate Coatings, and Chromate-Free Coatings, CORROSION. 59 (2003) 379–400.

[30]   P. Visser, S.A. Hayes, Low-temperature-curable coating composition useful as anticorrosive primer coating for non-ferrous metal substrates, particularly aluminum or aluminum alloy, comprises film-forming resin, curing agent, and lithium salt, patent nr. WO2010112605-A1, (2010), WO2010112605A1, 2010.

[31]   P. Visser, Y. Liu, H. Terryn, J.M.C. Mol, Lithium salts as leachable corrosion inhibitors and potential replacement for hexavalent chromium in organic coatings for the protection of aluminum alloys, J. Coat. Technol. Res. 13 (2016) 557–566.

[32]   Y. Liu, P. Visser, X. Zhou, S.B. Lyon, T. Hashimoto, M. Curioni, A. Gholinia, G.E. Thompson, G. Smyth, S.R. Gibbon, D. Graham, J.M.C. Mol, H. Terryn, Protective Film Formation on AA2024-T3 Aluminum Alloy by Leaching of Lithium Carbonate from an Organic Coating, J. Electrochem. Soc. 163 (2015) C45.

[33]   Y. Liu, P. Visser, X. Zhou, S.B. Lyon, T. Hashimoto, A. Gholinia, G.E. Thompson, G. Smyth, S.R. Gibbon, D. Graham, J.M.C. Mol, H. Terryn, An investigation of the corrosion inhibitive layers generated from lithium oxalate-containing organic coating on AA2024-T3 aluminium alloy, Surf. Interface Anal. 48 (2016) 798–803.

[34]   P. Visser, A. Lutz, J.M.C. Mol, H. Terryn, Study of the formation of a protective layer in a defect from lithium-leaching organic coatings, Prog. Org. Coat. 99 (2016) 80–90.

[35]   P. Visser, H. Terryn, J.M.C. Mol, On the importance of irreversibility of corrosion inhibitors for active coating protection of AA2024-T3, Corros. Sci. 140 (2018) 272–285.

[36]   A. Kosari, P. Visser, F. Tichelaar, S. Eswara, J.-N. Audinot, T. Wirtz, H. Zandbergen, H. Terryn, J.M.C. Mol, Cross-sectional characterization of the conversion layer formed on AA2024-T3 by a lithium-leaching coating, Appl. Surf. Sci. 512 (2020) 145665.

[37]   A. Kosari, F. Tichelaar, P. Visser, H. Zandbergen, H. Terryn, J.M.C. Mol, Laterally-resolved formation mechanism of a lithium-based conversion layer at the matrix and intermetallic particles in aerospace aluminium alloys, Corros. Sci. 190 (2021) 109651.

[38]   P. Visser, K. Marcoen, G.F. Trindade, M.-L. Abel, J.F. Watts, T. Hauffman, J.M.C. Mol, H. Terryn, The chemical throwing power of lithium-based inhibitors from organic coatings on AA2024-T3, Corros. Sci. 150 (2019) 194–206.

[39]   P. Visser, H. Terryn, J.M.C. Mol, Active corrosion protection of various aluminium alloys by lithium-leaching coatings, Surf. Interface Anal. 51 (2019) 1276–1287.

[40]   L. Li, G.M. Swain, Effects of Aging Temperature and Time on the Corrosion Protection Provided by Trivalent Chromium Process Coatings on AA2024-T3, ACS Appl. Mater. Interfaces. 5 (2013) 7923–7930.

[41]   P. Zhou, B. Yu, Y. Hou, G. Duan, L. Yang, B. Zhang, T. Zhang, F. Wang, Revisiting the cracking of chemical conversion coating on magnesium alloys, Corros. Sci. 178 (2021) 109069.

[42]   V. Laget, C.S. Jeffcoate, H.S. Isaacs, R.G. Buchheit, Dehydration-Induced Loss of Corrosion Protection Properties in Chromate Conversion Coatings on Aluminum Alloy 2024-T3, J. Electrochem. Soc. 150 (2003) B425.

[43]   Y. Guo, G.S. Frankel, Characterization of trivalent chromium process coating on AA2024-T3, Surf. Coat. Technol. 206 (2012) 3895–3902.

[44]   X. Liu, M. Wang, H. Li, L. Wang, Y. Xu, Electrochemical effects of pH value on the corrosion inhibition and microstructure of cerium doped trivalent chromium conversion coating on Zn, Corros. Sci. 167 (2020) 108538.

[45]   M.A. Kamde, Y. Mahton, J. Ohodnicki, M. Roy, P. Saha, Effect of cerium-based conversion coating on corrosion behavior of squeeze cast Mg-4 wt% Y alloy in 0.1 M NaCl solution, Surf. Coat. Technol. 421 (2021) 127451.

[46]   M. Yuan, J. Lu, G. Kong, C. Che, Effect of silicate anion distribution in sodium silicate solution on silicate conversion coatings of hot-dip galvanized steels, Surf. Coat. Technol. 205 (2011) 4466–4470.

[47]   Z. Li, A. Homborg, Y. Gonzalez-Garcia, A. Kosari, P. Visser, A. Mol, Evaluation of the formation and protectiveness of a lithium-based conversion layer using electrochemical noise, Electrochimica Acta. 426 (2022) 140733.

[48]   P. Visser, Y. Gonzalez-Garcia, J.M.C. Mol, H. Terryn, Mechanism of Passive Layer Formation on AA2024-T3 from Alkaline Lithium Carbonate Solutions in the Presence of Sodium Chloride, J. Electrochem. Soc. 165 (2018) C60–C70.

[49]   D.-H. Xia, Y. Behnamian, Electrochemical noise: a review of experimental setup, instrumentation and DC removal, Russ. J. Electrochem. 51 (2015) 593–601.

[50]   F. Mansfeld, Z. Sun, C.H. Hsu, Electrochemical noise analysis (ENA) for active and passive systems in chloride media, Electrochimica Acta. 46 (2001) 3651–3664.

[51]   F. Mansfeld, Z. Sun, Technical Note: Localization Index Obtained from Electrochemical Noise Analysis, CORROSION. 55 (1999) 915–918.

[52]   A.M. Homborg, T. Tinga, X. Zhang, E.P.M. van Westing, P.J. Oonincx, J.H.W. de Wit, J.M.C. Mol, Time–frequency methods for trend removal in electrochemical noise data, Electrochimica Acta. 70 (2012) 199–209.

[53] D.-H. Xia, S. Song, Y. Behnamian, W. Hu, Y.F. Cheng, J.-L. Luo, F. Huet, Review—Electrochemical Noise Applied in Corrosion Science: Theoretical and Mathematical Models towards Quantitative Analysis, J. Electrochem. Soc. 167 (2020) 081507.

[54] R.A. Cottis, Interpretation of Electrochemical Noise Data, CORROSION. 57 (2001) 265–285.

[55] H. Ashassi-Sorkhabi, D. Seifzadeh, M.G. Hosseini, EN, EIS and polarization studies to evaluate the inhibition effect of 3H-phenothiazin-3-one, 7-dimethylamin on mild steel corrosion in 1M HCl solution, Corros. Sci. 50 (2008) 3363–3370.

[56] A.M. Homborg, T. Tinga, E.P.M. van Westing, X. Zhang, G.M. Ferrari, J.H.W. de Wit, J.M.C. Mol, A Critical Appraisal of the Interpretation of Electrochemical Noise for Corrosion Studies, CORROSION. 70 (2014) 971–987.

[57] S.S. Jamali, A critical review of electrochemical noise measurement as a tool for evaluation of organic coatings, Prog. Org. Coat. (2016) 12.

[58] P. Visser, M. Meeusen, Y. Gonzalez-Garcia, H. Terryn, J.M.C. Mol, Electrochemical Evaluation of Corrosion Inhibiting Layers Formed in a Defect from Lithium-Leaching Organic Coatings, J. Electrochem. Soc. 164 (2017) C396–C406.

[59] A. Kosari, F. Tichelaar, P. Visser, P. Taheri, H. Zandbergen, H. Terryn, J.M.C. Mol, Nanoscopic and in-situ cross-sectional observations of Li-based conversion coating formation using liquid-phase TEM, Npj Mater. Degrad. 5 (2021) 40.

[60] A. Kosari, H. Zandbergen, F. Tichelaar, P. Visser, P. Taheri, H. Terryn, J.M.C. Mol, In-situ nanoscopic observations of dealloying-driven local corrosion from surface initiation to in-depth propagation, Corros. Sci. 177 (2020) 108912.

[61] A. Kosari, M. Ahmadi, F. Tichelaar, P. Visser, Y. Gonzalez-Garcia, H. Zandbergen, H. Terryn, J.M.C. Mol, Editors' Choice—Dealloying-Driven Cerium Precipitation on Intermetallic Particles in Aerospace Aluminium Alloys, J. Electrochem. Soc. 168 (2021) 041505.

[62] K. Marcoen, P. Visser, G.F. Trindade, M.-L. Abel, J.F. Watts, J.M.C. Mol, H. Terryn, T. Hauffman, Compositional study of a corrosion protective layer formed by leachable lithium salts in a coating defect on AA2024-T3 aluminium alloys, Prog. Org. Coat. 119 (2018) 65–75.

[63] B.R. Baker, R.M. Pearson, Water content of pseudoboehmite: A new model for its structure, J. Catal. 33 (1974) 265–278.

Supplementary Information for Chapter 4

Table S4.1 Relative energy distribution of selected timeframes for AA2024-T3 treated 0.01 M NaCl and 0.01 M Li₂CO₃ solution for 14500 s exposed in 0.01 M NaCl after different ageing treatment.

Ageing time	d1	d2	d3	d4	d5	d6	d7	d8
0 h	0.04	0.06	0.10	0.15	0.17	0.17	0.15	0.17
4 h	0.01	0.03	0.05	0.07	0.12	0.1	0.14	0.47
24 h	0.03	0.04	0.02	0.05	0.12	0.26	0.24	0.24
72 h	0.02	0.03	0.06	0.12	0.19	0.17	0.19	0.21
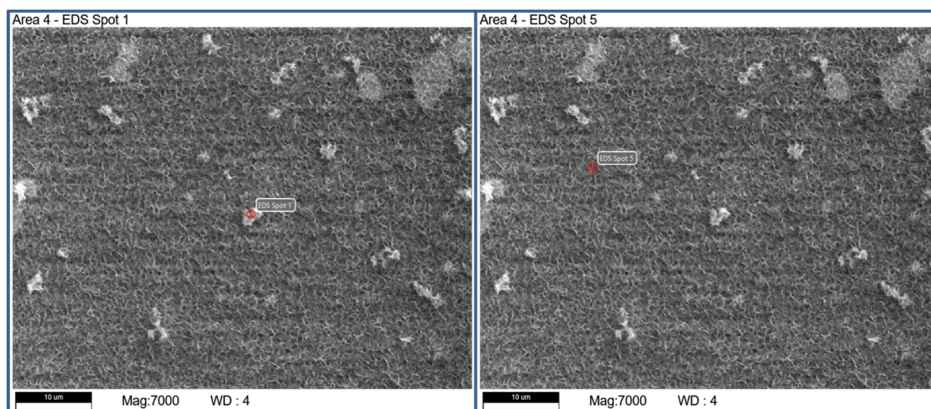
Fig. S4.1 Example of the selection of EDS spot analysis on particle (left) and matrix (right) for the lithium-based conversion layer with an ambient ageing for a duration of 4 h.

CHAPTER 5

Local Scanning Electrochemical Microscopy Analysis of a Lithium-based Conversion Layer on AA2024-T3 at Progressive Stages of Formation[1]

[1] **Z. Li,** G. Li, P. Visser, A. Homborg, Y. Gonzalez-Garcia, A. Mol, Local scanning electrochemical microscopy analysis of a lithium-based conversion layer on AA2024-T3 at progressive stages of formation, Electrochimica Acta. 469 (2023) 143270.

Abstract

Scanning electrochemical microscopy (SECM) is employed to characterize the evolution of local electrochemical surface activity during lithium-based conversion layer formation on legacy aerospace aluminium alloy AA2024-T3. Initially, three types of studied intermetallic particles - S-, θ- and constituent phases - act as active cathodic areas. Subsequently, θ- and constituent phases show passivation preceding that of S-phase particles during the later conversion layer formation stages. The entire surface, including the matrix region, shows a higher reactivity at the beginning and then gradually shows decreasing reactivity. Hydrogen evolution-generated bubbles attach to the alloy surface and locally hinder the conversion layer formation, weakening the corrosion protection the conversion layer provides at those locations.

Keywords: Aluminium alloy, Inhibitor, Lithium-based conversion layer, SECM

5.1. Introduction

The 2xxx and 7xxx series of heat-treatable wrought aluminium alloys, representing Al–Cu–(Mg) and Al–Zn–Mg(–Cu) systems, respectively, have been widely applied in high-performance structural aerospace and transportation applications owing to their high strength-to-weight ratio, good elastic stiffness, excellent ductility, modest price and very good manufacturability [1–4]. However, the lack of sufficient corrosion resistance in harsh environments due to the heterogeneous distribution of intermetallic particles (IMPs) restricts their practical use without pre-treatment [5,6] and active protective coatings [7,8]. In Al–Cu–Mg alloys, IMPs nominally include three broad particle classes: dispersoids, precipitates, including S-phase (Al$_2$CuMg) and θ-phase (Al$_2$Cu), and constituent particles [5,9]. Precipitates form during heating operations in the solid state due to variations in the alloying solid solubility with temperature and have an age hardening effect. Constituent phases are nominally >1 μm in size and have compositions often enriched in transition metals including Al, Mn, Fe, Cu and Si in various ratios. S-phase particles typically exhibit a higher electrochemical activity as compared to other IMPs [10]. Corrosion protective measures based on surface treatment and organic coating application have been widely implemented in industrial practice due to their cost effectiveness, versatility and relatively simple application process characteristics [11–13].

Lithium salts are considered a promising candidate within the range of environmentally friendly inhibitors loaded into organic coatings for the corrosion protection of aerospace aluminium alloys since 2010 [14–17]. Leached lithium salts have been shown to form a protective conversion layer at an artificial coating defect during neutral salt spray test (ASTM B-117) [16]. Early relevant studies date back to the 1980s when Gui et al. [18] generated a lithium-based conversion layer by applying anodic polarization on AA6061-T6 panels. Rangel et al. reported that such conversion layer is robust and remarkably resistant to chloride ion attack [19,20]. Subsequent research showed that lithium ions can gradually be intercalated into aluminium hydroxide when exposed to a highly alkaline liquid environment containing lithium salts, generating a stable protective film on aluminium alloy surfaces [20,21]. Further structural and compositional analysis carried out by Buchheit et al. showed that the generation of an Al-Li layered double hydroxide layer (LDH) contributed to the enhanced corrosion barrier performance [22,23]. Over the last decade, the lithium-based inhibitor coating technology has been well studied for both organic coating systems and conversion treatment of bare aluminium alloys,

indicating that lithium salts might be a promising alternative for the replacement of Cr(VI)-containing inhibitor chemistries for structural aerospace applications [24–29].

In prior studies, lithium-based conversion layers have been characterized by linear polarization resistance (LPR) and Electrochemical Impedance Spectroscopy (EIS) performed at discrete time frames to quantify their corrosion protective properties in an aggressive solution at short exposure times (ranging from hours to 7 days) [28,30,31]. The system must maintain a relatively stable dynamic equilibrium during the measurements to obtain reliable data. This condition might limit the detection of fast-kinetic electrochemical reactions and valuable information of the corrosion (inhibition) mechanism might be missed. This limitation can be overcome by applying electrochemical noise (EN) techniques. Instantaneous and continuous, i.e. time-resolved, information on corrosion (inhibition) processes can be obtained, also for metastable and fast-kinetic electrochemical systems [32,33]. Yet, without spatial resolution, EIS and EN can only provide electrochemical information generated over the complete exposed surface area. Aluminium alloys typically undergo localized corrosion processes when exposed to aggressive environments [2,34–36] and they are highly related to various types of intermetallic phases [5,6,37]. Therefore, a local electrochemical technique is needed to adequately reveal the local electrochemical differences with adequate lateral resolution. For that purpose, the scanning electrochemical microscopy (SECM) technique is considered a suitable method since it harvests spatially-resolved electrochemical information of a heterogeneous electroactive surface. This technique employs an ultramicroelectrode (UME) to probe and map the electrochemical activity of a local surface area of interest during exposure to an electrolyte [38]. SECM has been widely applied to evaluate the formation of inhibitor films on aluminium alloys [39], the heterogeneous electrochemical properties of aluminium alloys at IMP containing areas [40,41], and the electrochemical activity at an artificial coating defect in the absence or presence of inhibitors in the coating [42,43].

In the present work, SECM and EN techniques are applied to resolve the formation process of a lithium-based conversion layer spatiotemporally. Different stages during the conversion layer formation period are analysed to study the evolution of the surface electrochemical behaviour at a microscale level. Local areas, including IMPs and the adjacent aluminium matrix are compared to elucidate different stages of local formation during the growth of the lithium-based conversion layer.

5.2. Experimental methods

5.2.1. Materials and experimental set-up. All working electrodes originated from a commercial grade AA2024-T3 sheet with a thickness of 0.8 mm (Goodfellow, UK). Rectangular specimens with a size of 8 mm × 18 mm are produced. Two specimens are embedded in epoxy resin for EN measurements to prepare identical-electrode samples. A detailed description of sample fabrication and the electrochemical cell for the preparation of the conversion layer can be found in Chapter 3 [32,33]. Samples are immersed in a static conversion bath (0.01 M Li_2CO_3 and 0.01 M NaCl) for seven different time durations (0 s, 60 s, 200 s, 700 s, 2000 s, 4000 s, 14500 s) to prepare and study the conversion layers at different formation stages. Formed conversion layers are washed thoroughly using deionized water, dried using cool air, and left in a desiccator before subsequent SECM and EN measurements. The purpose of this step is to quench the conversion layer formation process. Laboratory-grade chemicals used in this work were ordered from Sigma-Aldrich (St. Louis, MO, USA).

For SECM samples, a cross-scribe is made on the conversion layers. This mark is used as a reference location so that both the SECM and scanning electron microscope/ energy dispersive X-ray (SEM/EDX) images can be matched. All specimens for SECM and EN are covered by a highly-impermeable sealing tape with an exposed round area of 4 mm diameter. Morphological information is obtained using a JEOL JSM-6500F field emission SEM using an acceleration voltage of 15 kV at a working distance of 25 mm. Backscattered electron images (BEI) and secondary electron images (SEI) are collected. The local chemical surface composition is analysed using EDX. A schematic representation of the sample processing sequence is shown in **Fig. 5.1**.
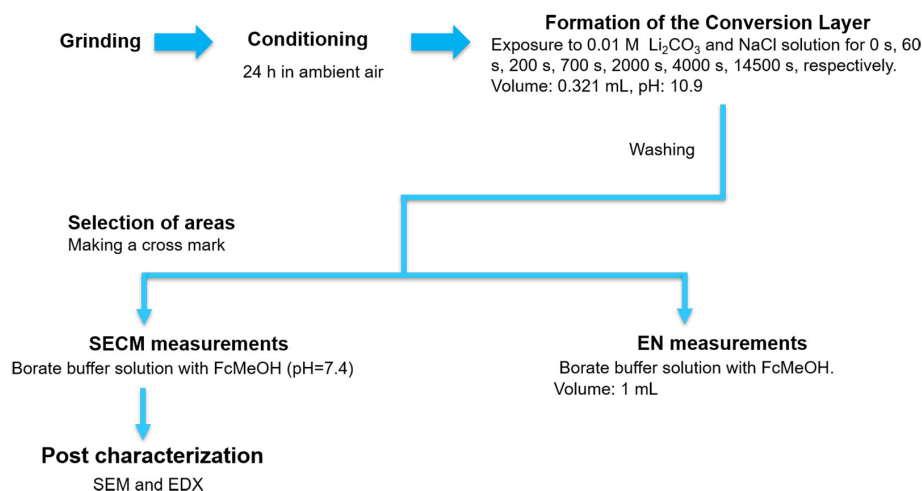
Fig. 5.1 Sequence diagram of the experimental procedure for the SECM, SEM and EN measurements.

5.2.2. SECM Instrumentation and experimental procedures. Scanning electrochemical microscopy (SECM) is executed using Biologic Instruments SECM model M370. A Pt disk UME (10 μm in diameter), with an RG (radius of the insulating glass sheath divided by the radius of the Pt disk) of 5, was purchased from CH Instruments Inc. and served as working electrode. A saturated Ag/AgCl, KCl and a Pt thin plate are used as reference electrode (RE) and counter electrode (CE), respectively. In this work, all voltages are with respect to the Ag/AgCl reference electrode unless otherwise stated. The SECM setup and the detailed apparatus are shown in **Fig. 5.2**. In addition to the high spatial resolution, SECM is well-known for its versatility and various operation modes such as feedback mode to differentiate insulating or conducting areas or generation/collection mode to investigate the interaction between an electroactive surface and chemical species in the electrolyte [38,44]. In this paper, a borate buffer solution containing 2 mM FcMeOH serving as mediator is used for SECM and EN measurements. The borate buffer is prepared using 10 mM sodium tetraborate, and then adjusted to pH 7.4 with 0.5 M boric acid to maintain the stability of the alloy surfaces during the SECM measurements [41,45–47]. Feedback mode data collection is utilized based on the redox mediator FcMeOH [41].

Cyclic voltammetry (CV) measurements are conducted to verify the cleanliness of the probe electrode with the probe held several millimetres away from the surface

before any SECM measurement. All current signals are normalized using the steady-state current obtained from the CV test (**Fig. S5.1**) for a better comparison amongst the various measurements. Before SECM measurements, the stage is levelled by measuring a negative feedback approach curve over the covering tape. SECM mapping in a constant height is obtained by scanning the tip in the x–y plane and recording the tip current simultaneously. The distance between the tip and substrate is adjusted to around 5 μm employing an approach curve. Each measurement was performed over a working area of 180 μm × 140 μm with a scanning speed of 10 μm/s. For approach curves, the tip is moved toward the substrate surface at a velocity of 10 μm/s (steps of 1 μm, waiting time of 0.1 s at each point). Before approaching, a quick mapping was performed so that local areas with relatively high current values were avoided to make sure that the approach curves were measured above the aluminium matrix. For both modes, the SECM tip is biased at a voltage of 0.5 V to oxidize FcMeOH while the substrate is maintained at open circuit potential (OCP) state. All experiments are performed at room temperature 22±2 °C, in solution open to the air. Experiments were repeated at least twice to confirm reproducibility.
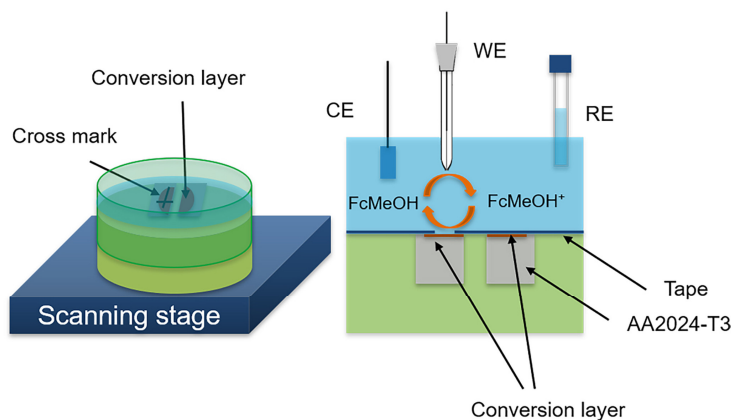
Fig. 5.2 Schematic illustration of SECM measurement.

5.2.3. EN measurements and analysis. For EN experiments, a two-electrode configuration is selected in this work. One exposed area chosen on either of the two panels is adopted to monitor the potential noise signal. Electrical contact is established with a Cu adhesive tape connected to the working electrode. The reference electrode used for EN is identical to that applied for SECM. Potential values

recorded here are with respect to this reference electrode unless mentioned otherwise. All EN measurements are performed under open circuit conditions. The volume of the solution for EN measurement is 1 mL each time. A Compactstat (Ivium Technologies) is employed to record potential signals. A Faradaic cage is used to place the Compactstat and the electrochemical cell to avoid interference from external electromagnetic sources. The sampling frequency is 20 Hz and a low-pass filter of 10 Hz was used to avoid aliasing. The EN data are analysed using Matlab from MathWorks. All EN tests were performed at least in triplicate.

In the EN noise, a DC component is inevitable due to the instability of the system and the changing outline of the electrode under corrosion attack. The DC component does not contain any useful information but generates false low frequencies and can interfere with the signal processing [48,49]. Therefore, the DC trend must be effectively removed but at the same time, useful data must be preserved as much as possible before data analysis. Previous researchers have proposed various strategies for trend removal, like moving average, polynomial and linear trend removal, wavelet analysis and empirical mode decomposition [48,49]. In this work, a time-frequency trend removal is adopted using an eight-level discrete wavelet decomposition (DWT) with a Daubechies 4 wavelet. This method has already proven to be valid in our previous work [32,33]. After removing the DC component, an energy distribution plot (EDP) is applied to resolve the frequency range of the dominant energy contribution [50]. The time window from 4000 s to 6000 s is selected for analysis since this timeframe is within the SECM imaging period. Apart from around 30 mins for levelling and locating the cross mark, SECM mapping lasts almost 90 mins each time. The dominant energy contribution with certain time scales indicates the electrochemical reactions which contribute most to shape the outline of the EN signal. In this work, eight different time scales ranging from short, medium to long correspond to activation-, mixed-, and diffusion-controlled processes, respectively [48].

5.3. Results and discussion

5.3.1. Early stages of the conversion layer growth. **Fig. 5.3** shows SECM imaging and corresponding BEI/EDX characterization for the unexposed sample, i.e. before being immersed in the conversion bath (t=0 s). Active areas in SECM mapping and corresponding IMPs are marked by black lines. FcMeOH is oxidized at the UME and then an enhanced current is obtained when the probe scans over an active region where FcMeOH$^+$ is reduced back to FcMeOH [41]. Although the native oxide

protective layer remains stable under a relatively neutral liquid environment, it is insufficient to suppress local electrochemical reactions occurring at the surface. The "hot spot" regions observed in **Fig. 5.3a** are associated with the locations of different types of IMPs, as shown by SEM/EDX pictures in **Fig. 5.3b-5.3g**. Enlarged images of several representative IMPs and their corresponding elemental compositions can be found in **Fig. S5.2**.

According to previous studies, the electrochemical interaction between the aluminium matrix and IMPs is driven by their dissimilar chemical compositions [40,41]. Previous work from our team has characterized the morphological evolution of S-, θ- and constituent phases, and the adjacent aluminium matrix at the AA2024-T3 surface during the formation process of a lithium-based conversion layer [51]. Herein, the variation of local electrochemical properties at and adjacent to IMPs is discussed. All S-, θ- and constituent phases form active sites for $FcMeOH^+$ reduction, meaning they all serve as cathodic areas when exposed to a borate buffer electrolyte. For the S-phase, it has been reported that anodic dealloying of the active elements Mg and Al occurs first and then the transition from anodic to cathodic region takes place due to Cu enrichment [6,34,35,37]. However, the S-phase acting as anodic zones is not observed in this work which may be due to the missing local electrochemical information of the S-phase immediately at the start [37] since levelling and locating the cross marks takes around 30 mins before starting the SECM measurements. The presence of Mg shown in the EDX elemental composition maps of **Fig. 5.3g** and **Fig. S5.2** indicates that the buffer solution used in this work is relatively mild and non-corrosive compared to other solutions such as Na_2SO_4, where Mg was not detected on the AA2024-T3 after short immersion experiments [40]. In addition, many small IMPs with a submicron size are seen in Fig. 3b, but their electrochemical activity cannot be distinctly located in Fig. 3a due to the resolution limit in this work: IMPs only larger than 2 μm are analysed.
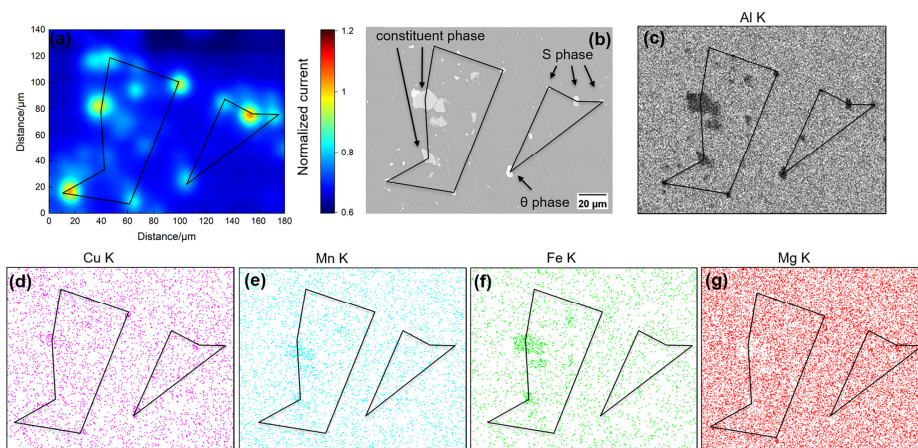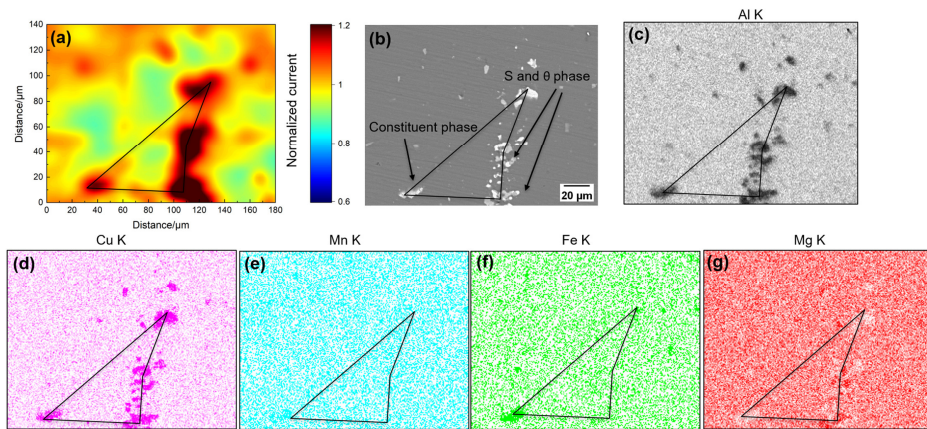
Fig. 5.3 SECM maps of AA2024-T3 without conversion treatment obtained in a borate buffer solution containing 2 mM FcMeOH (a) and corresponding BEI image (b), and EDX maps for Al (c), Cu (d), Mn (e), Fe (f), Mg (g).

Fig. 5.4 presents the SECM mapping and relevant SEM/EDX results for samples with a lithium-based conversion layer formation time of 60 s corresponding to the lowest OCP during the immersion period [32]. It is clear that the averaged current in **Fig. 5.4a** rises drastically compared to that shown in **Fig. 5.3a**. This phenomenon indicates a more active state due to the dissolution of the native oxide film by the highly alkaline conversion bath solution (pH=10.9). The S-, θ- and constituent phases still act as strong cathodic sites but present a wider "hot spot" area compared to that in **Fig. 5.3a**. Larger high current regions observed in **Fig. 5.4a** might be attributed to the faster dealloying of the S-phase in the aggressive conversion solution, leading to a larger redistributed-Cu area [51]. In addition, it is observed that the conducting activity is not uniform all over the aluminium matrix region. Regions far away from IMPs present a relatively lower reactivity which may be due to its lower alloying element content [4].

Fig. 5.5 reveals the SECM imaging and matched SEM/EDX for samples with a lithium-based conversion layer formation time of 200 s. The S-, θ- and constituent phases still behave as cathodic areas, albeit less significantly. The zoomed-in image of the θ-phase and its chemical composition on the left side of the mapped region is provided in **Fig. S5.3**. The averaged current in **Fig. 5.5a** is even higher than that shown in **Fig. 5.4a** although the OCP starts rising after 60 s duration in the conversion bath solution [32]. Furthermore, the current distribution becomes more homogeneous

as compared to the results shown in **Fig. 5.3a** and **Fig. 5.4a**. The observation implies a decrease of the potential difference between IMPs and the aluminium matrix. For IMPs, the initial growth of the conversion layer over the S-phase and copper enrichment for *s*-, θ- and constituent phases shift the OCP towards less negative values [51]. Similarly, noble elements, particularly Cu, reside in the aluminium matrix. These gradually enrich the surface during the aluminium surface dissolution stage, which drives the OCP of the aluminium matrix to more noble values as well [52].

Fig. 5.4 SECM maps of AA2024-T3 immersed in the conversion bath for 60 s obtained in a borate buffer solution containing 2 mM FcMeOH (a) and corresponding BEI image (b), and EDX elemental maps for Al (c), Cu (d), Mn (e), Fe (f), Mg (g).
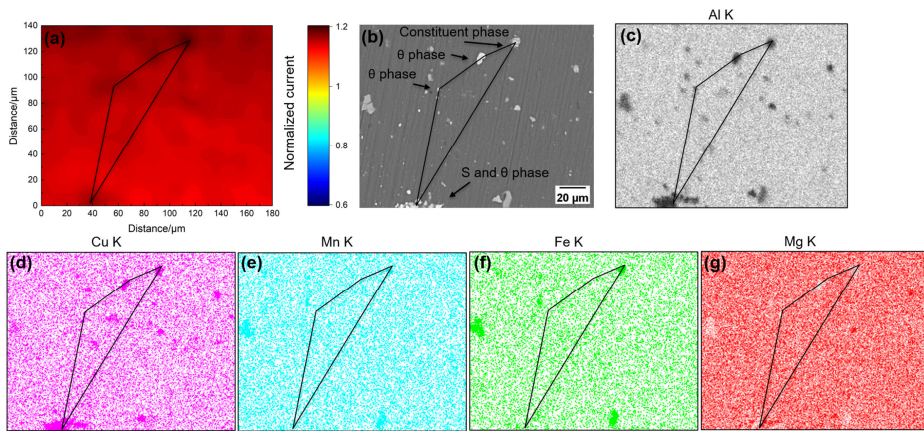
Fig. 5.5 SECM maps of AA2024-T3 immersed in the conversion bath for 200 s obtained in a borate buffer solution containing 2 mM FcMeOH (a) and corresponding BEI image (b), and EDX maps for Al (c), Cu (d), Mn (e), Fe (f), Mg (g).

Fig. 5.6 shows the SECM mapping and corresponding BEI/EDX images for the sample with a lithium-based conversion layer formation time of 700 s. The current distribution shows a heterogeneous behaviour again but with a lower average current in total, especially owing to the current contribution from the aluminium matrix. The S-, θ- and constituent phases still act as strong cathodic locations. The transition of the aluminium matrix from an active towards a passive behaviour is attributed to the formation of the columnar top layer [32,51], although the corrosion protection is still insufficient to inhibit electron exchange reactions. The petal-like Li-Al LDH barrier protection is too limited to effectively suppress the diffusion of ionic species between the alloy surface and electrolyte [32,51]. For the IMPs, the S-phase shows an insignificant growth of the conversion layer and a more severe dealloying, leading to a higher surface enrichment of noble elements [51]. Although θ- and constituent phases are electrochemically relatively stable compared to the S-phase, the absence of a protective conversion layer at this formation stage and, hence, further dealloying render these to act as cathodic regions as well [51].
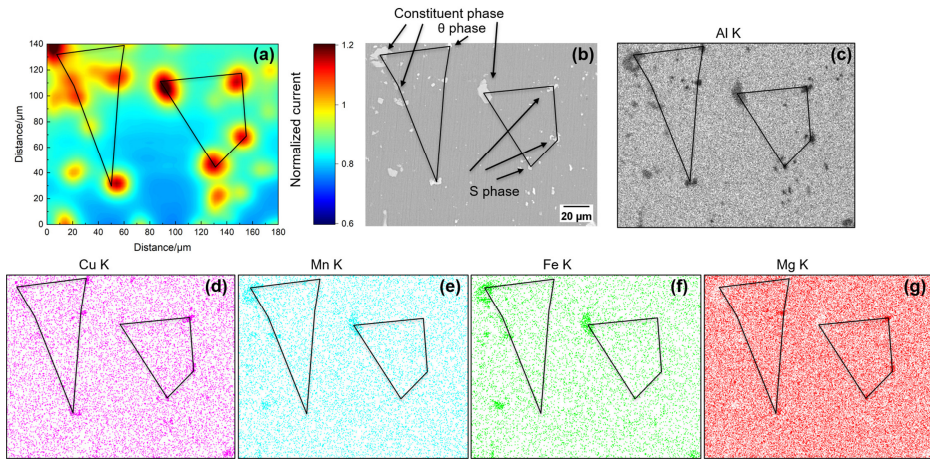
Fig. 5.6 SECM maps of AA2024-T3 immersed in the conversion bath for 700 s obtained at borate buffer solution containing 2 mM FcMeOH (a) and corresponding BEI image (b), and EDX maps for Al (c), Cu (d), Mn (e), Fe (f), Mg (g).

It has been reported that the lithium-based conversion layer growth period can be divided into five stages [32,51]. Up to 700 s after exposure, AA2024-T3 surface, except the S-phase does not show passivation (Stages I and II). Supersaturation of aluminate ions is realized at Stage III and the conversion layer then appears at the alloy surface. Stages IV and V correspond to the growth of the conversion layer and formation of the dense-like inner layer. The SECM results discussed above include the first two stages, where the alloy surface transits from an imperfect passive state to an active state and then gradually shifts back to a passive state. Initially, the alloy surface only undergoes a dissolution process, leading to the accumulation and supersaturation of aluminate ions which is the prerequisite for triggering the formation of the lithium-based conversion layer [24,51]. The S-, θ- and constituent phases act as active cathodic areas, but their potential differences compared to the potential of the aluminium matrix continue to change during the conversion layer formation process. **Fig. 5.7** shows the SEI images of the alloy surface with different immersion treatments and corresponding SECM approach curves over the aluminium matrix. The results of the approach curves shown in **Fig. 5.7e** are consistent with the results of the surface reactivity variation through SECM mapping as presented before. The aluminium matrix without any conversion treatment still indicates substrate conductivity to some extent, indicating that the native aluminium oxide film contains compositional, structural and electronic defects, effectively enabling electrochemical activity occurring at its surface. With the dissolution of the oxide

layer in the conversion bath, surface conductivity increases and reaches its highest level at 200 s. This is confirmed by the different behaviour of the approach curves. For 0 and 60 s, curves show negative feedback response (normalized current < 1), while for 200 s condition, the curve shifts to positive feedback (normalized current > 1), indicating an electroactive behaviour of the surface. At 700 s, the curve shows again non-electroactive response (negative feedback) associated with a more insulating surface.
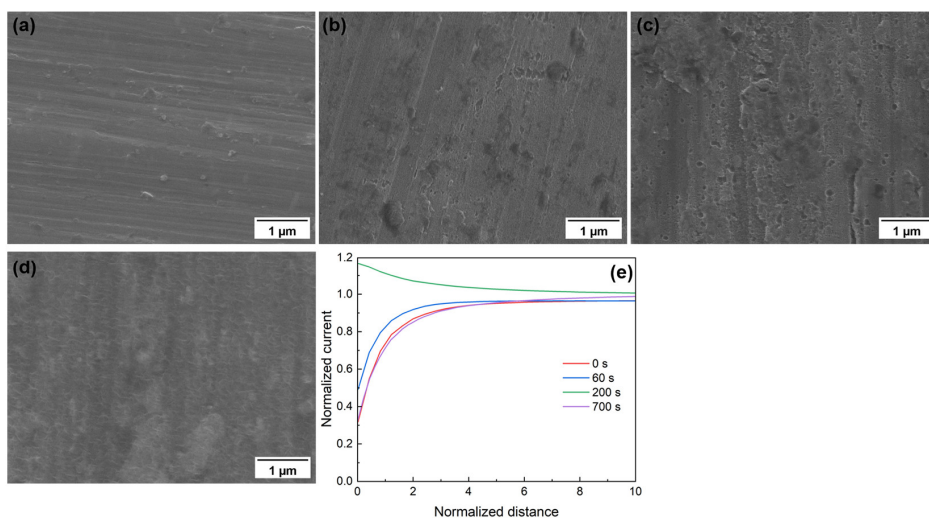
Fig. 5.7 SEM images for samples with a conversion treatment for 0 s (a), 60 s (b), 200 s (c), and 700s (d), and SECM approach curves over the conversion layer corresponding to different immersion times in a borate butter solution containing 2 mM FcMeOH (e).

5.3.2. EN analysis. EN potential signals are recorded for samples immersed for four different durations in the lithium-based conversion bath at early stages to better support the explanations for the variations of SECM mapping. After recording the EN raw data, an eight-level DWT trend removal was applied to extract the part of the signal that contains corrosion information. Subsequently, EDP analysis was performed to reveal the dominant timescales in these EN potential signals [48,49]. **Fig. 5.8** presents the samples initially immersed in the conversion solution for different times (0 s, 60 s, 200 s, 700 s) and then exposed to a borate buffer solution containing 2mM FcMeOH. The potential noise evolution provides an indication of the surface activity and a lower potential usually indicates a more active surface state. It is clear that the potential signal firstly endures a small drop from 0 s (**Fig. 5.8a)** to

60 s formation condition (**Fig. 5.8b)** which is caused by the dissolution of the air-formed oxide layer [32].

Later, with the Cu enrichment over the aluminium matrix and IMPs [51], the potential value gradually rises (**Fig. 5.8c**). The slight potential decrease shown in **Fig. 5.8d** might attribute to the presence of hydrogen bubble-covered area which is more active compared to the uncovered region. A detailed discussion of the effect of attached hydrogen bubbles will be presented later. Time-frequency analysis can be considered as a suitable strategy to distinguish the local and uniform nature of electrochemical reactions [50]. Therefore, in this work time-frequency analysis is employed to investigate the nature of the potential differences and hence the nature of local galvanic interactions between the aluminium matrix and IMPs. A larger local IMP-matrix potential difference usually generates an EN signal where localized electrochemical reactions are more dominant in energy contribution. In other words, dominant energy bands are more likely to be manifested at a higher frequency domain. **Fig. 5.9** shows the EDPs of samples with different conversion treatment times. D2 and D3 represent activation-controlled processes while D7 and D8 are related to more diffusion-controlled processes [50]. The sample without conversion treatment (**Fig. 5.9a**) shows the highest energy contribution in D7 and D8. This is probably due to the presence of the native oxide layer. For samples treated in the conversion bath for 60 s (**Fig. 5.9b)**, D2 and D3 become larger and a marked decrease of D7 and D8 is visible. When the immersion time is extended to 200 s (**Fig. 5.9c**), the EDP shifts back to an energy distribution similar to that of Fig. 9a. This is in agreement with the results shown in **Fig. 5.5,** where SECM mapping presents a homogeneous current distribution. Finally, the alloy surface retains a more heterogenous potential distribution with a longer immersion time of 700 s (**Fig. 5.9d**). This is visible in the EDP as a relative increase of D2 and D3 again.
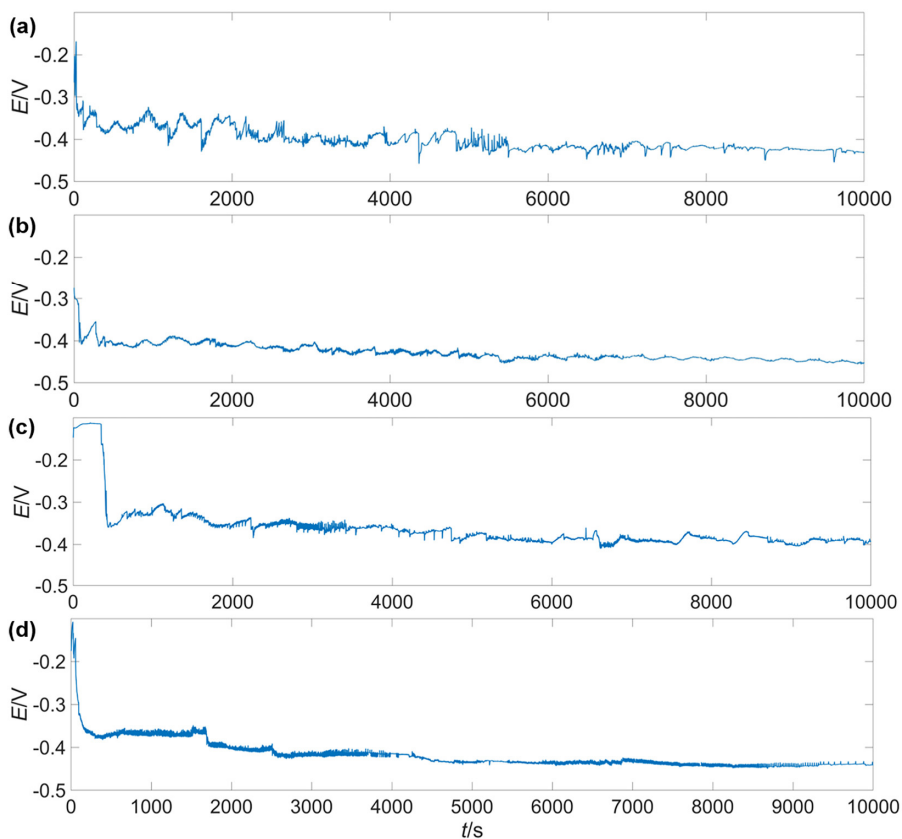
Fig. 5.8 EN potential signals for AA2024-T3 initially treated in 0.01 M NaCl and 0.01 M Li₂CO₃ solution for (a) 0 s, (b) 60 s, (c) 200 s, and (d) 700 s, and then exposed in a borate butter solution containing 2 mM FcMeOH for a duration of 10000 s.
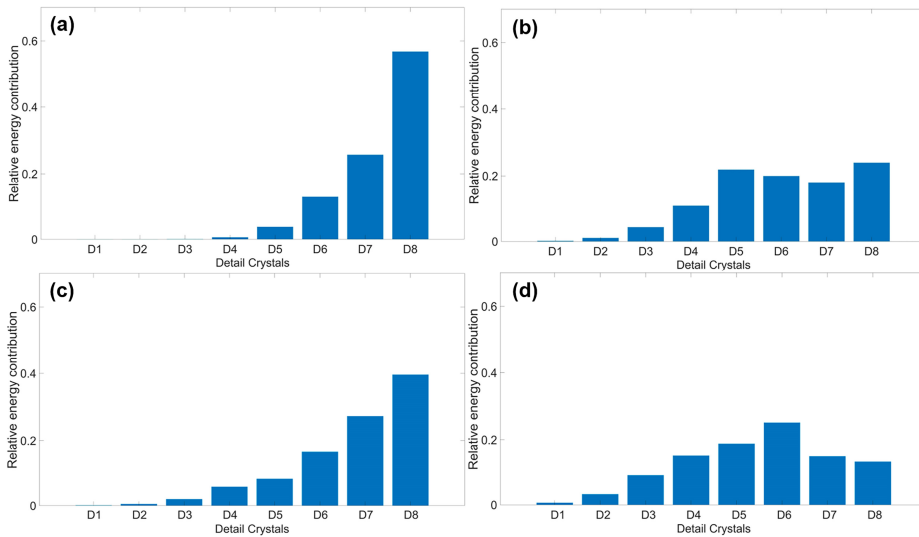
***Fig. 5.9 Energy distribution plots of the EN current signals for AA2024-T3 immersed in 0.01 M NaCl and 0.01 M Li₂CO₃ solution for (a) 0 s, (b) 60 s, (c) 200 s, and (d) 700 s, and then exposed in a borate butter solution containing 2 mM FcMeOH. Timeframes are between 4000 s to 6000 s.***

5.3.3. Late stages of the conversion layer formation. Three time points are chosen to represent the last three stages of the conversion layer formation process: 2000 s, 4000 s, and 14500 s. **Fig. 5.10** shows the SECM mapping and the corresponding BEI/EDX results for the specimen with a conversion layer formation time of 2000 s. It is observed that the averaged current continues to decline and that the potential difference between the IMPs and the aluminium matrix drops as well. Another finding is that not all types of IMPs act as active cathodes and that three active locations, marked in **Fig. 5.10,** are all related to the local presence of S-phase particles. The elemental composition of these three active zones is listed in **Fig. S5.4**. The potential differences between the aluminium matrix and the θ- or constituent phases are almost negligible. S-phase particles serving as active sites indicate that the potential of the S-phase is still higher than that of the surrounding aluminium matrix. This is possibly related to the more severe dealloying as compared to that of θ- and constituent phases, since the S-phase is a relatively active IMP [6,37,53]. A more pronounced dealloying leads to a larger extent of surface enrichment of Cu and a limited surface area coverage by the columnar outer layer which is not the dominant barrier for corrosion protection [28] is insufficient to supress electrochemical reactions.
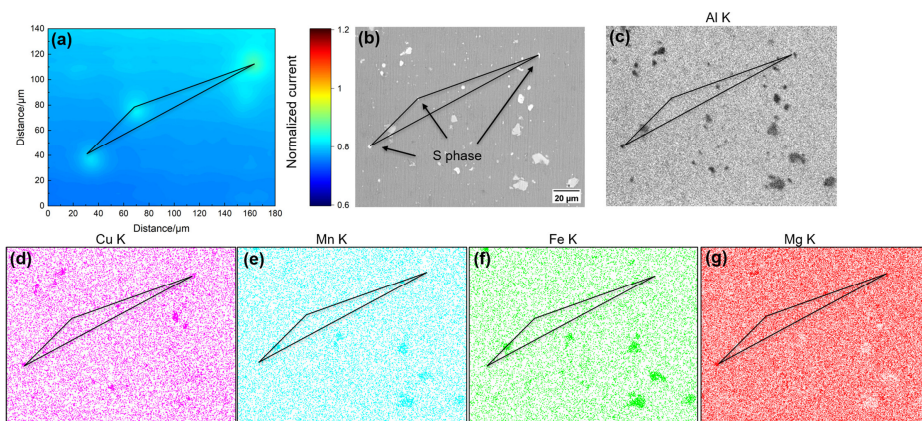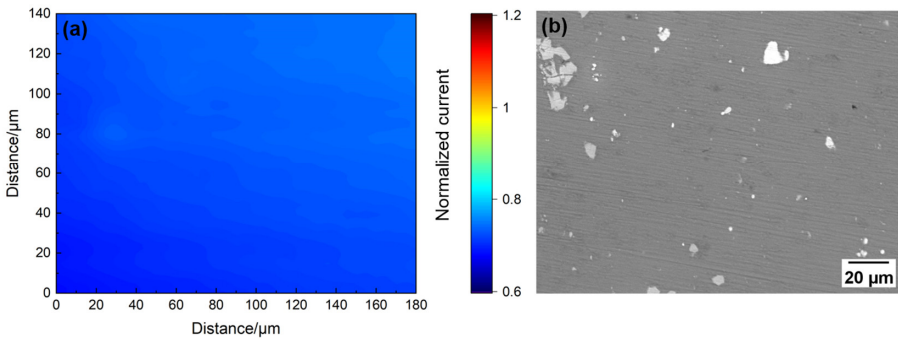
Fig. 5.10 SECM map of AA2024-T3 immersed in the conversion bath for 2000 s obtained at borate buffer solution containing 2 mM FcMeOH (a) and corresponding BEI image (b), and EDX maps for Al (c), Cu (d), Mn (e), Fe (f), Mg (g).

Fig. 5.11 and **Fig. 5.12** show the SECM mapping and the corresponding BEI images for a duration of a lithium-based conversion treatment for 4000 s and 14500 s, respectively. Their EDX results are shown in **Fig. S5.5** and **Fig. S5.6**, respectively. After a longer exposure time, the alloy surface exhibits a homogeneous electrochemical behaviour; the potential difference between all three types of IMPs and the aluminium matrix has now become insignificant. This implies that the lithium-based conversion layer finally reaches a relatively intact and protective state, in which it inhibits electron exchange reactions at the substrate surface. Although it was previously reported that the dense inner layer provides the highest corrosion protection of all sublayers and that the formation of this inner layer is limited over the locations of IMPs [51], the formed layer effectively suppresses electrochemical activity in this case.
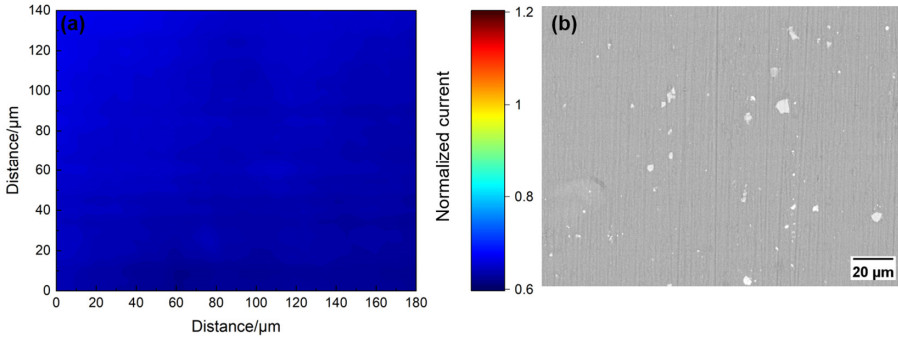
Fig. 5.11 SECM maps of AA2024-T3 immersed in the conversion bath for 4000 s obtained at borate buffer solution containing 2 mM FcMeOH (a) and corresponding BEI image (b).


Fig. 5.12 SECM maps of AA2024-T3 immersed in the conversion bath for 14500 s obtained at borate buffer solution containing 2 mM FcMeOH (a) and corresponding BEI image (b).

Fig. 5.13 shows the SEI images of the alloy surface with different immersion treatments during the last three stages and the corresponding approach curve over the aluminium matrix. The top columnar layer continues to grow at a relatively low speed for longer immersion times. The conversion layer, formed for a duration of at least 2000 s, shows a passive behaviour since the normalized tip current almost reaches zero when the tip virtually contacts the alloy surface. This indicates that the size of the top columnar structure reaches the required dimensions to hinder electrochemical reactions occurring on the alloy surface.
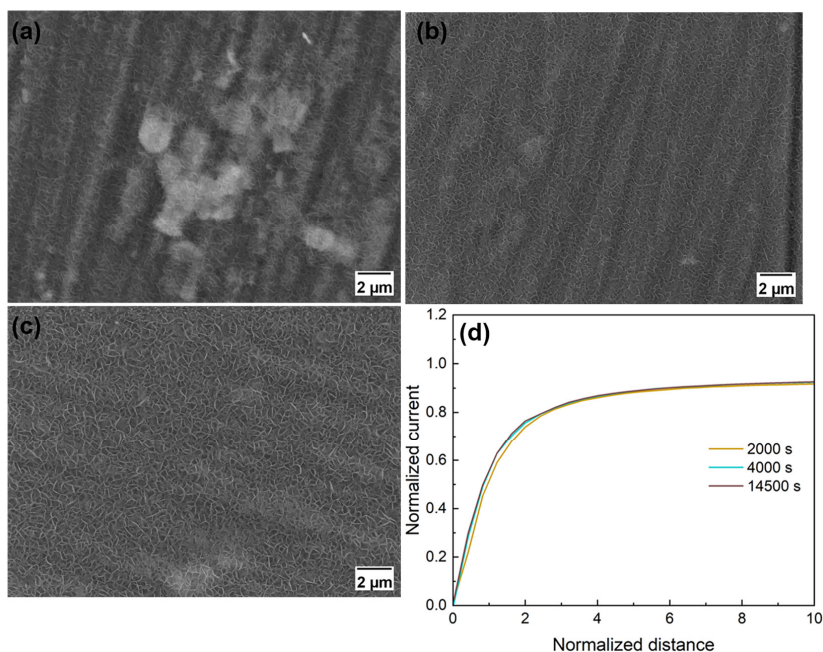
Fig. 5.13 SEM images for samples with a conversion treatment for 2000 s (a), 4000 s (b), and 14500 s (c), and probe approach curves over the conversion layer correspondingly in a borate butter solution containing 2 mM FcMeOH (d).

Finally, SECM mapping and morphological observations can be linked to the EN measurement of the formation process of the lithium-based conversion layer which was reported previously [32]. As shown in **Fig. 5.14**, early stages I and II represent a rapidly changing system; the potential difference between the aluminium matrix and IMPs varies considerably, generating large amounts of current transients simultaneously [32]. Later, from stage III onwards, the potential difference gradually decreases and finally becomes negligible. Correspondingly, both the intensity and the number of current transients gradually diminish as well.
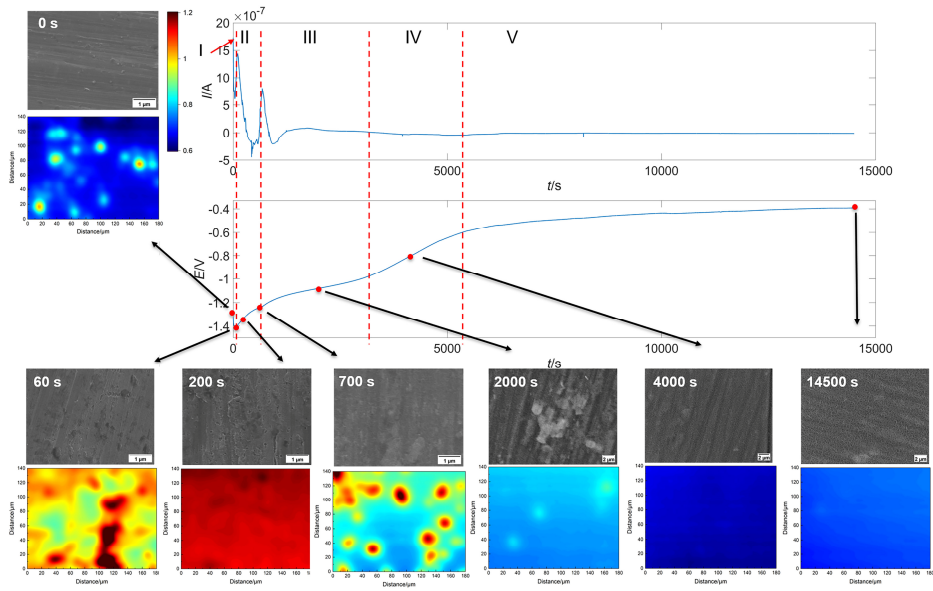
Fig. 5.14 Integral EN, SEM and SECM characterization results of the different stages of the formation process of a lithium-based conversion layer immersed in a 0.01 M NaCl and 0.01 M Li₂CO₃ solution for a duration of 14500 s. The round red markers indicate seven selected time points for analysis. The EN data originates from Chapter 3 [32].

5.3.4. The effect of hydrogen evolution on the protectiveness of the conversion layer. Previous work has revealed that hydrogen bubbles generated from hydrogen evolution during the conversion layer formation attach to the alloy surface, although some detach from the specimen surface spontaneously [32]. Hydrogen bubbles locally isolate the alloy surface from the conversion bath solution and interrupt the growth of the lithium-based conversion layer. Therefore, a less well-developed conversion layer is formed at these locations, which is detrimental to the local corrosion protective properties. **Fig. 5.15** shows an SECM normalized current map over a bubble-covered area after a lithium-based conversion bath for a duration of 14500 s and matching SEI images. The bubble-covered area can be easily observed before adding the electrolyte to the SECM cell due to apparent colour differences (silvery white in round outline). Clearly, the bubble-covered area shows a higher local electrochemical activity, which indicates that the passivation of this area is less effective. **Fig. 5.15b** presents the morphological characterization and the bubble-covered area is marked by a red dashed line. The enlarged image of the edge bubble-covered area marked by the orange arrow is shown in **Fig. 5.15c** and central area

indicated by the blue arrow in **Fig. 5.15b** is presented in **Fig. 5.15d**. The results show that the size of the petal-like structure of the columnar layer gradually shrinks in the direction toward the central bubble-occupied area (**Fig. 5.15c**). This indicates that the growth of the conversion layer stops at middle stages. As shown in **Fig. 5.15d**, the morphology in the central bubble-covered area is comparable to that of samples after a conversion bath for 700 s whose approach curve still indicates local surface activity, therefore manifesting insufficient passivation [28].
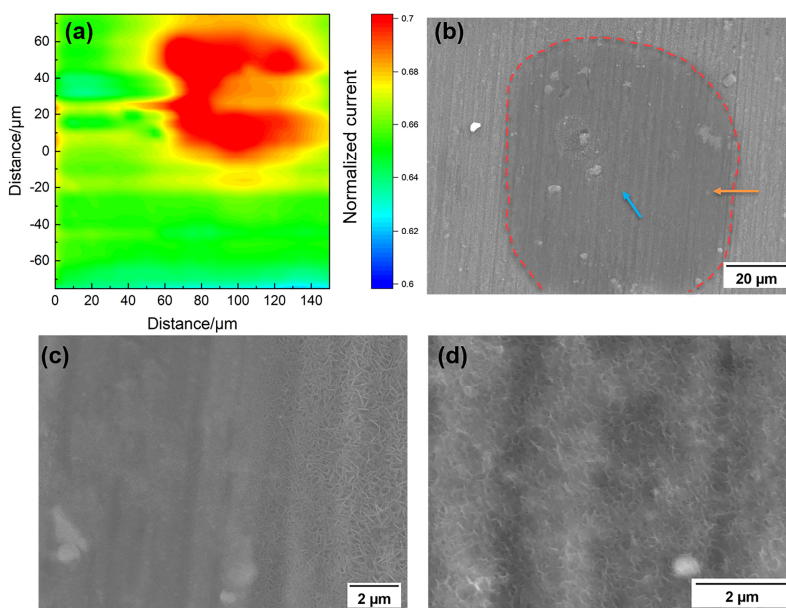
Fig. 5.15 SECM maps for a bubble-covered area of AA2024-T3 immersed in the conversion bath for 14500 s obtained at borate buffer solution containing 2 mM FcMeOH (a) and corresponding SEM images (b), the zoomed-in image in Fig. 15 (b) along the orange arrow (c), and the zoomed-in image in Fig. 5.15 (b) indicated by the blue arrow (d).

5.4. Conclusion

The local electrochemical behaviour of the alloy surface at and around IMPs at different stages of the formation process of the conversion layer at micrometre level was studied with SECM. At early stages (Stage I and II), the alloy surface does not show passivation but presents a rapidly changing characteristic. This largely dynamic system originates from the varying electrochemical potential differences at IMPs and that between the aluminium matrix and IMPs. At the last three stages (III to V), the potential difference gradually diminishes and finally the entire surface is

passivated. During the conversion layer evolution process, the alloy surface experiences a transition from insufficient passivation to activation and then back to passivation. In the beginning, S-, θ- and constituent phases all act as active cathodic sites, and the passivation process of θ- and constituent phases precedes that of the S phase due to their higher electrochemical stability. The differences in electrochemical properties at the IMPs and between the aluminium matrix and IMPs lead to the formation of distinct structures of the protective layers covering the aluminium matrix and the IMPs. The evaluation of their protectiveness against corrosion over time requires further study. As a final remark, hydrogen bubbles are shown to be detrimental to the growth of the conversion layer in case these attach to the alloy surface at the early stages of the conversion process.

References

[1]   N. L. Sukiman, X. Zhou, N. Birbilis, A.E. Hughes, J.M. C. Mol, S. J., X. Zhou, G. E., Durability and Corrosion of Aluminium and Its Alloys: Overview, Property Space, Techniques and Developments, in: Z. Ahmad (Ed.), Alum. Alloys - New Trends Fabr. Appl., InTech, 2012.

[2]   A. E., N. Birbilis, J. M.C., S. J., X. Zhou, G. E., High Strength Al-Alloys: Microstructure, Corrosion and Principles of Protection, in: Z. Ahmad (Ed.), Recent Trends Process. Degrad. Alum. Alloys, InTech, 2011.

[3]   A.E. Hughes, C. MacRae, N. Wilson, A. Torpy, T.H. Muster, A.M. Glenn, Sheet AA2024-T3: a new investigation of microstructure and composition, Surf. Interface Anal. 42 (2010) 334–338.

[4]   A. Boag, A.E. Hughes, N.C. Wilson, A. Torpy, C.M. MacRae, A.M. Glenn, T.H. Muster, How complex is the microstructure of AA2024-T3?, Corros. Sci. 51 (2009) 1565–1568.

[5]   N. Birbilis, Y.M. Zhu, S.K. Kairy, M.A. Glenn, J.-F. Nie, A.J. Morton, Y. Gonzalez-Garcia, H. Terryn, J.M.C. Mol, A.E. Hughes, A closer look at constituent induced localised corrosion in Al-Cu-Mg alloys, Corros. Sci. 113 (2016) 160–171.

[6]   A. Kosari, F. Tichelaar, P. Visser, H. Zandbergen, H. Terryn, J.M.C. Mol, Dealloying-driven local corrosion by intermetallic constituent particles and dispersoids in aerospace aluminium alloys, Corros. Sci. 177 (2020) 108947.

[7]   P. Visser, H. Terryn, J.M.C. Mol, Aerospace Coatings, in: A.E. Hughes, J.M.C. Mol, M.L. Zheludkevich, R.G. Buchheit (Eds.), Act. Prot. Coat. New-Gener. Coat. Met., Springer Netherlands, Dordrecht, 2016: pp. 315–372.

[8]   A.E. Hughes, J.M.C. Mol, M.L. Zheludkevich, R.G. Buchheit, eds., Active Protective Coatings: New-Generation Coatings for Metals, Springer Netherlands, Dordrecht, 2016.

[9]   R.G. Buchheit, R.K. Boger, M.C. Carroll, R.M. Leard, C. Paglia, J.L. Searles, The electrochemistry of intermetallic particles and localized corrosion in Al alloys, JOM. 53 (2001) 29–33.

[10]   N. Birbilis, R.G. Buchheit, Electrochemical Characteristics of Intermetallic Phases in Aluminum Alloys: An Experimental Survey and Discussion, J. Electrochem. Soc. 152 (2005) B140.

[11]   I. Milošev, G.S. Frankel, Review—Conversion Coatings Based on Zirconium and/or Titanium, J. Electrochem. Soc. 165 (2018) C127.

[12]   M. Becker, Chromate-free chemical conversion coatings for aluminum alloys, Corros. Rev. 37 (2019) 321–342.

[13]   P. Santa Coloma, U. Izagirre, Y. Belaustegi, J.B. Jorcin, F.J. Cano, N. Lapeña, Chromium-free conversion coatings based on inorganic salts (Zr/Ti/Mn/Mo) for

aluminum alloys used in aircraft applications, Appl. Surf. Sci. 345 (2015) 24–35.

[14] P. Visser, S.A. Hayes, Anti-corrosive coating composition, WIP Organ. Ed WO. 112605 (2010) A1.

[15] P. Visser, H. Terryn, J.M.C. Mol, Active corrosion protection of various aluminium alloys by lithium-leaching coatings, Surf. Interface Anal. 51 (2019) 1276–1287.

[16] P. Visser, Y. Liu, X. Zhou, T. Hashimoto, G.E. Thompson, S.B. Lyon, L.G.J. van der Ven, A.J.M.C. Mol, H.A. Terryn, The corrosion protection of AA2024-T3 aluminium alloy by leaching of lithium-containing salts from organic coatings, Faraday Discuss. 180 (2015) 511–526.

[17] P. Visser, H. Terryn, J.M.C. Mol, On the importance of irreversibility of corrosion inhibitors for active coating protection of AA2024-T3, Corros. Sci. 140 (2018) 272–285.

[18] J. Gui, T.M. Devine, Influence of lithium on the corrosion of aluminum, Scr Met. U. S. 21:6 (1987).

[19] C.M. Rangel, M.A. Travassos, The passivation of aluminium in lithium carbonate/bicarbonate solutions, Corros. Sci. 33 (1992) 327–343.

[20] C.M. Rangel, M.A. Travassos, Li-based conversion coatings on aluminium: An electrochemical study of coating formation and growth, Surf. Coat. Technol. 200 (2006) 5823–5828.

[21] G.R. Williams, D. O'Hare, A Kinetic Study of the Intercalation of Lithium Salts into Al(OH)3, J. Phys. Chem. B. 110 (2006) 10619–10629.

[22] C.A. Drewien, M.O. Eatough, D.R. Tallant, C.R. Hills, R.G. Buchheit, Lithium-aluminum-carbonate-hydroxide hydrate coatings on aluminum alloys: Composition, structure, and processing bath chemistry, J. Mater. Res. 11 (1996) 1507–1513.

[23] R.G. Buchheit, M.D. Bode, G.E. Stoner, Corrosion-Resistant, Chromate-Free Talc Coatings for Aluminum, CORROSION. 50 (1994) 205–214.

[24] P. Visser, A. Lutz, J.M.C. Mol, H. Terryn, Study of the formation of a protective layer in a defect from lithium-leaching organic coatings, Prog. Org. Coat. 99 (2016) 80–90.

[25] K. Marcoen, P. Visser, G.F. Trindade, M.-L. Abel, J.F. Watts, J.M.C. Mol, H. Terryn, T. Hauffman, Compositional study of a corrosion protective layer formed by leachable lithium salts in a coating defect on AA2024-T3 aluminium alloys, Prog. Org. Coat. 119 (2018) 65–75.

[26] M. Meeusen, P. Visser, L. Fernández Macía, A. Hubin, H. Terryn, J.M.C. Mol, The use of odd random phase electrochemical impedance spectroscopy to study lithium-based corrosion inhibition by active protective coatings, Electrochimica Acta. 278 (2018) 363–373.

[27] J.S. Laird, P. Visser, S. Ranade, A.E. Hughes, H. Terryn, J.M.C. Mol, Li leaching

from Lithium Carbonate-primer: An emerging perspective of transport pathway development, Prog. Org. Coat. 134 (2019) 103–118.

[28] P. Visser, Y. Gonzalez-Garcia, J.M.C. Mol, H. Terryn, Mechanism of Passive Layer Formation on AA2024-T3 from Alkaline Lithium Carbonate Solutions in the Presence of Sodium Chloride, J. Electrochem. Soc. 165 (2018) C60–C70.

[29] A. Kosari, P. Visser, F. Tichelaar, S. Eswara, J.-N. Audinot, T. Wirtz, H. Zandbergen, H. Terryn, J.M.C. Mol, Cross-sectional characterization of the conversion layer formed on AA2024-T3 by a lithium-leaching coating, Appl. Surf. Sci. 512 (2020) 145665.

[30] P. Visser, M. Meeusen, Y. Gonzalez-Garcia, H. Terryn, J.M.C. Mol, Electrochemical Evaluation of Corrosion Inhibiting Layers Formed in a Defect from Lithium-Leaching Organic Coatings, J. Electrochem. Soc. 164 (2017) C396–C406.

[31] Y. Liu, P. Visser, X. Zhou, S.B. Lyon, T. Hashimoto, M. Curioni, A. Gholinia, G.E. Thompson, G. Smyth, S.R. Gibbon, D. Graham, J.M.C. Mol, H. Terryn, Protective Film Formation on AA2024-T3 Aluminum Alloy by Leaching of Lithium Carbonate from an Organic Coating, J. Electrochem. Soc. 163 (2015) C45.

[32] Z. Li, A. Homborg, Y. Gonzalez-Garcia, A. Kosari, P. Visser, A. Mol, Evaluation of the formation and protectiveness of a lithium-based conversion layer using electrochemical noise, Electrochimica Acta. 426 (2022) 140733.

[33] Z. Li, A. Homborg, Y. Gonzalez-Garcia, P. Visser, M. Soleimani, A. Mol, The Effect of Ambient Ageing on the Corrosion Protective Properties of a Lithium-Based Conversion Layer, J. Electrochem. Soc. 170 (2023) 031504.

[34] A. Boag, A.E. Hughes, A.M. Glenn, T.H. Muster, D. McCulloch, Corrosion of AA2024-T3 Part I: Localised corrosion of isolated IM particles, Corros. Sci. 53 (2011) 17–26.

[35] A.E. Hughes, A. Boag, A.M. Glenn, D. McCulloch, T.H. Muster, C. Ryan, C. Luo, X. Zhou, G.E. Thompson, Corrosion of AA2024-T3 Part II: Co-operative corrosion, Corros. Sci. 53 (2011) 27–39.

[36] A.M. Glenn, T.H. Muster, C. Luo, X. Zhou, G.E. Thompson, A. Boag, A.E. Hughes, Corrosion of AA2024-T3 Part III: Propagation, Corros. Sci. 53 (2011) 40–50.

[37] A. Kosari, H. Zandbergen, F. Tichelaar, P. Visser, P. Taheri, H. Terryn, J.M.C. Mol, In-situ nanoscopic observations of dealloying-driven local corrosion from surface initiation to in-depth propagation, Corros. Sci. 177 (2020) 108912.

[38] D. Polcari, P. Dauphin-Ducharme, J. Mauzeroll, Scanning Electrochemical Microscopy: A Comprehensive Review of Experimental Parameters from 1989 to 2015, Chem. Rev. 116 (2016) 13234–13278.

[39] A. Singh, Y. Lin, W. Liu, S. Yu, J. Pan, C. Ren, D. Kuanhai, Plant derived cationic dye as an effective corrosion inhibitor for 7075 aluminum alloy in 3.5% NaCl solution, J. Ind. Eng. Chem. 20 (2014) 4276–4285.

[40] M.B. Jensen, A. Guerard, D.E. Tallman, G.P. Bierwagen, Studies of Electron Transfer at Aluminum Alloy Surfaces by Scanning Electrochemical Microscopy, J. Electrochem. Soc. (n.d.).

[41] J.C. Seegmiller, D.A. Buttry, A SECM Study of Heterogeneous Redox Activity at AA2024 Surfaces, J. Electrochem. Soc. 150 (2003) B413.

[42] V. Upadhyay, D. Battocchi, Localized electrochemical characterization of organic coatings: A brief review, Prog. Org. Coat. 99 (2016) 365–377.

[43] M.B. Jensen, M.J. Peterson, N. Jadhav, V.J. Gelling, SECM investigation of corrosion inhibition by tungstate- and vanadate-doped polypyrrole/aluminum flake composite coatings on AA2024-T3, Prog. Org. Coat. 77 (2014) 2116–2122.

[44] L. Niu, Y. Yin, W. Guo, M. Lu, R. Qin, S. Chen, Application of scanning electrochemical microscope in the study of corrosion of metals, J. Mater. Sci. 44 (2009) 4511–4521.

[45] H. Konno, S. Kobayashi, H. Takahashi, M. Nagayama, The hydration of barrier oxide films on aluminium and its inhibition by chromate and phosphate ions, Corros. Sci. 22 (1982) 913–923.

[46] S. Guo, J. J. Leavitt, X. Zhou, E. Lahti, J. Zhang, Corrosion of aluminium alloy 1100 in post-LOCA solutions of a nuclear reactor, RSC Adv. 6 (2016) 44119–44128.

[47] S. Doulami, K. Beligiannis, Th. Dimogerontakis, V. Ninni, I. Tsangaraki-Kaplanoglou, The influence of some triphenylmethane compounds on the corrosion inhibition of aluminium, Corros. Sci. 46 (2004) 1765–1776.

[48] A.M. Homborg, T. Tinga, X. Zhang, E.P.M. van Westing, P.J. Oonincx, J.H.W. de Wit, J.M.C. Mol, Time–frequency methods for trend removal in electrochemical noise data, Electrochimica Acta. 70 (2012) 199–209.

[49] Ł. Lentka, J. Smulko, Methods of trend removal in electrochemical noise data – Overview, Measurement. 131 (2019) 569–581.

[50] A.M. Homborg, T. Tinga, E.P.M. van Westing, X. Zhang, G.M. Ferrari, J.H.W. de Wit, J.M.C. Mol, A Critical Appraisal of the Interpretation of Electrochemical Noise for Corrosion Studies, CORROSION. 70 (2014) 971–987.

[51] A. Kosari, F. Tichelaar, P. Visser, H. Zandbergen, H. Terryn, J.M.C. Mol, Laterally-resolved formation mechanism of a lithium-based conversion layer at the matrix and intermetallic particles in aerospace aluminium alloys, Corros. Sci. 190 (2021) 109651.

[52] P. Cornette, S. Zanna, A. Seyeux, D. Costa, P. Marcus, The native oxide film on a model aluminium-copper alloy studied by XPS and ToF-SIMS, Corros. Sci. 174 (2020) 108837.

[53] A. Kosari, M. Ahmadi, F. Tichelaar, P. Visser, Y. Gonzalez-Garcia, H. Zandbergen, H. Terryn, J.M.C. Mol, Editors' Choice—Dealloying-Driven Cerium Precipitation on Intermetallic Particles in Aerospace Aluminium Alloys, J. Electrochem. Soc. 168 (2021) 041505.
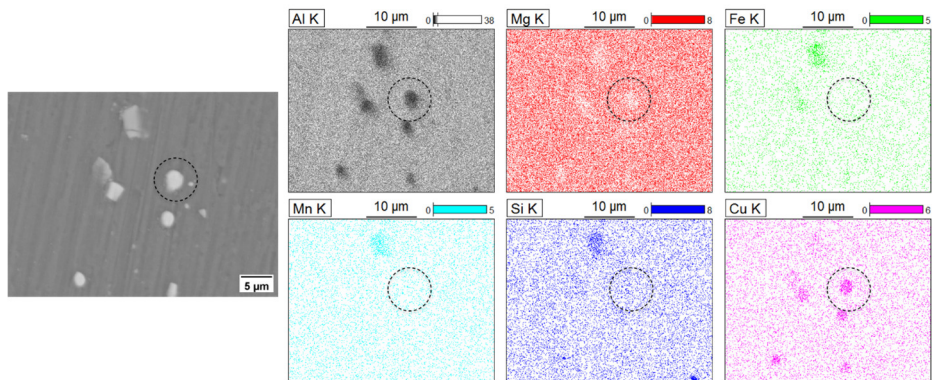
Supplementary Information for Chapter 5
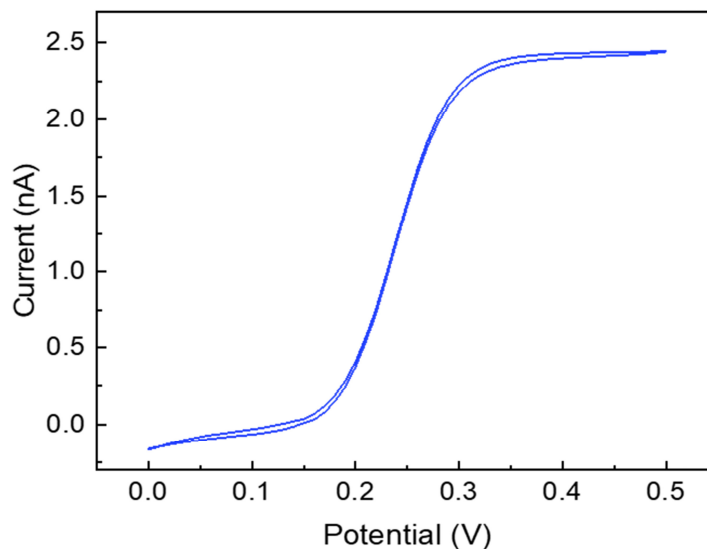
Fig. S5.1 Cyclic voltammetry at 10 μm Pt probe in a borate buffer solution containing 2 mM FcMeOH, pH=7.4, scan rate at 0.01 V/s.
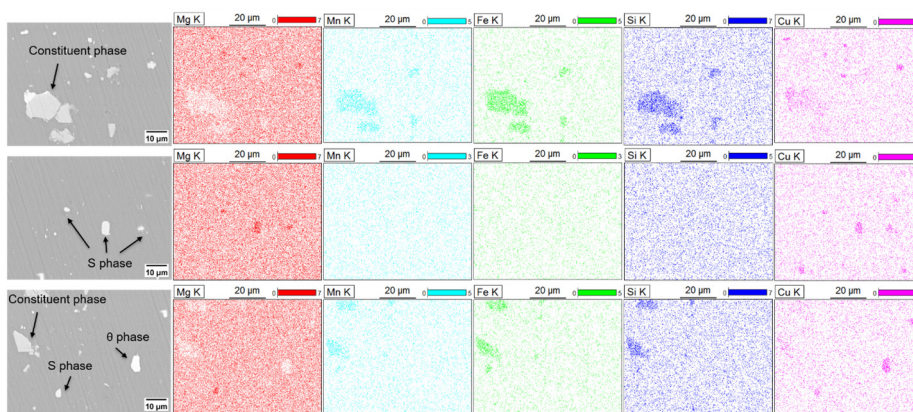
Fig. S5.2 Enlarged BEI images from areas presented in Fig. 3 (a) and corresponding EDX elemental distribution of Mg, Mn, Fe, and Cu.
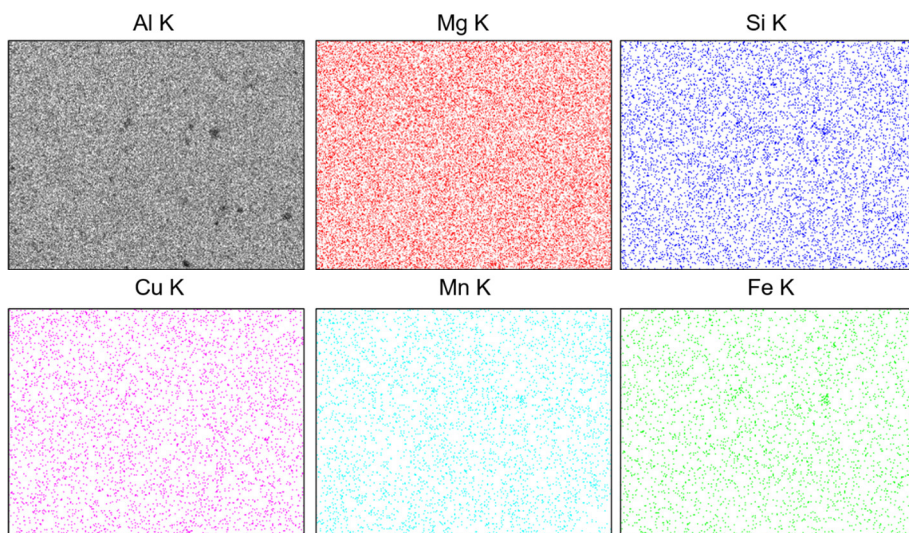
Fig. S5.3 Enlarged BEI images of θ phase (left side) in Fig. 5 (a) and corresponding EDX elemental distribution of Al, Mg, Fe, Mn, Si and Cu.
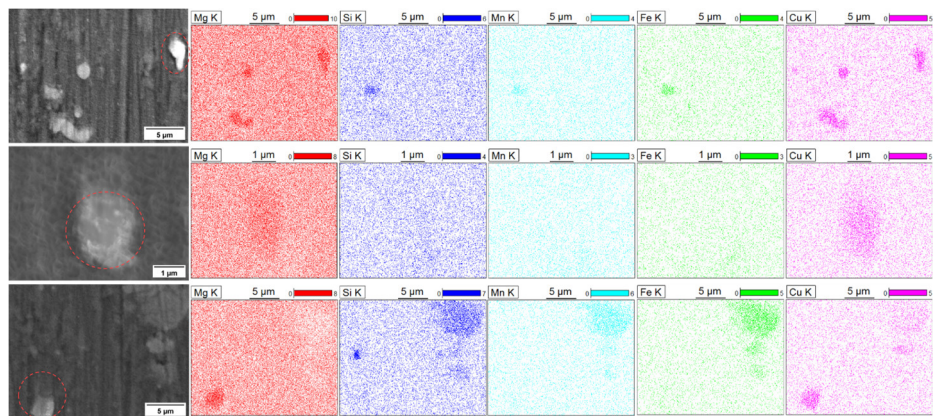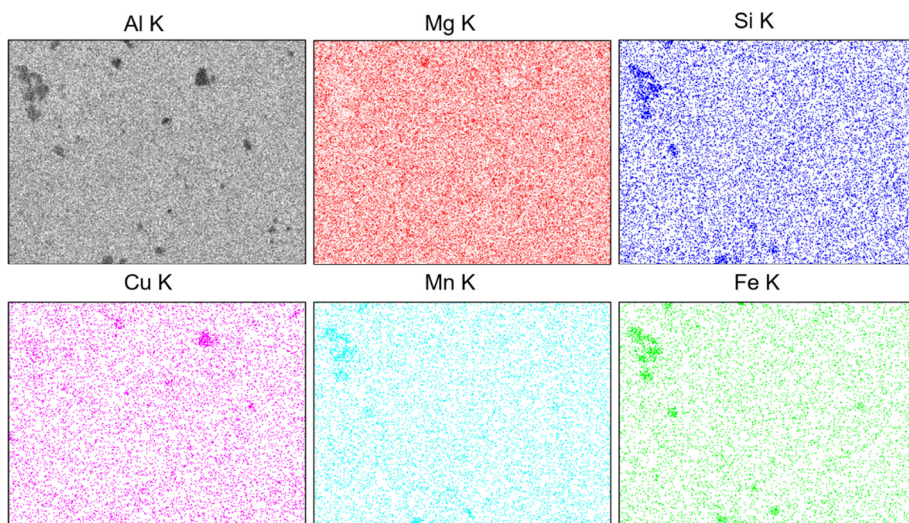

Fig.S5.4 Enlarged SEM images of three active sites (S phase) shown in Fig. 10b and corresponding EDX maps for Mg, Si, Mn, Fe, and Cu.

Fig.S5.5 EDX maps for Al, Mg, Si, Cu, Mn, and Fe elements corresponding to Fig. 11b.

Fig.S5.6 EDX maps for Al, Mg, Si, Cu, Mn, and Fe elements corresponding to Fig. 12b.

CHAPTER 6

Spatiotemporally Resolved Corrosion Protection of AA2024-T3 by a Lithium-based Conversion Layer[1]

Abstract

In this work, the corrosion mechanism of AA2024-T3 covered by a lithium-based conversion layer is studied with high spatial and temporal resolution. Although the entire aluminium alloy surface is protected by a multi-layered conversion layer, areas around intermetallic phases (IMPs) represent weak spots due to an insufficient generation of a protective inner dense layer. For the freshly formed conversion layer, both the top and the inner layer undergo a gradual dissolution upon exposure to relatively dilute NaCl solution within 2 h due to their chemical instability. In the case of the ambiently-aged conversion layer, most corrosion activity around IMPs is related to the S-phase and large constituent phases, due to the active nature of the former and the lower conversion layer quality for the latter. Moreover, S-phase-related corrosion activity lasts approximately 8 h due to fast dissolution whereas reactions induced by large constituent particles remain active over the entire re-immersion period of 12 h.

Keywords: Lithium inhibitor, SECM, electrochemical noise, aluminium alloy, AA2024-T3, conversion coating

6.1. Introduction

Aerospace aluminium alloys exhibit a high strength-to-weight ratio, favourable elastic modulus and cost-efficiency, which led to their widespread application in the aerospace industry [1–4]. However, due to their intricate microstructural heterogeneity, aerospace aluminium alloys are inherently vulnerable to localized corrosion. This necessitates the implementation of effective and active protection measures throughout their operational lifespan [5–7]. For decades, effective and reliable active protection has been achieved through the utilization of chromate-based conversion and organic coatings [8–11]. However, given its toxic and carcinogenic properties, an imperative has emerged for its substitution with chromate-free systems in response to the progressively stringent international health and safety regulations [12]. Consequently, there has been a growing focus on the advancement of alternative inhibitors that comply with current environmental, health, safety and sustainability regulations and can provide cost-effective, reliable and long-lasting corrosion protection.

In general, the exploration of chromate-free coating schemes for industrial applications can be divided into two categories: chromate-free conversion bath treatments and chromate-free organic coatings [13–16]. Based on the dominant chemical components for inhibition, these proposed strategies can be categorised into trivalent chromium [17,18], zirconium-based systems [14,19], transition metal oxyanion additives [20–22], rare earth-based compounds [23,24] and lithium salts [25–27]. Among these options studied, lithium salts have the merit of acting both as chemicals for conversion baths [28–30] and as compounds that are leachable from organic coatings [31–33]. The former was discovered in the 1980s when Gui et al. [30] generated a Li-based conversion layer on AA6061-T6 by anodic polarization. The latter application of lithium salts was first proposed by Visser and Hayes [34] as a leaching inhibitor from organic primers and has been considered as promising for the replacement of traditional hexavalent chromate-based inhibitors [15]. The anion of lithium salts like lithium carbonate or lithium oxalate can generate an alkaline environment (pH 9-11) in a liquid environment [35], promoting the removal of the natural oxide layer, the dissolution of the aluminium matrix and finally the precipitation of a protective layer in the presence of lithium. Lithium ions play a pivotal role in the stabilization of reaction products, leading to the gradual formation of a multi-levelled and robust barrier layer [26]. This protective layer is usually of a bilayer nature, formed in a lithium-containing conversion bath. A bilayer structure including a top columnar lithium/aluminium (Li/Al) layered double hydroxide (LDH)

layer and an inner dense lithium-containing pseudoboehmite (Li-pseudoboehmite) layer forms on the aluminium matrix.

In contrast, only a columnar layer is observed over IMPs (S-, θ- and constituent phases) [36]. At coating defect areas of lithium leaching organic coatings, a bilayer or triple layer (including an extra middle porous sublayer) configuration is typically formed since the local chemistry and pH from a leaching system is much more complex and dynamic [32,36]. Li et al. have presented a detailed summary of the protective layer formation mechanism in a recent review [37].

Various alloying elements and thermomechanical processing treatments contribute to a highly heterogeneous microstructure and the formation of intermetallic phases/particles (IMPs) in the bulk and at the surface of aluminium alloys [1]. The presence of IMPs significantly influences the conversion layer growth at and around IMPs at the aluminium alloy surface due to the distinct chemical interaction between the IMPs and the adjacent aluminium matrix [38,39]. Waldrop et al. [39] observed that the nucleation rate during the chromate conversion coating (CCC) on AA2024-T3 was different on various types of IMPs: the growth rate at IMPs with higher copper content was lower. Campestrini et al. [8,40] reported the negative effect of IMPs on the corrosion protection of CCC for AA2024-T3 due to the formation of large defects near IMPs. Šekularac et al. [41] studied zirconium conversion coating formation and the corrosion resistance on aluminium alloys of series 1xxx up to 7xxx. The results showed that copper rich-IMPs in AA2024-T3 were detrimental to the generation of a uniform conversion layer. The conversion layer was significantly thicker at Cu-rich IMPs than that over the matrix. For the case of AA7075-T6, although a uniform conversion layer was produced, zinc-rich areas were highly vulnerable to pitting corrosion when exposed to a NaCl solution. Up to now, already a proper understanding of the structure, morphology and composition of the lithium-based conversion layer on AA2024-T3 has been achieved [36,42]. In addition, our previous work has reported multiple types of experiments to evaluate the corrosion protective behaviour of a lithium-based conversion layer using traditional accelerated exposure and electrochemical characterization including salt spray testing, potentiodynamic polarization and electrochemical impedance spectroscopy (EIS) [43–45]. However, a detailed investigation at the microscale of the corrosion mechanism of lithium-based conversion coated AA2024-T3 is still missing. A profound understanding of the corrosion mechanism at the level of IMPs is of pivotal

importance to optimize the lithium-based conversion process and its further development towards a sustainable green corrosion protection technology.

Although IMPs in aerospace aluminium alloys contribute significantly to the improvement of their mechanical properties due to the generation of a heterogeneous microstructure, the same heterogeneity also governs a reduced local corrosion resistance of these alloys [5–7]. Therefore, it is of pivotal importance to investigate the mechanistic role of IMPs in local corrosion protection within corrosion inhibition strategies. This study is devoted to elucidating the corrosion mechanism of a lithium-based conversion coated AA2024-T3 at both IMPs and the aluminium matrix at high spatial and temporal resolution. Top-view and cross-sectional micrographs were obtained by focused ion beam-scanning electron microscopy (FIB-SEM) to compare the morphological and compositional variation before and after exposure to a corrosive NaCl solution. Electrochemical noise (EN) analysis was adopted to monitor the electrochemical signature resulting from localized corrosion in real time during exposure. Unlike traditional EIS which records electrochemical information at several discrete time points, the EN technique enables continuous and time-resolved monitoring of electrochemical reactions without external perturbation. This capacity is of vital importance in identifying relatively rapid electrochemical reactions such as those related to localized corrosion events. Scanning electrochemical microscopy (SECM) technique in feedback operation mode was applied to study the localized corrosion with high spatial resolution.

6.2. Materials and methods

6.2.1. Materials and experimental set-up. All the material used in this work originated from a single commercial AA2024-T3 sheet acquired from Goodfellow, with a thickness of 0.8 mm. Square specimens measuring 20 mm × 20 mm were fabricated from the aforementioned sheet. All specimens were ground up to grit 4000 SiC abrasive paper, then underwent subsequent gentle cleaning with distilled water, drying through compressed air and were subsequently left in an ambient laboratory environment for 24 hours preceding the experiments. For all samples, water-proof tape was used to cover the surfaces with a circular opening of 10 mm in diameter to affix and restrict the exposed surface area. Laboratory-grade chemicals used in this work were ordered from Sigma-Aldrich (St. Louis, MO, USA).

The detailed experimental procedure is shown in **Fig. 6.1**. The lithium-based conversion layer was firstly fabricated in a 0.01 M NaCl and 0.01 M Li_2CO_3 (pH

10.9) solution for an immersion duration of 7 h. This immersion duration was selected in order to be consistent with a previous work and to allow a relatively mature lithium-based conversion layer to be formed [36]. An electrolyte layer of 4 mm in height, equivalent to a volume of 0.321 ml at a diameter of a circular exposed surface of 10 mm, was established in the experimental sets to replicate the specific liquid environment within a 1mm width artificial defect inside an organic coating loaded with lithium inhibitors [42]. The prepared conversion coatings were divided into two groups: (i) the freshly-formed lithium-based conversion layer was evaluated using EN measurements and SEM whereas (ii) the 36 h ambiently-aged samples were studied using EN, SEM and SECM. Ambiently-aged samples were adopted here to reduce the interference of the dissolution of the freshly formed conversion layer with subsequent SECM measurements. Before subsequent re-immersion measurements, both types of samples were gently cleaned with distilled water and dried with cold compressed air. For re-immersion tests, the exposed surface was 1 mm in diameter, with the addition of 2 mL 0.01 M NaCl. For SECM measurements, 2 mM FcMeOH was added as the redox mediator. The exposed areas were examined using optical microscopy in order to guarantee the absence of visually large defects. The two types of the lithium-based conversion layers were measured by EN for a duration of 12 h. After re-immersion, samples were gently washed with distilled water and subsequently observed using the SEM. All experiments were performed under open-to-air conditions.
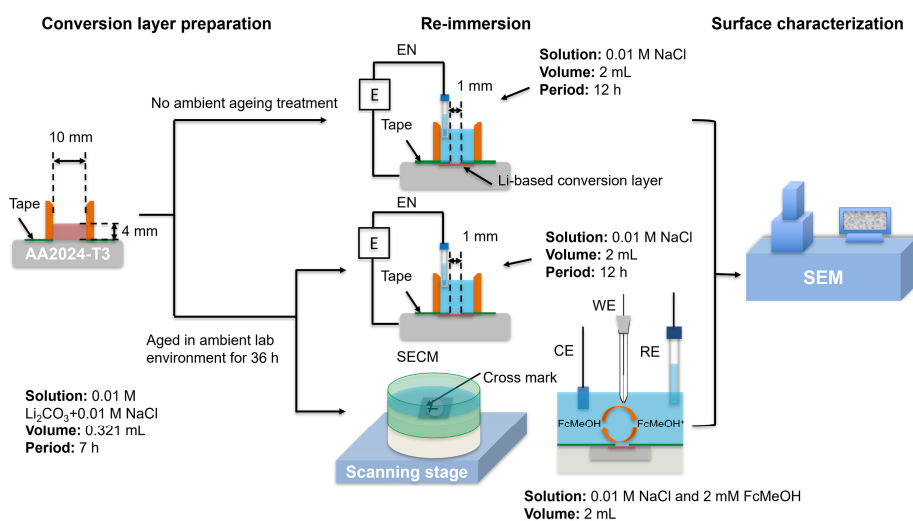
Fig. 6.1 Schematic overview of the experimental procedure.

6.2.2. Focused ion beam-scanning electron microscopy (FIB-SEM) characterization. In order to study the corrosion protection mechanism of the lithium-based conversion layer as a function of exposure time, a series of cross-sectioning measurements were performed using a FIB-SEM (Helios G4 PFIB UXe, Thermo Fisher Scientific, USA) equipped with a xenon plasma focused ion beam (PFIB), employing an accelerating voltage of 30 kV. The top-view and cross-sectional SEM characterizations were conducted at 20 keV collecting emitted secondary electrons (SE) in ultra-high-resolution mode. The chemical composition of distinct regions was assessed through Energy Dispersive Spectroscopy (EDS). It is noteworthy that, in order to mitigate the risk of potential damage to the lithium-based conversion layer, a protective Pt or C overlay coating was deposited before milling.

6.2.3. Electrochemical noise (EN) measurements and analysis. For the EN experiments, a two-electrode configuration was used in this work. Therefore, only potential signals were monitored. Electrical connection was established using a Cu tape connected to the working electrode. The reference electrode (RE) used for EN was an Ag/AgCl, saturated KCl electrode and all potential values presented are with respect to this reference unless stated differently. All EN measurements were conducted under open-circuit potential (OCP) conditions. A Compactstat (Ivium Technologies) was used to record the potential signals. A Faradaic cage was utilized to position the Compactstat as well as the electrochemical cell, thereby mitigating potential interference from external electromagnetic sources. The sampling frequency was set at 20 Hz and a low-pass filter of 10 Hz was used to avoid aliasing. The EN data were analysed using Matlab from MathWorks. All EN measurements were performed at least in triplicate.

In the EN potential signal, a DC component becomes unavoidable owing to the nonlinear and non-stationary corrosion system. The DC drift is reflected from the varying mean OCP value. The DC component, devoid of meaningful information, introduces false low frequencies and poses a potential interference in signal processing [46,47]. Consequently, effective removal of the DC trend is necessary, while concurrently preserving pertinent data to the greatest extent before subsequent analysis. Prior investigations have suggested different strategies for trend removal, like moving average, polynomial and linear trend removal, wavelet analysis and empirical mode decomposition [46,47]. In this work, a time-frequency trend removal was adopted using empirical mode decomposition (EMD), after which the signal was

analysed using the Hilbert–Huang transform (HHT). EMD is a data analysis technique used in signal processing, which is particularly useful for analysing non-linear and non-stationary signals [48]. The fundamental concept of EMD indicates that a given signal can be dissected into a series of Intrinsic Mode Functions (IMFs). These IMFs are elemental constituents expressing distinct frequency bands inherent to the process under investigation. The decomposition procedure involves the repeated extraction of IMFs through a sifting process, leaving behind a residue after each iteration [49]. The sifting process stops automatically when the residue becomes less than a predefined threshold value of significance, or when it manifests as a single oscillation [50]. EMD precedes HHT: the HHT is applied to each IMF component to obtain instantaneous frequencies and amplitudes at any moment in time [50]. All the amplitudes shown in this work are relative amplitudes of the instantaneous frequencies in the spectrum.

6.2.4. SECM instrumentation and experimental procedures. SECM was executed using Biologic Instruments SECM model M370. A Pt disk ultramicroelectrode (UME), 10 μm in diameter, with an RG (defined as the radius of the insulating glass sheath divided by the radius of the platinum disk) of 5, was purchased from CH Instruments Inc. and was employed as a working electrode. An Ag/AgCl, saturated KCl and a Pt thin plate were used as RE and counter electrode (CE), respectively. For SECM samples, a cross mark was made before the generation of the lithium-based conversion layer to locate the scanned area during SEM observations. Demonstrating exceptional spatial resolution and electrochemical sensing capabilities, SECM proves powerful for characterizing both morphology and the presence of redox reactions at the metal/electrolyte interface [51]. SECM not only provides insights into reaction mechanisms but also facilitates the evaluation of surface reactivity across heterogeneous surface phases [52]. Please note that in this study further specification and distinction of closely positioned anodic and cathodic sites is limited due to the similarity in dimensions of the UME and the microstructural heterogeneities studied. Its application has been widespread in corrosion-related investigations, such as studies on pitting [53,54] and inhibition [55,56]. In this work, the feedback mode was utilized based on the redox mediator FcMeOH. Cyclic voltammetry (CV) was performed to verify the cleanliness of the SECM probe, locating the probe several millimetres above the surface before any SECM measurement. All current signals were normalized using the steady-state current from the CV measurements. The stage was levelled by measuring at least three negative feedback approach curves (not in the same straight line). The levelling and localization of the mark took approximately

30 min before formal SECM mapping. The distance between the tip and the substrate was around 5 μm using a negative feedback curve over the conversion layer. Mapping was performed repeatedly over the same working area of 200 μm × 150 μm with a scanning speed of 10 μm/s, increment steps of 5 μm and waiting time of 0.1 s at each point. The UME was biased at a voltage of 0.5 V to oxidize FcMeOH while the substrate was kept at an OCP state. All experiments were performed under ambient lab conditions, in a solution open to air. Experiments were triplicated to validate reproducibility.

6.3. Results and discussion

6.3.1. SEM characterisation of the conversion layers before re-immersion. **Fig. 6.2** shows the top-view and cross-sectional view of the freshly-formed and 36 h ambiently-aged lithium-based conversion layer and cross-sectional EDS mapping (aluminium and oxygen) at the aluminium matrix. There is no visible difference in morphology between the differently aged samples (**Fig. 6.2a** and **6.2b**). This observation is in contrast to the results reported in Chapter 4 since the sample surface was dried by compressed air in this work whereas the conversion layer studied in Chapter 4 was kept wet. Therefore, the continuous growth of the lithium-based conversion layer was hindered due to the loss of water [57]. **Fig. 6.2c** and **Fig. 6.2d** present the cross-sectional views of 0 h and 36 h aged conversion layers, respectively. A bilayer structure is present including a top columnar layer and an inner dense layer [36,42]. Hence, the ambient ageing process does not seem to affect this dual-layer structure. EDS characterization shown in **Fig. 6.2e-6.2h** presents the elemental distribution of aluminium and oxygen. It is clear that the inner layer is relatively oxygen-rich, which corresponds well with previous reports [58,59].
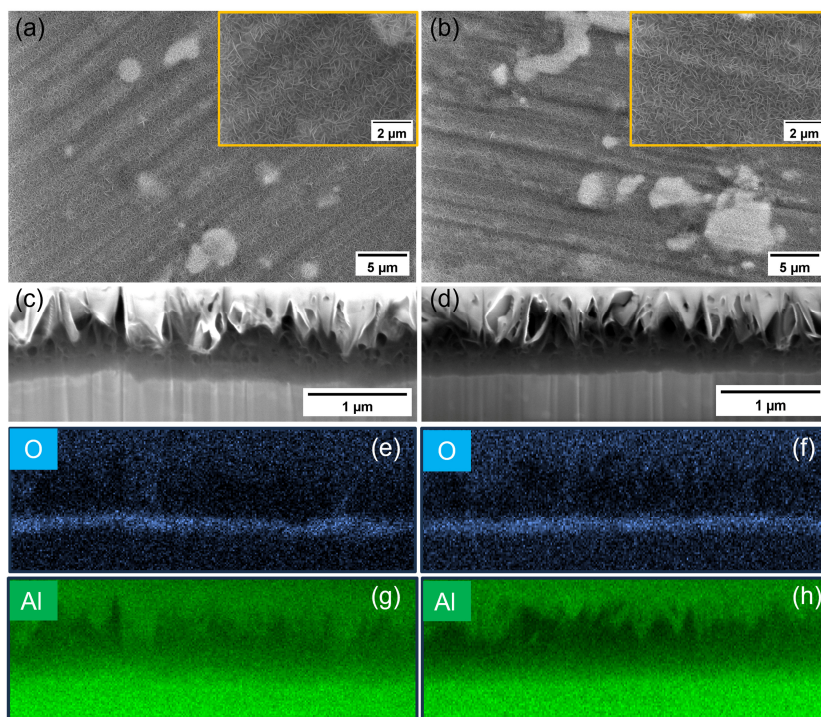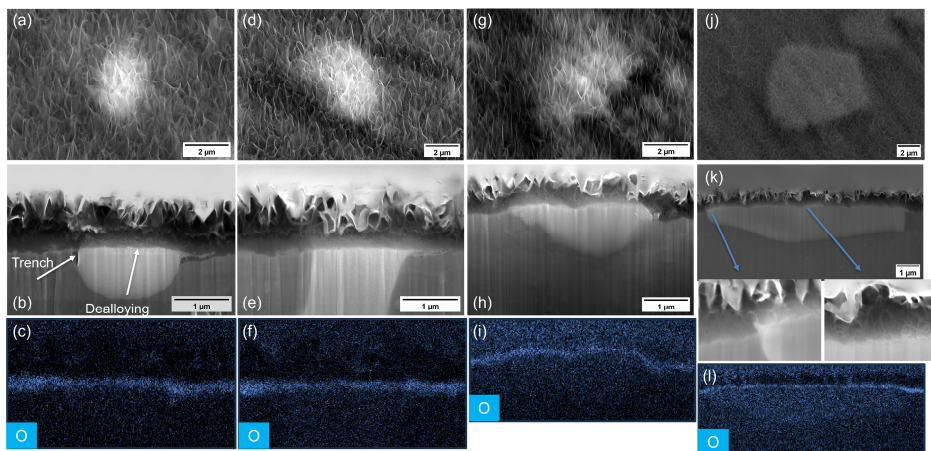
Fig. 6.2 (a, b) Top view, (c, d) cross-sectional view and corresponding EDS mapping of the element (e, f) oxygen and (g, h) aluminium of the lithium-based conversion layer after 0 h and 36 h ambient ageing, respectively.

The conversion layer morphological characterization over the IMPs was considered necessary since IMPs exhibit distinct electrochemical properties as compared to the surrounding aluminium matrix and may therefore result in different conversion layer configurations. In this work, three types of IMPs, involving S-, θ- and constituent phases, are investigated. In **Fig. 6.3**, the top-view, cross-sectional view and oxygen distribution are listed, respectively. The EDS characterization of the listed IMPs is shown in **Fig. S6.1**. **Fig. 6.3a-c** present the case for the S-phase. From the top view, the top columnar layer uniformly covers the surface at and around the S-phase (**Fig. 6.3a**). A detailed chemical conversion layer structure is presented in Fig. **6.3b**. Unlike the bilayer configuration formed over the aluminium matrix, the conversion layer on the S-phase mainly consists of a single columnar layer, accompanied by an incomplete inner dense layer. In addition, obvious trenching and dealloying are observed due to the high chemical instability of the S-phase [60]. The presence of this inner layer can be confirmed by the faint oxygen-rich layer in **Fig. 6.3c**. A similar phenomenon is also observed in the θ-phase (**Fig. 6.3d-f**) as well. For the case of the

constituent particles, two types of cases are revealed here: small (< 2 μm) and large (> 4 μm) constituent phases. As shown in **Fig. 6.3g-i**, the morphology and oxygen distribution for small constituent particles are similar to conversion layer structure features over the S- and θ-phase. However, for the situation of the large constituent phase (**Fig. 6.3j-l**), the columnar layer still uniformly covers the entire top face but the incomplete inner layer is nearly indistinguishable, which is indicated by the relatively low brightness of the oxygen mapping over the particle (**Fig. 6.3l**). The zoomed-in figures of the large constituent phase indicate that only the columnar structure is formed. According to previous studies by Kosari et al. [36], the dual layer structure of the lithium-based conversion layer only appears on the aluminium matrix while a single columnar layer forms on the S-, θ-, and constituent phases. The absence of the inner layer over the IMPs is possibly related to the insufficient supply of aluminium, since aluminium is one of the constituent elements distributed over the entire lithium-based conversion layer [58,59]. The chemically unstable S-phase endures a relatively fast dealloying (mainly magnesium and aluminium) when the aluminium alloy surface is exposed to the aggressive electrolyte [36,38,60] and the dissolved aluminium promotes the top columnar layer formation, even preceding that over the adjacent aluminium matrix [36]. However, the conversion layer growth over more electrochemically stable θ-, and constituent phases is slower than this process over the aluminium matrix, and the supply of aluminium relies on the lateral diffusion of dissolved aluminate ions to generate the columnar layer. The absence of the incomplete inner layer over IMPs in the work of Kosari et al. [36] may be attributed to the different experimental configurations used in that work. Although the ratio of the exposed surface to the volume of electrolyte, the composition of the conversion solution and the immersion duration are identical, the exposed surface in this work is only one-quarter of the size implemented by Kosari et al. [36]. Therefore, the generation of the incomplete inner dense layer observed in this chapter is expected to stem from the lateral diffusion of aluminate ions during the conversion layer formation. Considering that the inner layer is formed below the top columnar layer and also its relatively low growth rate [36,58], for the small particles, the lateral propagation can fully cover the entire surface whereas the large constituent particles cannot be reached within the time of immersion, due to their larger size and larger electrochemical stability. More evidence to support this explanation is the fact that an obvious and complete inner layer was observed over a copper-rich intermetallic particle at a coating defect area of a lithium-leaching organic coating system after exposure to a relatively long 168 h neutral salt spray test [61].
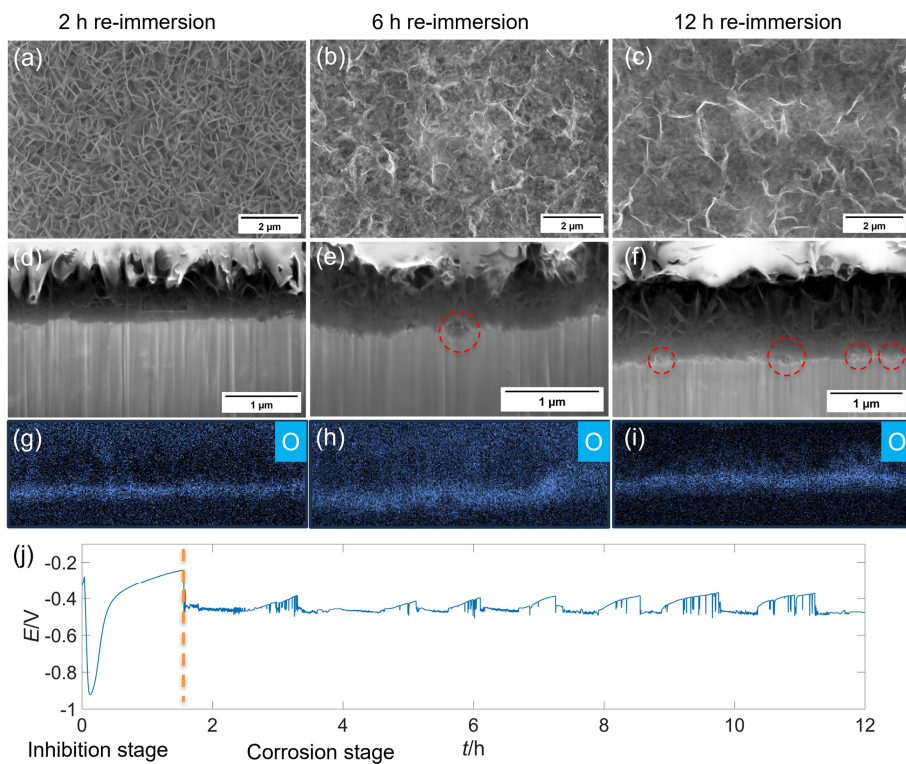
Fig. 6.3 Top view, cross-sectional view and corresponding oxygen distribution for the (a-c) S-phase, (d-f) θ-phase, (g-i) small constituent particle and (j-l) large constituent particle, respectively.

6.3.2. SEM characterization of the conversion layers after re-immersion. Previous works presented in Chapters 3 and 4 have focused on the re-immersion behaviour of the lithium-based conversion layer by exposing the freshly-formed or ambiently-aged conversion layer to a lithium-free NaCl solution [57,62]. However, these studies mainly focused on electrochemical characterization, which was insufficient to understand the corrosion mechanism in relation to specific microstructural heterogeneities. Here, morphological characterization combined with EDS analysis is adopted to elucidate the laterally resolved corrosion protection mechanism of the lithium-based conversion coated AA2024-T3 substrate.

For the freshly formed conversion layer, **Fig. 6.4** shows the top-view, cross-sectional view and oxygen distribution of the aluminium matrix after re-immersion in a lithium-free NaCl solution for 2 h, 6 h, 12 h and the corresponding EN potential signal, respectively. From **Fig. 6.4a-c**, it is clear that the top columnar layer undergoes a gradual decomposition. This instability might be attributed to the reversible intercalation process of the Li/Al LDH top layer [63]. For instance, the de-intercalation process of lithium ions proceeds when a freshly formed Li/Al LDH is exposed to a Li-free solution [64]. This phenomenon was not observed in Chapters 3 and 4 since the solution volume used in previous work is much smaller than that applied here (0.321 ml vs. 2 ml respectively). The rapid increase of the concentration of lithium ions in a small volume of solution gradually hinders a further de-

intercalation of Li/Al LDH. **Fig. 6.4d-f** present the cross-sectional view of the lithium-based conversion layer. Although the bilayer structure is still visible during the 12 h re-immersion, the corrosion attack indicated by the red circles is clearly observable and the number of corrosion sites gradually increases with the re-immersion duration. This can be attributed to corrosive chloride ions penetrating the conversion layer at certain specific sites. **Fig. 6.4g-i** show the corresponding oxygen mapping of **Fig. 6.4d-f**: the gradual drop of the intensity of oxygen in **Fig. 6.4g** (2h re-immersion) and **6.4h** (6 h re-immersion) reveals that the inner layer suffers from damage as well. In Chapter 4 it was presented that the inner dense layer can release lithium carbonate during re-immersion as well, therefore the decreased oxygen intensity might be related to the loss of lithium carbonate from Li-pseudoboehmite. The increased oxygen brightness shown in **Fig. 6.4i** may be caused by the thickening of oxide or hydroxide corrosion products after 12 h re-immersion. **Fig. 6.4j** shows the EN potential signal during re-immersion for the freshly formed conversion layer. As explained in Chapter 4, the entire process can be divided into two stages: the inhibition stage and the corrosion stage. The release of trapped lithium ions contributes to the appearance of the inhibition stage, and this stage gradually ends when the local concentration of lithium ions is below the minimum concentration for effective inhibition [57]. Trenches surrounding IMPs are also observed, but considering that the corrosion mechanism is nearly identical to that over the aged lithium-based conversion layer, a detailed description and explanation of the trench formation will be presented later in section 6.3.5. On the contrary, as shown in **Fig. 6.5**, the top-view characterization of the 36 h ambiently-aged lithium-based conversion layer after 12 h re-immersion (**Fig. 6.5a**) shows little difference as compared to **Fig. 6.2b**. This observation is consistent with the previous finding that ambient ageing is beneficial for the stabilization of the lithium-based conversion layer [57]. **Fig. 6.5b** and **Fig. 6.5c** exhibit the cross-sectional imaging and corresponding oxygen distribution, respectively. It is clear that fewer corrosion sites have originated as compared to that in **Fig. 6.4f** and the oxygen-rich layer is still relatively intact, which indicates enhanced corrosion resistance properties.

Fig. 6.4 Top view of the freshly formed lithium-based conversion layer after re-immersion for a duration of (a) 2 h, (b) 6 h, (c) 12 h; cross-sectional view of the freshly formed conversion layer after re-immersion for (d) 2 h, (e) 6 h, (f) 12 h and (g) corresponding oxygen distribution of 2 h, (h) 6 h, (i) 12 h. (j) EN potential signal during re-immersion for 2h in a 0.01 M NaCl solution.
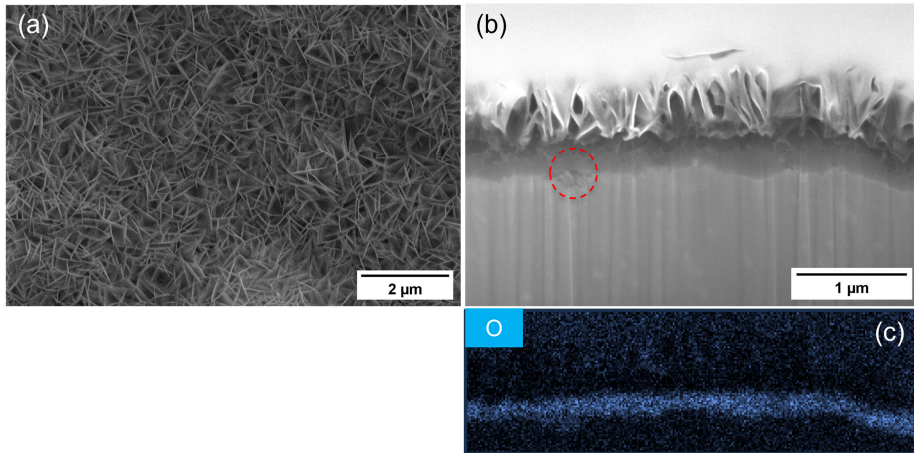
Fig. 6.5 (a) Top view, (b) cross-sectional view and (c) corresponding oxygen distribution mapping of the 36 h ambiently-aged lithium-based conversion layer after 12 h re-immersion in a 0.01 M NaCl solution. The dashed circle indicates localized corrosion underneath the conversion layer.

The corrosion morphology and oxygen mapping at and around IMPs is presented in **Fig. 6.6**. Among the studied specimens, trenches around the S-phase and large constituent particles are mostly observed. The EDS mapping of IMPs shown in **Fig. 6.6** is presented in **Fig. S6.2**. **Fig. 6.6a-c** and **Fig. 6.6d-f** present the top view, cross-sectional view and corresponding oxygen distribution of a constituent particle and a S-phase, respectively. Although the top columnar structure is relatively intact close to the IMP, the corrosion attack already penetrates deep underneath the conversion layer at the area in contact with the IMP. This result indicates that areas adjacent to IMPs are more prone to corrosion attack since the inner dense layer is not fully matured over the IMPs. A partial dealloying is seen in the top region of the constituent phase (**Fig. 6.6b**), whereas the S-phase (**Fig. 6.6e**) is totally dealloyed due to its higher electrochemical activity and smaller size [60]. Oxygen-rich zones (**Fig. 6.6c** and **6.6f**) underneath the conversion layer are mainly located at the aluminium matrix side (corrosion products), which indicates that the aluminium matrix serves as the anodic region. At the same time, IMPs, gaining nobility with dealloying, act as cathodic zones until the final detachment of IMPs from the aluminium matrix. Moreover, the corrosion products shown in **Fig. 6.6e** are thicker as compared to those of **Fig. 6.6b**, suggesting that the galvanic interaction between the matrix and the S-phase is stronger than that of the galvanic couple between the matrix and the constituent particle. **Fig. 6.6g** and **6.6h** show the top view and cross-sectional view

of a large constituent phase at its early corrosion stage, with the cut-out figures of the red dashed circles presented in **Fig. 6.6h1** and **6.6h2**, respectively. This observation clearly shows that the trench initiates from the edges of the IMPs, although any initial indication from the top-view is lacking. The oxygen distribution at the trench (**Fig. 6.6i**) shows that the edge of the constituent particle and the adjacent aluminium matrix underneath the conversion layer are both covered with an oxygen-rich layer, indicating the dealloying zone and aluminium hydroxide, respectively.
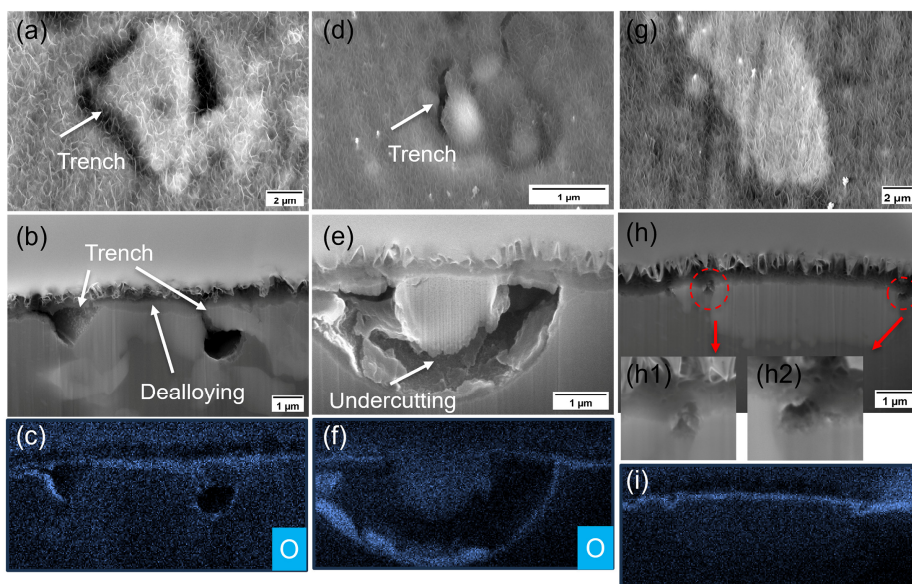

Fig. 6.6 (a) Top view, (b) cross-sectional characterization and (c) corresponding oxygen mapping for a constituent particle with trench from the 36 h ambiently-aged lithium-based conversion layer after 12 h re-immersion in a 0.01 M NaCl solution; (d) top view, (e) cross-sectional characterization and (f) corresponding oxygen mapping for a S-phase with trench from the aged lithium-based conversion layer after 12 h re-immersion; (g) cross-sectional view of a constituent phase at the early stage of trench formation, with (g1) and (g2) cut-outs indicated by the red dashed circles and (i) its corresponding oxygen mapping.

6.3.3. SECM characterization. SECM mapping was performed at a fixed location to monitor the localized corrosion activities over time. SECM imaging of the immersion periods from 0.5-1.5 h, 4.5-5.5 h and 8.5-9.5 h is shown in **Fig. 6.7a**, **6.7b**, and **6.7c**, respectively. The matched SEM figure is presented in **Fig. 6.7d** and its corresponding EDS mapping results are listed in **Fig. S6.3**. Initially, two active sites are detected (marked with numbers 1 and 2), corresponding to the location of two constituent

phases in **Fig. 6.7d**. This finding corresponds well with the results above those constituent particles, especially those with relatively large size, are more vulnerable to corrosion during re-immersion. With a re-immersion duration of 4.5-5.5 h, the two constituent phases remain active but at a lower reactivity. This may be caused by the in-depth penetration of the corrosion front, which hinders the outward diffusion of FcMeOH and the generation of corrosion products which partially cover the active surface. At continued re-immersion (8.5-9.5 h), the region at constituent phase 2 is almost passive and phase 1 still exhibits a very low reactivity. In addition, another active site is observed at the top of **Fig. 6.7c** (marked with 3), again corresponding with the location of a constituent particle. The corrosion related to the S-phase is marked with number 4 but their signal remains undetected by the SECM tip, which may result from the limitation of the tip resolution or the relatively fast corrosion kinetics since one complete surface area mapping takes almost 1 h. The SECM characterization corroborates the findings reported earlier that S-phases and large constituent particles are the weak spots in the lithium-based conversion layer. In addition, the active state of a constituent particle can last for several hours.
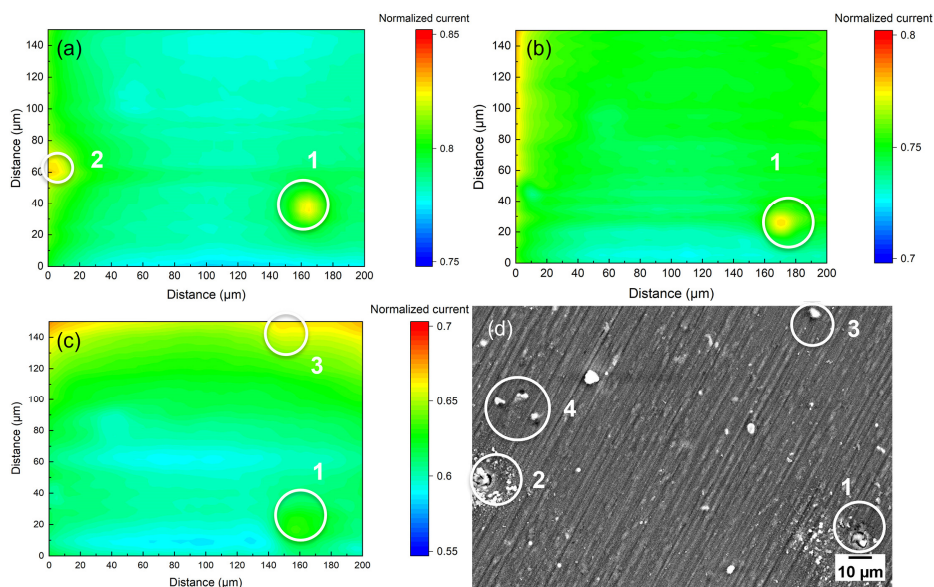
Fig. 6.7 SECM mapping of a fixed scanning area over a 36 h ambiently-aged lithium-based conversion layer during re-immersion in a 0.01 M NaCl electrolyte containing 2 mM FcMeOH. The scanning time duration is (a) 0.5-1.5 h, (b) 4.5-5.5 h, (c) 8.5-9.5 h. (d) Corresponding SEM micrograph.

6.3.4. EN analysis for the ambiently-aged conversion layer. **Fig. 6.8** presents the potential variation of the 36 h ambiently-aged conversion layer under re-immersion conditions for a duration of 12 h in a NaCl solution and the Hilbert spectrum analysis for the timeframes of 10000 s-12000 s, 16000 s-18000 s, 28000 s-30000 s, 33000 s-35000 s, respectively. Unlike the freshly-formed conversion layer, the inhibition stage is indiscernible due to the improved stability after ageing. Initially, the trend of the OCP mainly varies between −0.2 V and −0.5 V with large amplitude transients. At a later stage, the OCP settles at a relatively stable value of −0.4 V (shown in **Fig. 6.8a**). The large OCP variation at the beginning is probably caused by the competition between local penetration of water and chloride ions and re-passivation. It has been reported that LDH layers can act as chloride ion sorbent according to their anion exchange capabilities, which impairs the potential damage by chloride ions at the start of re-immersion [65,66]. In this work, several representative timeframes are analysed after the OCP becomes relatively stable. The original signals are schematically displayed at the background of the Hilbert spectra with their relative amplitudes in **Fig 6.8b** to **Fig 6.8e**. At the beginning, two parallel electrochemical reactions with typical electrochemical responses, i.e. fingerprints, at intermediate frequencies (0.01-0.1 Hz) and low frequencies (< 0.01 Hz) are present in the HHT spectrum. With the passing of the re-immersion time, the frequencies of the dominant reactions gradually move towards the intermediate frequency range, indicating that the time span of most transients becomes shorter over the course of the measurement. Based on the characterization results that the duration of S-phase-related corrosion from initiation to undercutting (i.e. loss of the related galvanic S-phase-to-matrix coupling) is typically is shorter than that of the large constituent particles, it can be inferred that the low-frequency transients that appear in the signal shown in **Fig. 6.8b** are mainly related to the corrosion activity surrounding the S-phase particles, whereas the intermediate-frequency transients are generated by corrosion attack related to large constituent phases. It can therefore be assumed that corrosion activity related to the S-phase particles is typically a lower-frequency process than corrosion related to large constituent phase particles, although the latter may last longer upon re-immersion. **Fig. 6.8c** and **6.8d** show the transition from reactions dominated by S-phase-related corrosion to constituent phase-related corrosion, since S-phase-related corrosion shows a higher activity and experiences undercutting from the matrix at an earlier stage (after approximately 8 h). In **Fig. 6.8e**, the relative energy contribution from S-phase-related corrosion is almost negligible. The EN results point out that S-phase- and large constituent phase-related corrosion activities occur almost

simultaneously, albeit that the corrosion activities at and around constituent phases last longer.
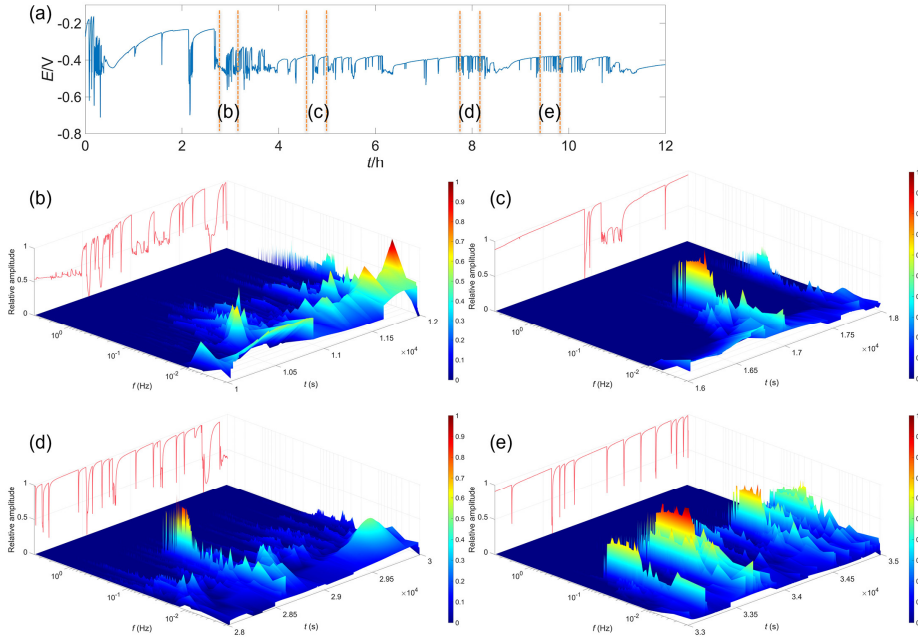
Fig. 6.8 EN potential signal for the 36 h ambiently-aged lithium-based conversion layer exposed to a 0.01 M NaCl solution for a duration of 12 h (a), Hilbert spectrum of the potential signal of a 36 h ambiently-aged lithium-based conversion layer exposed in a 0.01 M NaCl solution in the timeframe of (b) 10000 s-12000 s, (c) 16000 s-18000 s, (d) 28000 s-30000 s and (e) 33000 s-35000 s. The dashed lines in Fig. 6.8a correspond to the selected timeframes from Fig. 6.8b to 6.8e.

6.3.5. Schematic corrosion model for the lithium-based conversion layer. Current findings and previous work [57,62] in relation to the characterization of the corrosion behaviour of the lithium-based conversion layer during re-immersion are pivotal in proposing a more detailed corrosion mechanism to explain spatiotemporally resolved local degradation events. **Fig. 6.9** proposes a corrosion mechanism of the freshly formed conversion layer at the aluminium matrix during re-immersion. Immediately after re-immersion, the trapped lithium carbonate is released from the conversion layer due to the instability of the structure when it is exposed to a lithium-free liquid environment [64]. The released lithium carbonate can create a local alkaline environment that favours a continuous formation of the lithium-based conversion layer. Simultaneously, due to the loss of lithium and carbonate ions, the crystal

structure of the top Li/Al LDH layer gradually collapses. The inner dense layer undergoes a loss of lithium carbonate as well, which decreases its integrity. This suggests that the entire conversion layer matures insufficiently when removed from the lithium-containing solution immediately.
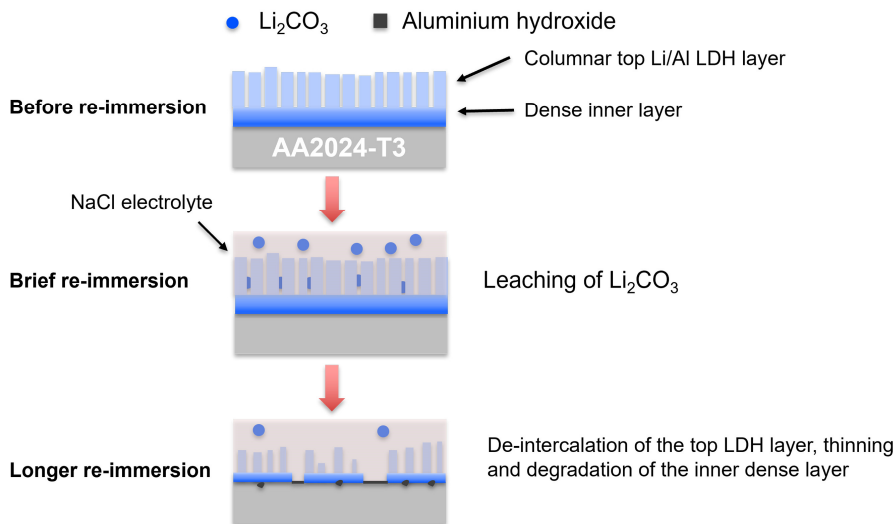
Fig. 6.9 Schematic representation of the proposed corrosion mechanism at the aluminium matrix of the freshly-formed lithium-based conversion layer during re-immersion.

Based on previous studies focused on dealloying-driven localized corrosion involving the IMPs in AA2024-T3, the localized corrosion at and around IMPs under the protection of the lithium-based conversion layer can be divided into several stages [38,60]. These include trench initiation, depth propagation and particle undercutting, as described in **Fig. 6.10** [38,60]. IMPs are more prone to corrosion attack due to insufficient coverage of the inner dense layer, especially for the large constituent particles. For the case of the S-phase, although its relatively small size facilitates its coverage by the incomplete inner layer, this is still insufficient to fully suppress its high chemical instability, since chloride ions can penetrate the conversion layer during re-immersion. Another issue is the fact that the S-phase undergoes significant and rapid dealloying during the conversion layer formation process, leading to a copper enrichment that acts as strong cathodic areas [36]. At the early stages of re-immersion, considering the different electrochemical properties between the aluminium matrix and IMPs, trenching is more likely to occur at the interface

between the matrix and the IMPs. At this stage, chloride ions and water gradually reach the bottom of the conversion layer, promoting the dissolution of the aluminium matrix and dealloying of the IMPs which make IMPs more prone to serve as cathodic zones. With the ongoing corrosion process underneath the conversion layer and the accumulation of corrosion products, the breakdown of the conversion layer commences. This process allows enhanced interaction of the corroding region with the external environment. Both the S- and constituent phases endure dealloying. The S-phase undergoes a selective dissolution of aluminium and magnesium, whereas the constituent phase particles experience the dissolution of manganese, aluminium and iron to a small extent [38]. Dealloying generates a local aggregation of remnant copper and/or iron establishing nano-galvanic coupling which drives the anodic dissolution of the rest of the particle and the adjacent aluminium matrix. At this stage, the dealloying of the IMPs and in-depth propagation of the trenches occur simultaneously, however the S-phase exhibits faster dealloying kinetics and establishes a stronger galvanic effect with the adjacent matrix than the large constituent phase [67]. Moreover, local degradation of the dealloying of the S-phase might occur and contribute to the release and redistribution of copper ions to nearby regions [60]. This phenomenon can greatly enhance the further dissolution of the nearby aluminium matrix and make the corrosion area to increase in size around the S-phase [60]. Finally, the local dissolution of the aluminium matrix around IMPs continues until the detachment of the IMPs. For constituent particles, this process takes into account a longer time. For this reason, this is less likely to occur within 12 h of re-immersion under conditions of the current study. After undercutting, the corroding IMPs acquire a higher corrosion potential and become fully dealloyed and may undergo further self-corrosion [60]. The undercutting also blocks the galvanic relationship between the matrix and the IMPs, resulting in a milder environment due to the significantly reduced oxygen reduction reaction and reduced production of H^+ caused by the hydrolysis of metal ions. This is beneficial for the stabilization of aluminium hydroxide corrosion products which gradually cover the aluminium matrix and isolate the matrix further from the external corrosive environment.
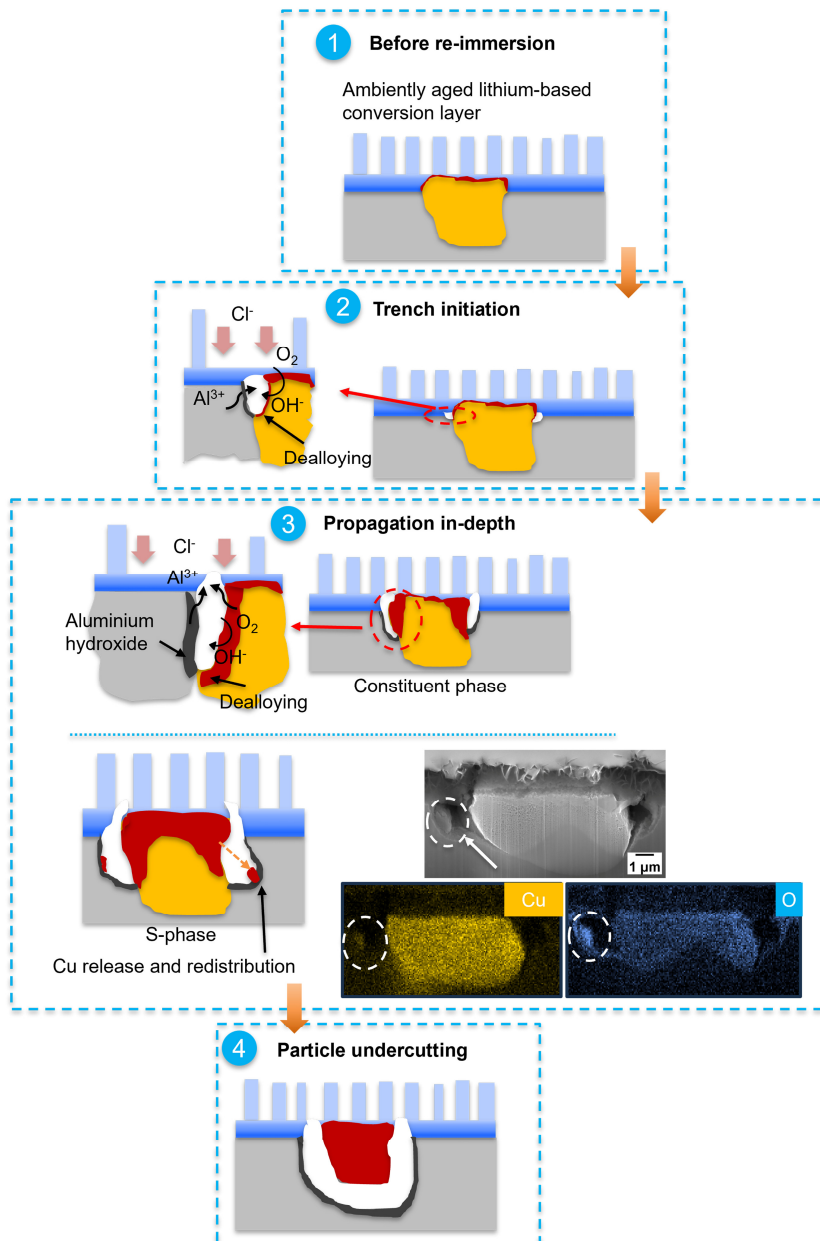
Fig. 6.10 Schematic overview of the localized corrosion mechanism at and around S- and constituent phase particles under the 36 h ambiently-aged lithium-based conversion layer during re-immersion. The insert in step 3 is a cross-sectional SEM micrograph with EDX results showing released copper from a dealloyed S-phase particle, redeposited locally at the trench wall.

6.4. Conclusions

Top-view and cross-sectional characterization of the lithium-based conversion layer grown on AA2024-T3 before re-immersion reveal that the aluminium matrix is covered by a complete bilayer conversion coating (a top columnar layer as well as an inner dense layer), yet the formation of the inner layer is incomplete over the IMPs. Although this deficient inner layer is able to cover small IMPs, it fails to develop over large constituent particles. This is caused by the relatively high electrochemical stability of these large particles, as well as by the fact that the conversion layer formation over constituent phases relies on the lateral propagation of aluminate ions derived from the adjacent aluminium matrix. During re-immersion in a NaCl solution, the freshly formed lithium-based conversion layer undergoes a gradual dissolution over the entire conversion layer which is triggered by its chemical instability. This makes the aluminium matrix underneath the conversion layer more prone to corrosion attack, although initially some trapped lithium carbonate is released which can inhibit the corrosion to a certain extent. In the case of the ambiently-aged sample, after re-immersion dealloying and trenching are more likely to occur at and around the S- and large constituent phase particles. Large constituent phase-related corrosion occurs due to the lower conversion layer quality locally, whereas S-phase-related corrosion can be attributed to the highly active nature of the S-phase and a greater extent of dealloying during the conversion layer formation, leading to increased copper enrichment at the surface of the S-phase. The galvanic couples between the aluminium matrix and the IMPs can be triggered when water and chloride ions reach the bottom of the conversion layer. Ongoing corrosion reactions allow the trench to propagate along the interface between the matrix and the IMPs until the particles are fully undercut. Simultaneously, the IMPs also undergo gradual dealloying, albeit the S-phase at a faster pace and exhibiting higher trench propagation kinetics as compared to the large constituent phase.

References

[1] N.L. Sukiman, X. Zhou, N. Birbilis, A.E. Hughes, J.M. C. Mol, S. J., X. Zhou, G. E., Durability and Corrosion of Aluminium and Its Alloys: Overview, Property Space, Techniques and Developments, in: Z. Ahmad (Ed.), Alum. Alloys - New Trends Fabr. Appl., InTech, 2012.

[2] A.E. Hughes, C. MacRae, N. Wilson, A. Torpy, T.H. Muster, A.M. Glenn, Sheet AA2024-T3: a new investigation of microstructure and composition, Surf. Interface Anal. 42 (2010) 334–338.

[3] A. Boag, A.E. Hughes, N.C. Wilson, A. Torpy, C.M. MacRae, A.M. Glenn, T.H. Muster, How complex is the microstructure of AA2024-T3?, Corros. Sci. 51 (2009) 1565–1568.

[4] A.E. Hughes, N. Birbilis, J.M.C. Mol, S.J. Garcia, X. Zhou, G.E. Thompson, High Strength Al-Alloys: Microstructure, Corrosion and Principles of Protection, in: Z. Ahmad (Ed.), Recent Trends Process. Degrad. Alum. Alloys, InTech, 2011.

[5] S.J. Andersen, C.D. Marioara, J. Friis, S. Wenner, R. Holmestad, Precipitates in aluminium alloys, Adv. Phys. X 3 (2018) 1479984.

[6] C. Blanc, B. Lavelle, G. Mankowski, The role of precipitates enriched with copper on the susceptibility to pitting corrosion of the 2024 aluminium alloy, Corros. Sci. 39 (1997) 495–510.

[7] N. Birbilis, Y.M. Zhu, S.K. Kairy, M.A. Glenn, J.-F. Nie, A.J. Morton, Y. Gonzalez-Garcia, H. Terryn, J.M.C. Mol, A.E. Hughes, A closer look at constituent induced localised corrosion in Al-Cu-Mg alloys, Corros. Sci. 113 (2016) 160–171.

[8] P. Campestrini, H. Terryn, J. Vereecken, J.H.W. de Wit, Chromate Conversion Coating on Aluminum Alloys : III. Corrosion Protection, J. Electrochem. Soc. 151 (2004) B370.

[9] M.W. Kendig, R.G. Buchheit, Corrosion Inhibition of Aluminum and Aluminum Alloys by Soluble Chromates, Chromate Coatings, and Chromate-Free Coatings, CORROSION 59 (2003) 379–400.

[10] G.O. Ilevbare, J.R. Scully, J. Yuan, R.G. Kelly, Inhibition of Pitting Corrosion on Aluminum Alloy 2024-T3: Effect of Soluble Chromate Additions vs Chromate Conversion Coating, CORROSION 56 (2000) 227–242.

[11] A.E. Hughes, R.J. Taylor, B.R.W. Hinton, Chromate Conversion Coatings on 2024 Al Alloy, Surf. Interface Anal. 25 (1997) 223–234.

[12] R. Saha, R. Nandi, B. Saha, Sources and toxicity of hexavalent chromium, J. Coord. Chem. 64 (2011) 1782–1806.

[13] M. Becker, Chromate-free chemical conversion coatings for aluminum alloys, Corros. Rev. 37 (2019) 321–342.

[14] I. Milošev, G.S. Frankel, Review—Conversion Coatings Based on Zirconium and/or Titanium, J. Electrochem. Soc. 165 (2018) C127.

[15] O. Gharbi, S. Thomas, C. Smith, N. Birbilis, Chromate replacement: what does the future hold?, Npj Mater. Degrad. 2 (2018) 12.

[16] R.L. Twite, G.P. Bierwagen, Review of alternatives to chromate for corrosion protection of aluminum aerospace alloys, Prog. Org. Coat. 33 (1998) 91–100.

[17] Y. Guo, G.S. Frankel, Characterization of trivalent chromium process coating on AA2024-T3, Surf. Coat. Technol. 206 (2012) 3895–3902.

[18] L. Li, G.M. Swain, Effects of Aging Temperature and Time on the Corrosion Protection Provided by Trivalent Chromium Process Coatings on AA2024-T3, ACS Appl. Mater. Interfaces 5 (2013) 7923–7930.

[19] P. Santa Coloma, U. Izagirre, Y. Belaustegi, J.B. Jorcin, F.J. Cano, N. Lapeña, Chromium-free conversion coatings based on inorganic salts (Zr/Ti/Mn/Mo) for aluminum alloys used in aircraft applications, Appl. Surf. Sci. 345 (2015) 24–35.

[20] O. Lopez-Garrity, G.S. Frankel, Corrosion Inhibition of Aluminum Alloy 2024-T3 by Sodium Molybdate, J. Electrochem. Soc. 161 (2013) C95.

[21] D.S. Kharitonov, J. Sommertune, C. Örnek, J. Ryl, I.I. Kurilo, P.M. Claesson, J. Pan, Corrosion inhibition of aluminium alloy AA6063-T5 by vanadates: Local surface chemical events elucidated by confocal Raman micro-spectroscopy, Corros. Sci. 148 (2019) 237–250.

[22] V. Moutarlier, M.P. Gigandet, B. Normand, J. Pagetti, EIS characterisation of anodic films formed on 2024 aluminium alloy, in sulphuric acid containing molybdate or permanganate species, Corros. Sci. 47 (2005) 937–951.

[23] A.K. Mishra, R. Balasubramaniam, Corrosion inhibition of aluminum alloy AA 2014 by rare earth chlorides, Corros. Sci. 49 (2007) 1027–1044.

[24] K.A. Yasakau, M.L. Zheludkevich, S.V. Lamaka, M.G.S. Ferreira, Mechanism of Corrosion Inhibition of AA2024 by Rare-Earth Compounds, J. Phys. Chem. B 110.

[25] R.G. Buchheit, G.E. Stoner, Chromate-free corrosion resistant talc coatings for aluminum alloys, Sandia National Labs., Albuquerque, NM (United States), 1992.

[26] P. Visser, H. Terryn, J.M.C. Mol, On the importance of irreversibility of corrosion inhibitors for active coating protection of AA2024-T3, Corros. Sci. 140 (2018) 272–285.

[27] P. Visser, Y. Liu, H. Terryn, J.M.C. Mol, Lithium salts as leachable corrosion inhibitors and potential replacement for hexavalent chromium in organic coatings for the protection of aluminum alloys, J. Coat. Technol. Res. 13 (2016) 557–566.

[28] C.A. Drewien, M.O. Eatough, D.R. Tallant, C.R. Hills, R.G. Buchheit, Lithium-aluminum-carbonate-hydroxide hydrate coatings on aluminum alloys: Composition, structure, and processing bath chemistry, J. Mater. Res. 11 (1996) 1507–1513.

[29] R.G. Buchheit, M.D. Bode, G.E. Stoner, Corrosion-Resistant, Chromate-Free Talc Coatings for Aluminum, CORROSION 50 (1994) 205–214.

[30] J. Gui, T.M. Devine, Influence of lithium on the corrosion of aluminum, Scr Met. U. S. 21:6 (1987).

[31] P. Visser, Y. Liu, X. Zhou, T. Hashimoto, G.E. Thompson, S.B. Lyon, L.G.J. van der Ven, A.J.M.C. Mol, H.A. Terryn, The corrosion protection of AA2024-T3 aluminium alloy by leaching of lithium-containing salts from organic coatings, Faraday Discuss. 180 (2015) 511–526.

[32] Y. Liu, P. Visser, X. Zhou, S.B. Lyon, T. Hashimoto, M. Curioni, A. Gholinia, G.E. Thompson, G. Smyth, S.R. Gibbon, D. Graham, J.M.C. Mol, H. Terryn, Protective Film Formation on AA2024-T3 Aluminum Alloy by Leaching of Lithium Carbonate from an Organic Coating, J. Electrochem. Soc. 163 (2015) C45.

[33] Y. Liu, P. Visser, X. Zhou, S.B. Lyon, T. Hashimoto, A. Gholinia, G.E. Thompson, G. Smyth, S.R. Gibbon, D. Graham, J.M.C. Mol, H. Terryn, An investigation of the corrosion inhibitive layers generated from lithium oxalate-containing organic coating on AA2024-T3 aluminium alloy, Surf. Interface Anal. 48 (2016) 798–803.

[34] P. Visser, S.A. Hayes, Anti-Corrosive Coating Composition, WIP Organ (2010), p. A1, Ed WO. 112605.

[35] P. Visser, A. Lutz, J.M.C. Mol, H. Terryn, Study of the formation of a protective layer in a defect from lithium-leaching organic coatings, Prog. Org. Coat. 99 (2016) 80–90.

[36] A. Kosari, F. Tichelaar, P. Visser, H. Zandbergen, H. Terryn, J.M.C. Mol, Laterally-resolved formation mechanism of a lithium-based conversion layer at the matrix and intermetallic particles in aerospace aluminium alloys, Corros. Sci. 190 (2021) 109651..

[37] Z. Li, P. Visser, A.E. Hughes, A. Homborg, Y. Gonzalez-Garcia, A. Mol, Review of the state of art of Li-based inhibitors and coating technology for the corrosion protection of aluminium alloys, Surf. Coat. Technol. 478 (2024) 130441.

[38] A. Kosari, F. Tichelaar, P. Visser, H. Zandbergen, H. Terryn, J.M.C. Mol, Dealloying-driven local corrosion by intermetallic constituent particles and dispersoids in aerospace aluminium alloys, Corros. Sci. 177 (2020) 108947.

[39] J.R. Waldrop, M.W. Kendig, Nucleation of Chromate Conversion Coating on Aluminum 2024-T3 Investigated by Atomic Force Microscopy, J. Electrochem. Soc. 145 (1998) L11.

[40] P. Campestrini, H. Terryn, J. Vereecken, J.H.W. de Wit, Chromate Conversion Coating on Aluminum Alloys: II: Effect of the Microstructure, J. Electrochem. Soc. 151 (2004) B359.

[41] G. Šekularac, J. Kovač, I. Milošev, Comparison of the Electrochemical Behaviour and Self-sealing of Zirconium Conversion Coatings Applied on Aluminium Alloys of series 1xxx to 7xxx, J. Electrochem. Soc. 167 (2020) 111506.

[42] P. Visser, Y. Gonzalez-Garcia, J.M.C. Mol, H. Terryn, Mechanism of Passive Layer Formation on AA2024-T3 from Alkaline Lithium Carbonate Solutions in the Presence of Sodium Chloride, J. Electrochem. Soc. 165 (2018) C60–C70.

[43] R.G. Buchheit, G.E. Stoner, Chromate-free corrosion resistant talc coatings for aluminum alloys, Sandia National Labs., Albuquerque, NM (United States), 1992.

[44] R.G. Buchheit, Alkaline oxide conversion coatings for aluminum alloys, Sandia National Lab. (SNL-NM), Albuquerque, NM (United States), 1996.

[45] R.G. Buchheit, M.A. Martinez, C.B. Cooper, Corrosion Resistant Coatings for Aluminum by Hydrothermal Film Formation in Alkaline Li-Salt Solutions, MRS Online Proc. Libr. OPL 432 (1996) 273.

[46] A.M. Homborg, T. Tinga, X. Zhang, E.P.M. van Westing, P.J. Oonincx, J.H.W. de Wit, J.M.C. Mol, Time–frequency methods for trend removal in electrochemical noise data, Electrochimica Acta 70 (2012) 199–209.

[47] Ł. Lentka, J. Smulko, Methods of trend removal in electrochemical noise data – Overview, Measurement 131 (2019) 569–581.

[48] N.E. Huang, Z. Shen, S.R. Long, M.C. Wu, H.H. Shih, Q. Zheng, N.-C. Yen, C.C. Tung, H.H. Liu, The empirical mode decomposition and the Hilbert spectrum for nonlinear and non-stationary time series analysis, Proc. R. Soc. Lond. Ser. Math. Phys. Eng. Sci. 454 (1998) 903–995.

[49] P. Frank Pai, A.N. Palazotto, HHT-based nonlinear signal processing method for parametric and non-parametric identification of dynamical systems, Int. J. Mech. Sci. 50 (2008) 1619–1635.

[50] A.M. Homborg, E.P.M. van Westing, T. Tinga, X. Zhang, P.J. Oonincx, G.M. Ferrari, J.H.W. de Wit, J.M.C. Mol, Novel time–frequency characterization of electrochemical noise data in corrosion studies using Hilbert spectra, Corros. Sci. 66 (2013) 97–110.

[51] N.A. Payne, L.I. Stephens, J. Mauzeroll, The Application of Scanning Electrochemical Microscopy to Corrosion Research, Corrosion 73 (2017) 759–780.

[52] D. Polcari, P. Dauphin-Ducharme, J. Mauzeroll, Scanning Electrochemical Microscopy: A Comprehensive Review of Experimental Parameters from 1989 to 2015, Chem. Rev. 116 (2016) 13234–13278.

[53] Z. Ye, Z. Zhu, Q. Zhang, X. Liu, J. Zhang, F. Cao, In situ SECM mapping of pitting corrosion in stainless steel using submicron Pt ultramicroelectrode and quantitative spatial resolution analysis, Corros. Sci. 143 (2018) 221–228.

[54] C. Gabrielli, S. Joiret, M. Keddam, H. Perrot, N. Portail, P. Rousseau, V. Vivier, Development of a Coupled SECM-EQCM Technique for the Study of Pitting Corrosion on Iron, J. Electrochem. Soc. 153 (2006) B68.

[55] K. Mansikkamäki, P. Ahonen, G. Fabricius, L. Murtomäki, K. Kontturi, Inhibitive Effect of Benzotriazole on Copper Surfaces Studied by SECM, J. Electrochem. Soc. 152 (2004) B12.

[56] J.J. Santana, J. Izquierdo, R.M. Souto, Uses of Scanning Electrochemical Microscopy (SECM) for the Characterization with Spatial and Chemical Resolution of Thin Surface Layers and Coating Systems Applied on Metals: A Review, Coatings 12 (2022) 637.

[57] Z. Li, A. Homborg, Y. Gonzalez-Garcia, P. Visser, M. Soleimani, A. Mol, The Effect of Ambient Ageing on the Corrosion Protective Properties of a Lithium-Based Conversion Layer, J. Electrochem. Soc. 170 (2023) 031504.

[58] A. Kosari, F. Tichelaar, P. Visser, P. Taheri, H. Zandbergen, H. Terryn, J.M.C. Mol, Nanoscopic and in-situ cross-sectional observations of Li-based conversion coating formation using liquid-phase TEM, Npj Mater. Degrad. 5 (2021) 1–9.

[59] A. Kosari, P. Visser, F. Tichelaar, S. Eswara, J.-N. Audinot, T. Wirtz, H. Zandbergen, H. Terryn, J.M.C. Mol, Cross-sectional characterization of the conversion layer formed on AA2024-T3 by a lithium-leaching coating, Appl. Surf. Sci. 512 (2020) 145665.

[60] A. Kosari, H. Zandbergen, F. Tichelaar, P. Visser, P. Taheri, H. Terryn, J.M.C. Mol, In-situ nanoscopic observations of dealloying-driven local corrosion from surface initiation to in-depth propagation, Corros. Sci. 177 (2020) 108912.

[61] P. Visser, M. Meeusen, Y. Gonzalez-Garcia, H. Terryn, J.M.C. Mol, Electrochemical Evaluation of Corrosion Inhibiting Layers Formed in a Defect from Lithium-Leaching Organic Coatings, J. Electrochem. Soc. 164 (2017) C396.

[62] Z. Li, A. Homborg, Y. Gonzalez-Garcia, A. Kosari, P. Visser, A. Mol, Evaluation of the formation and protectiveness of a lithium-based conversion layer using electrochemical noise, Electrochimica Acta 426 (2022) 140733.

[63] L. Huang, J. Wang, Y. Gao, Y. Qiao, Q. Zheng, Z. Guo, Y. Zhao, D. O'Hare, Q. Wang, Synthesis of LiAl2-layered double hydroxides for CO2 capture over a wide temperature range, J. Mater. Chem. A 2 (2014) 18454–18462.

[64] K.A. Tarasov, V.P. Isupov, L.E. Chupakhina, D. O'Hare, A time resolved, in-situ X-ray diffraction study of the de-intercalation of anions and lithium cations from [LiAl2(OH)6]nX·qH2O (X = Cl−, Br−, NO3−, SO42−), J. Mater. Chem. 14 (2004) 1443–1447.

[65] H.N. McMurray, G. Williams, Inhibition of Filiform Corrosion on Organic-Coated Aluminum Alloy by Hydrotalcite-Like Anion-Exchange Pigments, Corrosion 60 (2004) 219–228.

[66] Y. Su, S. Qiu, D. Yang, S. Liu, H. Zhao, L. Wang, Q. Xue, Active anti-corrosion of epoxy coating by nitrite ions intercalated MgAl LDH, J. Hazard. Mater. 391 (2020) 122215.

[67] S. Lebouil, J. Tardelli, E. Rocca, P. Volovitch, K. Ogle, Dealloying of Al2Cu, Al7Cu2Fe, and Al2CuMg intermetallic phases to form nanoparticulate copper films, Mater. Corros. 65 (2014) 416–424.
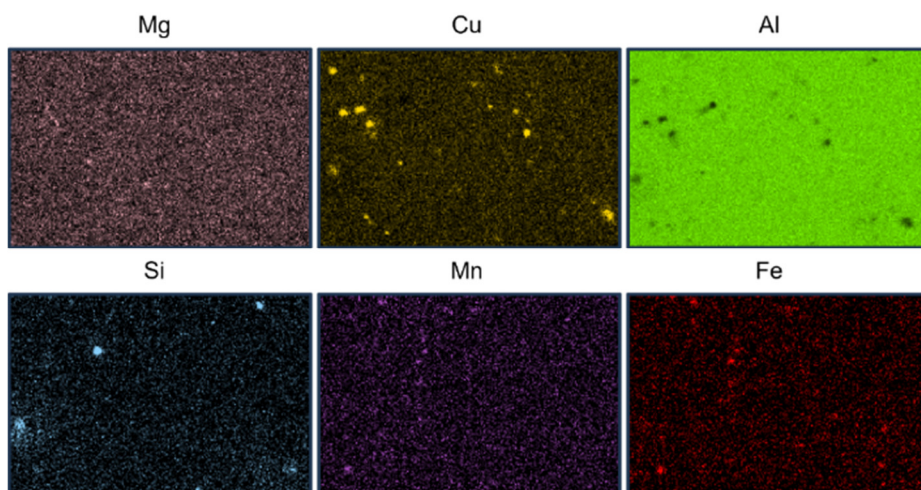
Supplementary Information for Chapter 6
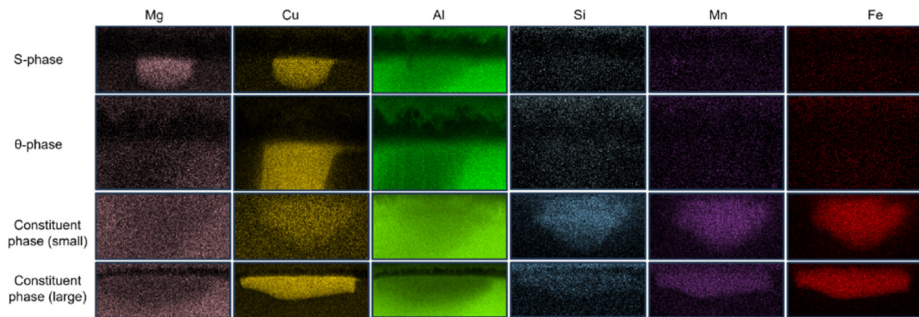
Fig. S6.1 EDS mapping of IMPs shown in Fig. 6.3.
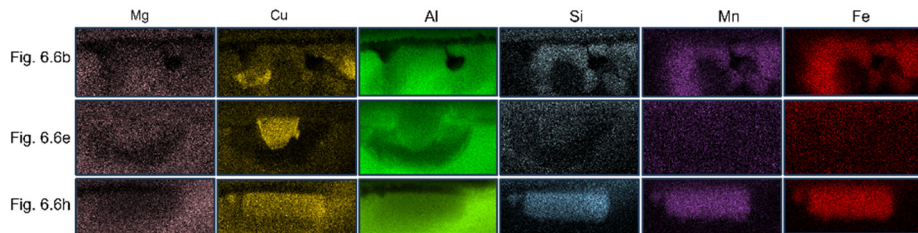
Fig. S6.2 EDS mapping of IMPs shown in Fig. 6.6b, 6.6e and 6.6h, respectively.

Fig. S6.3 EDS mapping of Fig. 6.7d.

CHAPTER 7

CONCLUSIONS AND

RECOMMENDATIONS

7.1. Introduction

While chromate-based chemistries for both surface conversion treatments as well as leaching inhibitors from organic coatings can provide excellent corrosion protection for various aluminium alloys, their toxic and carcinogenic nature has led to strict international health and safety regulations. This forces the industry to develop and implement more environmentally-friendly and non-toxic alternatives. Novel candidates for the replacement of traditional chromate-based processes require fundamental studies to understand their layer formation and corrosion protection characteristics, which is a prerequisite for the optimization of treatment procedures and for the development of organic coatings. Investigations at the microscale or even at the nanoscale are of vital importance to gain a profound understanding of the local formation and protective mechanisms, as well as the dominant factors which may influence the quality of the protective film. Meanwhile, real-time monitoring of the protective layer formation process and its protective behaviour under corrosive conditions should be considered as well.

In Chapter 2 of this thesis, the development of the lithium-based inhibitor coating technology for the corrosion protection of aluminium alloys is presented in detail. Since the discovery of the passivation capacity of lithium-containing alkaline solutions for aluminium alloys, conversion surface treatments based on this technology were studied, thanks to the extensive work of pioneer researchers. However, the conversion procedures were still relatively complex as compared to traditional chromate-based conversion bath processes and generally required elevated bath solution temperatures. This makes lithium-based conversion coating techniques less cost-effective. In 2010, lithium salts, serving as the leachable inhibitor in organic coatings, were identified as a promising alternative for chromates. Unlike the "static" conversion bath, the local electrolyte chemistry and protective layer formation at a defect in a lithium-leaching organic coating system is more complex and dynamic. The corrosion protection properties have been studied extensively using various electrochemical methods, most of which can be considered as conventional macroscopic evaluation techniques. However, these methods merely provide an averaged quantitative assessment of the corrosion resistance and therefore pose a high demand for the stability of the corroding system. Moreover, these macroscopic techniques typically lack a high spatial and temporal resolution. Previous work has reported the lithium-based conversion layer formation and the protective film generated inside the defect of an organic coating system in detail at the micro- and even at the nanoscale level, providing a fundamental understanding of the formation

mechanism. However, spatiotemporally resolved characterization during exposure to a lithium-free corrosive environment was still limited. Hence, the scientific objective of this PhD thesis was to apply scanning electrochemical microscopy (SECM) and electrochemical noise (EN) techniques combined with morphological and compositional characterization methods to study the corrosion mechanism of the lithium-based conversion layer. SECM possesses a high spatial resolution, while EN can detect electrochemical activity at a high temporal resolution, without imposing any interference to the electrolyte-substrate system. Moreover, the relatively straightforward configuration of EN makes it not only a versatile technique for scientific studies but also quite suitable for corrosion monitoring in the field. The conversion bath was therefore specified in order to represent the average concentration of lithium salts inside an artificial defect in a lithium-leaching organic coating. At first, it was important to investigate how to apply EN to study the lithium-based conversion layer and to determine the relationship with previous morphological and compositional variation studies. Secondly, the adoption of SECM allowed a study of the progressive formation stages of the lithium-based conversion layer with the support of EN measurements. SECM and EN results supported each other regarding the interpretation of the reactions occurring at the alloy surface with spatial and temporal resolution, respectively. Finally, SECM and EN were used together to study the corrosion mechanism of the conversion layer under corrosive conditions, elucidating the mechanism at a microscale level.

7.2. Application of EN in the study of the lithium-based conversion layer

In Chapter 3, the EN technique was first adopted to determine a suitable setup for the measurement of the lithium-based conversion layer formation process. It was found that the EN potential and current signals exhibit distinct shapes: current signals contain a large number of transients, whereas the potential curve is very smooth, which results from the highly alkaline electrolyte (pH=10.9), causing a fast uniform dissolution at the beginning. At a later stage, competitive dissolution and precipitation of the conversion layer become dominant during the entire conversion layer growth process, which suppresses the contribution of local reactions. This process is reflected in the low-frequency energy contribution in the continuous wavelet transform spectrum. A further analysis revealed that the EN current signal contains two types of transients, each with a distinct time constant. The high-frequency transients, which correspond to the detachments of hydrogen bubbles, usually last no more than 0.5 s. The typical time span of the intermediate frequency

transients is in the order of several seconds, which is attributed to the local activity of intermetallic particles (IMPs) on AA2024-T3.
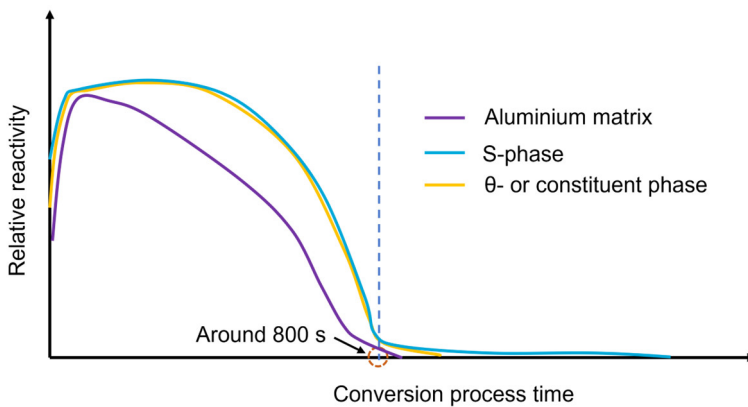
For the corrosion behaviour of the lithium-based conversion layer during re-immersion, samples with different ambiently aged treatments were measured using EN. The entire re-immersion can be divided into two stages: the inhibition stage and the corrosion stage. The results showed that the conversion layer with short ageing times presents a higher initial noise resistance and a longer duration of the inhibited state, but a lower resistance during the corrosion stage. This observation is mainly caused by the continuous growth of the conversion layer. Initially, the lithium-based conversion layer is chemically unstable when removed from the conversion bath; some lithium carbonate can be released from the conversion layer. This promotes the growth of the conversion layer where the surface is still wet. Therefore, this further growth is not homogeneous; the more matured areas showed more extensive local layer growth than that for adjacent regions. EN, accompanied by surface characterization methods, provided deeper insights into the corrosion behaviour of the lithium-based conversion layer. The main reasons for this are the fact that (i) rapid reactions occurring at the surface are unlikely to remain undetected and (ii) EN measurements do not require a stable system.

7.3. Application of SECM on the studies of lithium-based conversion layer

Considering that the fast dissolution of the substrate at the early stages of the conversion layer formation can easily pollute the SECM probe and reduce its sensitivity, firstly ex-situ SECM measurements were performed. Seven representative time points (0 s, 60 s, 200 s, 700 s, 2000 s, 4000 s, 14500 s) were selected according to previous studies, which divided the entire growing period of the conversion layer into five consecutive stages.

The areas at and around three types of IMPs (S-, θ- and constituent phases) presented varying surface activities over time. Prior to the conversion bath, the aluminium alloy surface is covered by a naturally formed oxide layer, but this thin oxide layer cannot effectively cover all IMPs at the surface of the AA2024-T3. All three types of IMPs are cathodically active. After an immersion of 60 s, the alloy surface becomes more active due to removal of the native oxide layer. At 200 s, the entire surface reaches its highest reactivity. The noble copper is less dissolved and enriches at the surface, driving the open-circuit potential towards a positive direction and acting as strong

cathodic regions. At a later stage, for a longer immersion duration of 700 s, the three types of IMPs are still active but the average reactivity starts to decrease. When the immersion time is extended to 2000 s, only the S-phase remains active, which is due to the larger extent of dealloying of these particles and consequently a locally larger quantity of enriched copper. Finally, when the conversion bath duration is longer than 4000 s, the entire surface becomes passive. Combined with the results in Chapter 3, the relative surface reactivity variations can be presented (**Fig. 7.1**). Upon exposure to the highly corrosive electrolyte, the reactivity of both the aluminium matrix and the IMPs increases sharply. IMPs sustain a relatively stable high reactivity, whereas the surface reactivity of the aluminium matrix decreases gradually. After an immersion period of 800 s, the energy contribution of the IMPs becomes almost negligible, which indicates a lower surface reactivity of the aluminium and IMPs. However, the S-phase still consumes longer time to become fully passivation. Hydrogen bubble evolution areas hinder the development of the lithium-based conversion layer locally, leaving defects at the alloy surface and leaving these areas more vulnerable to local corrosion attack.

Fig. 7.1 Schematic representation of the surface reactivity evolution of the aluminium matrix and IMPs during conversion.

## 7.4. Corrosion protection of AA2024-T3 by a lithium-based conversion layer

The corrosion mechanism of the lithium-based conversion layer was studied at the microscale level. Previous work had demonstrated that the lithium-based conversion layer formed on AA2024-T3 contains a top Li/Al LDH columnar layer, as well as an inner dense layer. The inner layer is absent at the location of IMPs. In Chapter 6, the

morphological and compositional analysis revealed that an incomplete layer can generate over small IMPs, whereas such a layer is virtually absent over larger constituent particles. Two types of conversion layers were investigated here: freshly-formed and ambiently-aged conversion layers. For the freshly-formed conversion layer, both the top columnar layer as well as the inner dense layer are unstable when re-immersed in a lithium-free solution. The release of lithium carbonate will cause the structure of the top Li/Al LDH to gradually collapse and will make the inner dense layer less corrosion resistant. Consequently, the corrosive chloride ions are more prone to penetrate the entire conversion layer and to cause localized corrosion. Trenching is observed on the freshly-formed conversion layer as well, and the trench formation mechanism is nearly identical to that on the ambiently aged conversion layer.

The results showed that areas around S- and constituent phases were more prone to corrosion attack as compared to the aluminium matrix. In the case of the S-phase, as confirmed in Chapter 5, the S-phase shows the largest active time span of conversion layer growth. Although an incomplete inner layer is formed, a strong galvanic couple between the S-phase and the adjacent matrix is established when the chloride ions and water penetrate the conversion layer. For the large constituent phases, trenching is more likely to occur due to the less effective corrosion protection of the lithium-based conversion layer. When the corrosion products underneath the conversion layer accumulate, breakdown of the conversion layer occurs. At a later stage, the trench develops more in-depth and the IMPs simultaneously undergo dealloying. For the S-phase, copper is released and redistributed locally at the surface of the aluminium matrix. Finally, particle undercutting occurs, promoting the dealloying kinetics of IMPs and cutting off the galvanic coupling between the IMPs and the aluminium matrix. Furthermore, trench formation and propagation around the S-phase is faster than that around the constituent particles. Based on the knowledge from Chapter 4 and previous studies, the influence of ambient ageing on the quality of the lithium-based layer and the inhibition effect of lithium-based conversion layer on localized corrosion induced by IMPs are summarized in **Fig. 7.2**. No matter the wet or dry conditions on the freshly-formed conversion layer, ambient ageing is beneficial for the improvement of the corrosion protective capacity of the conversion layer, but a wet surface can promote the continuous growth of the conversion layer and in this way enable local thickening of the conversion layer. For the unprotected AA2024-T3 surface, the order of vulnerability of localized corrosion induced by IMPs is: S-phase > θ-phase > constituent phase. In case the alloy surface is protected by the lithium-

based conversion layer, the S-phase still shows the highest electrochemical instability, followed by the large constituent phase, the θ-phase and the small constituent phase. However, the occurrence of corrosion initiation upon exposure to a corrosive environment is postponed considerably in all cases.
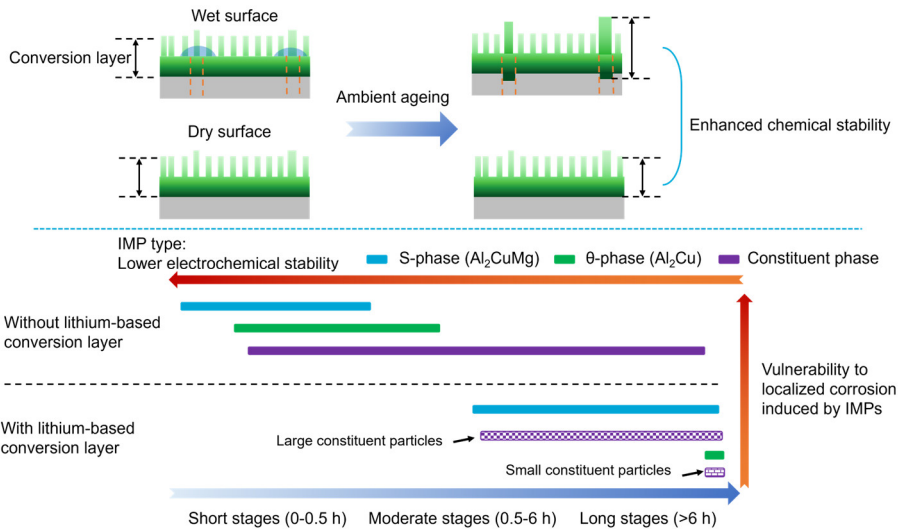
Fig. 7.2 (top) The influence of ambient ageing on the quality of the lithium-based conversion layer and (bottom) the progressive development of localized corrosion induced by IMPs with or without the protection of the lithium-based conversion layer. The lines with different colours in the figure indicate the time duration from corrosion initiation to particle undercutting for different IMPs.

8.5. Recommendations

This study has embraced an in-depth spatiotemporally resolved electrochemical characterization of the corrosion inhibition provided by lithium salts for AA2024-T3. The collected electrochemical information was successfully linked to the morphological and compositional variations over the aluminium matrix and IMPs during the lithium-based conversion formation stages and its corrosion protection process. Based on the outcome of this research, the following recommendations can be formulated:

1. The current understanding of local chemical conditions inside the defect of a lithium-leaching organic coating system is still relatively rudimentary, since only the local concentration and pH are considered. The conversion layer growth was

assumed to occur relatively "static", which is quite different from the actual protective layer formation process inside the scratch. Dynamic effects including droplet evolution, evaporation, condensation and varying lithium leaching rates should be considered in future studies. Especially for EN measurements, the question on how to collate the recorded electrochemical signals to the morphological and compositional changes at the aluminium alloy surface under a dynamic environment is challenging. A system with complex kinetics will pose a higher demand on the data analysis protocol. Furthermore, macroscale EN electrodes are prone to generate overlapping corrosion signals. A successful study of the influence of defects at the sample surface therefore requires a specially designed micro-electrode for EN measurements. This is considered meaningful for the identification of multiple electrochemical reactions occurring at the metal surface.

2. SECM provides high spatial resolution in the local characterization of a lithium-based conversion layer. One of the drawbacks of SECM is that it has to be performed under strict laboratory conditions. In-situ measurements during the formation stages are still challenging since the fast dissolution of the substrate may impede SECM detection. Finding a suitable strategy to collect electrochemical information close to the substrate during the lithium-based conversion layer growth remains necessary, not only for a more profound understanding of the corrosion mechanism, but also for the design of simulation models. Moreover, other SECM modes, such as local pH measurements, should be performed as well, in order to harvest useful electrochemical information from different environmental descriptors (pH, concentrations of ions of interest, etc.).

3. Based on the experience with the employment of SECM and EN for the characterization of the lithium-based conversion layer, similar experiments should be performed for lithium-containing organic coating systems as well. Current studies merely test the corrosion protective behaviour of the protective film at the artificial defect using salt spray tests and traditional electrochemical methods. The corrosion protection mechanism of this protective layer at the microscale level is however still unclear. Based on the results presented in this work, it can be expected that the corrosion mechanism would be quite complex; the varying leaching kinetics of the lithium salts would lead to a heterogeneous morphology and composition of the lithium-containing protective layer.

List of publications

○ Ph.D. work

[1] **Z. Li**, P. Visser, A. Homborg, Y. Gonzalez-Garcia, A. Mol, Spatiotemporally resolved corrosion protection of AA2024-T3 by a lithium-based conversion layer, **Corrosion Science**. 233 (2024) 112061.

[2] **Z. Li**, P. Visser, A.E. Hughes, A. Homborg, Y. Gonzalez-Garcia, A. Mol, Review of the state of art of Li-based inhibitors and coating technology for the corrosion protection of aluminium alloys, **Surface and Coatings Technology**. 478 (2024) 130441.

[3] **Z. Li**, G. Li, P. Visser, A. Homborg, Y. Gonzalez-Garcia, A. Mol, Local scanning electrochemical microscopy analysis of a lithium-based conversion layer on AA2024-T3 at progressive stages of formation, **Electrochimica Acta**. 469 (2023) 143270.

[4] **Z. Li**, A. Homborg, Y. Gonzalez-Garcia, P. Visser, M. Soleimani, A. Mol, The Effect of Ambient Ageing on the Corrosion Protective Properties of a Lithium-Based Conversion Layer, **Journal of The Electrochemical Society**. 170 (2023) 031504.

[5] **Z. Li**, A. Homborg, Y. Gonzalez-Garcia, A. Kosari, P. Visser, A. Mol, Evaluation of the formation and protectiveness of a lithium-based conversion layer using electrochemical noise, **Electrochimica Acta**. 426 (2022) 140733.

○ Other works

[6] Z. Liu, S. Baluchová, **Z. Li**, Y. Gonzalez-Garcia, C.E. Hall, J.G. Buijnsters, Unravelling microstructure-electroactivity relationships in free-standing polycrystalline boron-doped diamond: A mapping study, **Acta Materialia**. 266 (2024) 119671.

[7] Z. Liu, S. Baluchová, A.F. Sartori, **Z. Li**, Y. Gonzalez-Garcia, M. Schreck, J.G. Buijnsters, Heavily boron-doped diamond grown on scalable heteroepitaxial quasi-substrates: A promising single crystal material for electrochemical sensing applications, **Carbon**. 201 (2023) 1229–1240.

[8] W. Chang, Y. Li, **Z. Li**, Y. Lou, T. Cui, H. Qian, A. Mol, D. Zhang, The effect of riboflavin on the microbiologically influenced corrosion of pure iron by Shewanella oneidensis MR-1, **Bioelectrochemistry**. 147 (2022) 108173.

[9] L. Huang, W. Chang, D. Zhang, Y. Huang, **Z. Li**, Y. Lou, H. Qian, C. Jiang, X. Li, A. Mol, Acceleration of corrosion of 304 stainless steel by outward extracellular electron transfer of Pseudomonas aeruginosa biofilm, **Corrosion Science**. 199 (2022) 110159.

[10] **Z. Li**, W. Chang, T. Cui, D. Xu, D. Zhang, Y. Lou, H. Qian, H. Song, A. Mol, F.

Cao, T. Gu, X. Li, Adaptive bidirectional extracellular electron transfer during accelerated microbiologically influenced corrosion of stainless steel, **Communication Materials**. 2 (2021) 1–9.

[11] H. Qian, L. Ma, D. Zhang, **Z. Li**, L. Huang, Y. Lou, C. Du, Microbiologically influenced corrosion of 304 stainless steel by halophilic archaea Natronorubrum tibetense, **Journal of Materials Science & Technology**. 46 (2020) 12–20.

[12] B. Liu, **Z. Li**, X. Yang, C. Du, X. Li, Microbiologically influenced corrosion of X80 pipeline steel by nitrate reducing bacteria in artificial Beijing soil, **Bioelectrochemistry**. 135 (2020) 107551.

[13] H. Qian, P. Ju, D. Zhang, L. Ma, Y. Hu, **Z. Li**, L. Huang, Y. Lou, C. Du, Effect of Dissolved Oxygen Concentration on the Microbiologically Influenced Corrosion of Q235 Carbon Steel by Halophilic Archaeon Natronorubrum tibetense, **Frontiers in Microbiology**. 10 (2019).

[14] H. Qian, D. Zhang, Y. Lou, **Z. Li**, D. Xu, C. Du, X. Li, Laboratory investigation of microbiologically influenced corrosion of Q235 carbon steel by halophilic archaea Natronorubrum tibetense, **Corrosion Science**. 145 (2018) 151–161.

[15] H. Qian, J. Yang, Y. Lou, O. ur Rahman, **Z. Li**, X. Ding, J. Gao, C. Du, D. Zhang, Mussel-inspired superhydrophilic surface with enhanced antimicrobial properties under immersed and atmospheric conditions, **Applied Surface Science**. 465 (2019) 267–278.

[16] L. Huang, **Z. Li**, Y. Lou, F. Cao, D. Zhang, X. Li, Recent Advances in Scanning Electrochemical Microscopy for Biological Applications, **Materials**. 11 (2018) 1389.

Acknowledgements

As I reflect on this long and challenging journey of my Ph.D. career, I am deeply grateful for the support and encouragement of many individuals without whom this milestone would not have been possible. First and foremost, I would like to thank China Scholarship Council for the financial support of this Ph.D. work and the guidance of my supervisor team.

I extend my heartfelt thanks to my promotor Arjan, whose expertise and insightful guidance have been invaluable throughout this process. It was an amazing moment for me when we first met in Beijing, and I am glad it finally ended up with the opportunity of working on this project at Delft University of Technology under your supervision. You are a mentor, a critic, and an inspiration, pushing me to refine my ideas and broaden my thinking. You are always positive toward challenging tasks and available despite your tight schedule. I am also deeply grateful for the manuscript revisions, which significantly improved my writing skills. Beyond your academic guidance, your personal support during challenging times, particularly during the COVID-19 pandemic, has been invaluable, especially when returning home was nearly impossible for me at that time. I cherish the precious memories of enjoying meals with you and your families at your home during the Christmas holiday.

I am deeply thankful to my copromotor Axel, for introducing me to the fascinating field of electrochemical noise. It is astonished for me that you are always passionate, creative, and motivated in carrying out electrochemical noise measurements and signal processing methods. Thank you for mostly being the first to review my drafts and conference abstracts since this process is usually time-consuming. You are always at your earliest convenience whenever I request an online or in person discussion, means a great deal to me. Thank you for recommending me the fascinating places in the Netherlands, which has deepened my understanding and appreciation of this beautiful country. I am also deeply grateful to my copromotor Yaiza, whose expert knowledge in local electrochemical techniques help me a lot in my work. Thank you for your support, patience, and scientific input during our discussions. Your expertise and passion for SECM have profoundly shaped my approach to research and have greatly enriched my academic journey.

My gratitude extends to my colleagues and friends at Delft University of Technology, Peyman, Joost, Ali, Aytac, Agnieszka, Ursa, Prakash, Maxine, Sven, Eszter, Keer,

Curriculum Vitae

Ziyu Li

Born on 06 February 1994, Shandong, China

Education

09.2023-present	Postdoc. Department of Materials Science and Engineering, Delft University of Technology, Delft, the Netherlands
09.2019-09.2023	Ph.D. Department of Materials Science and Engineering, Delft University of Technology, Delft, the Netherlands
2016.09-2019.01	Master of Materials Science and Engineering, University of Science and Technology Beijing, Beijing, China
2012.08-2016.06	Bachelor of Materials Science and Engineering, University of Science and Technology Beijing, Beijing, China